RICE UNIVERSITY

# Plasmonic Nanostructures for Biological and Solar Application

by

**Oara Neumann**

A THESIS SUBMITTED
IN PARTIAL FULFILLMENT OF THE
REQUIREMENTS FOR THE DEGREE

**Doctor of Philosophy**

APPROVED THESIS COMMITTEE:

Naomi J. Halas, Chair
Stanley C. Moore Professor in Electrical and Computer Engineering, Professor of Physics and Astronomy, Professor of Biomedical Engineering, Professor of Chemistry and Director of Laboratory for Nanophotonics

Peter J. Nordlander
Professor of Physics and Astronomy
Professor of Electrical and Computer Engineering

Stephan Link
Assistant Professor of Chemistry, Assistant Professor of Electrical and Computer Engineering

HOUSTON, TEXAS
March 2013

# ABSTRACT

## Plasmonic Nanostructures for Solar and Biological Application

by

Oara Neumann

The electromagnetic absorption properties of plasmonic nanostructures were utilized to develop mesoscopic sites for highly efficient photothermal generation steam, SERS biosensing, and light-triggered cellular delivery uptake. Plasmonic nanostructures embedded in common thermal solutions produces vapor without the requirement of heating the fluid volume. When particles are dispersed in water at ambient temperature, energy is directed primarily to vaporization of water into steam, with a much smaller fraction resulting in heating of the fluid. Solar illuminated aqueous nanoparticle solution can drive water-ethanol distillation, yielding fractions significantly richer in ethanol content than simple thermal distillation and also produced saturated steam destroying Geobacillus stearothermophilus bacteria in a compact solar powered autoclave.

Subwavelength biosensing sites were developed using the plasmonic properties of gold nanoshells to investigate the properties of aptamer (DNA) target complexes. Nanoshells are tunable core-shell nanoparticles whose resonant absorption and scattering properties are dependent on core/shell thickness ratio. Nanoshells were used to develop a label free detection method using SERS to monitor conformational change induced by aptamer target binding. The conformational changes to the aptamers induced by target binding were probed by monitoring the aptamer SERS spectra reproducibility.

Furthermore, nanoshells can serve as a nonviral light-controlled delivery vector for the precise temporal and spatial control of molecular delivery in vitro. The drug delivery concept using plasmonic vectors was shown using a monolayer of ds-DNA attached to the nanoshell surface and the small molecular "parcel" intercalated inside ds-DNA loops. DAPI, a fluorescent dye, was used as the molecular parcel to visualize the release process in living cells. Upon laser illumination at the absorption resonance the nanoshell converts photon energy into heat producing a local temperature gradient that induces DNA dehybridization, releasing the intercalated molecules.

# Acknowledgements

I would like to thank my advisor Dr. Naomi J. Halas for her guidance during my graduate career. She has been a personal role model that has led me to reach my highest academic goals as a graduate student. I am grateful to her for providing me the opportunity to dive into many different projects and pursue different ideas. I have continuously benefited from her enormous source of knowledge, unique new ideas, and encouragement throughout the past several years. She has helped me to become a better scientist overall.

I am highly honored to have Dr. Peter Nordlander and Dr. Stephan Link in my dissertation committee. I would like to express my sincerest gratitude to both of them. Dr. Peter Nordlander, as my second advisor, has inspired new ideas and theoretical calculations for our solar projects. My various projects have benefited enormously from my interactions with many professors, post-docs, and students who gave generously of their time: Dr. Pernilla Wittung-Stafshede, Dr. Ben Janesko, Dr. Jeffrey D. Hartgerink, Dr. Gustavo Scuseria, Dr. Bruce Johnson, Dr. Maria Oden, Dr. Andrew Dick Dr. Kui Bao and Dr. Heidar Sobhani. I would also like to extend my appreciation to Ulrich Schrems and Gregory Giese who donated turbines, heat exchangers, and related equipments to the steam project.

I want to express my appreciation to all members of the Halas group for their friendships and collaboration on different projects: Dr. Tumasang N. Fofang, Dr. Surbhi Lal, Jared Day, Christyn Thibodeaux, Amanda Jones, Dr. Alexander Urban, Ciceron Orazco, Lisa Brown, Andie Schlather, Dr. Britt Lassiter, Mark Knight, Nick King, Yu Zhang, Shaunak Mukherjee, Fangfang Wen, Michael McClain, Nathaniel Hogan, Bob

Zheng, Greg Bond, Sam Gottheim, Ali Sobhani, Dr. Zheyu Fang, Lian Zhou, Valeria Spolon Marangoni, Dan Duan, Julius Mueller, and all former members of the Halas group: Bruce Brinson, Felicia Tam, Hui Wang, Nikolay Mirin, Priya Sundararajan, Ryan Huschka, Aoune Barhoumi, Rizia Bardhan, Janardan Kundu, Joe Cole, Jeremy Dumoit, Serge Grabtchak, Dongmao Zhang, Chaitra Rai, Cyre Kalu, and Joe Young. I would like to acknowledge Dr. Nathaniel Grady for additional help in building together the solar steam "Generation I" closed-loop system prototype.

Several undergraduate students worked at times on the steam project with me. Thanks to Kevin Schell, Eric Kim, Ben Lu, Mary K. Quinn, Shea Thompson, Michael Eastwood, Anjie Dong, Curtis Feronti, Michaela Blank, Leticia Comin, Benjamin Crabtree, Zachary Casias, Isadora Calderon, Guil Abreu, Anand Desai, Larissa Rangel, Amanda Wonnell, and Ryan Kellogg for all of their hard work. Many others at Rice University who have aided me along the way: Martha Alexander, Carolyn Aresu, Yvonne Kambourelis, Bo Chen, Wenhua Guo, Angelo Benedetto, Dwight Dear, Christopher Harris, Carlos Amaro, and for their assistance at all times.

Special thanks to my family and friends for their help, support, love, and encouragement; no words can express how much I love them.

# Table of Contents

# Table of Figures

**Figure 2.7** (i) Experimental powder Raman spectrum of adenine, and experimental SERS spectrum of adenine at (ii) pH 2.5 and (iii) 8.5. Intensities are in arbitrary units. Starred peaks are dominated by motions of the external amine group

**Figure 2.8** Schematic of proposed adenine-Au binding modes through ring nitrogens N3 (left) or N7 (right)

**Figure 2.9** Calculated IR absorbance spectra of (i) adenine and (ii) adenine-$H^+$. Asterisks "*" denote the $NH_2$ stretching mode; other details are in the text

**Figure 3.1** Schematic of aptamer SAM SERS-based analyte detection. Aptamers whose secondary structure is essentially eliminated by thermal treatment form SAMs on nanoshell substrates. Conformational changes in the aptamers induced by target molecule interaction are monitored by SERS.

**Figure 3.2** The SERS spectra of the anti-PDGF aptamer SAM (i) prior to exposure to PDGF, (ii) following PDGF exposure, and (iii) following Lysosyme exposure (a control protein). Insert: Γ values for the DNA aptamer SAM-PDGF and –lysozyme interaction. Error bars represent the standard deviation.

**Figure 3.3** The SERS spectra of anti-cocaine aptamer (i) alone, (ii) with cocaine, (iii) with benzocaine, and (iv) with caffeine. Insert: the cross correlation SERS spectra demonstrate that different target bindings induce spectral variation by re-inducing the hairpin structure of the aptamer. Error bars represent one standard deviation.

**Figure 3.4** (A) The average SERS spectra of anti-cocaine aptamer (i) alone, (ii) with benzocaine, and (iii) benzocaine. Insert: Γ values for the anti-cocaine aptamer SAM and aptamer–benzocaine interaction. (B) The average SERS spectra of random DNA (i) alone, (ii) with benzocaine, and (iii) benzocaine Insert: Γ values for the random DNA SAM and DNA-benzocaine interaction.

**Figure 3.5** The CD spectra of (A) anti-PDGF aptamer and (B) anti-cocaine aptamer showed a structural transition from a folding state (red) or hairpin state (blue) to an extended single-stranded state (black).

**Figure 3.6** The effect of concentration increase of PDGF-BB on the CD signal of anti-PDGF aptamer in solution concentrations of (a) 0 μM; (b) 0.022 μM; (c) 0.044 μM; (d) 0.088 μM; (e) 0.176 μM; (f) 0.22μM. Insert: linear relationship of the ellipticity of anti-PDGF aptamer at 218 nm with low PDGF-BB concentrations. The aptamer concentration is 4 μM.

**Figure 3.7** The melting curves at 274 nm of anti-PDGF aptamer (black), anti-PDGF aptamer with PDGF (red), anti-PDGF aptamer with Lyz (blue). Insert: The melting curves of anti-PDGF aptamer with PDGF taken after one cycle. This indicates that the aptamer returns to the original conformation.

**Figure 3.8** Temperature-dependent CD spectra of (a) anti-cocaine aptamer and (b) anti-cocaine aptamer thermal treated where the concentration of aptamer was $5x\ 10^{-6}$ M in TE buffer (pH=7.5) at the indicated temperature.

**Figure 4.1** Light-induced DAPI release. (a) Schematic diagram of the light-induced DAPI release and diffusion inside the cell. (b) Fluorescence emission of (i) DAPI only, (ii) DAPI with *ss*DNA, and (iii) DAPI with *ds*DNA.

**Figure 4.2** Nanoshell-*ds*DNA-DAPI cell uptake. Dark field/epifluorescence images of (a) H1299 lung cancer cells incubated with nanoshell-*ds*DNA-DAPI complexes, (b) nonincubated cells (control). (c) Bright-field image of middle slice of H1299 lung cancer cells incubated with nanoshell-*ds*DNA-DAPI complex.

**Figure 4.3** Light-induced DAPI release. (a,b) Flow cytometry histograms of DAPI Fluorescence (Ex:355 nm; Em:460 nm) versus number of isolated nuclei from H1299 cells incubated with (a) nanoshell-*ds*DNA-DAPI and (b) DAPI (control). Negative control (gray), treated cells without laser irradiation (blue) and treated cells with laser irradiation (red). Bar graphs display the mean DAPI fluorescence intensity (SEM before and after laser irradiation. (c) Epifluorescence images of H1299 cells incubated with nanoshell-*ds*DNA-DAPI (left) before and (right) after laser treatment. The cell membrane is marked by the green dye, Alexa-Fluor 488.

**Figure 4.4** Flow cytometry cytotoxicity assay. All plots are propidium iodide (PI) fluorescence intensity versus side-scattered light. (a) Negative control: H1299 cells not incubated with nanoshell-*ds*DNA-DAPI and no laser treatment. Cells incubated with nanoshell-*ds*DNA-DAPI for 12 h: (b) without laser treatment and (c) with laser treatment. (d) Positive control: cells were treated with 0.1% Citrate/ 0.1% Triton, which permeates the cell membrane, allowing PI to stain the *ds*DNA in the nucleus.

**Figure 5.1** Schematic of SEROA sample morphology: first layer: Au NPs; second layer: functionalized NPs with analyte of interest (hot spots junction, with molecules inside, excited at normal incidence (blue).

**Figure 5.2** Characterization of the Au NP film: (A) Optical extinction spectra of (i) NPs in solution, (ii) first layer of NPs on quartz PVP functionalized substrate, and (iii) second NPs layer functionalized with analyte molecules, and B) SEM image of a 3D-analyte nanoparticle film.

**Figure 5.3** Chemical structures of (S)- and (R)-Trp and (SS)- and (RR)-Cys-Phe-Gly-Gly with the chiral centers (Cα) indicated in red and the torsion center (XCβ) indicated in blue.

**Figure 5.4** (A) Vibrational spectra for Trp: (i) SERS, (ii) Raman, and SEROA spectra of (iii) (R)-Trp and (iv) (S)-Trp. (B) Γ values for the (i) (S)- and (ii) (R)-tryptophan spectra for SERS and SEROA. Error bars represent standard deviation**.**

**Figure 5.5** (A) Vibrational spectra for Cys-Phe-Gly-Gly: (i) SERS, (ii) Raman, and SEROA spectra of (iii) (SS)-Cys-Phe-Gly-Gly and (iv) (RR)-Cys-Phe-Gly-Gly. (B) Γ values for the (i) (RR)- and (ii) (SS)-Cys-Phe-Gly-Gly spectra. Error bars represent standard deviation.

**Figure 5.6** (A) Circular dichroism (CD) spectra of (i) (S)- Trp and (ii) (R)-Trp in aqueous solution. The inset shows the CD spectra of (iii) (S)-Trp and (iv) (R)-Trp monolayer on a

experiment schematics and (D) the photograph of the setup for the mass loss experiments. A 26.7 x 26.7 cm Fresnel lens with a 44.5 cm focal length was used to focus light into a 40 ml beaker which contained the nanoparticle solution. The beaker was placed on an analytical balance (AD500 series with 1 mg resolution from Fulcrum Inc., NJ).

**Figure 7.4:** The steam generation experimental apparatus with (A) electrical or (B) solar heat systems used for steam formation efficiency quantification.

**Figure 7.5:** Solar steam generation efficiency: (A) The steam formation efficiency vs. Au nanoshell concentration under solar irradiation (red) and electrical resistive heating (blue).

**Figure 7.6:** Steam bubble formation through solar absorption by gold nanoshells. (a) The absorption cross section of the gold nanoshells is tuned to overlap the solar spectral irradiance (AM 1.5 G). (b) Comparison of the combined weight of a gold nanoshell and its surrounding steam bubble (red curve) with the weight of the displaced water (blue curve) over time. After 4 μs, the density of the encapsulated nanoshell becomes less than that of the surrounding water, causing the nanoshell to rise to the surface, releasing the steam bubble. (c) Size of the steam bubble surrounding a nanoshell over time (red curve). After 20 ms of steam generation, the size of the bubbles becomes larger than half the average distance between the nanoshells (horizontal gray line), allowing the bubbles to coalesce, thus further enhancing the steam generation process.

**Figure 7.7:** Solar distillation of ethanol: (A) Photo of the solar distillation apparatus including (a) vacuum-jacketed glass container, (b) connector tube, (c) water condenser, and (d) fraction collector vessel. The solution was irradiated by a (e) 26.67 x 26.67 cm Fresnel lens with a 44.5 cm focal length (inset). (B) Vapor-liquid diagram of ethanol-water fractions produced by solar distillation. Mole % of ethanol in vapor phase for Au nanoshell alcohol-water mixtures under solar exposure (red dots) and standard equilibrium distillation curve at 1 atm and 25°C (blue curve). The Au nanoshell concentration is $2.5 \times 10^{10}$ particles/mL.

**Figure 7.8:** (A) The calibration curve used for determining the ethanol content in water-ethanol mixture after solar distillation process; (B) The GC signal of (i) ethanol reference, (ii) methanol-ethanol solution as reference, and (iii) ethanol from distillation process demonstrating that no degraded ethanol is detectable as a result of the solar distillation process.

**Figure 8.1:** Temperature evolution of solar steam generation**.** (A) The temperature vs. time for Au nanoshell-dispersed water: (i - liquid, ii – vapour) and for water without nanoparticles (iii - liquid, iv – vapour) under solar exposure. (B) Photograph of system used in the temperature evolution of solar steam generation: (a) transparent vessel isolated with a vacuum jacket to reduce thermal losses, (b) two thermocouples for sensing the solution and the steam temperature, (c) pressure sensor, and (d) 1/16 inch nozzle.

**Figure 8.2:** (A) Schematic of the compact solar autoclave showing: I: steam generation module, II. connection module, and III. sterilization module. The components of the system are: (a) sterilization vessel, (b) pressure sensor, (c) thermocouple sensor, (d) relief

valve, (e-f) control valves, (g) solar collector containing the nanoparticle-based heater solution, (h) check valve, (k) solar concentrator (a plastic Fresnel lens of 0.67 $m^2$ surface area), and (B) a photograph of the solar closed loop system.

**Figure 8.3: The autoclave temperature evolution under solar illumination.** The steam temperature vs. time measured at the input and output of the sterilization module: input (top of vessel, red) and output (bottom of vessel, blue). The dashed line indicates the temperature required for sterilization and the red segment indicates the sterilization cycle (115$^o$C for 30 minutes). The ambient temperature (green curve) was monitored as a reference.

**Figure 8.4:** B**iological indicators used to test solar autoclave sterilization**. Test vials of Geobacillus stearothermophilus placed in various locations in the sterilization module: (a) top of vessel, (b) bottom of vessel, (c) unprocessed control. Sterilization is confirmed by color change of vial.

**Figure 9.1**: Schematic and photograph of the solar autoclave for human waste sterilization. The components of the system are: (a) solar concentrator (44-inch dish mirror) (b) heat collector containing metallic nanoparticles, (c) waste sterilization vessel that contains a pressure sensor, two thermocouple sensor, a steam relief valve, two hand pumps and valves that control the input and output of waste. The solar concentrator dish system has a dual tracking system powered by a small car battery recharged by a solar cell unit.

**Figure 9.2:** (A) The autoclave temperature evolution under solar illumination. The steam temperature vs. time measured at the input and output of the sterilization module: input (top of vessel, red) and output (bottom of vessel inside the fecal simulant, blue). The dashed line indicates the temperature required for sterilization and the red segment indicates the sterilization cycle (132$^o$C for 5 minutes). The ambient temperature (green curve) was monitored as a reference. (B) Biological indicators of Geobacillus stearothermophilus placed in fecal stimulant and unprocessed control was used to test solar autoclave sterilization. The sterilization is confirmed by color change of vial.

Figure 10.1: Solar distillation of ethanol: (A) Photo and (B) Schematics of the solar distillation setup including (a) vacuum-jacketed glass container, (b) connector tube, (c) water condenser, and (d) fraction collector vessel. The solution was irradiated by a (e) 26.67 x 26.67 cm Fresnel lens with a 44.5 cm focal length.

**Figure 10.2:** The vapor-liquid equilibrium diagram of alcohol-water fractions produced by distillation of Au nanoshell-alcohol-water mixtures. Mole % of ethanol in vapor phase for Au nanoshell alcohol-water mixtures under (A) solar, (B) laser exposure (red dots) and standard equilibrium distillation curve at 1 atm. and 25$^o$C (blue curve). The black line in the figures represents an equal concentration of alcohol in both the liquid and the vapor state. The Au-nanoshell concentration was $0.25x10^{10}$particles/mL for all the measurements.

**Figure 10.3:** Picture of the setup used to measure the heat of vaporization under (A) solar and (B) laser exposure and (C) Schematic of the setup: (a) vacuum jacketed glass

container, (b) two thermocouples that measure the solution/steam temperature, and (c) a pressure sensor. The solution was irradiated by (d) 26cm x 26cm Fresnel lens with a 44 cm focal length, and a (e) 15 W power laser beam, 808nm.

Figure 10.4: Types of boiling during the distillation of Au nanoshell-ethanol-water mixtures: The photographs show the boiling behaviour of the Au nanoshell-water mixture: (a) boiling, (b) few periodic explosions, (c) one initial explosion at the beginning of the heating where one bubble is generated and moves along the mixture surface with an oscillating motion, and (d) the evaporation without boiling. The time dependent (a'-d') pressure and (a''-d'') temperature (red-steam, blue-solution temperature) corresponds to each type of boiling.

**Figure 10.5:** (A) Enthalpy (Heat) of vaporization and (B) Boiling temperature vs. mole fraction of the Au nanoshell-ethanol-water mixtures under solar illumination at atmospheric pressure. The line corresponds to the fitting curve with the equations: (A) y=42.9-23.57x+20.4x2 and (B) y=23.85e (-x/0.18199).

**Figure 10.6:** vaporization enthalpy of Au nanoshell suspend in proof ethanol under (black) solar and (red) NIR laser exposure and the Temperature/pressure vs. time curves used to calculate the vaporization enthalpy.

**Figure 10.7:** The vapor-liquid equilibrium diagram of alcohol-water fractions produced by distillation. Mole % of ethanol in distillate vapor phase: (red) Au nanoshell and (black) Carbon nanoparticles alcohol-water mixtures distillation under solar exposure.

**Figure 11.1:** SEM images of Au self-similar nanostructures synthesized with different PVP concentration: (i) 6.25μM, (ii) 13.75μM and (iii) 25μM. The L-ascorbic acid concentration is constant 0.4M.

**Figure 11.2:** The SEM images of nanostructure synthesized with different L-ascorbic acid concentration (i) 0.02M, (ii) 0.2M and (iii) 0.4M. The PVP concentration is constant.

**Figure 11.3:** Extinction spectra of Au self-similar structures: (i) 150nm, (ii) 500nm, and (iii) 1μm diameters.

**Figure 11.4:** (A) FTIR spectra and (B,C) the corresponding SEM image of Au self-similar structures showing multiple gold branches of 25-30nm diameter and a very narrows size distribution.

**Figure 11.5:** (A) $N_2$ adsorption-desorption isotherms of gold corals using BET, (B) pore size distribution of the samples calcinated at 150ºC for 8 hours, (C) BET plots of Au self-similar structures.

**Figure 11.6:** A heating scan at 15 deg $min^{-1}$ for (A) High-resolution XPS spectrum and (B) DSG spectrum of gold coral nanostructures. Insert are images of Au self-similar structures (black) powder in a ceramic pan illustrating the melted structure (yellow) at 800ºC.

**Figure 11.2:** The SEM images of nanostructure synthesized with different L-ascorbic acid concentration (i) 0.02M, (ii) 0.2M and (iii) 0.4M. The PVP concentration is constant.

**Figure 12.1** Schematic representation of experimental set-up showing a DC power supply connected between two Pt electrodes (gray bars), separated by 0.014 m, immersed in aqueous gold nanorice solution.

**Figure 12.2** Electron microscopy and crystallographic studies of mezostars prepared at 5V. (A) SEM image of Mezostars. (B) XRD spectra of (i) α-Fe2O3 cores, (ii) nanorice (showing gold peaks), and (iii) mezostars. The spectra are offset for clarity.

**Figure 12.3** TEM micrographs of (A) a star-shaped structure obtained after 6 h of electrolysis and ED pattern showing polycrystalline rings provided as inset, (B) a mesostar formed after 24 h of electrolysis and corresponding SAED pattern representing orthorhombic α-FeOOH single crystalline domain, (C) an α-FeOOH nanocrystals observed in solution and SAED pattern showing orthorhombic α-FeOOH single crystalline domain, (D) tip of a mesostar and corresponding SAED pattern representing orthorhombic α-FeOOH single crystalline area, (E) dark field image of mesostar tip corresponding to panel D, and (F) mesostar obtained after 24 h of electrolysis; ED pattern showing polycrystalline rings provided as top inset, and SAED pattern representing cubic Au single crystalline area provided as bottom inset. The selected area corresponding to the SAED patterns in panels B-D, F are shown in circle.

**Figure 12.4** (A) Schematic representation of mesostar formation mechanism. (B) SEM images supporting the mesostar formation mechanism starting with (i) nanorice, (ii) 2 h of electrolysis, (iii) 4, (iv) 6, (v) 8, (vi) 10, (vii) 12, and (viii) 24 h.

**Figure 12.5** SEM image of long chain branched structures obtained both at 5 V and 10 V in addition to the mesostars.

**Figure 12.6** SEM images of (A) α-Fe2O3 cores, (B) assembled α-Fe2O3 cores formed after 10 hrs of applying 5 V, (C) pyramidal mesostructures 500 ± 50 nm in length and width, and 350 ± 20 nm in height formed after 14 hrs, (D) larger pyramidal mesostructures 650 ± 100 nm in length and width, and 370 ± 50 nm in height formed after 24 hrs; (E) XRD spectra of (i) α-Fe2O3 cores, and (ii) pyramidal mesostructures.

**Figure 12.7** SEM images of mesostructures obtained by varying the voltage while keeping electrolysis time constant at 24 h: (A) aggregated nanorice formed at 0.5 and 1 V and high resolution image provided as inset; (B) stars ~4 ± 0.2 μm in length and width, and 1.1 ± 0.2 μm in height formed at 2 V; (C) stars ~3.1 ± 0.7 μm in length and width, and 0.8 ± 0.3 μm in height obtained at 3 V; (D) mesostars 650 ± 80 nm in length and width, and 380 ± 30 nm in height observed at 5 V; and (E) distorted stars 450 ± 150 nm in length observed at 10 V.

**Figure 12.8** Extinction spectra of (i) α-Fe2O3 cores with $\lambda_{max}$ ~ 390 nm, (ii) nanorice particles with longitudinal Plasmon $\lambda_{max}$ ~ 1100 nm and transverse plasmon $\lambda_{max}$ ~ 650 nm, and (iii) mesostars with $\lambda_{max}$ ~ 430 nm. The samples measured are monolayers of nanoparticles immobilized on PVPglass slides. The spectra are offset for clarity.

# Table of Tables

# Chapter 1: Metallic Nanoparticles

Metallic nanoparticles have been used by artisans since the 9th century, but their optical properties were first described by Michael Faraday in 1857. Since then nanoparticles have generated an ever-increasing interest because they stand as a bridge between macro materials and atomic or molecular structures. In plasmonic nanostructures, conduction band electrons are not bound to individual atoms, instead they form a "cloud" around the atomic cores. When a metal absorbs light of a resonant wavelength it causes the free electrons cloud to oscillate with respect to the fixed positively charged ions in the metallic nanostructure. These coherent oscillations of the conduction electrons are called plasmons. For nanoparticles, the plasmons are confined in the interior of a small finite volume; therefore, close to the surface, the metallic nanoparticles exhibit a strong field enhancement. This highly localized field, decays rapidly away from the nanoparticle/dieletric interface into the dielectric background. Moreover, the oscillations are very sensitive to any dielectric changes in the immediate environment and exhibit enhanced near-field amplitude at the resonance wavelength. This effect was theoretically described by Mie in 1908.[1] In the case of nanoparticles smaller than half the wavelength, only the dipole oscillation contributes significantly to the extinction cross section whereas for large nanoparticles, retardation effects lead to the excitation of high-order modes.[2] The plasmon energy is partially dissipated in the metal and partially reradiated in the far-field. The relative intensity of these two processes is strongly influenced by their structural parameters: size, shape, and metal composition. Recent computational and theoretical models have been developed to describe the coupling between plasmon modes

in nanostructures. Additionally, the theories show that the plasmons of neighboring metallic nanostructures can interact and hybridize similar to the electronic wave functions of simple atomic and molecular orbitals.[3]

Advances in synthesis and modeling of plasmonic nanostructures, such as nanospheres, nanorods, silica/gold nanoshells, nanowire, nanocubes, nanorice, or nanostars, have led to various applications, such as biochemical sensors,[4] whole blood immunoassays,[5] drug delivery,[6-9] photothermal ablation of cancer cells [10-13] and the imaging/therapy,[14-15] genomics,[16] optical imaging,[17] optical coherence tomography,[18] two-photon luminescence,[19] as well as in catalysis.[20] Another outstanding example is the rapid development of metamaterials [21-23] with negative optical refractive index. Furthermore, as plasmons relax to the ground state, heat is released and transferred to the lattice via electron-phonon interactions. The heat is then transferred from the metal surfaces to the environment via phonon-phonon interactions, leading to a thermal distribution gradient around the particles. This process is useful for developing high efficiency energy generators in industry. [20,24-27]

Metal nanoshells, comprised of a spherical dielectric core covered by a thin Au shell, possess distinct advantages over other types of tunable plasmonic nanostructures; first, nanoshells (NS) are symmetric particles. Second, their respective plasmon resonance wavelengths can be both easily tuned by varying the ratio of its core/shell radii and can be predicted by the plasmon hybridization model[3] and Mie scattering theory.[1] The NS plasmon resonance also allows for the manipulation and enhancement of local electromagnetic fields at nanoparticle surfaces. When coupled with the high degree of

biocompatibility of gold surfaces, nanoshells become suitable for a wide variety of biological applications.

### 1.1 Silica-gold nanoshell

Metal nanoshells are concentric nanoparticles with a dielectric core often silica, surrounded by a thin metal shell such as gold or silver.[28] Gold nanoshells (NS) possess physical properties similar to gold colloids, meaning that when exposed to light they share a strong optical absorption due to the collective electronic response of the metal. The optical response of gold NS depends dramatically on the relative size of the nanoparticle core and the thickness of the gold shell. Hence, by varying the relative core and shell thicknesses, the plasmonic resonance of a NS can be tuned over a wide spectral range, all without varying the overall particle size or shape.[29-30] Figure 1.1 demonstrates the plasmon tunability spectra of NS using Mie theory calculation. In this figure, the core and shell of the nanoparticles are shown to relative scale directly beneath their corresponding optical resonances. The optical resonant properties are much more sensitive to thickness of the metal shell than the overall size of the nanoparticle. For example, the dipole resonance of a nanoshell with 60 nm silica core and 10 nm gold shell thickness shows significant red shift from that of nanoshell with 65 nm and 10 nm shell thickness.

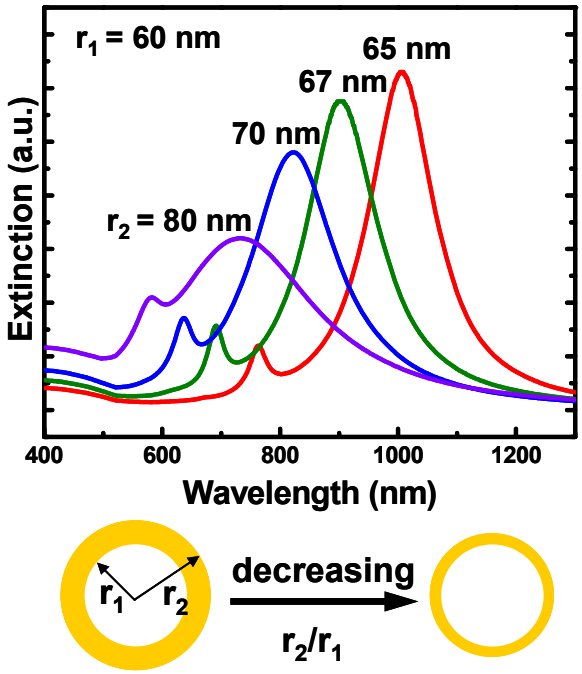


**Figure 1.1**: Theoretically calculated (Mie scattering) optical resonances demonstrating plasmon tunability for nanoshells with an inner silica core radius $r_1$ = 60 nm and an overall particle radius $r_2$ = 65, 67, 70, and 80 nm (corresponding to 5, 7, 10, and 20 nm thick Au shells). The plasmon resonance of the particles red shifts with the increase of $r_1/r_2$ increases; modified from Oldenburg *et al*.[31]

Such optical tunability enables the use of NS in a broad range of biomedical applications, ranging from whole blood immunoassays,[5] drug delivery,[6-7,9] photothermal ablation of cancer cells,[10-11] and the dual imaging/therapy.[14-15] Their spectral region which includes the 800-1300 nm "water window" of the near infrared is also particularly interesting due to the absence of significant absorption from either biological chromophores or water thereby, permitting deep optical penetration into biological samples. Furthermore, gold NS are particularly attractive for use in biological applications due to various reasons such as: the gold metal being resistant to corrosion,

the exceptional lack of low toxicity in medical applications, and the easy conjugation of organic molecules onto its surface. [32] In addition, irradiation of nanoshells at their peak extinction coefficient leads to the conversion of light into heat energy that produces a local rise in temperature, all of which allows the development of highly efficient industrial energy generators.[20,27] The plasmon-induced enhancement of the electromagnetic field, near the metal surface, can then be used to amplify the signals of Raman scattering, fluorescence, and infrared absorption spectroscopies.

### 1.2 Plasmon hybridization

The optical properties of metal nanoparticles are governed primarily by their coherent oscillations of conduction-band electrons, known as plasmons. The plasmon response of metal-based nanostructures can be explained by Plasmon Hybridization Model,[3] which describes an interaction between the metallic sphere and the spherical cavity inside the bulk metal. This is analogous to the bonding and antibonding that is noted in molecular orbital theories (Figure 1.2). This interaction will then split the NS plasmons into two modes: a high-energy anti-symmetric plasmon and second low-energy symmetric plasmon mode. This latter mode can be observed experimentally, as it couples more strongly to the optical field; however, its amount of splitting depends on the factor $r_1/r_2$. As the shell thickness is decreased, the interaction between sphere and cavity plasmon increases, resulting in an increased splitting of the nanoshell plasmon and a shifting of the optically active plasmon resonance to larger wavelength.

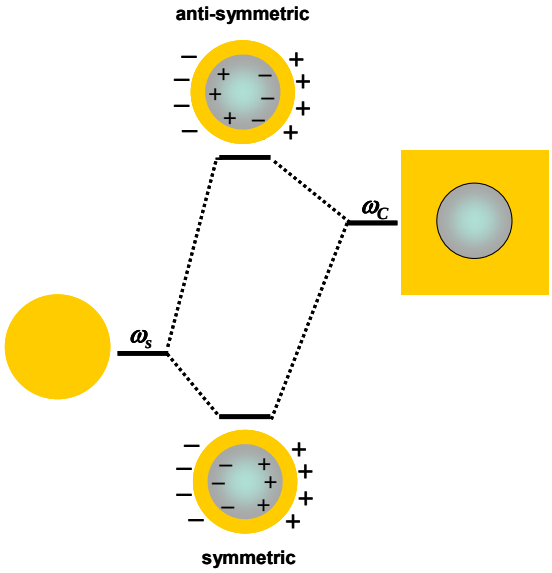


**Figure 1.2:** Plasmon hybridization diagram (the sphere-cavity model) for gold nanoshells.

This Plasmon Hybridization Model explains why the NS Plasmon will shift to lower energies as the shell thickness is decreased and agrees quantitatively with classical electromagnetic Mie scattering theory.[1] This Plasmon Hybridization Model predicts not only the optical plasmon resonance of NS, but also the multi-particle interactions noted in dimmers, trimmers, or quadrumers.[33-35] The geometrical sensitivity of plasmon resonances of metallic nanoparticles and the ability to tune the plasmon resonances to wavelengths of interest is important because it provides a simple and general principle that can be used to guide the design new metallic nanostructures.

### 1.3 Nanoshell fabrication and characterization

The Au-silica nanoshells are fabricated using a bottom-up wet chemistry synthesis[28,36] developed by Oldenburg. Figure 1.3 presents schematic illustration of nanoshell

fabrication and TEM images of experimentally fabricated nanoshells. The silica cores used this work were from Precision Colloids, LLC (Cartersville, GA).

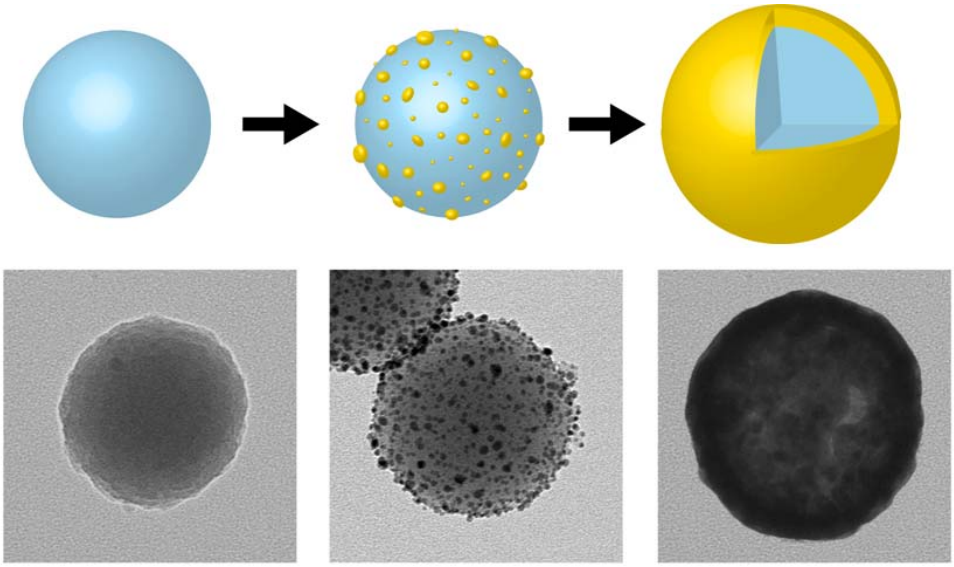

**Figure 1.3:** Schematic of nanoshell fabrication accompanied by corresponding TEM micrographs.

The Stöber particles surface is functionalized with 3-aminoproplytriethoxysilane (APTES) or aminopropyltrimethoxysilane (APTMS) (from Sigma- Aldrich). This chemical functionalization of the silica surface provides an amine moiety at the surface, which is used to attach small gold colloid. The gold shell is grown on the silica cores via seed-mediated electroless plating. First, small gold colloids (1-3 nm) in size are synthesized by reducing chloroauric acid using tetrakis (hydroxymethyl) phosphonium chloride (THPC) (from Sigma- Aldrich) as a reducing agent. The THPC-Au attached to the silica surface act as nucleation sites for the electroless deposition of Au to form a complete shell on the silica core. The electroless deposition was achieved by reducing gold from a solution of 1.8 mM potassium carbonate and 0.4 μM chloroauric acids by

formaldehyde. The sizes of the silica cores and the completed nanoshells were determined using UV-Visible spectroscopy and electron microscopy- both a scanning electron microscope (SEM) and a transmission electron microscope (TEM; Figure 1.3.2).

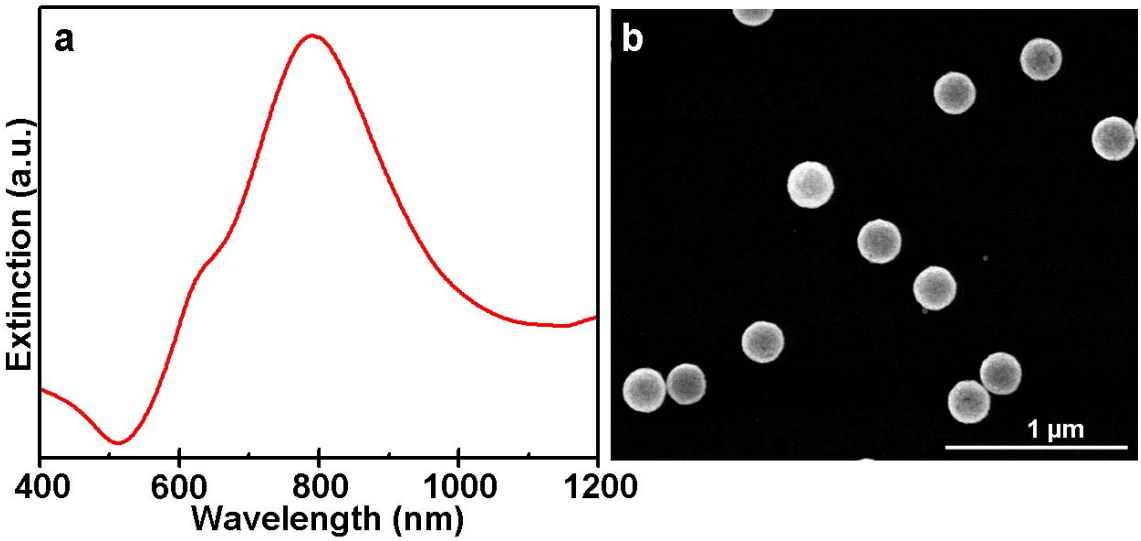


**Figure 1.3.2:** (a) The extinction spectrum in water and (b) the SEM image of nanoshells. The nanoshells dimensions are: $[r_1, r_2] = [63, 75]$ nm.

### 1.4 Surface plasmon-enhanced spectroscopy

When plasmonic nanostructures interact with light, they produce a strong local field enhancement near the surface, thereby further augmenting the spectra of the molecules that are attached to the plasmonic nanostructures. These molecules have a unique set of energy levels that depends on their unique atomic and molecular structure like the mass of atom, the strength of the bond, the conformation, as well as the specific molecular arrangements. The atoms in the molecular arrangement can compress or stretch along the axes of a bond, or can bend symmetrically or asymmetrically; yields vibrations, which

occur at a unique frequency. Therefore, the vibrational spectroscopy can provide the "fingerprint" of any molecular system in gas, liquid, or solid phase.

### 1.4.1 Surface enhanced Raman spectroscopy (SERS)

In 1928 Sir Chandrasekhra V. Raman discovered a "feeble phenomenon" that includes a very small fraction, about 1 in $10^7$, of the incident photons. He used sunlight as the source, a telescope as the collector and his eye as the detector. This process, termed Raman spectroscopy, is the study of the complex interaction between the incident electromagnetic wave and the matter in which the light is inelastically scattered and vibrational modes of molecules and crystals are detected. Raman is a process where an incoming photon with frequency $\omega_i$ excites a molecular vibration with frequency $\omega_v$ while emitting a scattered photon at $\omega_s = (\omega_i - \omega_v)$ as illustrated in Figure 1.4.1a. When light is scattered from a molecule, the majority of photons are elastically scattered (the excited molecules returned back to the same vibrational state and emits light with the same frequency as an excitation source, Rayleigh scattered) while a small fraction of these photons interact with the vibrational mode. The difference in energy (or shift in frequency by the frequency of the bond vibration) between the incident photon and the Raman scattered photon is equal to the energy of vibration of the scattering as shown in the energy level diagram in Figure 1.4.1b. These Raman shifted photons can have a higher frequency (anti-Stokes) or a lower frequency (Stokes). The Stocks and anti-Stokes spectra contain the same frequency information.

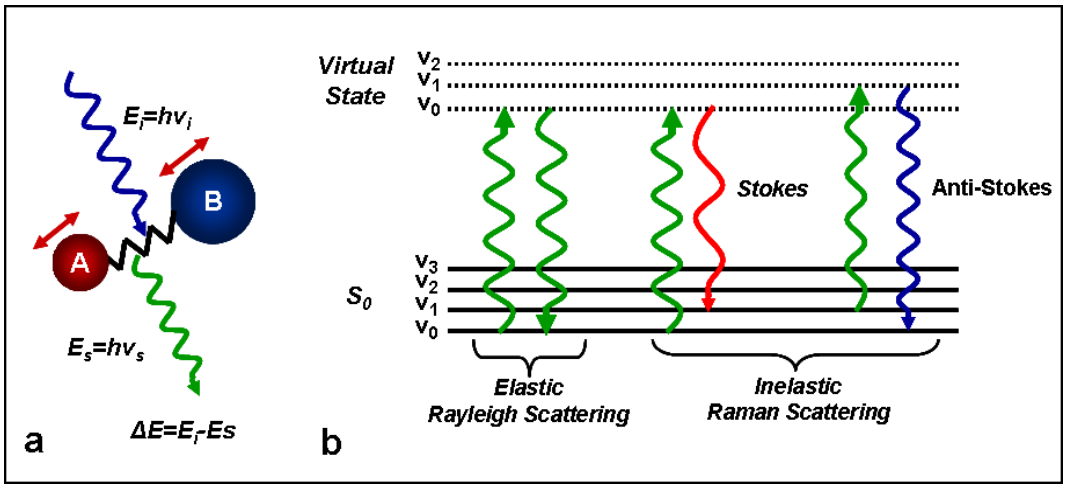


**Figure 1.4.1:** (a) Schematic illustration of Raman scattering and (b) Energy level diagram of the Raman scattering process. Modified from Talley *et al*. [37]

The vibrational modes of a molecule give rise to a spectrum that provides quantitative information about the molecular species in the probe volume. [37-39] The different functional groups of a molecule have different characteristic vibrational energies, so that every molecule presents a unique Raman spectrum that is akin to a molecular signature. This makes Raman spectroscopy a powerful technique as it provides a molecular fingerprint rich in structural information.[40] While the photon interacts with the matter, the electron orbits within the constituent molecules which are perturbed periodically; then, the nuclei and the electrons relax until equilibrium is reached. This distortion is known as polarizability. The intensity of Raman scattering is proportional to the amount of polarizability change and depends on the conformation of the molecule.

In practice, Raman spectroscopy is generally performed with a laser as the excitation source because this intense, collimated monochromatic light source enables the measurement of relatively small Raman shifts, while the intense beam allows for

improved spatial resolution and signal-to noise ratio. Raman spectroscopy is a nondestructive, fast analysis technique that requires only small sample volumes and nearly no interference of water occurs. Another important factor that lower the Raman signal is the cross section, it is about $10^{-31}$-$10^{-26}$ $cm^2$ per molecule.

Surface Enhanced Raman Spectroscopy (SERS) was discovered by Fleishmann [41] and Van Duyne [42] and independently by Albrecht and Creighton[43] in 1977 based on the observation of enhanced Raman signals from pyridine on a rough silver electrode. SERS is a form of Raman spectroscopy which involves the study of samples adsorbed to or interacting with roughened noble-metal substrate.[44] SERS may give rise to spectral enhancements of $10^5$ or even $10^6$ compared to normal Raman scattering. Being a very straightforward technique that requires very small analyte concentration, SERS facilitates single molecule detection, which is widely reported.[45-47]

The enhancement factor in SERS is a result of two main effects: the electromagnetic (EM) enhancement effect and the charge transfer (CT) effect.[48-49] These two effects arise due to the intensity of Raman scattering which is directly proportional to the square of the induced dipole moment ($\mu_{ind}$) in the molecule, which in turn, is the product of the Raman polarizability ($\alpha$) and the magnitude of the incident electromagnetic field.

$$I_{Raman} = \alpha\left|\mu_{ind}\right|^2 = \left|\alpha E\right|^2 \quad (1)$$

The EM theory essentially addresses the amplitude enhancement of the electric field, and the CT model is concerned with the enhancement of molecular polarizability. A common feature of both theories is that spectral enhancement requires surface roughness.[50-54]

SERS sensitivity is dependent on the distance between the metal surface and the Raman active molecules; and yet this does not require that the adsorbant to be in direct

contact with the surface rather it is deemed that it be within a certain sensing volume distance.[55-56] This is why the largest SERS response is to be expected from molecules that are directly adsorbed onto, or attached to the metal surface, while a smaller response is noted from molecules tethered away from the surface; meaning that when the near field decays, there is a monotonic decrease in the SERS signal. Another condition that will create a high SERS enhancement is when the laser excitation wavelength is near to, or within the linewidth of the plasmon resonance band. This latter enhancement results from the nanoparticles re-emitting a portion of their electromagnetic energy through their interactions with the scattering field intensity ($I_{surf}$)

$$E_{surf}^2 = 4E_0^2 g^2 \quad (2)$$

where g is related to the complex dielectric function of metal:

$$g = \frac{\varepsilon - \varepsilon_m}{\varepsilon + 2\varepsilon_m} \quad (3)$$

$\varepsilon = \varepsilon_1 + i\varepsilon_2$ and $\varepsilon_m$ is the medium's dielectric constant at optical frequencies ($\varepsilon = n^2$, for example n=1.33 for water). However the SERS intensity is the product of the square of incoming field and the outgoing field:

$$I_{SERS} \propto 16E_0^4 g^4 \quad (4)$$

Thus, the enhanced factor is determined by $g^4$. In contrast, the chemical enhancement may occur when molecules adsorbed on metal surfaces affect the charge transfer between adsorbates and metal surface. The polarizability of the molecule depends on the vibration mode and the surface plasmon enhancement. This is why the Raman signal from highly polar moiety, such as OH in water, is very weak, while moieties such as the π-electron cloud of the carbon double bond which can be easily distorted through bending or

stretching mode in an external electric field, will lead to a strong Raman signal. Despite these issues, Raman spectroscopy provides information that is complementary to absorption IR spectroscopy and is a non-destructive method.

### 1.4.2 Surface enhanced Raman optical activity (SEROA)

Molecules with asymmetric structures, this meaning that atoms in the molecule are not super-imposable on their mirror images, will show optical activity (OA) stemming from the rotation the direction by which light vibrates through the molecule. Louis Pasteur observed the connection between OA and molecular structure for the first time, in a mixture of tartaric acid salt. Pasteur used the physical appearance of the salt crystals to differentiate them based on how isomers polarized light differently. However, the concept of asymmetry was not established until 1874, when Jacobus Hendricus van't Hoff and Joseph Achille Le Bel independently developed the basis for the observed optical activity: tetrahedral carbon atoms bonded to four different atoms or groups of atoms. Optical active molecules did not have a plan of symmetry or a center of symmetry, each is the mirror image of the other. Such molecules, identified as isomers, have the same molecular formula but different spatial orientation of their atoms; therefore, they have a different bioactivity. While one enantiomer may produce the desired therapeutic activities, the other may be inactive, or produce unwanted side effects, for example ethambutol is a tuberculostatic agent whereas the other enantiomer causes neuritis than can lead to blindness.[57] Therefore, it becomes critical to quickly distinguish chiral molecules at low concentration, due to their human exposure liabilities.

Raman optical activity (ROA), also an inelastic scattering process, measures the tiny difference in the intensity of vibrational Raman scattering from chiral molecules by right-circular and left-circular incident polarized light, or equivalently the intensity of a small circularly polarized component in the scattered light using incident light of fixed polarization. [58] In other words, ROA measures the chirality associated with molecular vibrational transitions.[59] Since this spectroscopy is more sensitive to the backbone of a molecule than the side chains, it therefore, provides both biomolecular stereochemistry information of chiral molecules, and information concerning vibrational assignments in complex molecules.

Due to its origin in higher order effects, ROA is an extremely weak phenomenon, usually 3–5 orders of magnitude smaller than Raman scattering. ROA scattering cross-sections are $E^{-3}$ to $E^{-4}$, less than the cross-section of conventional Raman, while signal-to-noise ratios can be $E^{3}$ to $E^{4}$ greater than that of Raman spectra. Therefore, extracting ROA spectra from molecules of biological interest requires high sample concentration, high excitation powers, and long collection times up to hours. The fundamental scattering mechanism responsible for ROA discovered by Atkins and Barron showed that interference between the light waves scattered via the molecular polarizability and optical activity tensors of the molecule yields a dependence of the scattered intensity on the degree of circular polarization of the incident light and to a circular component in the scattered light.

The greater overall enhancement of ROA can be overcome by a several orders of magnitude enhancement through an electromagnetic enhancement mechanism that is a direct consequence of the presence of metal roughness features at the metal nanoparticles

surface. Surface-enhanced Raman optical activity (SEROA) use the enhancement in the optical field introduced by metallic nanoparticles and produces increases in the sensitivity, rapidity, and conformational information of chiralic molecules at metal interfaces.[60-63] Silver nanoparticle aggregates in solution have been used as a first plasmonic substrate for SEROA. A particular advantage of SEROA or SERS is that it is a nondestructive technique. Biological samples can benefit from such analysis as their native state can easily be analyzed using SERS or SEROA, since highly polar solvents like water do not possess a center of symmetry, meaning they are not a strong Raman scatterer, instead these are strong infrared absorber.

### 1.4.3 Surface enhanced infrared absorption (SEIRA)

Infrared Spectroscopy is a complementary technique to Raman and uses the effect of absorption of a photon having the same frequency as a vibrational mode. One photon is absorbed and generates a phonon of the same energy. The IR spectroscopy probes illustrate almost all bands of the adsorbed species as long as the vibrational mode includes a dipole component perpendicular to the surface.[64] To measure a spectrum the whole frequency range has to be covered by the incident radiation. Infrared absorption enhancement is highly dependent on the molecular structure of the adsorbed molecules and is significantly greater for vibrations of polar groups having large dipole moment gradients.

Using high surface sensitivity nanostructures, with controllable plasmon resonances having peak frequencies ranging from the visible spectral region to values well into the near IR, the vibrational modes of the adsorbed molecule may be enhanced by

approximately two orders of magnitude.[65-66] Although the enhancement factor of SEIRA is smaller than that of SERS, the cross-section for IR absorption is several orders of magnitude higher than the corresponding Raman cross-section. Similar to the SERS two different mechanisms are supposed to contribute to the total enhancement, i.e., an electromagnetic and a chemical effect. The chemical effect is due to molecule-metal electronic interaction modifying the molecular level structure and transition moments while the electromagnetic effect is due to the contribution of the "lightning-rod" effect and hybridized plasmons.[67] The lightning-rod effect occurs when metals act as perfect conductors and expel the electric field from the interior of the metals. This screening squeezes the electric field into the junctions between the metal nanoparticles, resulting in large field intensities enhancement in the mid-IR. This large electric field enhanced is not limited to the nanoshells array but depends strongly on the shape of the particles that constitute the SEIRA array substrate.

Hybridized plasmons which occur when two individual nanoparticles are placed adjacent to each other, such that their constituent plasmonic modes couples, is analogus to bonding and antibonding combinations noted in the molecular orbital theory.[68-70] In the quasi-static limit the in-phase dipole coupling modes interact strongly with incident radiation ("bright" modes), the antiphase dipole coupling modes have zero net dipole moment for identical dimer building blocks and are thus the "dark" modes. The hybridization plasmons can create regions of concentrated fields "hot-spots" in the junction between the nanoparticles at their corresponding frequencies. This interaction results in a wavelength shift that depends sensitively on the particle separation. These remarkable large plasmon shifts and concentrated electromagnetic fields must overlap to

the dipole vibrational modes of the adsorbate molecule. A fundamental challenge remains the highly reproducible nanostructures that exhibit spatially controlled hot-spots.

The largest advantage of surface enhanced vibrational spectroscopy is that of the time spent collecting the measurement. This makes SEIRA and SERS potentially useful for time resolved in situ monitoring of electrochemical reactions. However the nanostructure arrays can provide highly efficient substrates for both SERS and SEIRA simultaneously. This unique array structure simultaneously provides a near-IR wavelength corresponding to the monomer nanoparticles that enhances SERS and a broad peak extending into the mid-IR region for SEIRA enhanced on the same substrate.

### 1.5 Thermal properties of metallic nanoparticles

Plasmonic nanoparticles can be a key component in understanding the interactions between light and matter, namely the resonant absorption and conversion of photons into other forms of energy. In a metal structure, light induces collective oscillations of conduction electrons, called plasmons, in which the electrons are excited to energy states higher than the Fermi level. As they relax to the ground state, heat is released and transferred to the lattice via electron-phonon interactions. The heat is then transferred from the metal surfaces to the environment via phonon-phonon interactions, leading to a thermal distribution gradient around the particles.[24-26] The high conversion of absorbed light into heat demonstrates that metal nanoparticles can act as efficient nanoheaters of the surrounding media without melting or degrading.[24,71-73] The resonant optical absorption wavelength of metallic nanostructures can be tuned across the entire solar spectrum ranges by adjusting the size, shape, and metal composition. Therefore, these

features make them ideal sources for many applications that require localized heating and/or phase change, for example: drug release,[74-75] disease treatment,[76] direct steam generation,[27,72,77-78] infrared detectors,[79-80] or heater dissipaters.[81]

Novel plasmonic systems designed for high-quality energy capture and conversion for steam generation could revolutionize not only the production of solar-based energy but also industrial activity that relies upon steam production in coal, gas and nuclear power plants. For the process of converting energy from the sun into electricity, industrial solar generators are currently exploiting different heat trapping agents such as melted salt or He gas, but a steam based solar energy converter remains a challenge. Solar energy, which is available in a virtually unlimited supply, can be transformed into heat to yield one of the most promising methods for green energy production. Nanotechnology is making significant progresses in developing new materials that can overcome these problems.

### 1.6 Thesis outline

The work in this thesis is organized as follows: the first section describes the utilization of nanoshells in bio-molecular sensing and delivering processes, as well as inhibits the degradation process of NIR dye when attached to the plasmonic nanostructures. The second section details the designed broadband light-harvesting nanostructures that absorb sunlight and produce steam with remarkably high efficiency.

Chapter 1 provides a brief introduction of this research, establishing the importance and applications of plasmonic nanostructures. Chapter 2 discusses the interactions of adenine, thiolated polyadenine single-stranded (ss-polyA) and adenosine monophosphate (AMP) with gold NS surfaces. pH-dependent conformational changes of these molecular

species adsorbed on Au NS surfaces were observed using Surface-enhanced Raman spectroscopy (SERS) and Surface-enhanced IR absorption (SEIRA) spectroscopy. Both methods show significant pH dependence consistent with adenine protonation and reduced Au adenine binding at low pH. Chapter 3 demonstrates a direct label-free detection method of ss-DNA aptamer-target binding. SERS of thiol-bound DNA aptamer self-assembled monolayers on gold nanoshell surfaces was used to detect changes in the conformation of adsorbate induced by target analytes monitored by assessing the aptamer SERS spectra reproducibility. Circular dichroism (CD) spectroscopy independently supports the observations that change to the reproducibility of the SERS spectra; this data is a result of conformational changes to the aptamer induced by target binding. Chapter 4 describes the use of NS functionalized with ds-DNA to transport and deliver DAPI molecules into H1299 cells. DAPI molecules, initially bound to the ds-DNA on the NS surface, are released due to the illumination of the nanoshell-dsDNA-DAPI complex with NIR light. The staining of the cell nucleus with the released DAPI was quantified using flowcytometry. Acytotoxicity assay demonstrated that NS uptake is nontoxic and that laser irradiation of nanoshell-laden cells under the conditions where DAPI release occurs does not induce cell death. Chapter 5 investigates the conformational distribution of chiral molecules such as: (S)-/(R)-Tryptophan, and (SS)-/(RR)-Cysteine-Phenylalanine-Glycine-Glycine on Au nanoparticle substrates using near-infrared surface-enhanced Raman optical activity (NIR-SEROA) measurements. SERS and CD spectroscopy were also used to characterize the system. In order to measure the mirror-image scattered circular Raman intensity spectra, a 3D substrate was designed using the enhanced near field conditions met in the junction between resonant gold nanoparticles, known as a “hot

spot". Chapter 6 investigates the process in which adsorption onto gold nanoshells inhibits degradation of the infrared dye DNDTPC. The SERS spectra of un-oxidized DNDTPC on Au nanoshells are stable over several days under oxidizing conditions and are distinctly different from SERS spectra of oxidized DNDTPC. Extinction and 1H NMR measurements independently confirm that DNDTPC degrades over time in a methanol solution. Density functional theory calculations indicate that DNDTPC undergoes significant geometry changes upon oxidation, suggesting a mechanism for oxidation inhibition. Chapter 7 demonstrates the development of new nano-engineered solar photothermal conversion media for steam generation using broadband metal-based nanoparticles. Solar illumination of broadly absorbing metal or carbon nanoparticles dispersed in a liquid produces vapor without the requirement of heating the fluid volume. When particles are dispersed in water at ambient temperature, energy is directed primarily to vaporization of water into steam, with a much smaller fraction resulting in heating of the fluid. Here we show that sunlight-illuminated particles can also drive water-ethanol distillation, yielding fractions significantly richer in ethanol content than simple thermal distillation. These phenomena can also enable important compact solar applications such as sterilization of waste and surgical instruments in resource-poor locations. As a consequence, several solar applications using the broad-band nanostructures are demonstrated in Chapter 8, 9, and 10. Autoclave systems neutralize potentially infectious microorganisms by exposing them to high temperature pressurized steam for approximately 30 minutes depending on the size of the load and the contents. The lack of readily available sterilization processes for medicine and dentistry practiced in the developing world is a major risk factor for the propagation of disease. Modern

medical facilities in the developed world often use autoclave systems to sterilize medical instruments, equipment, as well as for the processing of waste products that could contain harmful contagions. In chapter 8 and 9, we design and demonstrate the use of broadband, sunlight-absorbing nanostructured particles as photothermal heaters to generate high pressure/temperature steam for a standalone, efficient autoclave useful for the sanitation of medical or dental equipment in resource-limited, remote locations or human waste. Additionally, in chapter 10, we demonstrate a larger quantity and more efficient ethanol distillate compared with thermal flash distillation using solar-powered nanoparticle heating in an inherently non-equilibrium vaporization process. Metallic light-harvesting nanoparticles can capture solar energy for direct liquid-vapor conversion, eliminating the energy-intensive requirement of electrically heating the fluid volume. Chapter 11 describes the synthesis of Au self-similar plasmonic structures that can serve as point-like black-body sites because of their remarkable broad-band optical properties. Their black color is due to the efficient broad spectrum absorption of the EM energy from a wide range of angles. Chapter 12 also presents the electrolytically formation, growth mechanism, and optical properties of Fe2O3-core and Au-shell mesostars structures. Finally, the results from this work are summarized in Chapter 13.

# Chapter 2: Adenine- and adenosine monophosphate (AMP)- gold binding interactions studied by surface enhanced Raman and infrared spectroscopies

## 2.1 Introduction

Knowledge of the interactions of biomolecules with noble metal surfaces is critically important to our development of functional materials or devices that interface well to living systems. In particular, the biocompatibility, relative chemical inertness, and useful optical properties of gold nanoparticles have permitted the development of many biomolecule-nanoparticle complexes for biomedical applications.[82-86] The work presented in this chapter discusses the interactions of adenine, thiolated polyadenine single-stranded (ss-polyA) and adenosine monophosphate (AMP) with gold NS surfaces probed by two surface enhanced vibrational spectroscopies: SERS and SEIRA. A pH-dependent conformational change of these molecular species adsorbed on Au NS surfaces were observed. Both methods show significant pH dependence consistent with adenine protonation and reduced Au adenine binding at low pH. These experimental observations have elucidated the local structure orientation of molecules on an Au nanoshell substrate surface. Reproduced with permission from J. Kundu, O. Neumnn, B. G. Janesko, D. Zhang, S. Lal, A. Barhoumi, G. E. Scuseria, and N. Halas, J. Phys. Chem. C, 2009, 113 (32), pp 14390–14397. Copyright 2009 American Chemical Society.

Nucleic acids are important biological molecules due to their multiple cellular functions, such as replication, transmission of genetic information, and molecular recognition. These attributes, along with their chemical and thermal stability, has led to

the increasing use of DNA in functional sensors and devices.[87-91] The performance of these types of devices is governed in part by details of the nucleic acid-metal surface interactions, such as the ability of pristine or functionalized DNA to form self assembled monolayers or superstructures on Au nanoparticle surfaces,[91] or the nonspecific binding of the nucleotide constituents to the Au nanoparticle surface.[92] Of the four nucleic acid constituents, adenine is of particular interest: with its high level of nonspecific binding on Au nanoparticle surfaces, and its widespread presence in the metabolome in addition to the genome, it is an extremely important molecule with which to study chemisorption to Au nanoparticle surfaces in detail.

Just like their bulk spectroscopy counterparts, Raman and infrared spectroscopy, surface enhanced Raman scattering (SERS), and surface enhanced infrared absorption (SEIRA) are complementary spectroscopic techniques that can be used for investigating the adsorption of biomolecules on metal surfaces.[91,93-96] Vibrational spectroscopy generally provides valuable, detailed information [97-100] concerning molecular structure and binding of adsorbates to surfaces. Combining SERS and SEIRA provides an opportunity to probe virtually all vibrational modes of a molecule or an adsorbate-substrate complex due to the complementary selection rules of these spectroscopies.

Au nanoshells, tunable plasmonic nanoparticles consisting of a dielectic (silica) core and a thin metallic (gold) shell,[28,101] were used as SERS and SEIRA substrates due to their large and reproducible SERS and SEIRA enhancements that even permit the opportunity to perform both SERS and SEIRA on the same substrate.[102-105] Combined SERS and SEIRA spectral analysis was performed to provide insight into the preferred orientation of the adenine-based molecules on the Au nanoshell surface. Density

functional electronic structure theory calculations were performed for free adenine and for adenine bound to an Au surface to obtain peak assignments and to confirm the molecular structure and orientation of the molecule on the Au surface.

It is known that adsorbed adenine is multidentate and can display a variety of orientations on different surfaces. This multidentate nature is due to the presence of several possible coordinating sites (nitrogen atoms) (Figure 2.1). For example, it is known that adenine can coordinate to surfaces through the exocyclic amino group and/or ring nitrogen atoms.[99,106-108] Adenine has been reported to adsorb on noble metal surfaces in a planar [109-112] or nonplanar [113-118] conformation due to interactions with the surface via N1, N7, the external amino group, or the purine ring. Studies on the organic reactivity of the adenine molecule have revealed that the N3 and N9 sites are more reactive functionalities than the external amino group.[99] Detailed information on the actual chemical and orientational nature of the adsorbed adenine moiety, which is the central unit that directs the self-assembly of biomolecules such as AMP and poly-adenine, is of fundamental chemical interest.

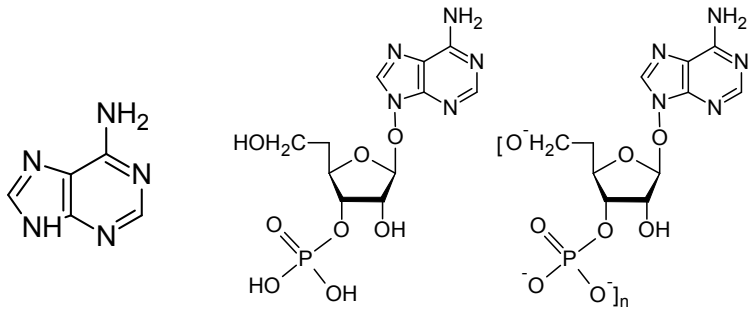


**Figure 2.1** Molecular structure and atom labeling of adenine, AMP, and poly-adenine

## 2.2 Experimental

**A. Materials.** Adenine (99%), adenosine 3′-monophosphate from yeast, DTT (1,4-dithio-DL-threitol sol 1M) were purchased from Sigma-Aldrich and employed without further purification. The thiolated ss-DNA, a 24-A base oligonucleotide was obtained from Integrated DNA Technologies (IDT). NaCl (Sigma- Aldrich), $K_2HPO_4 \cdot 3H_2O$ (Sigma-Aldrich) were used to prepare buffer solutions. The pH of the buffer was adjusted by adding HCl or KOH. The pH measurements were performed with a Fisher Scientific Accumet AP63 portable pH meter with an accuracy of 0.01 pH units.

**B. Reduction of Thiolated ss-DNA.** Prior to adsorption, the thiolated ss-DNA [(HS-$(CH_2)_6$-$(A)_{24}$] was incubated with 100 mM of DTT (reducing agent) in 100 mM sodium monophosphate buffer at pH ) 7.5. The mixture was incubated at room temperature for 1 h to allow for complete reduction of the disulfide bonds. The solution was then filtered through a NAP-5 column to remove the excess DTT and the oxidized form of DTT ($S_2$-$(CH_2)_2$-$(CH\text{-}OH)_2$). Elution of the column with water was performed to collect the purified ss-DNA in $H_2O$. The concentration of the ss-DNA stock solution was determined by measuring its absorbance at 260 nm using a UV-vis-NIR spectrophotometer (Cary 5000, Varian Inc.).

**C. Preparation of SERS and SEIRA Substrates.** Films of Au nanoshells supported on quartz and silicon were used as substrates for SERS and SEIRA, respectively. Quartz and silicon substrates were cleaned by immersing in “piranha solution” ($H_2SO_4$:$H_2O_2$ = 3:1) for 1 h, followed by copious rinsing with deionized water (18.3 MΩ, Millipore). Note that piranha solution is extremely oxidizing, reacts violently with organics, and should be stored in loosely covered containers to avoid pressure buildup. Silica core-gold

nanoshells were fabricated using a method previously described.[28,101] Nanoshells of inner and outer radii [r1, r2] = [63, 86] with a strong dipole plasmon mode at 780 nm were used for the SERS studies. Infrared resonant nanoshells of inner and outer radii of [r1, r2] = [190, 210] were fabricated to produce a film of nanoshell aggregates on silicon (by drop drying) with a broad plasmon response in the mid-IR for SEIRA measurements.

For the SERS measurements, nanoshells were immobilized by depositing 100 μL of aqueous nanoshells solution on PVP coated quartz substrate for 3h. These substrates were then rinsed with water several times to remove the free-floating nanoshells. These nanoshell films, immobilized on quartz substrates, were incubated overnight in a solution of analyte molecules (adenine (0.1 mM), AMP (0.1 mM), and polyadenine (100 μL of 40 μM solution). Before acquiring Raman spectra at different pH values, the sample was rinsed several times with the corresponding buffer solution.

For SEIRA measurements, as-prepared infrared resonant nanoshells were incubated overnight in solutions of analyte molecules at a given pH. Solutions of analyte molecules (adenine (0.1 mM) and AMP (0.1 mM)) were prepared at two values of pH: 2.5 and 8.5. The nanoshells, coated with analyte molecules deposited from solutions of different pH, were then drop-dried on a silicon wafer. Drop-drying results in the formation of films of nanoshell aggregates, which comprise active SEIRA substrates with analyte molecules in the interparticle junctions (electromagnetic "hot spots").[65] The analyte-functionalized nanoshell film was rinsed with the corresponding buffer solution prior to SEIRA measurements.

**D. Measurements.** SERS and Raman spectra were acquired on a Renishaw in Via Raman microscope (Renishaw, U.K.) with 785 nm excitation wavelength and 55 μW

laser power at the samples. Backscattered light was collected using a 63x water immersion objective lens (Leica, Germany) with a 40 seconds integration time. SEIRA and IR spectroscopy measurements were performed on dry samples using transmission geometry on a FTIR spectrometer (Nexus 670, Thermo Nicolet) equipped with liquid nitrogen cooled MCT (HgCdTe) detector. The reported FTIR spectra were collected under N2 environment at 4 $cm^{-1}$ resolution with the addition of 256 scans.

**E. Computational Methods.** Gas-phase Raman and IR spectra of protonated and deprotonated adenine, as well as adenine bound to a single $Au^+$ atom, were calculated. While clearly not a quantitative model of the solvated molecule at an Au surface, similar gas-phase cluster models have been successfully used to interpret vibrational frequency shifts in SERS.[119-122] All calculations were performed with a development version of the Gaussian electronic structure program[123] using the B3LYP[124-127] density functional. Calculations on isolated adenine and adenine-$H^+$ used the large Sadlej basis set, [128-129] obtained from the EMSL basis set library (except where noted). Calculations on Raman spectra of adenine-$Au^+$ complexes used the aug-cc-pVTZ-PP[130] basis set and ECP on Au, and the Sadlej polarized valence triple-ζ basis set on other atoms. Calculations on the IR absorbance spectra of isolated adenine used the polarizable continuum model[131] to simulate aqueous salvation and assumed that adenine is protonated at N1. All calculations were performed for isolated molecules, and all molecules are fully geometry optimized. Binding energies were evaluated without counterpoise correction.

## 2.3 Results and discussion

SERS spectra of adenine, adenosine monophosphate, and poly-adenine at the following pH values: 2.5, 5.1, 6.5, 8.5, and 11.5 are shown in Figure 2.2a-c. All spectra are normalized with respect to the strongest Raman band at 735 $cm^{-1}$ in each spectrum and offset for clarity. These pH values were chosen in order to observe the effects of protonation and deprotonation of the adenine (pKa = 4.1, 9.8),[132] and the phosphate (pKa = 1.9, 6.8, 12.5)[133] moieties present in the analyte molecules spectroscopically. For comparison purposes, normal Raman spectra of adenine, polycrystalline AMP, and in solution poly-A are shown (Figure 2.2d). A careful study of these spectra leads to several interesting observations. First, for a given pH, the SERS spectra of adenine, AMP, and poly-A are all seen to be very similar to each other. This suggests that all the analyte molecules bind to the surface through the same adenine moiety.

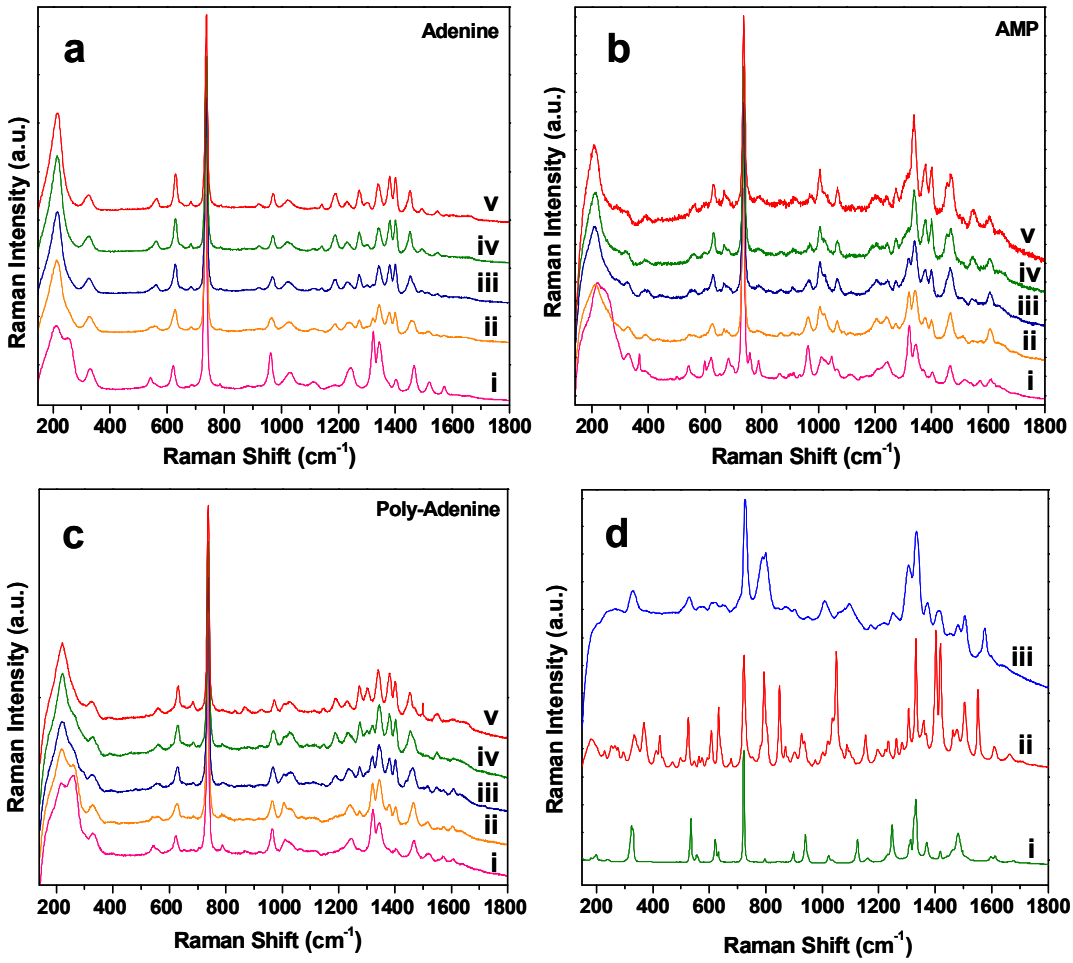


**Figure 2.2** SERS spectra of (a) adenine, (b) AMP, and (c) and polyadenine on nanoshell at different pH values of (i) 2.5, (ii) 5.1, (iii) 6.5, (iv) 8.5, and (v) 11.5 with (d) normal Raman spectra of (i) powder adenine, (ii) powder AMP, and (iii) in solution polyadenine.

The SERS spectra of all the analytes are dominated by the adenine ring breathing mode, which upshifts from 723 $cm^{-1}$ in normal Raman spectra (Figure 2.2d) to 735 $cm^{-1}$ in SERS (Figure 2.2a-c). The 735 $cm^{-1}$ mode in all the SERS spectra (Figure 2.2a-c) is pH-independent. Unlike AMP and poly-A, adenine is devoid of any phosphate and sugar moiety. However, the SERS spectra of AMP and poly-A (Figure 2.2 b, and c) are similar to the SERS spectra of adenine, showing no evidence of enhanced bands from the

phosphate groups. The peaks at 1010 and 1099 $cm^{-1}$ in Figure 2.2d, attributed to phosphate and sugar stretching modes, respectively,[134] are observed in the normal Raman spectra of AMP and polyadenine but are absent in the corresponding SERS spectra. This could be due to the small Raman cross-section of the phosphate band.[135] The C-$NH_2$ in-plane bend at 330 $cm^{-1}$ (Figure 2.2d) appear at ~326 $cm^{-1}$ in the SERS spectra (Figure 2.2a-c) and is observed to be insensitive to pH changes. The 1307 and 1337 $cm^{-1}$ mode in normal Raman spectra (Figure 2.3) are clearly seen to be shifted to 1323 and 1342 $cm^{-1}$ in the SERS spectra of the analytes (Figure 2.2a-c). The relative intensities of these bands are observed to change as a function of pH, which is a consequence of adenine protonation. The peak shifts of SERS bands from the corresponding normal Raman bands are consistent with "chemical effects" of adenine interaction with the metal nanoshell surface and are in accordance with the SERS results reported for adenine adsorbed on silver colloid, silver electrode, and silver island films.[111] These observed similarities between the SERS spectra of A, AMP, and poly-A along with a dominant adenine ring breathing mode suggest that all these molecules bind to the Au surface in a very similar way.

Adenine is known to be protonated at nitrogen N1 (Figure 2.1) with a pKa of 4.1.[132] This results in pH dependence of the SERS spectra of A, AMP, and poly-A (Figure 2).

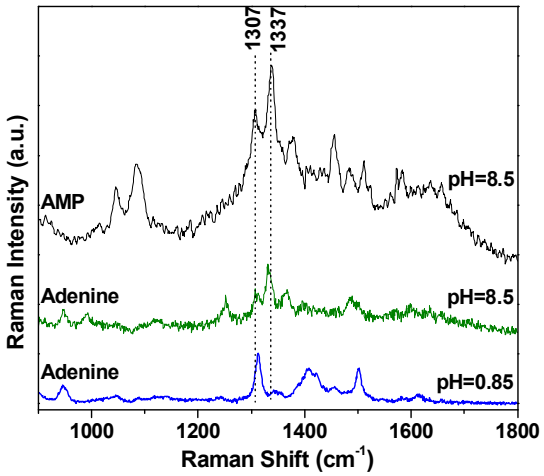


**Figure 2.3** Normal Raman spectra of adenine at pH = 8.5; 0.85 and AMP at pH = 8.5

The observed pH dependence of the SERS spectra is induced by buffer exchange and was found to be reversible under our experimental conditions. Changes in the SERS band intensity and shift of peak positions of adenine with pH are presented in Figure 2.4. Variation of pH most significantly affects the relative intensities of the 1323 and 1342 $cm^{-1}$ features (highlighted by "*" in Figure 2.2), assigned to a summation of two different vibration modes (see Appendix A). As the pH is changed from 2.5 to 11.5, the 1342 $cm^{-1}$ mode is seen to gradually intensify relative to the 1323 $cm^{-1}$ mode in the SERS spectra of A, AMP, and poly-A. This highly reproducible observation deserves special attention and is discussed below.

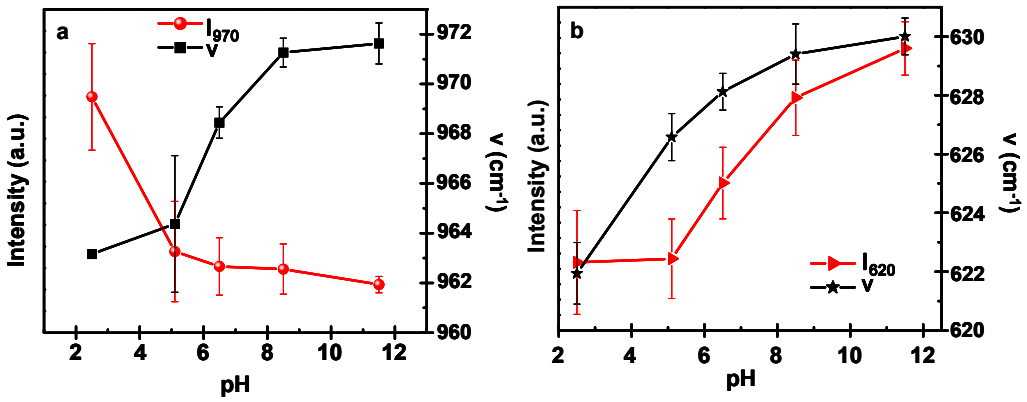


**Figure 2.4** The relative SERS intensity (solid line) and peak positions (dashed line) of adenine bands 970 cm-$^{1}$ (a) and 620 cm$^{-1}$(b) as a function of pH. The 1323 cm$^{-1}$ band indicates a similar trend as shown by the 970 cm$^{-1}$ band, while the bands at 1401, 1380, 1273, 1140 cm$^{-1}$ show the trend as shown by the 670 cm$^{-1}$ band

The study of the pH dependence of in solution normal Raman spectra of adenine and AMP, as shown in Figure 2.3, confirms that the observed pH-dependent differences in the relative intensities of the 1323 and 1342 cm$^{-1}$ modes in the SERS spectra are due to the protonation of the adenine moiety. While the signals are weaker for normal Raman studies in solution (Figure 2.3), the intensity ratio of the 1307 and 1337 cm$^{-1}$ peaks clearly shows the same pH dependence as the SERS spectra in Figure 2.2. The change in peak intensities as a function of pH in the normal Raman solution spectra is very similar to that observed in the SERS spectra. This strongly suggests that the pH-dependence of SERS is due to adenine protonation, with perhaps a small contribution from conformational changes brought about by the differences in orientation of the anchoring group at different pH.

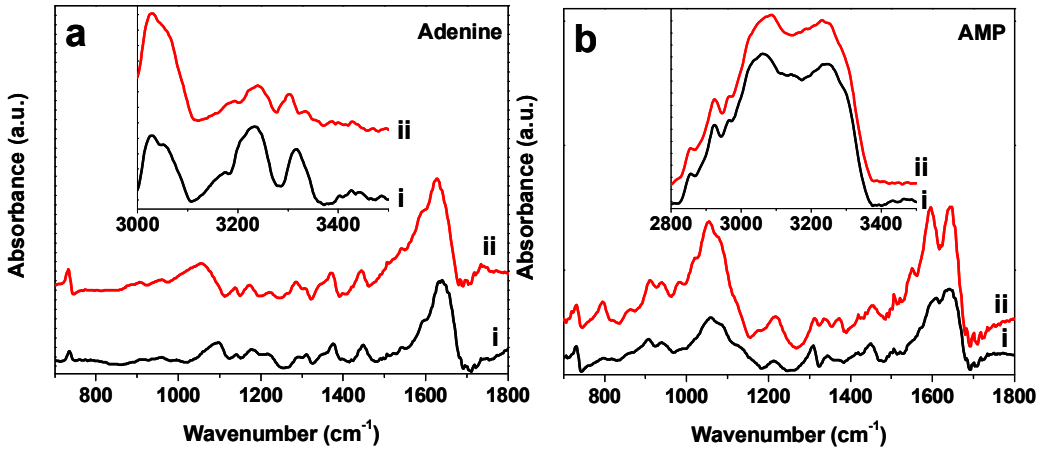


**Figure 2.5** SEIRA spectra of (a) adenine and (b) AMP molecules deposited on nanoshells from solutions of pH (i) 2.5 and (ii) 8.5 with the high wavenumber region shown as an inset. Spectra are offset for clarity.

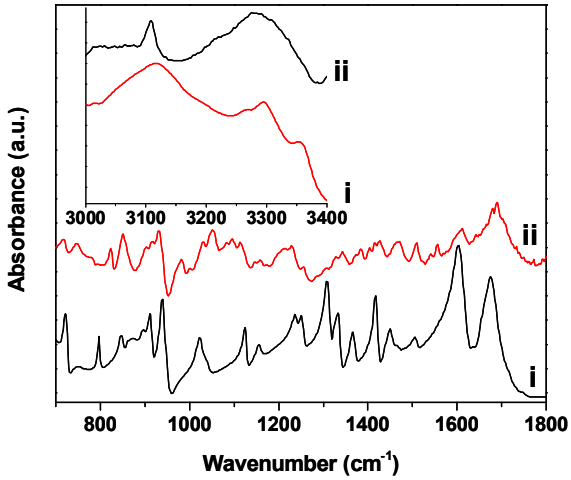


**Figure 2.6** Normal IR spectra of (i) adenine and (ii) AMP dispersed in KBr pellet in the low and high wavenumber (inset) region. Spectra offset for clarity.

Surface-enhanced infrared absorption (SEIRA) studies were performed to confirm the local structure and orientation of the analyte molecules on metal surface. SEIRA spectra of adenine and AMP deposited on nanoshells from solutions of pH 2.5 and 8.5 are shown

in Figure 2.5. For comparison purpose, normal IR spectra of adenine and AMP (dispersed in KBr pellet) are shown in Figure 2.6. It is important to note that normal IR spectra of solid adenine is well-known to have the effects of H bonding interactions that lead to downshifting of the $NH_2$ stretch modes (3440-3450, 3555-3570 $cm^{-1}$) and upshifting of the $NH_2$ scissor mode (1625-1640 $cm^{-1}$).[99,136-137] The SEIRA spectra of adenine deposited from solution at two different pHs are observed to be similar to each other. They all are dominated by the in-plane symmetric $NH_2$ scissor mode[99] at ~ 1620-1640 $cm^{-1}$ (a weak mode in the corresponding SERS spectra) and various ring modes. High wavenumber SEIRA spectra of adenine at both pH levels show the presence of the $NH_2$ symmetric stretch mode at 3290 $cm^{-1}$. However, the inplane symmetric $NH_2$ scissor mode presents a notable difference in its peak position. This peak appears at 1625 $cm^{-1}$ (Figure 2.5a, (ii)) and at 1640 $cm^{-1}$ (Figure 2.5a, (i)) in the SEIRA spectra of adenine deposited from solutions of pH 8.5 and 2.5, respectively. This blue-shift of the peak position (15 $cm^{-1}$) is due to the effect of a neighboring positive charge (protonation at N1) on the $NH_2$ group.[138] The intensity of the 1286 $cm^{-1}$ peak is lower than the 1310 $cm^{-1}$ peak in the SEIRA spectra of protonated adenine. However, the opposite holds true in the SEIRA spectra of deprotonated adenine. These subtle differences in the ring modes are secondary effects of protonation and are likely due to changes in the electronic distribution within the adenine ring caused by the protonation/deprotonation of the adenine molecule.

SEIRA vibrational analysis, based on the surface selection rule (vibrational modes that have a dynamic dipole moment directed normal to the metal surface are preferentially enhanced), [95] provides detailed information on the orientation and the probable binding sites of adenine on the Au nanoshell surface. The SEIRA spectra of adenine as shown in

Figure 2.5 are dominated by the in-plane symmetric $NH_2$ scissor mode at around 1620-1640 $cm^{-1}$. The presence of this strong bending mode precludes a flat orientation of the exocyclic amino group. The relative intensity of this scissor mode to that of the purine mode (1595 $cm^{-1}$)[138] in the SEIRA spectra of adenine is higher than in the normal IR spectra, suggesting that the molecule is preferentially aligned with C-$NH_2$ along the surface normal. Other vibrational modes of the exocyclic amino group are the symmetric and antisymmetric $NH_2$ stretches[99] that appear in the high wavenumber region at 3296 and 3355 $cm^{-1}$, respectively, in the normal IR spectrum (Figure 2.6). The high wavenumber SEIRA spectra of adenine (Figure 2.5a, inset) confirm the absence of the $NH_2$ antisymmetric stretch mode and the presence of a $NH_2$ symmetric stretch mode at 3290 $cm^{-1}$. This provides additional evidence that the $NH_2$ group is largely upright to the surface. Various in-plane ring modes[99] (1058, 1286, 1310 $cm^{-1}$) are also observed in the SEIRA spectra. The presence of these in-plane ring modes (band assignments provided in Appendix 1) strongly suggest the ring plane is not lying flat but is largely inclined from the surface with the C6-$NH_2$ bond aligned almost normal to the surface. This evidence suggests that adenine molecules bind to the metal surface through N3 and/or N9 sites, in agreement with the established fact that N3 and N9 sites are more reactive functionalities than the external amino group of adenine.[99]

The experimental SEIRA spectra of AMP deposited on nanoshells from solutions at different pH are also similar to each other. The presence of the sugar and phosphate groups give rise to the appearance of new bands in the 900-1200 $cm^{-1}$ region.[138-139] The peak intensity ratio at 1640 and 1595 $cm^{-1}$ is seen to decrease to almost unity with increasing pH. The 984 $cm^{-1}$ peak, attributed to symmetric stretching of the deprotonated

terminal phosphate,[138] is clearly observed under basic conditions and grows less intense under acidic conditions. These subtle differences in the pH-dependent SEIRA of AMP may be partially attributed to the effects of protonation in addition to pH-dependent AMP-nanoshell surface interactions. In the SEIRA spectra of AMP deposited from solution of pH ) 8.5 (Figure 2.5b, (ii)), the 1640 $cm^{-1}$ peak ($NH_2$ scissor mode) and the 1595 $cm^{-1}$ peak (purine mode) are of almost equal intensity, in contrast with the case of adenine, where the 1645 $cm^{-1}$ peak is stronger than the 1595 $cm^{-1}$ peak. This indicates that the ring of AMP, as opposed to adenine, orients itself with a wider variety of conformations. Hence, it is likely that the exocyclic amino group and/or other available ring nitrogen of AMP interacts with and coordinates to the metal surface. The ring modes in the SEIRA spectra of AMP and adenine show subtle differences. For example, the 1286 $cm^{-1}$ peak, which appears strongly in the SEIRA spectra of adenine, is very weak in the case of AMP. The relative intensities of the ring modes also vary. For example, in the SEIRA spectra of AMP, the 1372 and 1343 $cm^{-1}$ peak are of equal intensity, but for adenine, the intensity of 1372 $cm^{-1}$ peak is higher than the 1343 $cm^{-1}$ peak.

The observed differences in the various modes ($NH_2$ scissor and ring modes) between adenine and AMP SEIRA spectra are likely a consequence of differences in the manner that adenine and AMP bind to the metal surface. Unlike the adenine case, the in-plane $NH_2$ scissor mode does not dominate the SEIRA spectra of AMP. As discussed above, some of the ring modes that appear strongly in the SEIRA of adenine are weak in the SEIRA of AMP. These observations may indicate that the external amino group along with ring nitrogens can interact with the metal surface, leading to a different orientation of the ring of AMP as compared to adenine. For AMP, the exocyclic amino group, N3

and N1 are the only available possible coordinating sites because the most reactive N9 position is already blocked by the ribose sugar. Because of the relative positioning of these coordinating sites on the ring of AMP, it is anticipated that the tilt angle and orientation of the ring can be quite different when bonded through the exocyclic amino group and/or N3 and/or N1. The binding of adenine and AMP with different coordinating sites can potentially give rise to differences in the tilt angles of adenine and AMP on the Au surface.

Adenine adsorbed to metal surfaces has been extensively investigated, both experimentally and theoretically, over the past few decades. Here we review past work on adenine adsorption and confirm our assignments of the adenine SERS and SEIRA spectra using these results and our ab initio electronic structure calculations.

Previous studies of adenine at metal surfaces have proposed three main binding modes: flat "face-on" adsorption by the adenine π system, "end-on" coordination to a ring nitrogen, and binding via the external amine group. Koglin and co-workers[110] measured SERS of adenine, adenosine, and AMP at a roughened silver electrode. Like us, they found significant similarities between the adenine and AMP SERS spectra and concluded that the adenine ring vibrations dominate the spectra. Watanabe and co-workers[117] argued based on SERS experiments that adenine binds end-on at nitrogen N7. (Atom labels are shown in Figure 1.) Suh and Moskovits[111] measured SERS of nucleic acid bases on silver sol. They assigned adenine's intense 739 $cm^{-1}$ band to an unspecified $NH_2$ deformation and concluded based on the absence of a 3080 $cm^{-1}$ C-H stretch that adenine was bound flat to the surface. Otto and co-workers[118] also measured adenine SERS at a roughened Ag electrode. They concluded that the ring breathing mode at 732 $cm^{-1}$ was the most

enhanced. They also suggested that several enhanced bands involved vibrations of the external amine group and speculated that this group bound to Ag. Kim and co-workers[109] reported a significant concentration dependence of adenine SERS and assigned the spectral changes to a change between face-on adsorption at low concentration and end-on adsorption at nitrogen N1 at high concentration. Itoh and co-workers[140] measured voltage- and pH-dependent SERS of 9-methyladenine on Ag electrodes. They suggested a nearly flat N1-protonated geometry at high potential, with a deprotonated end-on orientation at more negative potentials.

Giese and McNaughton[114] (henceforth GM) performed a very extensive analysis of adenine Raman and SERS spectra, combining isotopic substitution experiments with density functional theory (DFT) calculations. Based largely on an analysis of relative SERS intensities, they concluded that adenine adsorbs end-on to a variety of silver SERS substrates via nitrogen N7 and the external $NH_2$ group. McNutt and co-workers[99] studied adenine on Cu(110) in ultra high vacuum (UHV) using reflection absorption infrared spectroscopy (RAIRS). They found that the spectra were dominated by the $NH_2$ scissors and in-plane ring modes, similar to our SEIRA spectra, and concluded that adenine tautomerized to coordinate with the surface at N3 and N9. Yamada and co-workers[107] studied DNA bases on Cu(110) in UHV using infrared reflection absorption spectroscopy (IRAS).They found a very low signal at submonolayer coverages and concluded that adenine adsorbed face-on. Higher coverages gave spectra dominated by the $NH_2$ scissors mode, suggested to be a second layer of tilted adenine. A recent temperature programmeddesorption study by O¨ stblom and co-workers[106] of adenine at polycrystalline Au films suggested multiple energetically distinct binding motifs, with the

strongest bonding assigned to adsorption by the external $NH_2$ group. Calculations by Piana and Bilic[116] showed face-on adsorption to Au(111) for UHV and submonolayer coverage. Badr and Mahmoud[113] reported endon coordination at N7 for adenine SERS on silver nanowires.

Theoretical studies of adenine SERS have so far provided only semiquantitative agreement with experiment. The most notable study to date is by Jensen,[141] who simulated adenine's surface enhanced Raman and Raman optical activity spectra by modeling adenine bound to a large Ag20 cluster via N7 and the external amine. These very sophisticated time-dependent DFT calculations did not reproduce typical experimental SERS spectra, predicting a small intensity for the ring breathing mode that tends to dominate adenine SERS. This points to the difficulty of quantitatively reproducing experimental SERS spectra and validates our focus on simple semiquantiative calculations (see below).

In the remainder of this section, we interpret our adenine SERS and SEIRA spectra and assign putative conformations for the adenine-Au interaction. The spectral interpretations are based largely on the assignments by GM, supported by additional ab initio calculations and information from the low pH spectra. For completeness, the Appendix A gives the calculated vibrational spectra for adenine, protonated adenine, and adenine-Au+ complexes with Au at nitrogens N3 and N7, as well as comparison between experimental and calculated Raman spectra.

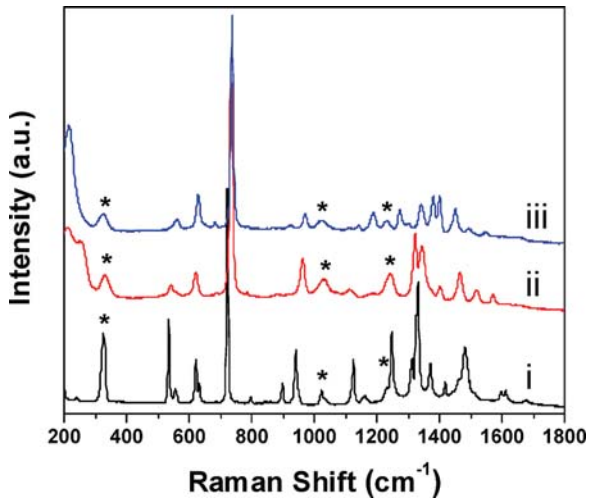


**Figure 2.7** (i) Experimental powder Raman spectrum of adenine, and experimental SERS spectrum of adenine at (ii) pH 2.5 and (iii) 8.5. Intensities are in arbitrary units. Starred peaks are dominated by motions of the external amine group.

Because the SERS of adenine, AMP, and polyadenine are so similar, we feel confident in assuming that the adsorption geometries are also similar and thus focus on assigning the adsorption geometry of adenine itself. As mentioned previously, the SEIRA of AMP suggests a slightly different binding mode for AMP on dried nanoshells. We also argue that these very strong and reproducible adenine SERS and SEIRA signals would not occur for disordered adenine weakly bound to the nanoshells, such that the "overlayer" model proposed by Kawai and coworkers does not apply here.[107] Figure 2.7 compares the experimental adenine powder Raman spectrum with the experimental adenine SERS obtained at pH 8.5 and 2.5. Peaks <1350 $cm^{-1}$ tend to be shifted up in frequency, while peaks >1350 $cm^{-1}$ are generally shifted down in frequency. GM suggested, on the basis of an argument of Muniz-Miranda and co-workers,[142-143] that this is due to a competition between the electronic and steric effects of end-on adenine-Au binding at the heterocyclic

ring nitrogens. Low frequency peaks are shifted to higher frequencies due to steric hindrance from the adjacent Au surface, while high frequency peaks are shifted to lower frequencies due to adenine f Au electron donation and adenine bond softening. Comparison of the high-pH and low-pH SERS shows that this effect is less pronounced at low pH, suggesting that protonated adenine binds less strongly. This is consistent with reduced adenine f Au electron donation from protonated, positively charged adenine. The low- and high-pH SERS spectra are otherwise rather similar, ruling out any dramatic pH-induced conformational change.

The adenine SEIRA spectra in Figure 2.5 are dominated by the $NH_2$ scissors mode at 1625 $cm^{-1}$. On the basis of SEIRA surface selection rules, the C6-N10 bond must be aligned close to the surface normal. Like other workers, our SERS spectra are dominated by adenine ring vibrations including the 737 $cm^{-1}$ ring breathing, suggesting that the adenine ring is nearly perpendicular to the Au surface. These two observations rule out the possibility of a "flat" adsorption geometry, although the adenine ring plane may still be somewhat tilted from the surface normal. Further evidence for slightly tilted adsorption geometry comes from the weak SERS peaks at 565, 682, and 787 $cm^{-1}$, assigned by GM to out-of-plane adenine vibrational modes. (The peak at 565 $cm^{-1}$ might also be a shifted version of the 536 $cm^{-1}$ ring deformation.)

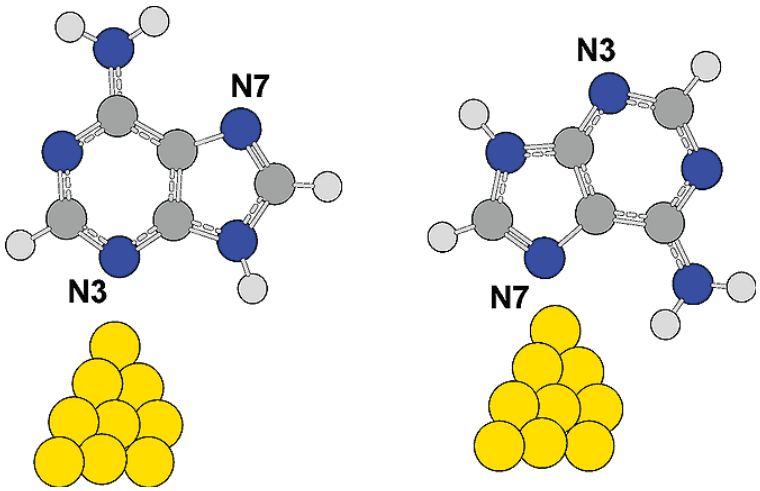


**Figure 2.8** Schematic of proposed adenine-Au binding modes through ring nitrogens N3 (left) or N7 (right)

| binding site | energy (Kcal/mol) |
|---|---|
| N1 | 79.2 |
| N3 | 79.5 |
| N7 | 73.5 |
| $NH_2$ | 64.7 |

**Table 2.1** Calculated Binding Energy (Kcal/mol) between Adenine and $Au^+$

On the basis of this analysis, adenine is most likely bound to Au by one of the ring nitrogens N1, N3, N7, or N9, with possible additional contributions from the external amine. While adenine itself could adsorb at nitrogen N9 via tautomerism (as suggested by McNutt and co-workers[99]), this binding mode is not possible for AMP and polyadenine and is thus ruled out. Binding at N1 is also unlikely, as this is the only protonation site with a pKa above 1.0,[144] suggesting that the observed pH dependence can only occur if adenine is protonated at N1. Binding at N3 is somewhat unlikely for AMP and poly-A due to steric hindrance from the substituents bound at N9. GM argued that adenine binds

via N7 and the external $NH_2$ group. However, we have some questions about this assignment. Figure 2.7 shows that the C6-$NH_2$ bend at 330 $cm^{-1}$, the $NH_2$ rock at 1025 $cm^{-1}$, and the $NH_2$ rock at 1234 $cm^{-1}$ (marked by "*") are not strongly shifted in the low-pH or high-pH SERS spectra, in contrast to the substantial SERS shifts seen for the adenine ring modes. This suggests that the $NH_2$ group does not contact the surface. Further evidence for this conclusion comes from the $NH_2$ scissors mode in the high-pH SEIRA, whose position at 1625 $cm^{-1}$ is only slightly shifted from the 1618 $cm^{-1}$ seen in matrix isolation IR.[136] We suggest that adenine and its derivatives bind the Au surface exclusively at nitrogen N7, with the C6-$NH_2$ bond aligned near the surface normal. Binding at N3 is also possible. Figure 2.8 gives a schematic of two proposed adenine-Au binding modes.

As further evidence for this assignment, Table 2.1 presents calculations on adenine bound to a single $Au^+$ atom. Giese and McNaughton and others have stated that the SERS spectra of adenine on Ag is qualitatively quite similar to Raman of adenine-Ag+ complexes,[114] thus we assume that this is also a reasonable first-order model of the energetics. Binding is strongest to ring nitrogens N1 and N3, somewhat weaker to N7, and quite a bit weaker to the external $NH_2$ group. While this model system is rather crude, it indicates that our suggested possible binding sites (N3 and N7) are both energetically reasonable.

Table 2.2 further demonstrates that the low-pH adenine SERS and SEIRA involve protonation at nitrogen N1. The table presents B3LYP/6-31G(d,p) calculations on neutral adenine, and adenine-H+ protonated at the N1, N3, or N7 ring nitrogens. As expected, protonation at N1 is energetically most favorable. Moreover, the C-$NH_2$ bend, ring

breathing, and $NH_2$ rock vibrational modes are shifted very little by N1 protonation, while the $NH_2$ scissors mode is dramatically shifted to higher frequencies. This is consistent with the differences between low pH and high-pH SERS and SEIRA spectra.

| species | energy | C-$NH_2$ bend | ring breathing | $NH_2$ rock | $NH_2$ scissor |
|---|---|---|---|---|---|
| neutral | 0 | 275 | 728 | 1020 | 1674 |
| $H^+$ on N1 | -239 | 276 | 724 | 1004 | 1732 |
| $H^+$ on N3 | -238 | 278 | 721 | 999 | 1712 |
| $H^+$ on N7 | -231 | 295 | 724 | 1003 | 1701 |

**TABLE 2.2** Calculated Relative Energy (kcal/mol) and Selected Vibrational Frequencies ($cm^{-1}$) of Neutral Adenine and Adenine Protonated at the N1, N3, and N7 Ring Nitrogens

| molecules | C6-$NH_2$ bend | $NH_2$ rock | $NH_2$ rock | $NH_2$ scissor |
|---|---|---|---|---|
| adenine | 276 | 1017 | 1246 | 1661 |
| adenine-$Au^+$, N1 | 292 | 1016 | 1224 | 1687 |
| adenine-$Au^+$, N3 | 284 | 1012 | 1228 | 1686 |
| adenine-$Au^+$ N7 | 322 | 1016 | 1234 | 1671 |
| adenine-$Au^+$ $NH_2$ | 228 | 1141 | 1272 | 1617 |

**TABLE 2.3** Calculated Frequencies ($cm^{-1}$) of the Vibrational Modes Marked with "*" in Figure 6 for Four Adenine-$Au^+$ Complexes

Table 2.3 illustrates why adenine binding at nitrogen N7 is somewhat inconsistent with the $NH_2$ modes marked with "*" in Figure 2.7. The table shows calculated vibrational frequencies of these modes for isolated adenine and adenine bound to Au+ at the N1, N3, and N7 ring nitrogens or the external $NH_2$ group. Details are as in Table 2.1. Au+ binding

at N3 yields relatively small shifts of these $NH_2$ modes, and binding at N7, N3, and (especially) the external $NH_2$ group produces rather significant frequency shifts. While none of these calculations perfectly reproduce experiment, they demonstrate that N3 binding is consistent with the experimental spectra.

Figure 2.9 illustrates that the observed pH dependence of the adenine SEIRA spectra in Figure 2.5 is consistent with the effects of adenine protonation. The figure shows the calculated IR absorbance spectra of adenine and protonated adenine.

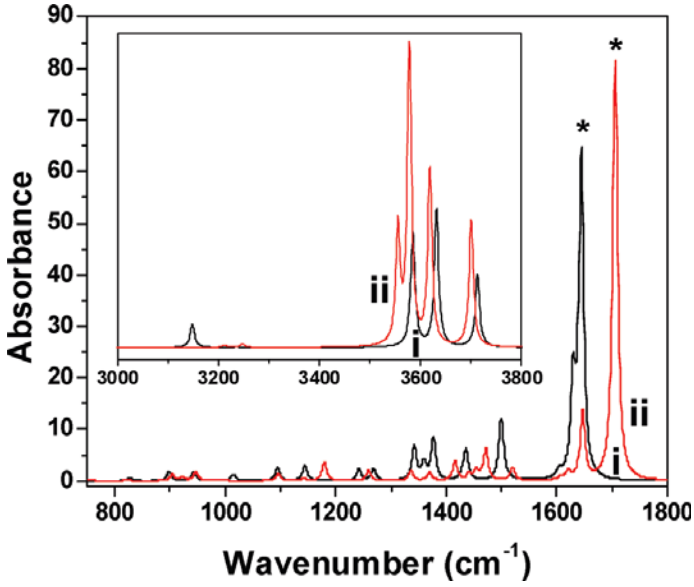


**Figure 2.9** Calculated IR absorbance spectra of (i) adenine and (ii) adenine-$H^+$. Asterisks "*" denote the $NH_2$ stretching mode; other details are in the text.

The calculated spectra clearly show that the intense $NH_2$ scissors mode shifts to higher frequency upon protonation. Protonation also makes the $NH_2$ scissors mode more intense relative to the purine ring mode observed at 1595 $cm^{-1}$. The $NH_2$ stretch modes and the N9-H stretch calculated in the 3400-3700 $cm^{-1}$ range shift to slightly lower frequencies upon protonation and become slightly less intense. All of these effects are consistent with

the experimental adenine SEIRA in Figure 2.5a. As mentioned previously, the antisymmetric $NH_2$ stretch calculated at ~3630 $cm^{-1}$ appears absent in the experimental SEIRA spectra, providing further evidence that the C6-$NH_2$ bond is aligned near the surface normal. The C-H stretches around 3000 $cm^{-1}$ is calculated to have rather low IR intensities. As mentioned previously, the SEIRA of AMP shows some differences from the adenine SEIRA, which may be consistent with a different binding motif for AMP.

## 2.4 Conclusions

Surface-enhanced Raman spectra (SERS) of adenine, adenosine monophosphate (AMP), and polyadenine adsorbed on Au nanoshells in aqueous solution of different pH values have been investigated to study the pH-induced conformational changes of the analyte adsorbate molecules. The pH dependent SERS spectra were found to be reversible under experimental conditions. The SERS spectra of the analytes were found to be very similar to each other, suggesting that all the analytes bind to the surface in very similar way. Normal modes obtained from electronic structure theory calculations at DFT level for Au+ -adenine complexes along with the existing literature on adenine binding were used to assign the observed SERS bands of adenine. The local structure and orientation of adenine and AMP molecules on an Au nanoshell substrate surface was confirmed using surface-enhanced infrared absorption (SEIRA) spectroscopy. The effect of protonation of the adenine moiety can clearly be observed in the acquired SERS and SEIRA spectra. Spectral analysis indicates that the ring planes of both adenine and AMP are not lying flat but have upright orientation with a small angle from the surface normal. Experimental results suggest that adenine adsorbs “end-on” to Au surface with the C6-

$NH_2$ bond almost aligned normal to the surface, while AMP binds through N3 and/or the external $NH_2$ group. DFT calculations for adenine support the experimental SERS-SEIRA spectra and provide insight to the local binding geometry. Adenine binding "endon" through N3 with C6-$NH_2$ bond aligned near the surface normal, as shown in the left schematic of Figure 2.8, is proposed as the plausible orientation on Au nanoshell surface.

# Chapter 3: Direct optical detection of aptamer conformational changes induced by target molecules

## 3.1 Introduction

Aptamers are nucleic acid macromolecules of single-stranded DNA or RNA that can fold into three-dimensional complexes upon interaction with other molecules, providing preferential binding sites for molecular recognition of analytes.[145-147] The work presented in chapter 3 discusses the interaction of target molecules to aptamer surface ensemble monolayer on Au nanoshell surfaces. The interaction induces conformational modifications in the aptamer molecules, monitored by assessing the aptamer SERS spectra reproducibility. Circular dichroism (CD) spectroscopy independently supports the observed changes to the reproducibility of the SERS spectra which are a result of conformational changes to the aptamer induced by target binding. These experimental observations have resulted in the first direct label-free detection of an aptamer to its target. Reproduced with permission from: O. Neumann, D. Zhang, F. Tam, S. Lal, P.Wittung-Stafshede, and N. J. Halas, Anal. Chem., 2009, 81 (24), pp 10002–10006. Copyright 2009 American Chemical Society

Single stranded DNA typically possesses a complex secondary structure due to many intramolecular base pairing opportunities,[148-149] which imparts increased stability to the folded complex. This provides a binding affinity in the picomolar to nanomolar range for highly target dependent aptamer-large molecule complexes and in the micromolar range for complexes formed with small molecules.[150-155] While numerous aptamer-based detection methods have been reported,[152-154,156-166] these techniques typically require

complex labeling and sample preparation. The goal of direct optical detection of aptamer-target binding remains a key analytical challenge.

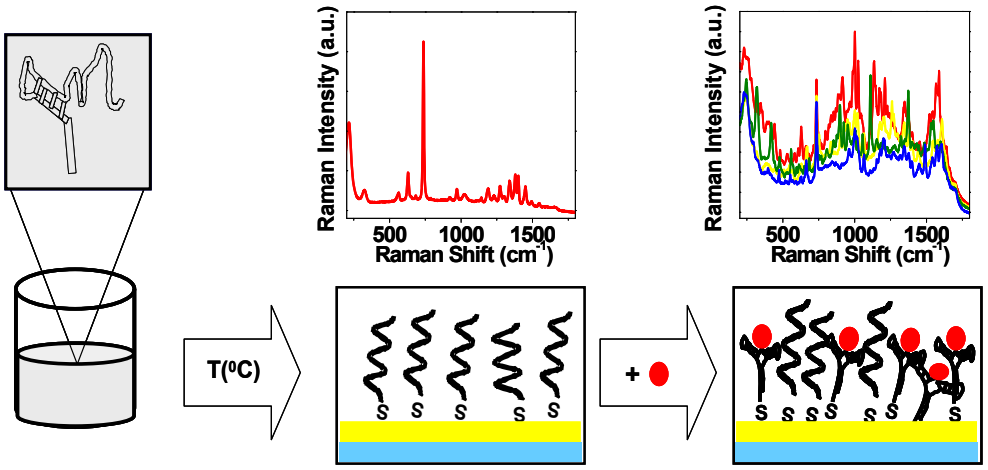


**Figure 3.1** Schematic of aptamer SAM SERS-based analyte detection. Aptamers whose secondary structure is essentially eliminated by thermal treatment form SAMs on nanoshell substrates. Conformational changes in the aptamers induced by target molecule interaction are monitored by SERS.

In the past several years, interest in surface-enhanced Raman spectroscopy (SERS) for chemical detection has increased dramatically. SERS exploits the intense, localized optical fields at metal surfaces and junctions due to surface plasmons to probe substrate-adsorbed molecules spectroscopically. Substrates with a strong plasmon excitation near the pump laser wavelength and a plasmon bandwidth to excite strong local fields at the Stokes frequencies of the adsorbate provide strong SERS enhancements.[167-168] While substrates with large field enhancements over nanoscale volumes may be most appropriate for single molecule SERS,[169-170] substrates with strong yet highly regular enhanced fields over a larger sensing volume are more practical for many sensing

applications. SERS substrates such as nanoshells and film-over-nanoparticle geometries provide this latter type of electromagnetic nanoenvironment: the usefulness of these types of SERS substrates has been documented extensively.[167,171]

Nanoshell-based SERS substrates have shown excellent spot-to-spot and sample-to-sample spectral reproducibility.[171-172] Changes in molecular conformation of adsorbate molecules will typically result in changes in the SERS spectrum of adsorbate. Therefore, SERS provides an optical method to detect changes in the conformation of adsorbate molecules. Since DNA aptamers respond to their target molecules by changing conformation, aptamer-target interactions should be detectable using SERS. This approach to detect aptamer-target binding is direct and label-free, requiring only that the aptamer be thiolated on one terminus so it is stationary on the SERS substrate (Figure 3.1). The SERS spectrum of a thiolated DNA oligomer self-assembled monolayer (SAM) on Au nanoshell SERS substrates has a characteristic, highly reproducible SERS spectrum dominated by adenine and guanine and largely independent of the base sequence.[172-173] Changes in conformation of the aptamer molecules in the SAM upon exposure to analyte molecules are directly observable as complex, random changes in the SERS spectrum. These randomization of the aptamer SAM due to interactions with the target molecules can be quantified by obtaining several SERS spectra and calculating the pairwise spectral correlation function, Γ, before, then after, exposure to the target analyte.[172] The pairwise spectral correlation function is calculated using:

$$\Gamma = \frac{\sum_{i=1}^{m}\sum_{j=1}^{n} P_{i,j}}{mn} \qquad (1)$$

where *i* and *j* are the matrix column vectors (spectral intensities) to be analyzed, m, n is the total number of spectra analyzed. The correlation coefficient between all non-identical spectral pairs ($i \neq j$) in the same data set were determinate by

$$P_{i,j} = \frac{\sum_{k=1}^{W} (I_i(k) - \overline{I_i}) - (I_j(k) - \overline{I_j})}{\sigma_i \sigma_j} \qquad (2)$$

were W is the spectral range, $\sigma_i$ is the standard deviation of the *i*th row, and I is the spectral intensity. Simply put, the correlation function $\Gamma$ measures the degree of randomness introduced into the SERS spectrum by the ensemble aptamer-target molecule interactions: for identical spectra, $\Gamma = 1.0$ and for completely randomized spectra, $\Gamma = 0$. Determining $\Gamma$ before, then after, exposure of the aptamer to the target molecules assesses the degree of the conformation change induced in the ensemble of aptamer molecule absorbates by the target molecules.

With this approach we observe changes in the SERS spectrum for thiolated aptamer SAMs specific to a protein, platelet-derived growth factor (PDGF-BB), and a small molecule analyte, cocaine. These aptamers were chosen to allow us to examine two distinct detection regimes: high-specificity detection of biomolecules and lower specificity detection of small molecules. For both cases, aptamer SAM-target molecule interactions were compared to interactions with nonspecific control molecules. The SERS studies were correlated with Circular Dichroism (CD) spectroscopy, a method used extensively to study and characterize conformational structures of biomolecules.[174-176] CD spectroscopy of the anti-PDGF and the anti-cocaine DNA aptamers before and after exposure to analyte provided independent confirmation that the SERS spectra are indeed detecting conformational changes due to aptamer-analyte molecule interactions.

### 3.2 Experimental

**A. Materials:** ss-DNA oligonucleotides and Tris EDTA, buffer (TE), pH=7.5 were purchased from Integrated DNA Technologies (IDT) and were employed without future purification. In our study we used two kinds of aptamers: anti-cocaine aptamer HS-C6H12-5'AGACAAGGAAAATCCTTCAATGAAGTGGGTCG3', and anti-PDGF aptamer HS-C6H12-5'CAGGCTACGGCACGTAGAGCATCACCATGATCCTG3'. Recombinant human Platelet-Derivate Growth Factor-BB (PDGF) was purchased from Sigma-Aldrich. DTT (1, 4 Dithio -DL-threitol sol. 1M), cocaine, benzocaine and caffeine were purchased from Sigma-Aldrich and employed without further purification. NaCl (Sigma –Aldrich) and $K_2HPO_4x3H_2O$ (Sigma Aldrich) were used to prepare buffer solutions. The concentration of ss-DNA stock solutions was determined by UV spectroscopy at 260nm at room temperature, using a Cary 5000 UV-Vis Spectrophotometer.

**B. Substrate preparation:** Nanoshells were prepared as reported in chapter 1.[31] Cleaned quartz slides were modified with poly (4-vinylpyridine) (PVP) to facilitate subsequent attachment of a dispersed submonolayer of nanoshells on the quartz surface.[177] Au-silica nanoshells were fabricated with the core and shell radii $[r_1, r_2] = [63, 75]$ nm, corresponding to a nanoshell plasmon resonance of 785 nm (Raman laser wavelength) in $H_2O$. The nanoshells were immobilized on the quartz substrates by depositing 100μL nanoshell solution onto the substrate, incubating overnight, and then removing the excess nanoshells by rinsing with water. Thiolated ss-DNA aptamers were first treated with a 100mM of the reducing agent 1, 4 dithio-DL-threitol solution for 1 h to allow for the complete reduction of disulfide bonds in solution. To prepare the

aptamers for attachment to the SERS substrates, they were thermally treated by heating for 5 min at 100ºC in Tris EDTA (TE) buffer followed by rapid cooling with an ice bath.

### 3.3 Results and discussion

Freshly prepared nanoshell SERS substrates were then incubated with the thermally treated aptamer solution (100μM) overnight at room temperature and with high humidity. SERS spectra of the DNA aptamer SAMs on the nanoshell SERS substrates were acquired in a Renishaw inVia Raman microscope at a laser intensity of 55μW. A 63x immersion lens (Leica, Germany) was used to collect high-resolution Raman spectra of hydrated aptamers with a 40s integration time.

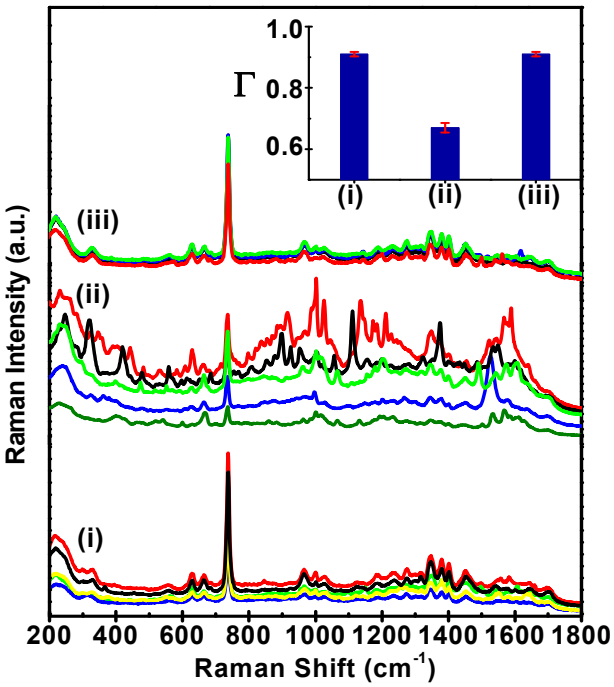


**Figure 3.2** The SERS spectra of the anti-PDGF aptamer SAM (i) prior to exposure to PDGF, (ii) following PDGF exposure, and (iii) following Lysosyme exposure (a control

protein). Insert: Γ values for the DNA aptamer SAM-PDGF and –lysozyme interaction. Error bars represent the standard deviation.

After overnight incubation with the target molecules, changes to the Raman spectra were quantified. Spectra acquired using the highly specific anti-PDGF aptamer SAM are shown in Figure 3.2 Prior to the introduction of the target molecules, the anti-PDGF aptamer SAMs yield highly reproducible spectra with $\Gamma = 0.91 \pm 0.01$ (Fig 3.2(i)). This high degree of reproducibility is due to the thermal pretreatment of the aptamer, which relaxes the ss-DNA aptamer molecules into an extended conformation prior to SAM formation on the nanoshell surfaces.[172] The spectra of the DNA aptamer modified SAM are dominated by the adenine ring breathing mode at 735 $cm^{-1}$. SERS spectra reproducibility was dramatically changed as target molecules were introduced in the system. Upon PDGF-BB incubation, the target protein modifies the secondary structure of aptamer molecules. In solution, this is performed by adopting a loop-step structure characteristic to aptamers.[150,163,178] Because the aptamer conformation has been modulated by the target molecules, due to differences in the orientation of the folded bound complexes, the reproducibility of the SERS spectra from these substrates is dramatically reduced ($\Gamma = 0.67 \pm 0.02$) as is demonstrated in Figure 3.2(ii). In contrast, when the anti-PDGF aptamer SAMs on nanoshells are incubated with lysozyme, a control protein, no changes in the spectral reproducibility are observed, an observation consistent with the known high specificity of the anti-PDGF aptamer for its target molecule. It is interesting to note that the SERS spectra of the anti-PDGF aptamer SAMs are modified quite dramatically by interaction with PDGF-BB for the 1 μM PDGF-BB

concentrations used, despite the fact that the ability of the target analyte molecules to access and induce conformational changes in the aptamer SAM molecules is likely to be hindered by steric and chemical factors. [150] Some aptamers posses very high affinity and selectivity for their targets, with dissociation constant (Kd's) comparable to or surpassing those of some monoclonal antibody.[179] The Kd constant of an aptamer with its target can range from 0.04 pM (i.e. anti-PDGF) to 10 μM (i.e. anti-cocaine) with the majority falling in the low nanomolar range[154],[160],[180]. Nanoshell-based SERS substrates can in fact be used to assess the specificity of an aptamer for its particular target.

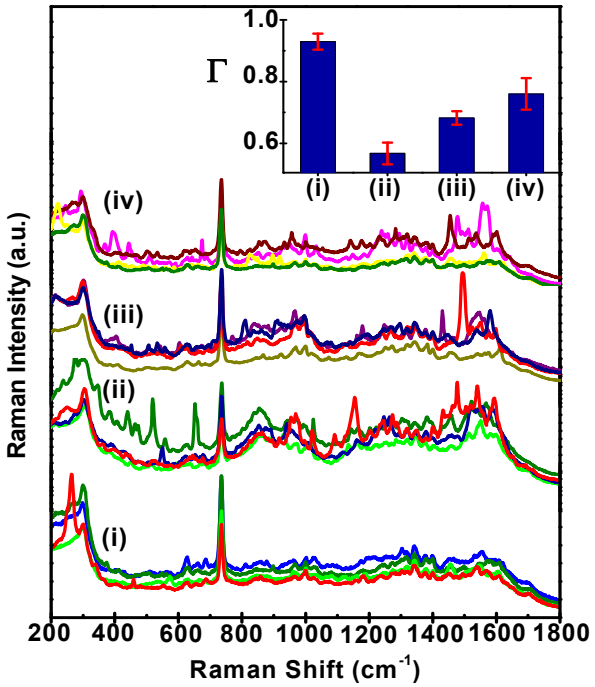


**Figure 3.3** The SERS spectra of anti-cocaine aptamer (i) alone, (ii) with cocaine, (iii) with benzocaine, and (iv) with caffeine. Insert: the cross correlation SERS spectra demonstrate that different target bindings induce spectral variation by re-inducing the hairpin structure of the aptamer. Error bars represent one standard deviation.

The specificity of the anti-cocaine aptamer SAM was studied by comparing the variation of the aptamer SAM SERS spectra upon interaction with target and non-target molecules (Figure 3.3). As in the case of anti-PDGF, the anti-cocaine aptamer SAMs exhibit highly reproducible SERS spectra, $\Gamma$=0.93±0.03, prior to exposure to their target molecules, due directly to the high degree of uniformity of the ss-DNA aptamer modified SAM. Incubation with cocaine (20 μM) induces conformational changes in the aptamers, with an increase in variability in the SERS spectra resulting in a decrease in gamma to 0.57±0.04. In this case, however, nonspecific molecules were also able to induce conformational changes in the aptamer SAM. When the aptamers SAMs were incubated with benzocaine or caffeine (100 μM) for the same length of time as the cocaine aptamer, the spectral correlation function $\Gamma$ decreased to 0.68±0.02 and 0.76±0.05, respectively. The decrease in $\Gamma$ for both benzocaine and caffeine is easily observable, indicating some conformational response of the anti-cocaine aptamer to these molecules, although it is clearly not as pronounced as the decrease induced by the cocaine target molecule. This effect is likely due to the presence of three non-specific base-pairs in the folded state of the anti-cocaine aptamer, which can confer some stability to the binding of non-target molecules. This type of measurement may provide a method for assessing the degree of specificity of an aptamer for its target. Conversely, since the $\Gamma$ values for each target analyte are distinct and reproducible, this limited degree of specificity may in fact be advantageous, and may lead to new optics-based strategies for the identification of multiple targets by a single aptamer where aptamer-target specificity is inherently limited.

To understand the correlation between the conformational changes of aptamers in solution observed by CD and the conformational changes observed in SAM aptamers used in the SERS studies, control experiments were performed. The SERS spectra of random ss-DNA sequences alone and incubated with target molecules were obtained (Figure 3.4). As the target molecules we chose benzocaine because it has an inherent strong SERS signal. As expected, after overnight incubation with benzocaine, no conformational changes in the randomly chosen DNA sequences were observed (confirmed by a $\Gamma = 0.9968 \pm 0.01$ for ss-DNA alone and $\Gamma = 0.9889 \pm 0.03$ for ss-DNA with benzocaine). The SERS spectra of randomly ss-DNA incubated with benzocaine does not exhibit any peaks from benzocaine (Figure 3.4). This leads us to conclude that benzocaine does not bind to the DNA (and is thus not close to the surface) to produce a SERSA signal.

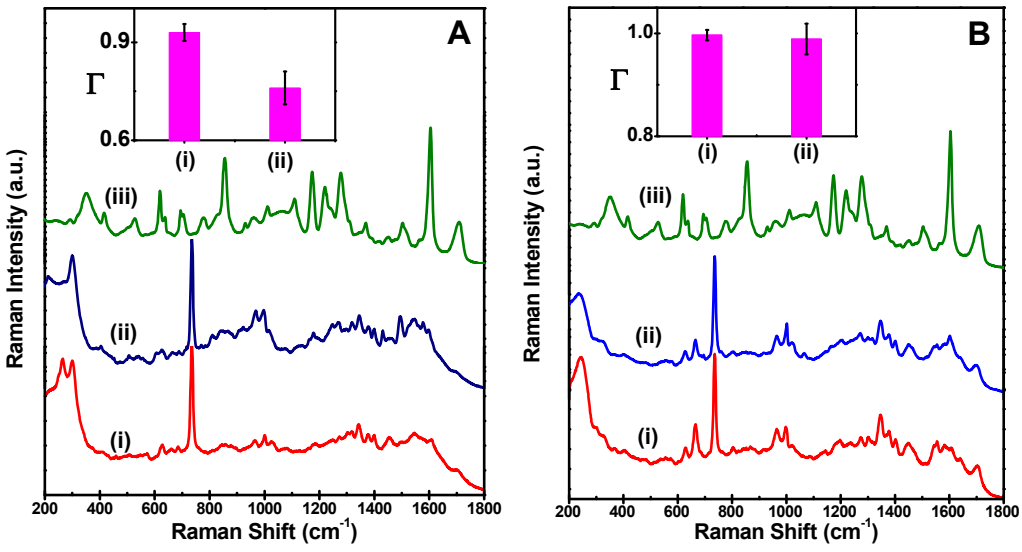


**Figure 3.4** (A) The average SERS spectra of anti-cocaine aptamer (i) alone, (ii) with benzocaine, and (iii) benzocaine. Insert: Γ values for the anti-cocaine aptamer SAM and aptamer–benzocaine interaction. (B) The average SERS spectra of random DNA (i)

alone, (ii) with benzocaine, and (iii) benzocaine Insert: Γ values for the random DNA SAM and DNA-benzocaine interaction.

To confirm that the changes in the SERS spectra observed in the presence of target molecules resulted from changes in molecular conformation of the aptamer molecules, circular dichroism (CD) spectroscopy was performed in correlation with the SERS experiments. CD spectroscopy has been valuable for studying the secondary structure of biomolecules, including aptamers, and for detection of aptamer-target interactions [174, 175, 176]. CD spectra were acquired in TE buffer (pH = 7.5) using DNA concentrations of 5 μM in a 1 cm path length quartz cell. Measurements were made using a JASCO J-810 spectropolarimeter equipped with a Peltier-type temperature control system for wavelengths ranging from 200 to 350 nm. Thermal unfolding and folding curves were obtained by monitoring the decrease in ellipticity with temperature in the desired wavelength range. The temperature was varied between $5^0$C and $100^0$C after an equilibration time of 300 sec. at a heating rate of $2^0$C per minute.

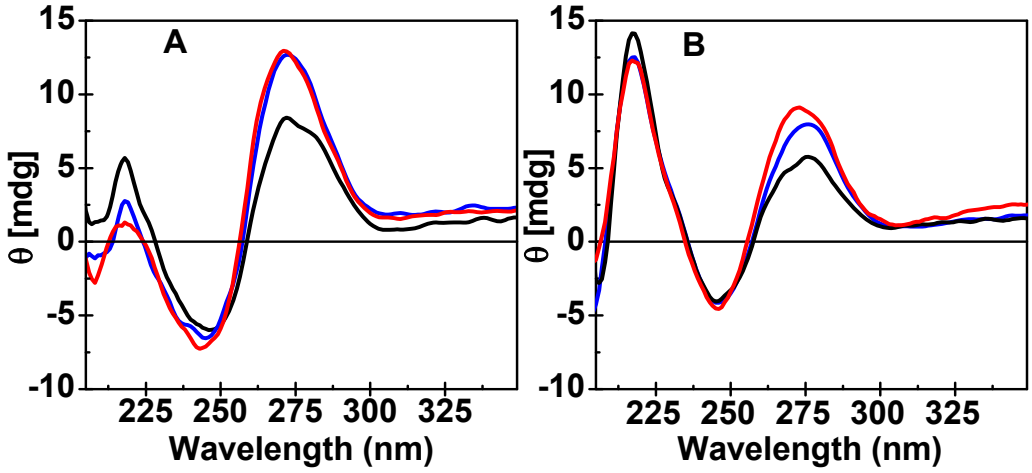

**Figure 3.5** The CD spectra of (A) anti-PDGF aptamer and (B) anti-cocaine aptamer showed a structural transition from a folding state (red) or hairpin state (blue) to an extended single-stranded state (black).

The CD spectra of the anti-PDGF and anti-cocaine aptamers before and after thermal treatment and target introduction are shown in Figure 3.5. The aptamer CD spectrum is characterized by two positive-going features at 272 nm and 217 nm and a negative-going feature at 244 nm. Prior to thermal treatment the CD spectrum showed a high CD intensity at 270 nm, indicating a high hairpin content of the aptamers in their natively folded state (red curve). Thermal treatment then destroys this secondary structure, as indicated by the decrease in the 270 nm peak for both aptamers (black curve). Introduction of the target molecules to these thermally treated aptamers causes the 270 nm to increase in intensity again, indicating that the target molecules have induced a refolding of the aptamers to their hairpin-conformational state (blue curve). The high stability of the anti-PDGF aptamer-PDGF complex stabilizes the secondary structure formed by this interaction and restores the 270 nm spectral feature to its original level prior to thermal treatment. The increase in PDGF-BB concentration showed by the CD signal of anti-PDGF aptamer in solution and the linear relationship of the ellipticity of anti-PDGF aptamer at 218 nm with low PDGF-BB concentrations is presented in Figure 3.6.

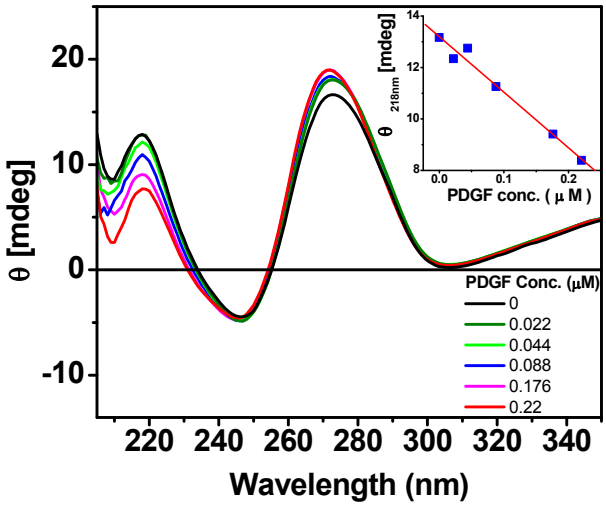


**Figure 3.6** The effect of concentration increase of PDGF-BB on the CD signal of anti-PDGF aptamer in solution concentrations of (a) 0 μM; (b) 0.022 μM; (c) 0.044 μM; (d) 0.088 μM; (e) 0.176 μM; (f) 0.22μM. Insert: linear relationship of the ellipticity of anti-PDGF aptamer at 218 nm with low PDGF-BB concentrations. The aptamer concentration is 4 μM.

Thermal reversibility of the conformational changes of aptamer in solution was tested by performing many cycles of thermal measurements between 5 and 95 degree Celsius (Figure 3.7). Considering the aptamer PDGF complex formation as a reversible reaction, any disturbance in aptamer concentration will slightly displace the system from its equilibrium condition. The data suggest that the aptamer wasn't destroyed during the heating process and it would return to the previous conformation if the perturbation will be removed. The melting CD spectra of anti-cocaine aptamer, which show structural transitions from the hairpin state to the single-strand state is presented in Figure 3.7

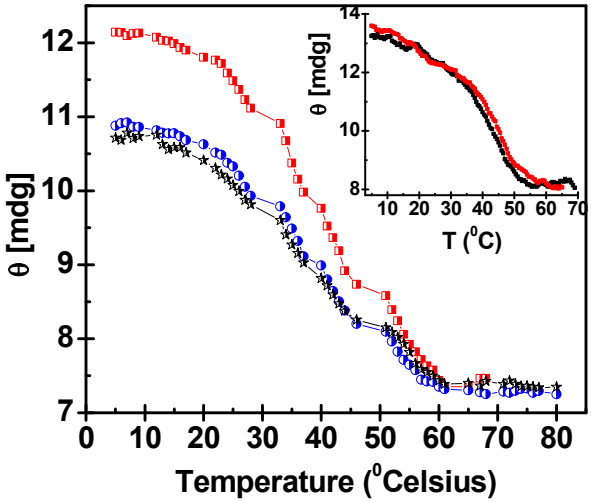


**Figure 3.7** The melting curves at 274 nm of anti-PDGF aptamer (black), anti-PDGF aptamer with PDGF (red), anti-PDGF aptamer with Lyz (blue). Insert: The melting curves of anti-PDGF aptamer with PDGF taken after one cycle. This indicates that the aptamer returns to the original conformation.

The data suggest that the aptamer was not destroyed during the heating process and would be expected to return to its initial conformation if the perturbation were removed. The melting CD spectrum of the anti-cocaine aptamer, which shows structural transitions from hairpin state to the single-stranded state, is shown ii Figure 3.8.

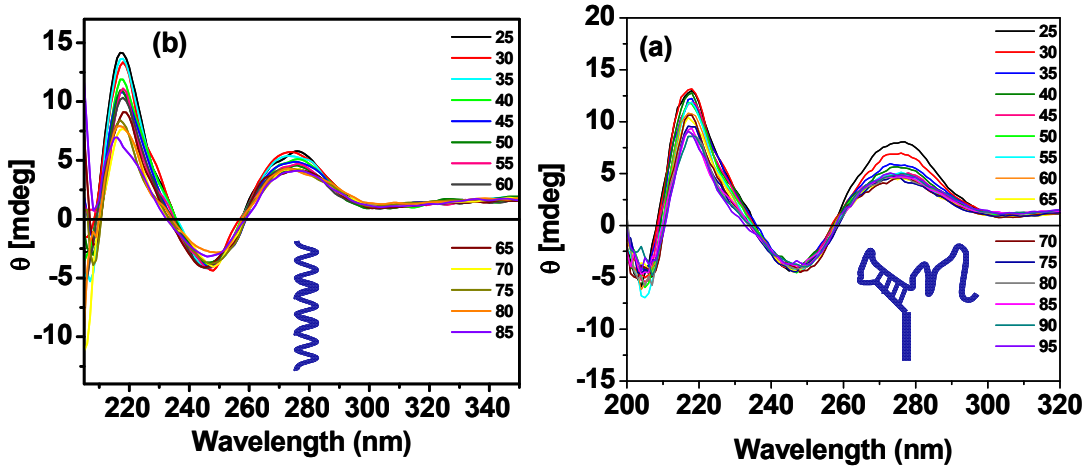


**Figure 3.8** Temperature-dependent CD spectra of (a) anti-cocaine aptamer and (b) anti-cocaine aptamer thermal treated where the concentration of aptamer was 5x $10^{-6}$ M in TE buffer (pH=7.5) at the indicated temperature.

These CD results confirm independently that thermal treatment eliminates the secondary structure of the aptamers, and that interaction with target molecules induces aptamer refolding, entirely consistent with our SERS results.

### 3.4 Conclusions

In chapter 3, we have demonstrated a direct, label-free, optical method for monitoring the binding of an aptamer to its target. Interaction of target molecules to aptamer SAMs induces conformational modifications in the aptamer molecules, monitored by assessing the aptamer SERS spectra reproducibility. CD spectroscopy independently supports our

observations that changes to the reproducibility of the SERS spectra are a result of conformational changes to the aptamer induced by target binding.

# Chapter 4: Visualizing light-triggered DNA release by nanoshell-based nonviral vectors in living cells

## 4.1 Introduction

Strategies for the directed release of controlled quantities of molecules inside living cells are in high demand for drug delivery,[74] gene therapy,[181-182] and tissue engineering.[183-184] In this chapter, the use of NS functionalized with ds-DNA to transport and deliver DAPI molecules into H1299 cells is presented. A released mechanism of DAPI molecules, initially bound to the ds-DNA on the NS surface, is presented due to the illumination of the nanoshell-dsDNA-DAPI complex with NIR light. An acytotoxicity assay demonstrated that NS uptake is nontoxic and that laser irradiation of nanoshell-laden cells under the conditions where DAPI release occurs does not induce cell death. These experimental observations have resulted in the first demonstration of laser induces release molecules from nanoparticle surfaces inside the cells. Reproduced with permission from R. Huschka, O. Neumann, A. Barhoumi, and N. J. Halas, Nano Lett., 2010, 10 (10), pp 4117–4122. Copyright © 2010 American Chemical Society.

The release mechanisms of most delivery vectors depend on processes such as diffusion, dissolution, chemical and enzymatic reactions, or changes in various environmental factors such as temperature, pH, solvent, and ionic concentrations.[181,185-188] For example, transfection reagents such as polyethylenimine act as a proton sponge following endocytosis, absorbing protons in the low-pH environment of the endosome, causing it to swell and eventually rupture, facilitating gene delivery.[189] This type of environmental control of molecular release varies with cellular location and cell type and

can result in unpredictable release. A physical release mechanism that does not rely on the specific chemical properties of the cellular environment would be highly useful and more easily generalizable to various cell types.[190] Light-induced release is a particularly attractive option; the high spatial and temporal control that lasers provide would be highly useful for initiating and following intracellular processes dynamically at the single cell level.[191-198]

Plasmonic nanoparticles, metal-based nanostructures supporting collective electronic oscillations, are highly promising potential candidates for facilitating controlled light-triggered release due to their large optical cross sections, their geometrically tunable optical resonances,[3,199-200] and their strong photothermal response.[201-202] Because of their large cross sections and extremely low quantum yield, metallic nanoparticles convert optical energy to thermal energy with high efficiency upon resonant optical illumination.[203-204] Resonant optical illumination of the nanoparticle triggers the controlled dehybridization and release of DNA molecules adsorbed onto the nanoparticle surface.[195,197] Gold nanoparticles are also biocompatible, easy to fabricate, and can be functionalized with a wide variety of host-carrier molecules capable of noncovalent accommodation of guest molecules.[185,197]

Au nanoshells have been successfully employed in a range of biomedical applications [205-207] including photothermal cancer therapy.[13-14,202,208-209] The plasmon resonance wavelength of a nanoshell can be varied by changing the core size and shell thickness.[3,101,200] This tunability is particularly important for biomedical applications because the nanoshell can easily be designed to have a large absorption efficiency in the

near-infrared (NIR) water window (690 900 nm), where blood and tissue are maximally transparent and light can penetrate tissue to depths of several inches.[210]

Recently, we demonstrated light-induced dehybridization of double-stranded DNA (*ds*DNA) attached to Au nanoshells.[197] Nanoshells of dimensions $[r_1, r_2]=[63, 78]$ nm with the plasmon resonance wavelength at 800 nm were coated with *ds*DNA, where one strand of the DNA had a thiol moiety on its 5' end, facilitating covalent attachment to the nanoshell surface by a Au-thiol bond. The complement DNA sequence was nonthiolated, and therefore bound only to its complementary DNA sequence and not to the nanoparticle surface. Upon illumination with NIR light at the nanoshell plasmon resonance wavelength, the *ds*DNA was dehybridized, releasing the nonthiolated antisense sequence. This process is highly efficient, resulting in the dehybridization and release of nominally 50% of the DNA from the complexes upon illumination with no apparent temperature increase in the solution ambient. DNA antisense therapy has been explored extensively as a class of gene therapy and has highly promising potential to provide safe and effective treatments for a multitude of diseases and genetic disorders.[211] Here we show that in addition to light-controlled release of DNA the nanoshell-*ds*DNA complex serves as an effective host and light-triggered release vector for other types of molecules. Many types of guest molecules can associate with *ds*DNA, either by intercalating between adjacent base pairs or by binding in either the major or minor groove of the DNA double helix.[212] The driving forces for association can include $\pi$ -stacking, hydrogen bonding, van der Waals forces, hydrophobic and polar interactions, and electrostatic attractions; therefore, *ds*DNA can host a large variety of guest molecules via noncovalent bonds.[212-213] DAPI (4',6-diamidino-2-phe-nylindole), a water-soluble blue

fluorescent dye that binds reversibly with dsDNA (Appendix B, Figure B4), is the molecule we chose to deliver to demonstrate and clearly visualize the light-induced intracellular release. DAPI was chosen because of its bright fluorescent properties, stability, and negligible toxicity.[214] DAPI binds preferentially to the minor grooves of dsDNA; its association with DNA causes a large increase in its quantum yield.[214-218] The selectivity of DAPI to dsDNA makes it a frequently used, standard stain for cell nuclei in fluorescence microscopy.[217-218]

### 4.2 Results and discussion

A schematic of the light-triggered molecular release is shown in Figure 4.1. Initially, nanoshell-*ds*DNA complexes were loaded with DAPI by incubation of DAPI with the nanoshell-*ds*DNA complexes (Appendix B). Next, the nanoshell-*ds*DNA-DAPI complexes were incubated with H1299 lung cancer cells (Appendix B), where intracellular uptake was verified using both dark-field and bright-field microscopy. Upon illumination with an 800 nm CW laser, corresponding to the peak resonant wave-length of the nanoshell complexes (Appendix B, Figure B5), the DAPI molecules were released from the nanoshell complexes. Subsequent to release, the DAPI diffused through the cytoplasm and into the cell nucleus, where it preferentially bound and stained the nuclear DNA. To the best of our knowledge, this is the first light-controlled delivery system that can be tailored to release quantifiable amounts of nonbiological molecules within living cells by remote means on demand.

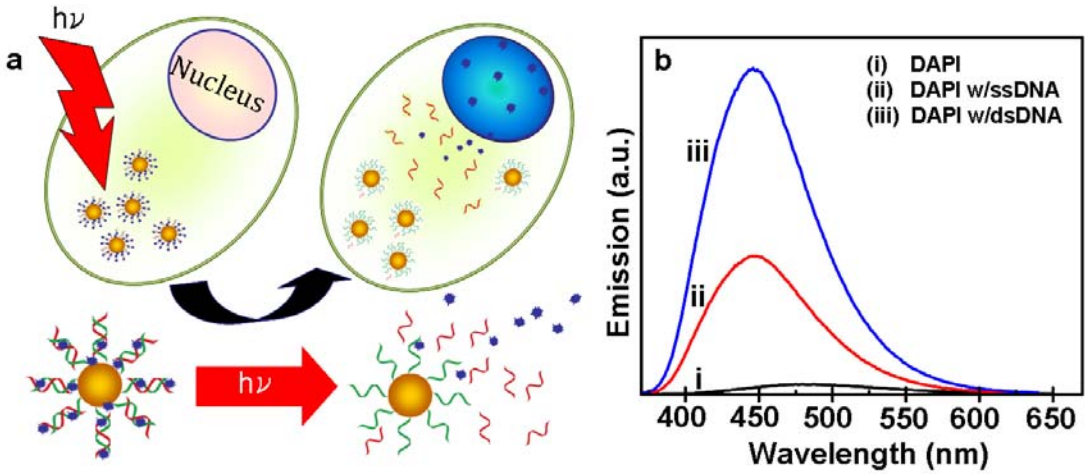


**Figure 4.1** Light-induced DAPI release: (a) Schematic diagram of the light-induced DAPI release and diffusion inside the cell; (b) Fluorescence emission of (i) DAPI only, (ii) DAPI with *ss*DNA, and (iii) DAPI with *ds*DNA.

The DAPI fluorescence emission intensity drastically increases as a result of DAPI molecules binding to DNA (Figure 4.1b). As an isolated molecule, DAPI has a low quantum yield (Figure 4.1b, i),[215] however, when DAPI is attached to single-stranded DNA (*ss*DNA) (Figure 4.1b, ii), a weak electrostatic attraction binds the cationic DAPI molecules to the negatively charged phosphate backbone of the DNA, resulting in a slight increase in its fluorescence intensity.[215] When the DAPI molecules bind to the minor grooves of the *ds*DNA (Figure 4.1b, iii),[215,218] the increased rigidity and stabilization significantly increases its quantum yield.[214] DAPI binding to the *ds*DNA also displaces $H_2O$ molecules initially solvating the DNA oligomers, significantly reducing intermolecular proton transfer between $H_2O$ and DAPI, resulting in an additional increase of DAPI fluorescence intensity.[215-216,219] (Additional characterization of DAPI-DNA binding is provided in the Appendix B Figure B1).

The specific base-pair composition of the *ds*DNA plays an important role in determining the number of DAPI molecules that will bind to the *ds*DNA.[220] Previous studies have shown that DAPI preferentially binds to regions rich with adenine (A) and thymine (T) nucleotide bases because DAPI forms hydrogen bonds with A-T bases pairs.[218] The DAPI molecule is 14-15 Å long, corresponding to an overlap of three base pairs.[215-217,220] In our experiments, since it is desirable to bind as many DAPI molecules as possible to improve the staining of the nucleus after light-induced release, we designed a 26-base pair sequence with multiple A-T-rich regions with segments of three or more consecutive A-T base pairs to specifically enhance DAPI loading (Figure B2, Appendix B).

To use this light-triggerable complex for molecular release in live cells, the complex must first be effectively taken up by the cells of interest. To facilitate cell uptake, the nanoshell-*ds*DNA-DAPI complexes were incubated with H1299 lung cancer cells in serum containing cell culture medium for 1 h. After incubation, the cells were fixed and internalization of the nanoshell-*ds*DNA-DAPI complexes was imaged using both dark field (Figure 4.2a,b) and bright-field (Figure 4.2c) microscopy. Nanoshells in this size range both absorb and scatter light; their strong scattering cross section enables them to be easily visualized by optical microscopy. In Figure 4.2a, H1299 cells with their cell membranes marked by the green fluorescence dye Alexa Fluor 488 WGA (wheat germ agglutinin) are shown. Internalized nanoshells are easily seen as diffraction-limited bright spots in this image. As a control, cells not incubated with the nanoshell-*ds*DNA-DAPI complexes showed no observable bright spots when imaged in the same manner (Figure 4.2B).

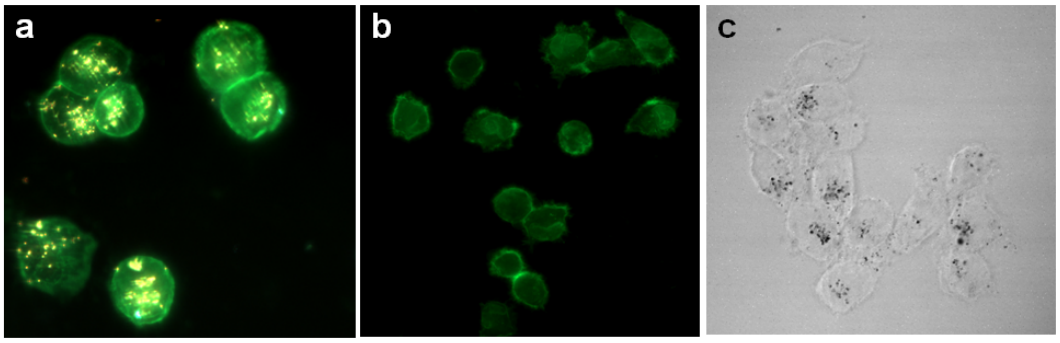


**Figure 4.2** Nanoshell-*ds*DNA-DAPI cell uptake: Dark field/epifluorescence images of (a) H1299 lung cancer cells incubated with nanoshell-*ds*DNA-DAPI complexes, (b) nonincubated cells (control); (c) Bright-field image of middle slice of H1299 lung cancer cells incubated with nanoshell-*ds*DNA-DAPI complex.

Because the dark-field images are two-dimensional, these images alone do not give clear evidence whether the nanoshell complexes have been endocytosed or are merely adsorbed onto the outer membrane of the cell. Bright-field imaging was used to further investigate cellular uptake. Obtaining images at varying depths of field within an individual cell allows us to clearly visualize in three dimensions the nanoshell distribution within the cell. Figure 4.2c is a slice from the middle of the cell showing clear diffraction-limited dark spots corresponding to nanoshell complexes, verifying that the nanoparticles are internalized within the cell. A video sequence of two-dimensional projections obtained as the depth of field is scanned through the cell resolves the 3D distribution of nanoshell complexes. Internalization of nanoshells is in agreement with observations by Ochsenkühn et al., who used TEM sections of NIH-3T3 fibroblast cells to confirm nanoshell uptake.[221]

At first thought, it is surprising that the nanoshell-*ds*DNA-DAPI complex is internalized into cells because the negatively charged phosphate backbone on the DNA

should experience electrostatic repulsions with the negatively charged cell membrane.[222] However, previous studies by Chithrani et al. and Giljohann et al. suggest that Au nanoparticles functionalized both with and without DNA adsorb extracellular serum proteins from the cell culture media.[222-223] The adsorbed extracellular proteins then interact with the cell membrane and facilitate cellular uptake in an adsorptive endocytosis pathway. Conversely, recent studies by Ochsenkühn et al. show that nanoshell uptake increases in the absence of extracellular proteins, suggesting the possibility of a passive, nonendocytotic uptake mechanism.[221] While in our studies nanoshell complex uptake is clearly visualizable in H1299 cells, the precise uptake mechanism is not clearly identifiable and is likely to depend on a variety of factors including cell type, functionalization of the nanoparticle, and incubation conditions.

To investigate intracellular light-induced molecular release, the H1299 cells incubated with nanoshell-dsDNA-DAPI complexes were illuminated with a NIR CW laser (1 W/cm$^2$, 800 nm) for 5 min. This irradiation time and laser power level were determined from previous experiments,[197] which demonstrated after 5 min of laser irradiation that no additional dehybridization of the DNA occurred. This laser power and time allow the DAPI to be released while minimizing laser exposure to the H1299 cells. After laser irradiation, samples were placed in an incubator for one hour to allow time for released DAPI molecules to diffuse to the nucleus. Next, the nuclei of the cells were isolated by lysing the cell membrane and the DAPI fluorescence intensity was quantified by flow cytometry. Nuclei isolation is necessary to ensure that flow cytometry only measures fluorescence from DAPI molecules bound to genomic DNA in the nucleus and does not measure fluorescence from DAPI molecules in the cytoplasm.

Evidence of DAPI release is shown by the normalized flow cytometry histograms of DAPI fluorescence intensity versus number of nuclei from H1299 cells incubated with nanoshell-*ds*DNA- DAPI before and after laser treatment (Figure 4.3). After laser treatment, the fluorescence intensity of the nuclei increased, demonstrating that DAPI molecules were released from the nanoshells, diffused through the cytoplasm and into the cell nuclei, binding with the genomic DNA. Prior to laser irradiation, some DAPI fluorescence is observed within the cells (Figure 4.3c, left) and measured by flow cytometry (Figure 4.3a,b, before laser). This DAPI fluorescence signal originates from both excess DAPI molecules present in the sample and DAPI molecules that were noncontrollably released from the complexes during the incubation and prior to laser irradiation. The bar graph depicts the mean DAPI fluorescence intensity ±SEM (standard error of the mean) increase from before laser (59.7±0.21) to after laser (79.9±0.33) (Figure 4.3a) (a ~33% increase in fluorescence intensity.) An unpaired t test of the two means was performed at a 95% confidence level, which resulted in a two-tailed p value of $p < 0.0001$, which is statistically significant. This observed increase in DAPI fluorescence after laser treatment (~33%) demonstrates that the nanoshell-*ds*DNA complex effectively released its guest molecules from the *ds*DNA host carriers inside the cells. Epifluorescence images of H1299 cells incubated with nanoshell-*ds*DNA-DAPI before (Figure 4.3c, left) and after (Figure 4.3c, right) laser treatment visually show the increase in DAPI fluorescence intensity. The cell membrane is marked by the green dye, Alexa-Fluor 488 wheat germ agglutinin.

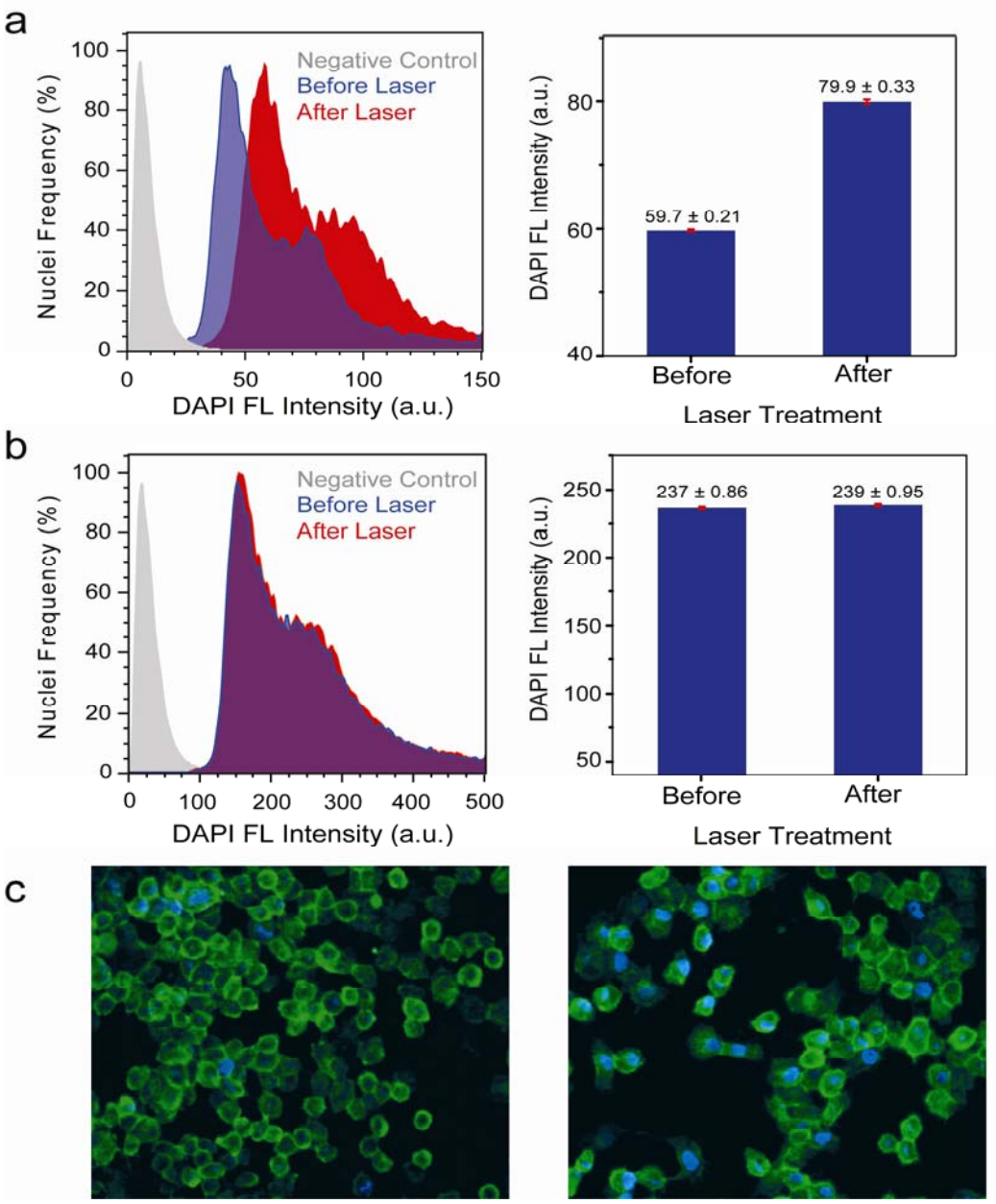


**Figure 4.3** Light-induced DAPI release. (a,b) Flow cytometry histograms of DAPI Fluorescence (Ex:355 nm; Em:460 nm) versus number of isolated nuclei from H1299 cells incubated with (a) nanoshell-*ds*DNA-DAPI and (b) DAPI (control). Negative control (gray), treated cells without laser irradiation (blue) and treated cells with laser irradiation (red). Bar graphs display the mean DAPI fluorescence intensity (SEM before and after laser irradiation. (c) Epifluorescence images of H1299 cells incubated with

nanoshell-*ds*DNA-DAPI (left) before and (right) after laser treatment. The cell membrane is marked by the green dye, Alexa-Fluor 488.

The plasmon resonant illumination of the nanoshells is crucial for DAPI release into the cells. To test this hypothesis, a control experiment consisting of H1299 cells incubated with DAPI only (no nanoshells) was conducted (Figure 4.3b). The cells were irradiated with the NIR laser under conditions identical to the previous experiment. The mean DAPI fluorescence intensity (SEM did not significantly increase after laser irradiation (237±0.86 to 239±0.95, p=0.1188), indicating that DAPI release does not occur without the presence of the nanoshell-*ds*DNA complex. It is important to note that the mean fluorescence intensity is higher for the control (Figure 4.3b) compared to the nanoshell-*ds*DNA-DAPI sample (Figure 4.3a) due to multiple washings of the nanoshell-*ds*DNA-DAPI sample.

The shape of the flow cytometry histograms for both before laser and after laser are consistent with nuclei stained with DAPI.[224-225] DAPI is routinely used to study the cell cycle because it binds to DNA stoichiometrically. Looking at the before laser histogram in Figure 4.3a as an example, the tallest peak (~40) originates from nuclei with two sets of chromosomes. This peak is the tallest because in a typical cell cycle, a cell spends the longest portion of time with two sets of chromosomes; therefore, the probability of a cell having two sets of chromosomes is the highest. The second, smaller peak (~80), double the fluorescence intensity of the tallest peak, indicates nuclei that have exactly double the amount of DNA, four sets of chromosomes, and are ready to enter mitosis and divide. The nuclei with fluorescence intensities in between these two peaks indicate cells that are

currently synthesizing DNA prior to mitosis. The negative control histogram (gray) has a single peak because in the absence of DAPI every nuclei essentially fluoresces identically resulting in a signal that is attributed to autofluorescence (background).

To ensure that this method for light-triggered intracellular molecular release would be useful for biomedical applications, such as drug delivery, a cytotoxicity assay was performed to investigate both the effects of nanoshells and laser irradiation on cell viability. (PI) was chosen as a marker to distinguish viable from nonviable cells, because it is a membrane-impermeable dye that is excluded from viable healthy cells.[226] When a cell membrane is damaged, PI enters the cell, stains the *ds*DNA in the nuclei, and emits red fluorescence; however, undamaged cells will not fluoresce. Flow cytometry was used to observe changes in PI fluorescence intensity for a large sample size of 30 000 cells. The negative control (Figure 4.4a) consisted of cells that were not incubated with nanoshell-*ds*DNA-DAPI and did not undergo laser treatment. The fluorescence observed in Figure 4.4a is attributed to autofluorescence and PI staining caused by apoptotic and necrotic cells already present in the experiment with damaged membranes. The nanoshell-*ds*DNA-DAPI complexes were then incubated with H1299 cells for 12 h. Following incubation, the cells were divided into two samples: cells not treated with the laser (Figure 4.4b) and cells treated with the laser for 10 min (Figure 4.4c). Figure 4.4b shows no significant increase in PI fluorescence intensity, demonstrating that nanoshell-*ds*DNA-DAPI complexes are not cytotoxic under the experimental conditions of the study.

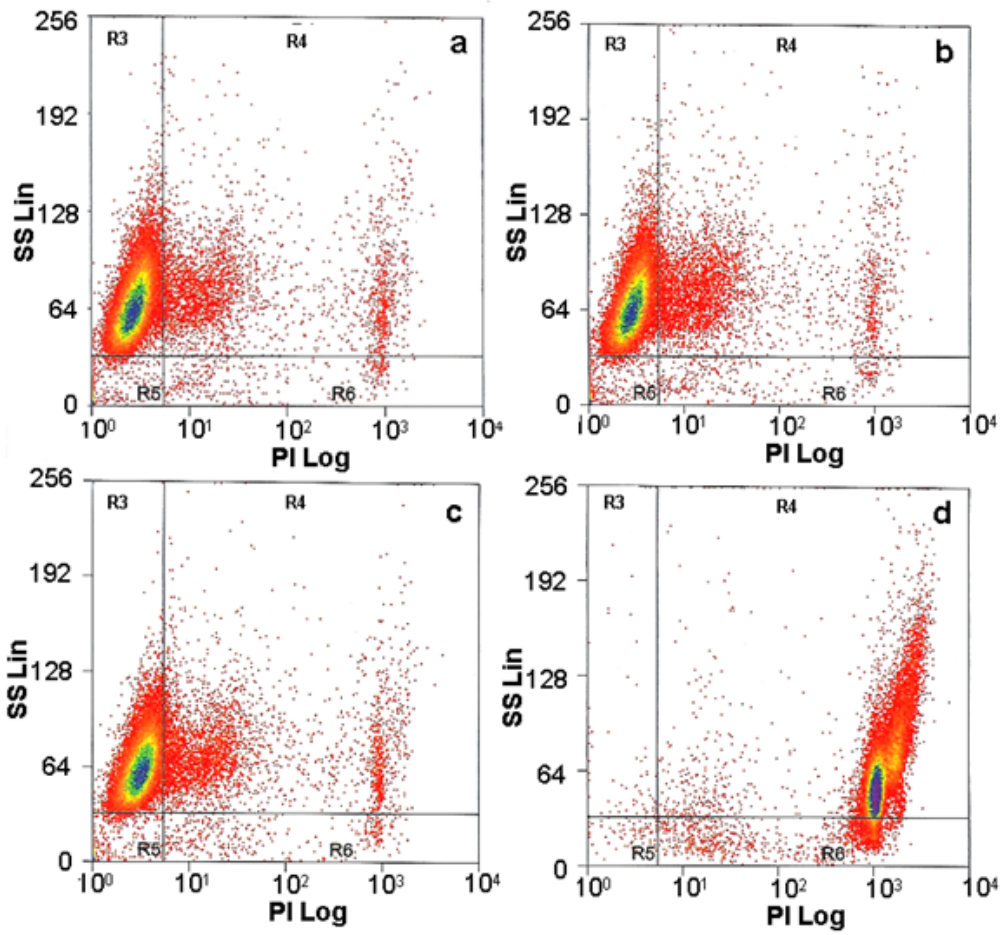


**Figure 4.4** Flow cytometry cytotoxicity assay. All plots are propidium iodide (PI) fluorescence intensity versus side-scattered light. (a) Negative control: H1299 cells not incubated with nanoshell-*ds*DNA-DAPI and no laser treatment. Cells incubated with nanoshell-*ds*DNA-DAPI for 12 h: (b) without laser treatment and (c) with laser treatment. (d) Positive control: cells were treated with 0.1% Citrate/ 0.1% Triton, which permeates the cell membrane, allowing PI to stain the *ds*DNA in the nucleus.

More interestingly, cells incubated with nanoshell-*ds*DNA-DAPI complexes and irradiated with the laser for 10 min also show no significant increase in PI fluorescence intensity. This demonstrates that the light-triggered release procedure did not adversely

affect the cells. Considering nanoshells are well known for their use in photothermal therapy, this result may be surprising; however, the illumination conditions for this experiment (1W/cm$^2$, 5 min) were significantly below those used for photothermal induction of cell death in cell culture (4W/cm$^2$ ,4-6 min).[202] Figure 4.4d represents a positive control sample of cells treated with 0.1% Citrate/0.1% Triton solution, which permeates the cell membrane, allowing PI to enter the cell and stain the nucleus, resulting in a large increase in PI fluorescence intensity.

### 4.3 Conclusions

In conclusion, nanoshells functionalized with *ds*DNA were successfully used to transport DAPI molecules into living cells. Successful uptake of nanoshells into H1299 cells was achieved. DAPI molecules, initially bound to the *ds*DNA on the NS surface, are released due to the illumination of the nanoshell-*ds*DNA-DAPI complex with the appropriate NIR light. DAPI molecules initially released in the cell cytoplasm diffuse into the cell nucleus and bind to the genomic DNA of the cell. The staining of the cell nucleus with the released DAPI was quantified using flowcytometry. Acytotoxicity assay demonstrated that nanoshell uptake is nontoxic and that laser irradiation of nanoshell-laden cells under the conditions where DAPI release occurs does not induce cell death.

This nanoshell-*ds*DNA system could be extended to a multitude of other guest molecules that associate with the host *ds*DNA carrier including small organic fluorophores,[213] steroid hormones,[227] and therapeutic molecules.[212-213,227] For example, the quest to find *ds*DNA intercalators that inhibit the uncontrollable replication of tumor cells comprises an entire field of cancer research. Currently, there are more than 130

FDA approved anticancer drugs that specifically target DNA.[228] For in vivo clinical applications, however, before the DNA intercalator can reach the genomic DNA, it must overcome several hurdles, such as metabolic pathways and cytoplasmic and nuclear membranes. As a result, the failure of DNA therapies to offer successful clinical treatments is primarily due a lack of viable delivery methods rather than effectiveness of the DNA intercalator to treat cancer.[212] This nanoshell-*ds*DNA delivery vector preserves the guest molecule by minimizing nondesired interactions with other molecules and it provides light-triggered release with controllable delivery.

### 4.4 Materials and Methods

**A. Reduction of thiolated *ss*DNA:** The oligonucleotides used in this study are: 26-bp DNA oligo: 5'-GAT ATC CTA TAC GGA ATT CGA ATT CG-3', 50bp DNA oligo: 5'-GAC TGC GAC CAA CCT AGC CTG CTA TGA TGT ACG GTC AAC CTG ATT GCC GC-3', and the complementary 26bp and 50bp *ss*DNA sequences for both strands. DNA was purchased from Integrated DNA Technologies (IDT) Inc. The thiolated *ss*DNA (26 or 50 bp) was incubated with 100 mM of DTT (reducing agent) in 100 mM sodium mono-phosphate buffer at pH=7.5. The mixture was incubated at room temperature for 1 hour to allow for complete reduction of the disulfide bonds. The solution was then filtered through a NAP-5 column to remove the excess DTT. Elution of the column with water was performed to collect the purified *ss*DNA in $H_2O$. The concentration of the *ss*DNA stock solution was determined by measuring its absorbance at 260 nm, using a UV-vis-NIR spectrophotometer (Cary 5000, Varian Inc.).

**B. Nanoshells preparation and DNA Functionalization:** Silica core-gold nanoshells were fabricated using a method previously described.[31,101] Au-silica nanoshells were

fabricated with core and shell dimensions of $[r_1, r_2]$ = [63, 78] nm, corresponding to a nanoshell plasmon resonance at 800 nm in aqueous solution, which is the wavelength of the excitation laser used in the photothermal experiments. *ds*DNA was hybridized by mixing two complementary ssDNA sequences at a 1:1 molar ratio in DNA hybridization buffer (Tris EDTA (TE)/50mM NaCl, pH=7.5), heating the solution to 950C for 10 min in a large water bath and then cooling slowly to room temperature. *ds*DNA was attached to nanoshells via overnight incubation and continuous shaking. To remove the excess *ds*DNA the solution was washed three times by centrifugation and resuspension in TE buffer.

**C. DAPI stained DNA-functionalized nanoshells:** DAPI (Sigma) was used without further purification. The concentration of the DAPI stock solution was determined spectrophotometrically using the molar absorption coefficient ($\varepsilon_{342nm}$=23,000 $M^{-1}cm^{-1}$ for DAPI in water). The stock DAPI solution was kept stored at -20°C. After purification the NS-*ds*DNA complexes were incubated overnight with DAPI solution and then washed three times by centrifugation and resuspension in TE buffer to remove the excess DAPI.

**D. Cell Preparation and Nanocomplex incubation:** The H1299 lung cancer cells are cultured in media (Gibco) supplemented with 5% heat-inactivated fetal bovine serum, 1% antibiotics and maintained in a 37°C incubator with 5% $CO_2$ air. Cells were initially seeded in 6-well plates at a density of 400,000 cells/well 24 hours prior to incubation with nanoshell-*ds*DNA-DAPI complexes. The nanoshells were added to the serum containing media in a NS:Cell ratio of 10,000:1. After 1 hours of incubation with nanoshell-*ds*DNA-DAPI complexes, the media was aspirated off. Cells were washed two

times with PBS. Cells were detached from the plate with trypsin and the cells were finally suspended in additional media.

**E. Laser Treatment:** Half of this cell/media suspension underwent laser treatment (5 minute illumination at 800 nm with continuous wave laser, 1W/cm$^2$). The other half did not receive a laser treatment. This laser power and time is chosen from previous DNA dehybridization studies. After laser treatment, both samples (laser and no laser) were allowed to incubate for 1 hour to allow released DAPI molecules to diffuse to the nucleus.

**F. Isolation of Nuclei and Flow Cytometry:** Nuclei were isolated using Nuclei Isolation Kit: Nuclei EZ Prep (Sigma Aldrich, NUC101-1KT). Briefly, the cells were collected via centrifugation (500xg/4°C/5min).Washed once with PBS. Resuspended and centrifuged twice in Nuclei EZ Prep lysis buffer. Final suspension was in 250 uL of PBS. Flow cytometry was performed on BD influx. The excitation laser was a 355nm solid state UV laser. Emission was collected at 460nm. Data was analyzed by FlowJo and the histograms were normalized by % of max. H. Statistical Analysis: For statistical analysis, the SEM (standard error of the mean) was calculated by dividing the standard deviation by the sample size. Sample size for Figure 3a: 19,100. Sample size for Figure 3b: 47,800. Because of the large sample sizes, the data was treated as being normally distributed, which is preferred over using a nonparametric statistic test. An unpaired t-test was performed to determine the significance at a 95% confidence interval. The p-value reported is a two-tailed p-value. A p-value less than 0.05 is determined to be statistically significant.

**G. (a) Cytoviva Microscope:** The Cytoviva microscope is a dark-field/epifluorescence microscope. Excitation and emission filters on the dual mode fluorescence microscope are used to choose the right wavelengths of light for fluorophore excitation and emission collection. All images are taken with a 40x objective. The white light source is an Expo Cytoviva X-cite series 120 light source, mounted on an Olympus BX41 microscope. The camera is a Dage Technologies Exponent CCD camera.

**(b) Cytoviva Sample Preparation**: After laser treatment, cells were plated and grown on chamber slides as previously described. Chamber slides are used so that the walls of the slide can be removed and imaging can be done on the slide. After 12 hours of incubation, cells were washed three times with 1x PBS. A fixing solution (4% paraformaldehyde) was added to the chamber slide and allowed to incubate for 15 minutes at room temperature. The fixing solution was aspirated off and the cells were washed three times in 1x PBS. A staining solution of Alexa Fluor 488 (5.0 g/mL in PBS) was added to the chamber slide and allowed to incubate for 10 minutes at room temperature. Staining solution was aspirated off and the cells were washed twice with 1x PBS. The cells were then mounted with anti-fade fluorescence mounting medium and glass coverslip.

**H. Image analysis:** Epifluorescent images were taken on Zeiss Axioplan 2 epifluorescence microscope. The change in areal DAPI fluorescence inside the cells provides a way to quantify dsDNA dehybridization on NS surface upon laser irradiation. It is been implemented by marking the cells nucleus with blue dye (DAPI) and cells membrane with green dye (Alexa Fluor 488) followed by computer assisted shape recognition and pixel statistics for all the nuclei and membranes areas. Using the cell

membrane as guides, the program places appropriate regions of interest for measuring the blue fluorescence of individual cells. Analysis was done on 8 fluorescence images to obtain standard deviation. Although simple in principle, this analysis has served as a useful model for a deeper understanding of the in vitro *ds*DNA dehybridization.

# Chapter 5: Surface enhanced Raman optical activity of biomolecules

## 5.1 Introduction

Chirality is a subtle geometrical concept of asymmetry implemented at the molecular level. It is essential role is revealed by the impressive number of chiral-specific applications in nanotechnology, pharmaceutics, agriculture, and flavors.[229-230] In this chapter a qualitative, nondestructive assay based on NIR-SEROA is presented. We for the first time to determine the chirality and the conformation of (S)- and (R)-Tryptophan and (SS)- and (RR)- Cysteine-Phenylalanine-Glycine-Glycine molecules on Au nanoparticles surface. Scattered polarization circular intensity differences have been observed and correlated to complementary enantiomers of Trp and Cys-Phe-Gly-Gly while chemically bound to Au nanoparticle films.

Chirality is seen in many biological molecules including proteins, DNA, drugs, pesticides, and many other agents.[231] Enantiomers that possess a double existence of mirror related structures have a different bioactivity. For example, one enantiomer of penicillamine is a potent anti-arthritic agent whereas the other enantiomer is highly toxic.[232] Therefore a precise method for sensing chirality is critical to the synthesis of chiral-specific products as well as catalysis.

Raman optical activity (ROA) measurements can elucidate the stereochemistry of chiral molecules based on the intensity differences between right- and left-circularly polarized Raman-scattering. ROA is an extremely weak phenomenon with a scattering cross-section of $E^{-3}$ to $E^{-6}$ smaller than that of conventional Raman, while the signal-to-

noise ratio is greater.[233] Therefore, it requires high-purity, high-concentrated samples, and long data collection times of several hours or days.

Surface-enhanced Raman optical activity (SEROA) takes advantage of the high-intensity optical field introduced by metallic nanoparticles (NPs) when resonantly excited. Known as a plasmon, this phenomenon results in an increased inelastic scattering cross section of the analyte molecule on the surface, therein improving the sensitivity of detection and reduceing the data collection time.[60-61,234] Moreover, the electric field is further enhanced at the junction between resonant NPs, known as a "hot spot".[235] The SEROA signal enhancement critically depends on the local electromagnetic intensity and the degree of order in the analyte monolayer on metallic surface [236-237]. SEROA was initially observed using silver nanoparticle aggregates as plasmonic substrates.[60] In later studies, enantiomeric molecules were analyzed but only as isolated species.[60,238] To date, there has been no evidence of distinction between two different enantiomers in SEROA measurements.[234]

### 5.2 Experimental

**A. Materials:** Powder (S)- and (R)-tryptophan (Trp) (C11H12N2O2), HAuCl4·3H2O (99%), and poly(4-vinylpyridine) (PVP, MW 160,000) were purchased from Sigma-Aldrich. Powder (SS)- and (RR)-amine terminated phenylalanine-cysteine-glycine-glycine oligomers (Phe-Cys) was synthesized by aaddtec™. The manufacture's stated purity of the analytes was ≥ 98%. All analytes were used without further modification. Liquid phenylethylamine was purchased from TCI America. Common laboratory chemicals were supplied by Sigma-Aldrich or Fisher Scientific and used without further

modification. Deionized water (18 M□) was provided by a Milli-Q™ system. Quartz substrates were purchased from Technical Glass, Inc.

**B. Aqueous gold nanoparticle preparation:** The gold NPs were fabricated by reducing 30 mL of the aged chloroauric acid solution (3 mL of 25 mM HAuCl4 with 50 mg K2CO3 dissolved in 200 mL of water and aged in dark for a minimum of 3 days before used) with 200 μL formaldehyde (37%) under rapid stir for 30 minutes at room temperature. The resulting colloid solution was several times centrifuged (2500 RCF, 10 min.), and the nanoparticles were redispersed in 20 mL water. The concentration of the gold nanoparticle was estimated to be 20 pM using absorbance measurements and Mie scattering theory.

**C. Sample Preparation:** Films of NPs supported on fused silica quartz were used as substrates. Quartz substrates were cleaned by immersing in "piranha solution" (H2SO4:H2O2=3:1) for 20 minutes followed by rinsing with deionized water (18.3MQ, Millipore). Note that piranha solution is extremely oxidizing, reacts violently with organics, and should be stored in loosely covered containers to avoid pressure buildup. The substrates were then coated with a PVP adhesion layer by immersion in a 1 wt % ethanol solution overnight. They were subsequently rinsed with ethanol, dried with filtered N2, and used immediately. Three dimensional (3D), Au nanoparticle (NP) samples are prepared in two stages. In the first stage the NPs were immobilized by depositing 100μL of aqueous NP solution on PVP coated quartz substrate and allowing it to incubate overnight, followed by rinsing with water several times to remove the excess of NPs and drying with nitrogen gas. The substrate was incubated with a fresh solution of analyte molecules (50 μM) and allowed to incubate overnight. In the second step aqueous

analyte functionalized NP are deposited onto the functionalized analyte-NP film. In case of tryptophan samples were allowed to dry, then gently rinsed with water and dried with N2 gas. Phe-Cys samples were allowed to incubate overnight, gently rinsed with water, and dried with filtered N2. All samples were isolated and stored in an N2 environment before use. Surface functionalization reduces the NP surface charge facilitating hot spots junction (blue) formation, with molecules inside enhanced the SERS or SEROA signal.

In the case of a saturated monolayer, the $SH^-$ group is expected to displace N-Au bonds. This results in an amine-terminated surface. When additional Au or Phe-Cys functionalized particles are added to the sample, molecularly bound aggregates are expected to form. To confirm the molecular binding of NP on film substrates, a study of aqueous NP aggregation by Phe-Cys was conducted. When Phe-Cys was combined with gold NP suspensions, the samples immediately began to change color from red to pink to violet and continued to darken. The initial tint of the sample (pink to dark purple) is dependent on the Phe-Cys concentration. The final tint was both molecule and particle concentration dependent. The color change indicates a plasmon red-shift and hence the NP aggregation. The rapid aggregation of NPs into colloids, that remain suspended in solution, implies molecular binding of the NP by both functional groups and an amine-termination of exposed NP surfaces.

### 5.2 Results and discussion

Here, we give the first report of clear mirror-image scattered circular Raman intensity in (S)- and (R)-Tryptophan (Trp), and (SS)- and (RR)- Cysteine-Phenylalanine-Glycine-Glycine (Cys-Phe-Gly-Gly) layers assembled on Au nanoparticle substrates. In order to

measure the differences between right- and left-circularly polarized Raman-scattering intensities induced by chiralic analytes, a NIR-SEROA spectrometer was developed by the addition of a 780 nm diode laser with a line width of 1 MHz (Sacher Lasertechnic, Marburg, Germany), NIR optical components and software modifications to a ChiralRAMAN™ SCP-ROA spectrometer (BioTools, Inc, Jupiter).[239] Surface-enhanced Raman spectroscopy (SERS) was also performed with Renishaw in Via Raman microscope (Renishaw, United Kingdom) to obtain even more accurate information about the molecular composition.

Theoretical investigations have established that SERS enhancement is induced by the electric dipole of the surface plasmon while SEROA enhancement requires effects from the magnetic/electric quadrupole.[236,240-241] We have designed a three-dimensional SEROA substrate which uses junctions between Au NPs to produce an aggregate plasmon. Samples were prepared in two stages (Figure 5.1). In the first stage, the NPs were immobilized by depositing 100 μL of aqueous NP solution on a quartz substrate coated with poly(vinyl pyridine) (PVP) and allowing it to incubate overnight, followed by rinsing with water and drying with nitrogen gas. The substrate was then incubated overnight in a fresh solution of analyte molecules (50 μM). In the second stage, aqueous analyte functionalized NP are deposited onto the functionalized analyte-NP film. When Trp was used as the analyte, the samples were dried in air, gently rinsed with water, and then dried with $N_2$ gas. Samples with Cys-Phe-Gly-Gly were immediately rinsed with water and dried with $N_2$ gas. NPs surface functionalization facilitates the hot spots junction formation, with molecules inside the aggregates hence enhancing the SERS or SEROA signal.

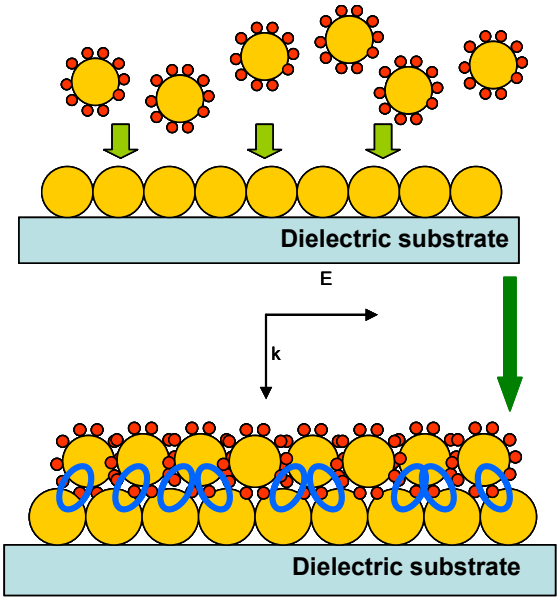


**Figure 5.1** Schematic of SEROA sample morphology: first layer: Au NPs; second layer: functionalized NPs with analyte of interest (hot spots junction, with molecules inside, excited at normal incidence (blue).

UV-Vis-NIR extinction spectroscopy and scanning electron microscopy (SEM) were used to characterize the NP films. Figure 5.2A shows the extinction spectra of (i) non-functionalized NPs in aqueous solution, (ii) a single layer of non-functionalized NPs on a PVP-coated quartz substrate, and (iii) a layer of non-functionalized NPs covered with a second layer of NPs functionalized with analyte molecules on a PVP-coated quartz substrate. The extinction spectra show the NP plasmon resonance peak at 520 nm and a broad aggregate resonance peak in the NIR region. The 3D morphology of the samples was confirmed by SEM. (Figure 5.2B).

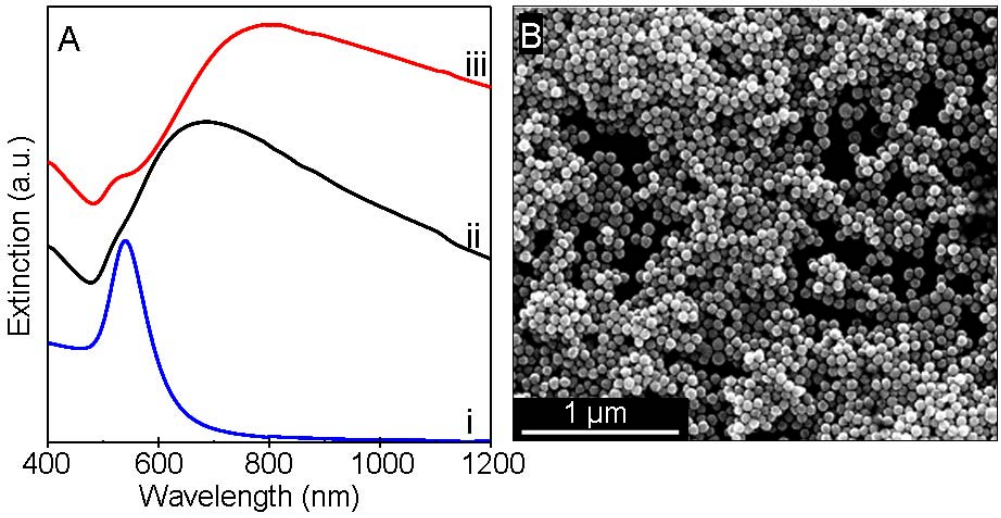


**Figure 5.2** Characterization of the Au NP film: (A) Optical extinction spectra of (i) NPs in solution, (ii) first layer of NPs on quartz PVP functionalized substrate, and (iii) second NPs layer functionalized with analyte molecules, and B) SEM image of a 3D-analyte nanoparticle film.

The structure of the molecules investigated in this study, (S)- and (R)-Trp and (SS)- and (RR)-Cys-Phe-Gly-Gly, are presented in Figure 5.3. Trp has several analytical advantages: (i) it is present in several protein molecules, (ii) it has a strong Raman signal, and (iii) it has an environmentally sensitive fluorescence due to its conjugated ring system. Therefore, it is extensively used for analytical detection of proteins and to determine their folding and unfolding states. The dipeptide sequences (SS)- and (RR)-Cys-Phe-Gly-Gly contain a phenylalanine group as a Raman marker, a cysteine group to bind to the gold NP surface through the thiol group, and an amine-terminated glycine linker that also binds to the NP while giving rigidity to the structure.

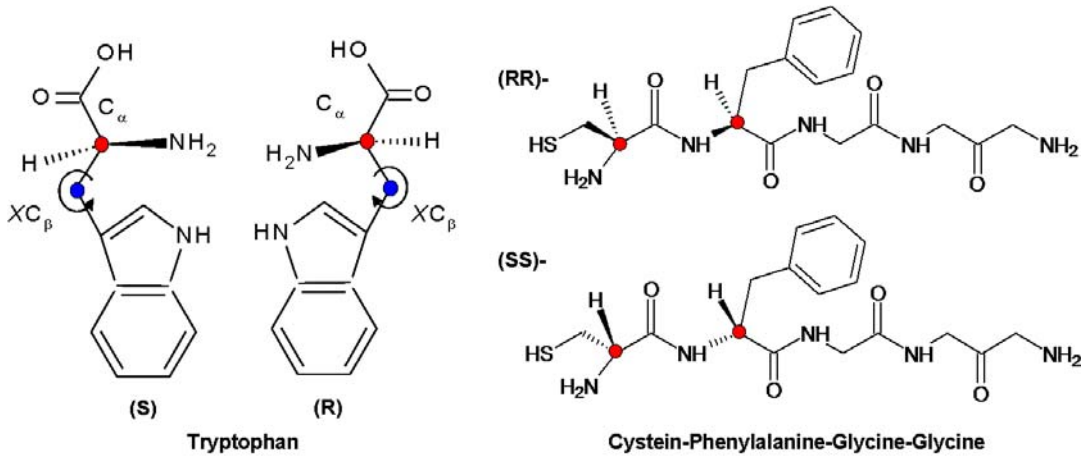


**Figure 5.3** Chemical structures of (S)- and (R)-Trp and (SS)- and (RR)-Cys-Phe-Gly-Gly with the chiral centers (Cα) indicated in red and the torsion center (XCβ) indicated in blue.

SEROA and SERS spectra of Trp and Cys-Phe-Gly-Gly enantiomers were collected simultaneously on each substrate. A Raman spectrum was collected from Trp and Cys-Phe-Gly-Gly powder as a control measurement. Presented in Figure 5.4A are the (i) SERS, (ii) Raman, and (iii, iv) SEROA spectra of tryptophan, where panel (iii) shows the *R* conformation and panel (iv) shows the *S* conformation. Mirror symmetry was clearly observed in the SEROA spectra between 250 $cm^{-1}$ and 1600 $cm^{-1}$. Vibrational modes observed in the SERS and Raman spectra coordinate well with those in the SEROA spectra. The characteristic double peak of Trp at 823 $cm^{-1}$ and 843 $cm^{-1}$ due to the out-of-plane ring vibration is observed in SERS and Raman posses mirror symmetry in SEROA spectra. The indole vibration ring at 1550 $cm^{-1}$ indicating the torsion angles about the $XC_\beta$ atom on the tryptophan backbone ($C_2 = C_1 - C_\beta - C_\alpha$) is clearly defined in the Raman and SEROA spectra, albeit very weak in the SERS spectra.[242-243] This peak contributes to the

determination of the absolute stereochemistry of a tryptophan residue in complex molecules.[242,244] The peak at 250 $cm^{-1}$ assigned to a linear Au-O bond is present in both the SEROA and SERS spectra but absent in the Raman spectrum, which was obtained without NPs.[245] The SEROA peaks at 250 $cm^{-1}$ have a common sign, line shape and amplitude for both (R)- and (S)-Trp. This suggests that interaction with the NP did not introduce a new chiral center, and therefore, the 250 $cm^{-1}$ serves as an internal reference. Moreover, several strong Raman peaks assigned to the vibration of benzene rings at 1551 $cm^{-1}$ and the carboxilate group at 1590 $cm^{-1}$ and 1604 $cm^{-1}$ are difficult to distinguish in the SERS data but are clearly present with opposite signs in the SEROA spectra for (R)- and (S)-Trp.

The reproducibility of SEROA and SERS spectra can be quantified by analyzing several spectra and calculating the pair-wise spectral correlation function[246] ($\Gamma$) that can range between $\Gamma = 1.0$ for the most reproducible spectra and $\Gamma = 0$ for completely randomized spectra. The SERS spectra for tryptophan show a highly reproducible character with $\Gamma = 0.997 \pm 0.002$ for (S)-Trp and $\Gamma = 0.992 \pm 0.017$ for (R)-Trp. The SEROA spectra are similar with $\Gamma = 0.8\ 2\pm\ 0.027$ for (R)-Trp and $\Gamma = 0.798 \pm 0.04$ for (S)-Trp (Figure 5.4B).

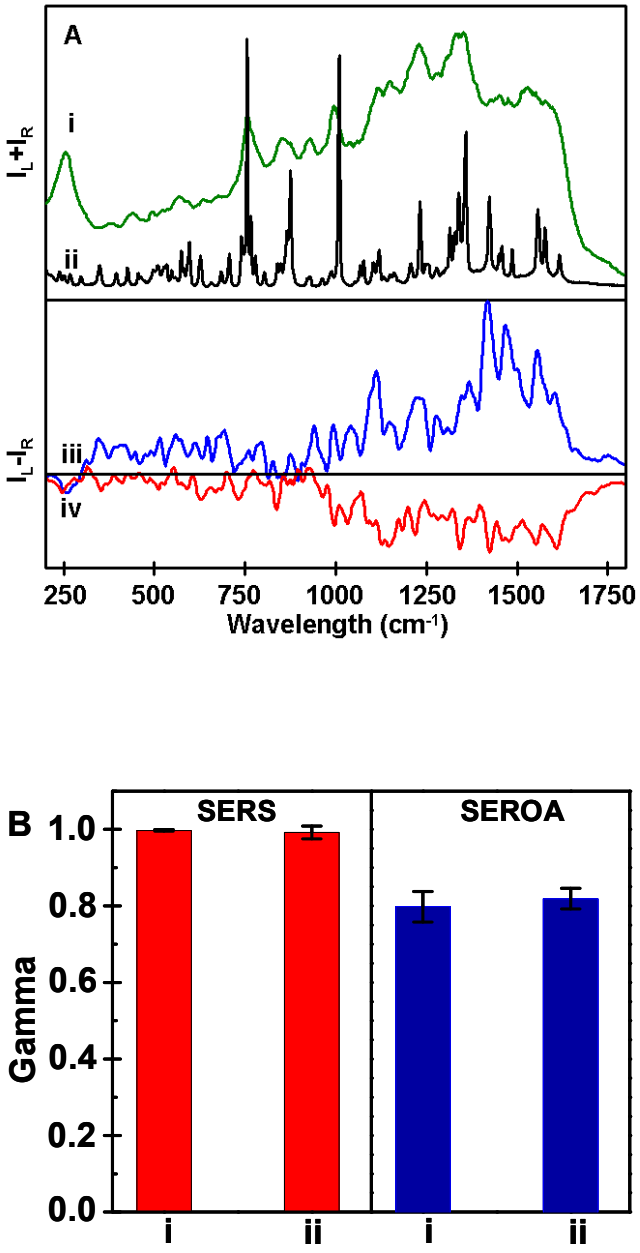


**Figure 5.4** (A) Vibrational spectra for Trp: (i) SERS, (ii) Raman, and SEROA spectra of (iii) (R)-Trp and (iv) (S)-Trp. (B) Γ values for the (i) (S)- and (ii) (R)-tryptophan spectra for SERS and SEROA. Error bars represent standard deviation**.**

The SEROA and SERS spectra of the amino acid sequence (SS)- and (RR)- Cysteine-Phenylalanine- Glycine-Glycine (Cys-Phe-Gly-Gly) give us an inside understanding of the conformation of the peptide. Figure 5.5 presents similar data as Figure 5.4 except for Cys-Phe-Gly-Gly as the analyte, where A(iii) and B(ii) show the SS conformation and A(iv) and B(i) show the RR conformation. The mirror symmetry and line shape of the SEROA spectra confirm the conservation of chirality of Cys-Phe-Gly-Gly on the NP film. The vibrational modes of the SEROA spectra are consistent with the peaks observed in the SERS and Raman spectra. The characteristic double peaks for phenylalanine at 1000 $cm^{-1}$ and 1030 $cm^{-1}$ are assigned to the breathing vibration of the benzene ring and a plane ring C-H bending mode, respectively. In the SEROA spectra, a strong difference in sign and amplitude is observed for the 1030 $cm^{-1}$ peak but not for the 1000 $cm^{-1}$ peak. The $CH_2$ bending mode centered at 1430 $cm^{-1}$ with a well-pronounced Raman mode becomes a broad shoulder of the SERS peak at 1490 $cm^{-1}$, which is almost nonexistent in the Raman spectra.[247] Both peaks are resolved in the SEROA spectra. This suggests a tilted but close to flat orientation of the aromatic ring on the metal surface. The C-S main vibrational modes of Cys at 620 $cm^{-1}$ show mirror symmetry (Figures 5.5A(iii, iv)). Similarly, the peak at 1604 $cm^{-1}$ assigned to amide vibrational modes [248] exhibits two well-defined peaks of opposite sign in the SEROA spectra. The SEROA and SERS peaks at 258 $cm^{-1}$ and 300 $cm^{-1}$ assigned to Au-S and Au-N modes establish dimer formation.

The Γ factor values for the dipeptide molecules are: SERS $\Gamma = 0.997 \pm 0.015$ for (SS)-Cys-Phe-Gly-Gly, $\Gamma = 0.98 \pm 0.02$ for (RR)-Cys-Phe-Gly-Gly, and SEROA $\Gamma = 0.36 \pm 0.17$ for (SS)-Cys-Phe-Gly-Gly, $\Gamma = 0.43 \pm 0.1$ for (RR)-Cys-Phe-Gly-Gly respectively (Figure 5.5B). The Γ values for Cys-Phe-Gly-Gly are lower than those for Trp because

Cys-Phe-Gly-Gly has a broader distribution of molecular orientations on the nanoparticle surface, causing a decrease in the signal-to-noise ratio in the SEROA spectra, especially below ~750 $cm^{-1}$ where weak Phe and Cys backbone modes may convolute the spectra. We note that in the general literature, ROA spectra below 800 $cm^{-1}$ are rarely presented.

The SEROA spectra for both analytes: Trp and Cys-Phe-Gly-Gly, the mirror image of the plasmonic substrate, have a background contribution from the photoluminescent effect. All complementary SEROA spectra include a consistently signed, chirally dependent photoluminescent background. It is possible that the binding of a chiral molecule to the SEROA substrate has induced chirality at the particle surface by breaking the Au symmetry.[249-250] Secondly, following the emission of randomly polarized photoluminescence by the substrate, the electromagnetic interaction with the chiral molecule induces a circularly polarized component in the substrate emission just as it does for ROA scattering.

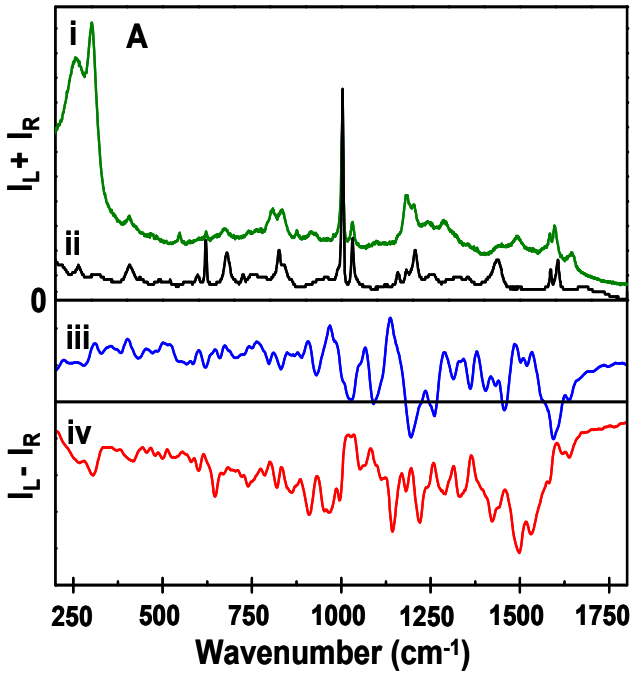

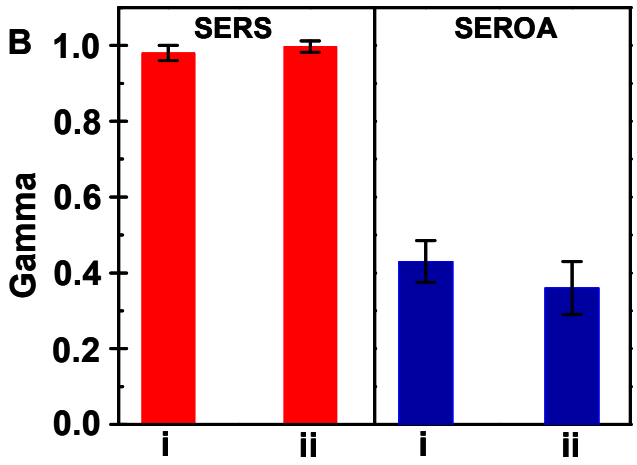


**Figure 5.5** (A) Vibrational spectra for Cys-Phe-Gly-Gly: (i) SERS, (ii) Raman, and SEROA spectra of (iii) (SS)-Cys-Phe-Gly-Gly and (iv) (RR)-Cys-Phe-Gly-Gly. (B) Γ values for the (i) (RR)- and (ii) (SS)-Cys-Phe-Gly-Gly spectra. Error bars represent standard deviation.

Circular Dichroism (CD) spectroscopy was performed to achieve information on the chemical and chiral structure of the analytes. Figure 5.6 presents the CD spectra of: (A) (i) (S)-Trp, (ii) (R)-Trp; and (B) (i) (SS)-Cys-Phe-Gly-Gly, (ii) (RR)-Cys-Phe-Gly-Gly. The difference in sign amplitude of the CD spectra of (S)- and (R)-Trp and (SS)- and (RR)- Cys-Phe-Gly-Gly demonstrates the presence of chirality, and a striking mirror symmetry of the spectra suggest a similar degree of purity for each enantiomer (Figures 5.6A and B). The CD spectra on Au NP films show the same mirror symmetry as in solution despite the fact that the signal is very weak.[251]

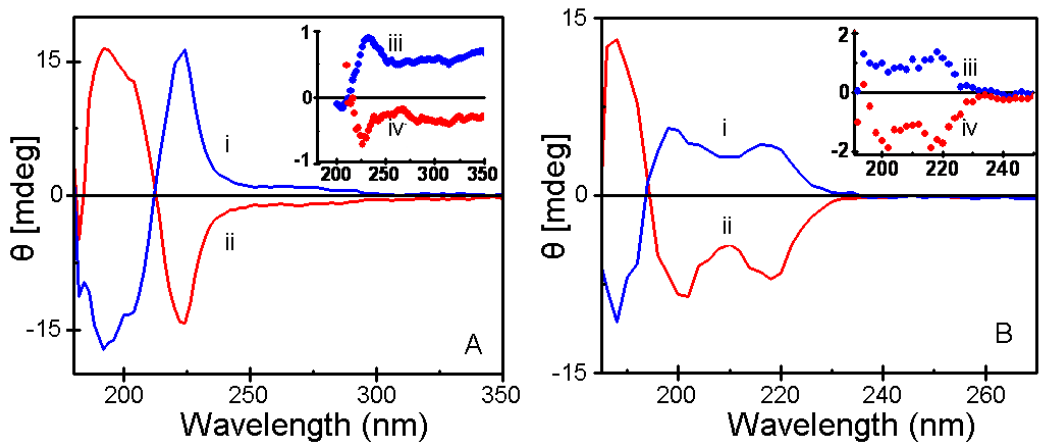


**Figure 5.6** (A) Circular dichroism (CD) spectra of (i) (S)- Trp and (ii) (R)-Trp in aqueous solution. The inset shows the CD spectra of (iii) (S)-Trp and (iv) (R)-Trp monolayer on a Au NP film; (B) CD spectra of (i) (SS)-Cys-Phe-Gly-Gly and (ii) (RR)- Cys-Phe-Gly-Gly in aqueous solution. The inset shows the CD spectra of (iii) (SS)- Cys-Phe-Gly-Gly and (iv) (RR)- Cys-Phe-Gly-Gly on a Au NP film.

### 5.4 Conclusions

In this chapter we present for the first time an NIR-SEROA spectra of (S)- and (R)-Tryptophan and (SS)- and (RR)- Cysteine-Phenylalanine-Glycine-Glycine molecules on a Au nanoparticle substrate. Scattered polarization circular intensity differences have been observed and correlated to complementary enantiomers of Trp and Cys-Phe-Gly-Gly while chemically bound to Au nanoparticle films. The reproducibility of SEROA spectra was monitored by assessing the spectra reproducibility, the correlation factor Γ. The lower Γ values and broader peak widths for Cys-Phe-Gly-Gly relative to Trp are attributed to the broader range of molecular surface conformations of Cys-Phe-Gly-Gly and the convolutions of the Cys-Phe-Gly-Gly backbone mode. SERS spectroscopy

enables us to understand the conformation of molecules at nanoparticles surface and CD spectroscopy in solution or on the gold nanoparticle surfaces independently demonstrates the presence of chirality.

# Chapter 6: Inhibition of DNDTPC-P dye oxidation through adsorption on nanoshells surface

## 6.1 Introduction

Oxidative degradation of organic materials is an area of significant interest.[252-255] The oxidation of dyes that absorb in the near-infrared (NIR) is particularly interesting. NIR dyes are used in high energy lasers,[254,256-257] nonlinear optical devices, digital image storage, color photography,[258] and many industrial processes in the leather, textile and printing industries. The photo- and chemical stability of infrared dyes, [259-262] which is strongly correlated with the dye structure, is an important prerequisite for many of these applications. The adsorption of molecules on a solid within solutions is important in controlling a variety of interface processes. Here we show that a NIR dye oxidizes rapidly in solution within less then 3-4 hours. This chapter demonstrates that the NIT dye attached on Au nanoshells surface is stable for more than two weeks in solution. Theoretical calculations indicate that the geometric changes upon surface attachment prevent the oxidation process by stabilizing the adsorbed, unoxidized NIR dye.

NIR dyes are typically composed of long chains of conjugated double bonds. Oxidation breaks the conjugation, increasing the occupied-virtual orbital energy gap and the onset of adsorption. [259,263-264] The chemical stability of NIR dyes may be increased by embedding them into silica matrices, but this brings the disadvantage of reducing surface viability.[261] Thus the photo-stability of the NIR dyes remains problematic.

Another route to stabilizing a dye is by adsorbing it onto a metallic nanoparticle. Our group has investigated gold nanoshells (NS), highly tunable plasmon resonance

nanoparticles, for applications ranging from building blocks for photonic devices to biosensing and light triggered drug delivery.[265-268] Gold nanoshells are particularly useful as substrates for surface-enhanced Raman spectroscopy (SERS). SERS provides a sensitive, surface-specific probe of species on the nanoshell surface, and may be used in water under ambient conditions.

The NIR molecular dye 3-ethyl-2-[[3-[3-[3-[(3-ethylnaphtho [2, 1-d] thiazol-2(3H)-ylidene) methyl]-5,5-dimethyl-2-cyclohexen-1-ylidene]-1-propenyl]-5,5-dimethyl-2-cyclohexen-1-ylidene]methyl]-naphtho [2,1d] thiazolium perchlorate (DNDTPC, Figure 6.1) has high extinction coefficients and a high quantum yield, which make it promising for applications in bioimaging, nonlinear optics, and solar cells. However, DNDTPC has poor chemical stability, which limits widespread use of the molecule. Therefore it is important to understand the mechanism behind this instability and find ways to prevent it.

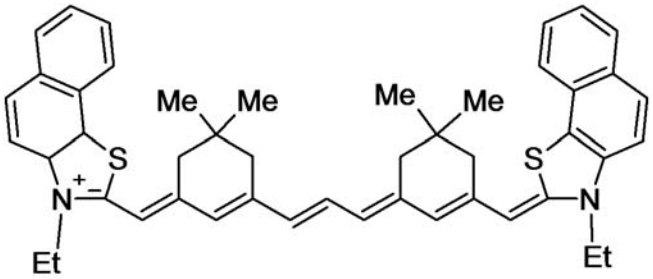


**Figure 6.1:** Structural formula of DNDTPC

In the present study, we measure the stability of DNDTPC adsorbed onto Au nanoshells. We demonstrate that the SERS spectrum of the dye differs significantly from its oxidation products and that the unoxidized species is stable for several days when the dye is adsorbed onto Au nanoshells. We also include calculations by the density functional theory, which indicate a possible geometric mechanism for this stability.

## 6.2 Experimental

**A. Preparation of SERS substrates:** Films of Au nanoshells supported on quartz and silicon were used as substrates for SERS. Quartz and silicon substrates were cleaned by immersion in a piranha solution ($H_2SO_4$:$H_2O_2$ = 3:1) for 1 hour followed by rinsing with deionized water (18.3MQ, Millipore). Note that piranha is extremely oxidizing, reacts violently with organics, and should be stored in loosely covered containers to avoid pressure buildup. Nanoshells consisting of a silica core and a gold shell were fabricated using a method previously described.[269-270] For maximum SERS enhancement, the particles had a strong dipole plasmon mode at 785 nm in water, which was the same wavelength of the laser used for SERS analyses (Figure 6.2). The nanoshells were immobilized by depositing 100 µL of aqueous nanoshells solution on a quartz substrate coated with poly(vinyl pyridine) (PVP) and allowing it to incubate overnight. The substrate was then rinsed with water, dried with nitrogen gas, and placed in a fresh solution of dye molecules (100 µM). Before SERS spectra were taken, the sample was rinsed with methanol.

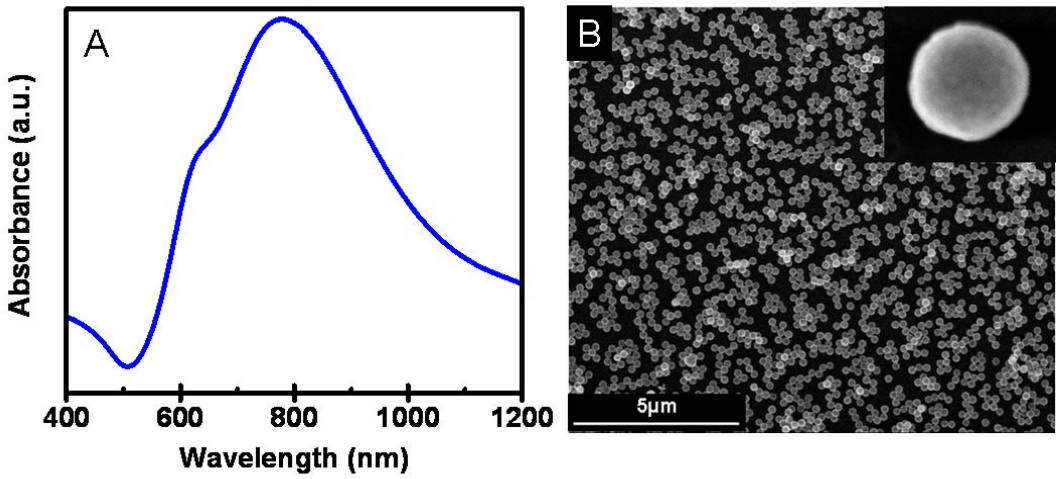

**Figure 6.2: (A)** Absorption spectrum in water and (B) SEM image of nanoshells that confirms the corresponding nanoshell plasmon peaks resonance with Raman laser wavelength of 785 nm.

**B. Materials:** DNDTPC dye was purchased from Exciton and used without further purification. Pure and deuterated methanol was obtained from Sigma-Aldrich.

**C. Measurements**: SERS spectra were acquired on a Renishaw in Via Raman microscope (Renishaw, United Kingdom) with 785 nm excitation wavelength and 55 μW laser power at the samples. Backscattered light was collected using a 63x water immersion objective lens (Leica, Germany) with a 40 second integration time.

The absorption measurements were performed on a Varian Cary UV-Vis-NIR Spectrophotometer. Solutions were prepared by dissolving the dye in pure methanol for absorption measurements and deuterated methanol solution for NMR measurements. The dye concentration was kept sufficiently low at 50-100 μM. Before the dye was dissolved in pure methanol, the solution was saturated by bubbling nitrogen gas for ½ hours.

**D. Computational methods:** The geometries, relative energies, and vibrational spectra of DNDTPC and its oxidation products were evaluated with gas-phase spin-polarized B3LYP/6-31G(d) calculations. Each calculation used tight convergence criteria to optimize the SCF and geometry. All species were assumed to be closed-shell singlets. Zero-point energies, thermal corrections, and basis set superposition error were ignored. All calculations used the Gaussian suite of programs.

### 6.3 Results and discussion

The experimental SERS spectra for (a) fresh DNDTPC dye attached to nanoshells, (b) fresh DNDTPC after 2 weeks in solution on Au nanoshells, and (c) oxidized DNDTPC is presented in Figure 6.3. Spectrum (c) was obtained by incubating DNDTPC in methanol for 6 hours for oxidation prior to nanoshell attachment. The SERS spectrum of fresh DNDTPC is significantly different from that of its oxidation product. After 2 weeks in solution, the SERS spectrum of DNDTPC on nanoshells is more similar to that of fresh DNDTPC than the oxidized product. This indicates that deposition on Au nanoshells retards DNDTPC oxidation (Further evidence of this is given in the Appendix C, Figure C1).

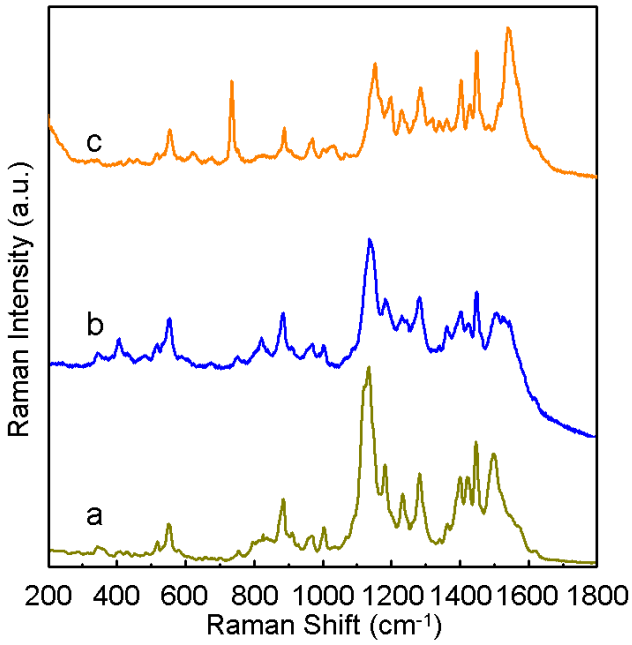


**Figure 6.3**: SERS spectra of DNDTPC dye (a) in a fresh state attached to nanoshells (b) in a fresh state attached to nanoshells after two weeks in the initial solution, (c) in an

oxidized state attached to nanoshells. Spectrum (b) proves that DNDTPC is chemically stable once it is attached to the nanoshell surface.

Interpreting the SERS spectra of DNDTPC gives additional insight into the degradation caused by oxidation. Calculated vibrational frequencies for the dye are given in Table C1 (appendix C). The SERS spectrum of the fresh state (Figure 6.3a) is dominated by the naphthalene in-plane vibrational mode at 1300-1600 $cm^{-1}$ and by $CH_2$ wags at 1100-1200 $cm^{-1}$ for the aliphatic carbons in the linker group. Peaks at frequencies higher than 1200 $cm^{-1}$ are all assigned to in-plane double-bond vibrations of the naphthalene group or the conjugated linker. The sharp peak at ~750 $cm^{-1}$ (a much more intense peak in the oxidized product) is likely an in-plane vibration of the naphthalene group. Overall, the spectrum suggests that the dye has equal contributions from the naphthothiazole fused-ring system and the conjugated linker. For unoxidized DNDTPC dye, the rings and the linker are all in the same plane, such that all parts of the molecule are providing significant SERS signal from all the three parts. This suggests that the dye is adsorbed flat to the NS surface.

The SERS spectrum for the oxidized product (Figure 6.3c) shows an increase in the intensity of the ring modes at 1300-1600 $cm^{-1}$ and a decrease in the aliphatic region at 1100-1200 $cm^{-1}$. This observation suggests that the structure of the dye changes significantly. Prior to oxidation, the carbon atoms that are joining the naphthothiazole group to the linker are $sp^2$ hybridized. After oxidation, these carbons are $sp^3$ hybridized, making it impossible for the dye to lie flat on the surface of the nanoshell. Instead, the oxidized molecule mainly binds to the surface via the naphthothiazole groups, supporting

an increase in SERS signal for the ring modes and a decrease in signal for the aliphatic carbon groups.

There are multiple sites at which oxidation can occur to cause a change in the geometry of DNDTPC. DFT calculations allow us to explore the different oxidation products of DNDTPC and propose a mechanism for the dye conformation shown in Figure 6.4. Table 6.1 gives the calculated oxidation energy for the carbon atoms labeled in Figure 6.1. Our simulations indicate that the unoxidized species (Figure 3a) is quite flat, but oxidation at C1 and C3 causes the $\pi$ conjugation of the molecule to break and the carbon backbone to rehybridize from $sp^2$ to $sp^3$ (Figure 6.4b and 6.4c). While oxidation at C7 provides a rather planar geometry (Figure 6.4d), other effects may arise from the added OH group, making this species less stable than those with oxidation sites at C1 and C3.

| **Oxidation site** | **Oxidation energy (kcal/mol)** | **HOMO-LUMO Gap ($cm^{-1}$)** |
|---|---|---|
| Unoxidized | 0 | 488 |
| C1 | -153 | 726 |
| C2 | -125 | 430 |
| C3 | -152 | 814 |
| C5 | -147 | 862 |
| C6 | -126 | 405 |
| C7 | -146 | 903 |

Table 6.1: Calculated oxidation energy (kcal/mol) of DNDTPC at the sites marked in Figure 6.1, and HOMO-LUMO energy gaps ($cm^{-1}$) of the oxidized species. Oxidation energies are calculated relative to unoxidized DNDTPC and (1/2) $H_2O_2$.

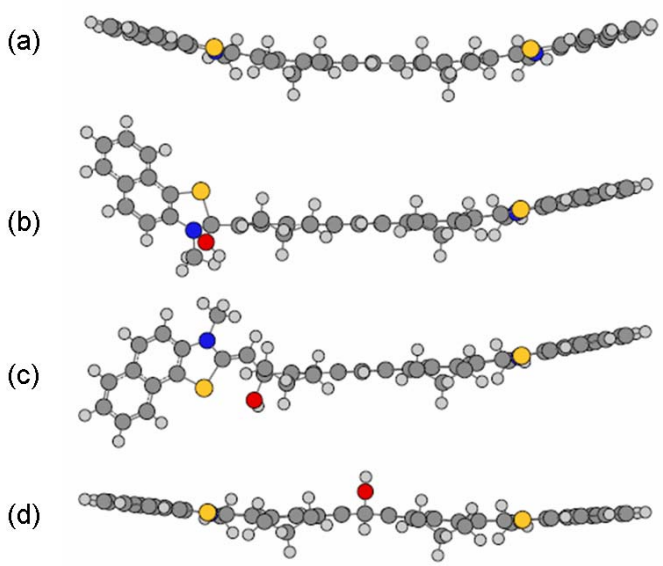


**Figure 6.4** Side view of the molecular structure of unoxidized DNDTP (a) and DNDTPC oxidized at carbons C1 (b), C3 (c), and C7 (d). Yellow, blue, red, and grey atoms indicate nitrogen, sulfur, oxygen, and carbon, respectively.

This result suggests that geometric effects play a role in preventing the oxidation of DNDPTC that is adsorbed onto a nanoshell surface. After adsorption, oxidation will disrupt the DNDTPC-nanoshell interactions, especially given our conclusion that DNDTPC adsorbs "flat" to the nanoshell surface. Disrupting these interactions creates an additional energetic penalty for oxidation, stabilizing the unoxidized DNDTPC.

The calculations in Table 6.1 show a pronounced odd-even alternation in oxidation energies; consistent with the fact that oxidation breaks conjugation of the π system. The table also shows the calculated HOMO-LUMO gap of the stable oxidized species. This provides a first approximation to the UV-Vis adsorption. The stable oxidation sites (C1, C3, C5, and C7) give HOMO-LUMO gaps significantly larger than the isolated molecule, indicating that oxidation should reduce the IR absorbance. Note that the orbital energy

gaps are much smaller than the experimental adsorption frequencies. (Red and blue light are at ~ 13000 $cm^{-1}$ and ~ 25000 $cm^{-1}$, respectively.) This is a well-known pathology of ground-state DFT. However, we expect trends in the HOMO-LUMO gaps to reproduce trends in the IR absorbance.

The adsorption process of dye on nanoshell surfaces is very fast and the SERS measurements indicate extremely reproducible data from spot to spot. The SERS spectra were recorded versus time and reproducing the SERS spectra of the initial state proving that DNDTPC-P dye is chemically stable once it is attached to NS surface (Figure S3 and S4 supporting information).

We also performed UV-Vis-NIR absorption and $^{1}H$ NMR studies of DNDTPC in methanol in the absence of nanoshells. These confirm that DNDTPC does indeed degrade over time in solution. UV-Vis-NIR spectra were collected in spectroscopically pure methanol with nitrogen gas bubbled for 2.5 hours (Figure 6.5a). The degradation process was observed through changes in the absorbance peaks at 852 and 1018 nm. These peaks arise from electronic transitions involving the mobile $\pi$ electrons along the conjugated spacer. Oxidation breaks the $\pi$ conjugation at the oxidation site, removing the low-energy transitions. This would be the reason for the vanishing bands at 852 and 1018 nm, the peaks broadening at lower wavelength, and the increase in amplitude for the peak at 250 nm.

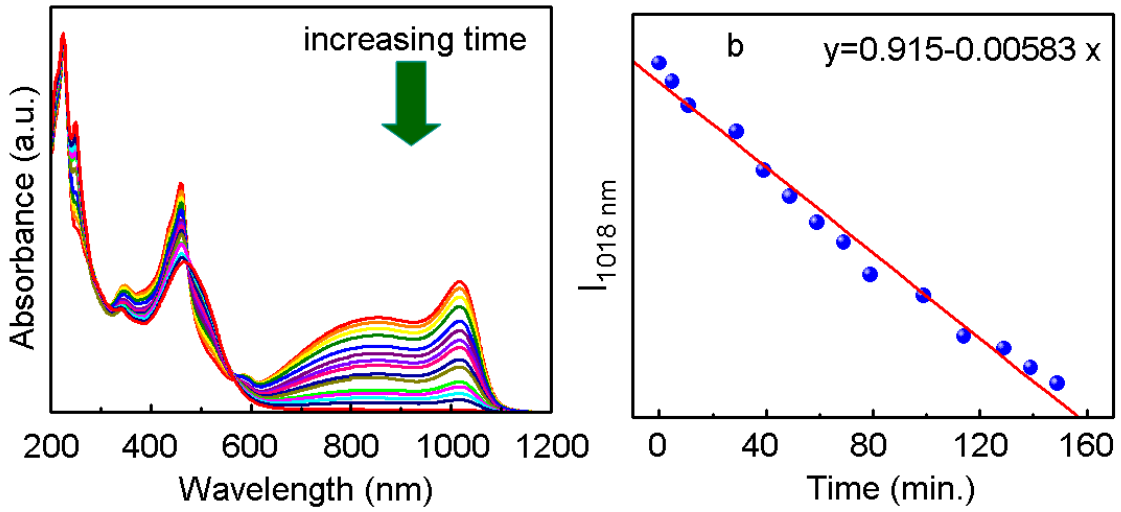


**Figure 6.5** (a) Absorption spectra of DNDTPC dye vs. irradiation time and (b) the intensity of the absorption peak at 1018 nm vs. time

Figure 6.5b shows that the NIR absorbance peak at 1018 nm decays approximately linearly with time, giving evidence of a linear trend in the kinetics of the oxidation process. The percentage decrease in absorption was calculated as

$$\% \text{ decrease in adsorption} = \frac{A_{initial} - A_{final}}{A_{initial}} * 100 \ ,$$

and the rate of dye degradation was calculated using

$$\ln(A_{initial}) - \ln(A_{final}) = kt \ ,$$

where k is the slope constant, t is the exposure time. This suggests that 92% of the dye oxidizes within 2.5 hours with a rate of k = 0.03023 ($min^{-1}$).

In addition, $^{1}H$ NMR spectra of DNDTPC dye solution versus time were performed to investigate the oxidation process. $^{1}H$ NMR spectra were measured on a Bruker AVANCE-500 NMR spectrometer (500.13 MHz $^{1}H$). The $^{1}H$ NMR spectrum is

presented in Figure 6.6**.** To our knowledge, this is the first report of NMR data for DNDPTC.

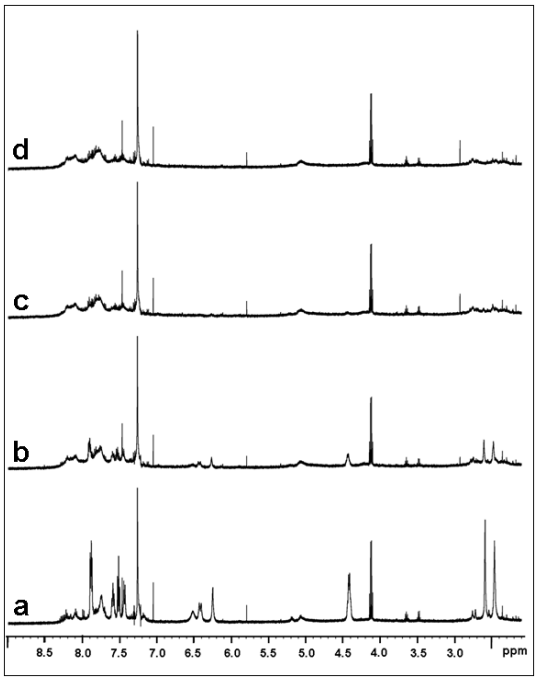


**Figure 6.6:** The $^{1}H$ NMR spectra of DNDTPC in $CD_3OD$ solution (a) freshly prepared, (b) after 4 days, (c) after 8 days, and (d) after 12 days.

The $^{1}H$ NMR spectrum of the DNDTPC in $CD_3OD$ solution showed different peaks in the aromatic range between 7.2 ppm and 8 ppm, while the peaks around 6.5 ppm correspond to C=CH. For 2.5 ppm, the peaks were observed at the beginning of the experiment when the dye is in the unoxidized form and it decreased in time significantly. The $^{1}H$ NMR spectra collected between 8 and 12 days did not show any differences, showing that the reaction was complete after 8 days.

Tunneling electron microscope (TEM) images in Figure 6.7a and 6.7b clearly shows an increase in particle size due to the dye monolayer formation.

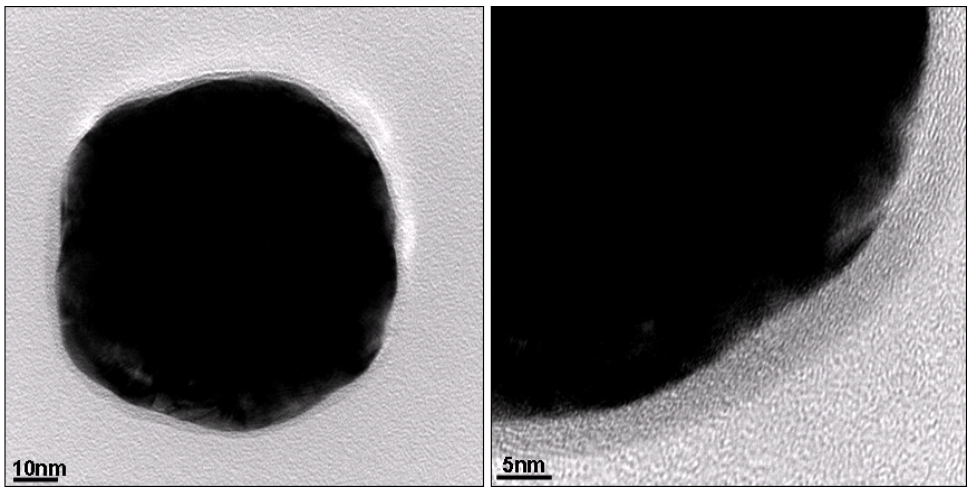


**Figure 6.7:** The TEM image of DNDTPC dye-NS complex.

### 6.4 Conclusions

Adsorption of molecules on solids within solutions is important in controlling a variety of interface processes. We have shown in this chapter that DNDTPC oxidizes rapidly in methanol, with 92% degradation within 2.5 hours. In contrast, SERS spectra indicate that unoxidized DNDTPC adsorbed onto Au nanoshells is stable for at least two weeks in methanol. DFT calculations indicate that the geometric changes upon oxidation may play a role in stabilizing the adsorbed, unoxidized DNDTPC dye.

# Chapter 7: Solar Vapor Generation Enabled by Nanoparticles

## 7.1 Introduction

Solar energy has engendered extraordinary interest for its potential to provide power for a variety of processes without relying on fossil fuels.[271-272] While large-scale solar thermal installations are being developed for electrical power generation, an alternative and currently unmet need is in compact solar energy sources that drive vital processes directly, in addition to the generation of electrical power. These types of smaller scale, stand-alone solar energy converters could directly enable a range of applications, both in first-world countries and in the developing world. In this chapter we demonstrate a new nano-engineered solar photothermal conversion media for steam generation using broadband metallic nanoparticles. The absorptive nanoparticles dispersed in water shows that 80% of the absorbed sunlight is converted into water vapor and only 20% of the absorbed light energy is converted into heating of the surrounding liquid. These experimental observations have resulted in the first demonstration of a high-efficiency solar steam generation process that has the broad potential for use in a wide variety of energy- and sustainability-relevant applications. Reproduced with permission from O. Neumann, A. S. Urban, J. Day, S. Lal, P. Nordlander, and N. J. Halas, ACS Nano, 2013, 7 (1), pp 42–49. Copyright © 2012 American Chemical Society.

Light-to-heat conversion by conductive nanoparticles, under laser illumination, has been shown to induce dramatic localized heating and even vaporization of their host medium.[72,273-284] Here we show that this process can be used for solar-based direct steam generation, without the requirement of heating the liquid volume to the boiling point.

Submicrometer particles that can absorb light across the solar spectrum produce steam in a matter of seconds when dispersed in water and can achieve steam temperatures well above 100°C in compact geometries. With particles dispersed in an ethanol-water mixture, solar distillation yields a distillate substantially richer in ethanol than what would be obtained using a conventional heat source. Under these unusual nonequilibrium conditions, the water-ethanol azeotrope is breached and ethanol fractions approaching 99% are straightforwardly obtained.

Subwavelength metallic particles are intense absorbers of optical radiation, due to the collective oscillations of their delocalized conduction electrons, known as surface plasmons. When excited on resonance, energy not reradiated through light scattering is dissipated through Landau (nonradiative) damping,[285] resulting in a dramatic rise in temperature in the nanometer-scale vicinity of the particle surface. This heat generation process has been of great interest for applications, for example, in biomedicine, where photothermal cancer therapy,[13] laser-induced drug release,[286] and nanoparticle enhanced bioimaging[287] all rely on this property. Carbon-based particles have also been shown to give rise to very strong photothermal heating effects.[288-289] Particle-based approaches have also been of interest for solar energy applications;[290-291] however, such studies have focused primarily on improving the thermal conductivity of working fluids and have not addressed the energy advantage of directly capturing the latent heat of vaporization required for liquid-vapor phase transitions.

Light-absorbing nanoparticles, when appropriately illuminated,[20,25,72,292] can reach temperatures well above the boiling point of liquid water,[72] creating a nonequilibrium condition between the hot nanoparticle surface and the cooler fluid (Figure 7.1).[293-294]

Once vapor is formed at the particle-liquid interface, the metallic nanoparticle is enveloped in a thin layer of steam with a reduced thermal conductance compared to the liquid. Under continued illumination, the vapor volume increases, may possibly coalesce with other nanobubble complexes, and eventually moves to the liquid-air interface, where the vapor is released and the nanoparticles revert back to the solution to repeat the vaporization process. While steam is produced virtually instantaneously and quite vigorously, even explosively, depending on illumination geometry, the nanoparticles remain in the fluid volume and are not conveyed into the vapor phase. As the nanoparticles move to the liquid-vapor interface, they exchange heat with the fluid, slightly raising the fluid temperature. During prolonged periods of illumination, the bulk temperature of the liquid gradually increases, ultimately resulting in conventional boiling of the fluid volume as a parallel effect. However, because there is no need to heat the fluid, the process is intrinsically more efficient than any vapor-producing method that requires volume heating of the fluid in macroscopic quantities, such as conventional thermal sources.

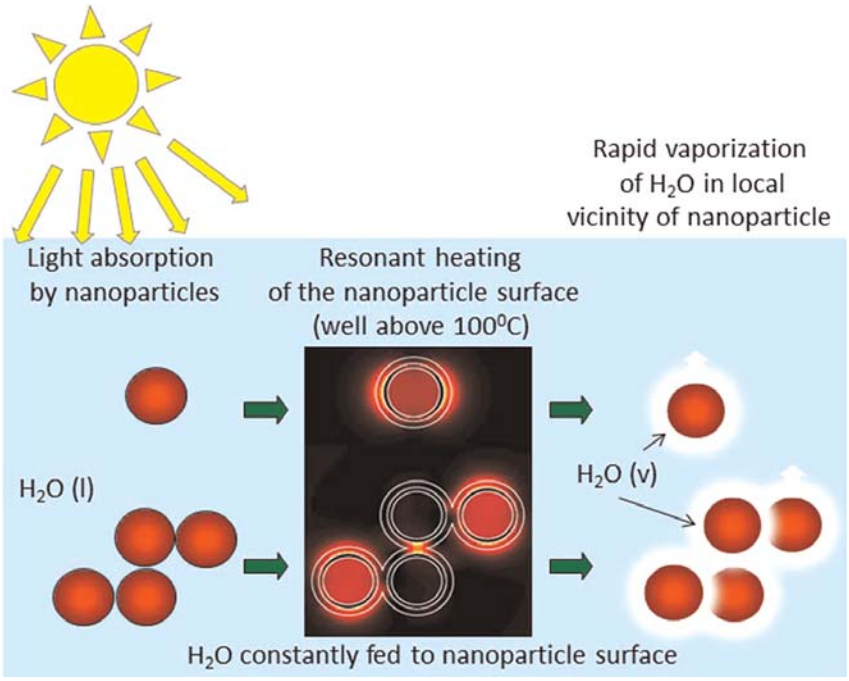


**Figure 7.1:** Schematic of nanoparticle-enabled solar steam generation: initially, light is absorbed by nanoparticles, raising their surface temperature above the boiling point of the fluid. The nanoparticle surface serves as a boiling nucleation site. Vapor is formed around the nanoparticle surface, and the complex moves to the liquid-air interface, where the steam is released. New liquid is replenished at the hot nanoparticle surface, and the process is repeated.

## 7.2 Results and discussion

**Solar Steam Generation Experiments:** To quantify the particle-nucleated solar steam generation process, two solutions of absorbing nanoparticles, (i) $SiO_2$/Au nanoshells (were fabricated as previously described)[295-296] and (ii) water-soluble N115 carbon nanoparticles, (purchased from Cabot, Inc. Billerica, MA, USA)[289] with equivalent integrated optical densities (from 400 to 1300 nm in wavelength), were prepared. Each

solution was placed in its own transparent tube, where a small thermocouple was inserted into the fluid volume far from the region of optical illumination. The tube was then partially immersed in an ice bath, except for the region of the tube that was illuminated. As the tube was illuminated, the steam pressure and the temperature of the fluid volume were monitored (Figure 7.2). Upon solar illumination, the pressure over the solution of nanoshells began to increase, indicating steam generation, less than 5s after illumination commenced (at t = 0), while for carbon nanoparticles the pressure increase was delayed by just over 20s. Once started, however, the steam is generated at a very similar rate for both solutions. Steam generation from the metallic nanoparticle solution occurred in small, microexplosive "bursts", which can be seen in the relatively noisier pressure increase for these nanoparticles. Although both suspensions of particles show a similar increase in the rate of steam generation with time, there is a dramatic difference between the temperatures of the fluid volume during illumination for the carbon nanoparticle and for the nanoshell solution over this initial time period (Figure 7.2B). We observe a slow and measurable increase in the fluid temperature for the illuminated nanoshell solution, while the carbon nanoparticle solution shows only a negligible increase in temperature for the same illumination conditions during this initial time period.

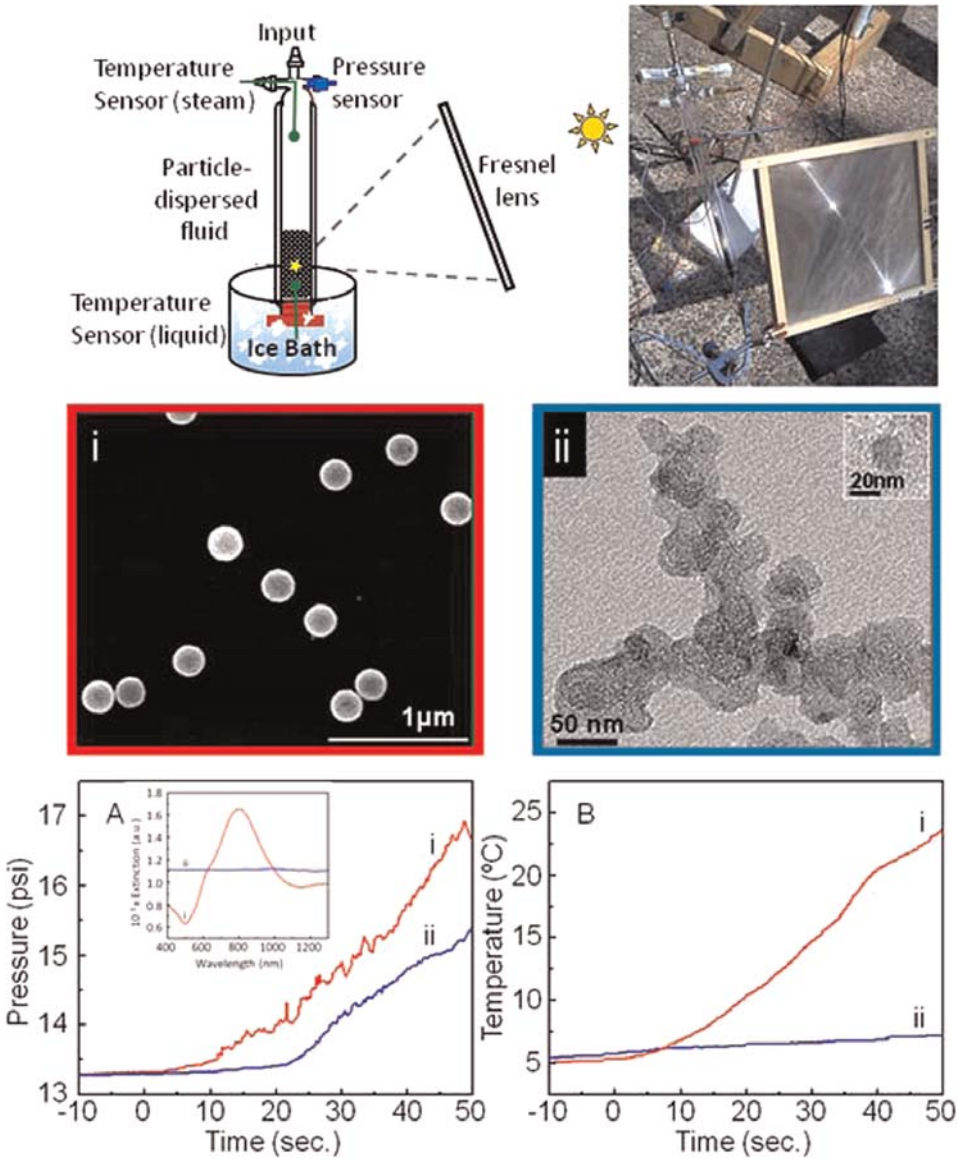


**Figure 7.2:** Pressure-temperature evolution with time of solar steam generation in ice bath conditions: (A) Pressure vs. time and (B) temperature vs. time for (i) $SiO_2$/Au nanoshells dispersed in water and (ii) carbon particles N115 dispersed in water under solar exposure, measured in a transparent vessel isolated with a vacuum jacket to reduce thermal losses and with a solid copper base for enhanced thermal conductivity. Inset: UV-vis spectra of Au nanoshells (red) and carbon particles (blue). The vessel was illuminated with solar radiation focused by a 26.67 cm x 26.67 cm Fresnel lens with a

44.5 cm focal length, while the nanoparticle solution was immersed in an ice bath. The optical density was equivalent for both particle solutions.

The observed fluid heating is due to heat transfer into the solution from the nanoparticle-bubble complexes, an effect that is most probably linear in nanoparticle concentration generally, but concentration independent in this optically dense regime. The difference in the initial increase in fluid temperature between the two types of nanoparticles is most likely due to the metallic nanoparticles heating more rapidly than the carbon nanoparticles. The carbon nanoparticles initially lose less energy to the surrounding solution than the metallic nanoparticles, quite possibly due to their greater buoyancy during the steam generation process. When this experiment is performed without an ice bath, the secondary fluid heating seen in the case of metallic nanoparticles leads ultimately to conventional boiling in addition to particle-induced steam generation. Under these conditions, elevated steam temperatures (140°C) are observed within a ten-minute irradiation time. Analysis of the volatile and condensed vapor showed no evidence of chemical modification.

To quantify the energy efficiency of solar steam generation, an open volume with an aqueous solution of particles was irradiated using focused sunlight for ten minute duration, while both the mass loss due to steam generation and the temperature increase due to heating of the liquid were simultaneously monitored (Figure 7.3A and B). The experiment schematics and the photograph of the setup for the mass loss experiments are presented in Figure 7.3C and D. We examined solutions of nanoshells and carbon nanoparticles with equal optical densities and different solution volumes (25 and 35 mL).

Following the initial "turn-on" period, constant rates of mass loss and fluid heating, the latter dependent upon the fluid volume, were observed (Figure 7.3A, B). These constant rates allow us to assume that additional loss mechanisms are minimal and, therefore, quantify the relative amount of solar energy used in the steam generation process and that used to heat the fluid. For constant incident solar power, the temperature increases for both fluid volumes correspond to a 5 W consumption of power: however, the rate of energy consumption by steam generation, as determined by mass loss, is 23.5 W. These measurements indicate that 82% of the solar energy absorbed by the nanoparticles contributes directly to steam generation.

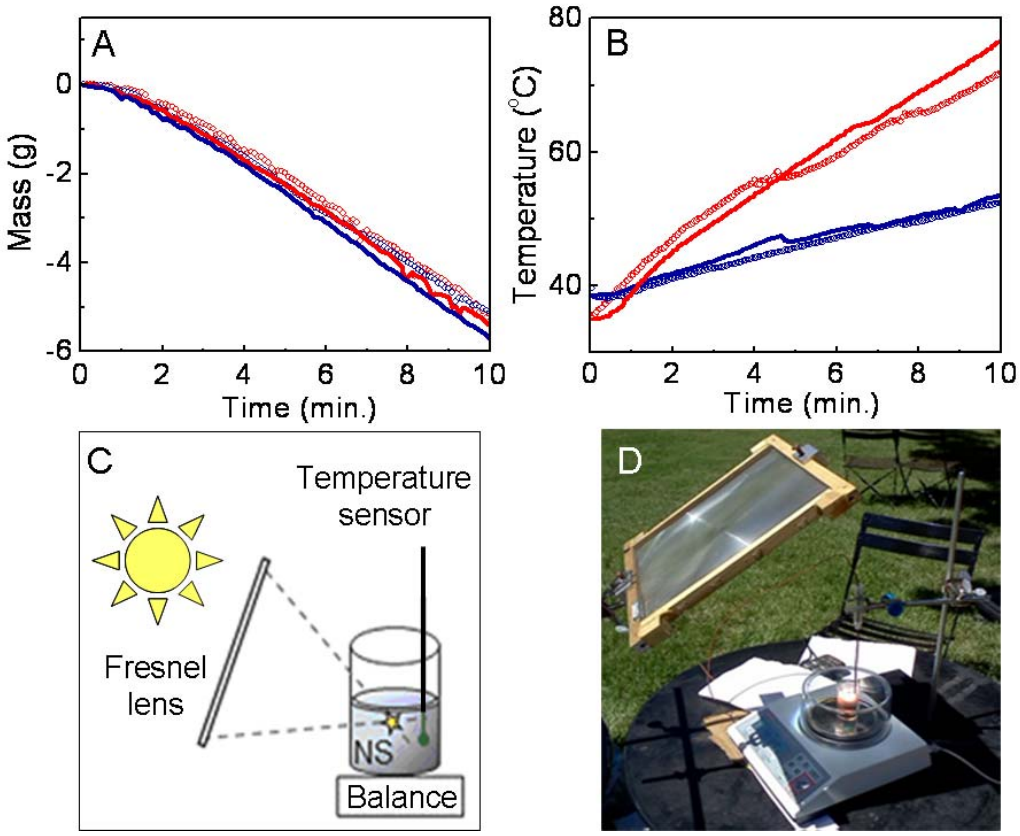


**Figure 7.3**: Measurements of mass loss due to steam generation and heating of the fluid volume during solar irradiation of particle suspensions. (A) Mass loss and (B)

temperature increase of solution for two different solution volumes, 25 mL (blue) and 35 mL (red), for nanoshell solution (solid dots) and (open dots) carbon particles. (C) The experiment schematics and (D) the photograph of the setup for the mass loss experiments. A 26.7 x 26.7 cm Fresnel lens with a 44.5 cm focal length was used to focus light into a 40 ml beaker which contained the nanoparticle solution. The beaker was placed on an analytical balance (AD500 series with 1 mg resolution from Fulcrum Inc., NJ).

We analyze the energy distribution in the system between minute 4 and minute 8 in the experimental data in all cases (Figure 7.3). For the 25 ml solution volumes, the temperature increase is 12 degrees; for the 35 ml solution the temperature increase is 8 degrees. This temperature increase requires 1.2 kJ of energy. The mass loss, equal to the mass of water converted to steam, is 2.5g over this same 4 min period in all cases. The energy consumed to generate 2.5g of steam over this time period is 2.26 kJ/g x 2.5 g = 5.6 kJ. Thus the energy efficiency of steam generation relative to fluid heating is 5.6kJ/ (1.2 kJ) = 466%.

For a conservative estimate of the overall efficiency of solar steam generation in this experiment, assuming a 1.4 $kW/m^2$ solar irradiance, the area of our lens is 26.67 x 26.67 $cm^2$ which captures a solar power of 100 W. Over this four minute time period the total solar energy available to the system is 24 kJ. The energy efficiency of solar steam generation in this unoptimized system is therefore approximately 5.65 kJ/24 kJ = 24%. This estimate ignores losses induced by absorption and scattering in the collection lens, which would be minimized using reflective optics.

A prototype reactor was built to quantify the energy efficiency of steam generation (the solar energy absorbed by the nanoparticles and converted directly to steam) in nanoparticle-dispersed water due to solar irradiance relative to heating the same solution using a conventional electrical resistive heat source Figure 7.4. A 100 ml round-bottom Pyrex flask was thermally insulated, with a 2.5 cm window for access. Either directly focused solar irradiation, or, alternatively, an electrical heating element was used to deliver energy to the vessel. The temperature and pressure of the steam generated in the flask were monitored. The steam generated in the flask was throttled through a symmetric convergent-divergent nozzle (0.15 mm throat diameter), cooled, and collected into an ice bath maintained at 0ºC. The steam generation efficiency is defined as the ratio of the heat transferred out of the flask as steam ($\Phi_{out}$) to the electromagnetic energy influx crossing a control volume just above the liquid surface in the vessel ($\Phi_{in}$):[297-298]

$$\eta = \frac{\Phi_{out}}{\Phi_{in}} \tag{1}$$

The incident solar energy is $\Phi_{in} = P_{in}t$, where $t$ is the exposure time, and $P_{in}$ is the instantaneous solar power, which was a tabulated value according to the time of day and year at the experimental latitude (29o 45' 47'', Houston, TX) and confirmed by power meter measurements. For electric heating, the incident energy is given by: $\Phi_{in} = RI^2t$, where $R$ is the electrical resistance, $I$ is the constant electric current and $t$ is time.

$$\dot{\Phi}_{out} = \dot{m}(h_e + \frac{c_e^2}{2g_c}) \tag{2}$$

where $m$ is the mass of the steam produced and $h_e$ is the (tabulated) enthalpy of steam at the measured temperature, $g_c$ is a constant that relates the units of force, mass, length,

and time ($g_c$= 32.174 $\frac{\text{lbm} \cdot \text{ft}}{\text{lbf} \cdot \text{sec}^2}$); and $c_e$ is the saturated steam velocity through the control volume (feet per second). Due to the relatively low pressure involved in this particular apparatus, the ideal gas model can be applied for the isentropic transfer of steam along the steam path:

$$PV^{-n} = \text{constant}, \tag{3}$$

where $P$ and $V$ are the saturated pressure and specific volume (cubic feet per lb), respectively, and $n$ is the isentropic exponent. Therefore, the velocity of the gas ($c_e$) at nozzle inlet is calculated by:

$$c_e = \sqrt{2g \frac{n}{n-1} P_1 V_1 (1 - r^{\frac{n-1}{n}})} \ , \tag{4}$$

This relation produces a kinetic energy in the inlet about seven orders of magnitude smaller than the steam enthalpy $h_e$. Thus, the ordered motion induced by pressure forces in the system, namely $\frac{c_e^2}{2g_c}$ in equation (2), can be ignored. This is the case because although there is an increase in pressure caused by a nanoparticle-induced boost in steam production, the gas flow speed is greatly limited by the narrow passage. However, the overall energy transfer is not limited by the nozzle obstruction as the mass rate through a pipe section A defined by the product vAc depends on the steam specific volume v.

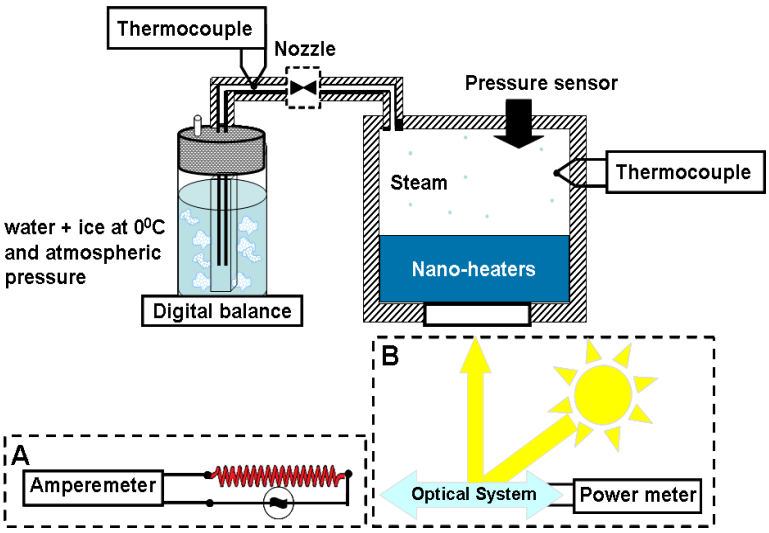


**Figure 7.4:** The steam generation experimental apparatus with (A) electrical or (B) solar heat systems used for steam formation efficiency quantification.

The steam generation efficiency increases as a function of particle concentration for solar and electrical heating, but at very different rates (Fig. 7.5A). For water with no particle dispersants, solar steam generation occurs below 10% efficiency, where under resistive heating conditions (normal boiling) the measured efficiency is nominally 60%. For solar steam generation using $Au/SiO_2$ nanoshells, the efficiency rapidly increases with increasing nanoparticle concentration, reaching a saturation value of near 80% at a concentration corresponding to $10^{12}$ particles/$m^3$, at which density the optical absorption of the nanoparticles limits light transmission into the liquid volume. The steam generation efficiency also increases, but more weakly, for resistive heating, likely due to the small overlap in energy between the blackbody emission spectrum of the resistive heat source and the nanoparticle absorption spectrum.

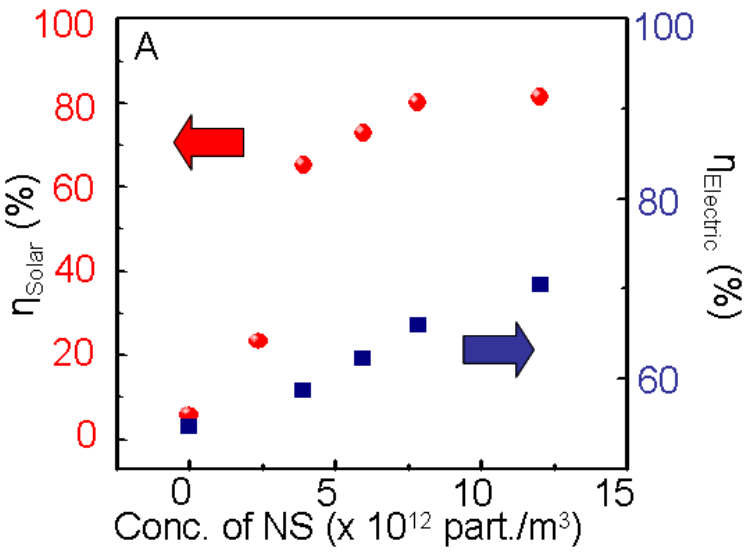


**Figure 7.5:** Solar steam generation efficiency: (A) The steam formation efficiency vs. Au nanoshell concentration under solar irradiation (red) and electrical resistive heating (blue).

**Theoretical Analysis:** The steam generation in this present experiment is a dramatic nonequilibrium process. A bubble without an encapsulated heat-generating nanoparticle has no chance of escaping the liquid, but instead would collapse within milliseconds. In the following, we analyze the heat generation around a gold nanoshell of the same dimensions as those used in the experiment. A calculation using the conventional macroscopic model for nanoparticle-induced heating of a surrounding liquid yields a negligible heating of the surrounding water. In the conventional approach, the temperature of the nanoparticle is estimated using the heat transfer equation:

$$\rho(\vec{r})c(\vec{r},t)\frac{\partial T(\vec{r},t)}{\partial t} = \nabla \bullet [k(\vec{r},t)\nabla T(\vec{r},t)] + P(\vec{r},t) \tag{5}$$

Considering the time scales on which the processes involved here occur, the time dependence of the thermal conduction and heat capacity due to convection are negligible, and the equation can be solved analytically in the steady-state regime, yielding a maximum temperature located at the surface of the nanoparticle:[72]

$$\Delta T(R_{NP}) = \frac{V_{NP} P_{abs}}{4\pi k_0 R_{NP}} \tag{6}$$

where $R_{NP}$ = 85 nm and $V_{NP} \approx 2.57\text{x } 10^6$ nm$^3$ are the radius and volume of the nanoparticles, $k_0$ = 0.6062 W/(m K)[299] is the thermal conductivity of the surrounding liquid, and $P_{abs}$ is the local light induced heating of the nanoparticle, which in the present experiment is equal to $9.93\text{x } 10^{12}$ W/m$^3$. Using these parameters, the conventional model predicts a steady-state temperature increase of the surrounding water of only $\Delta T_{water}$ = 0.04°C. With such a modest heat increase, no bubble formation can occur, in drastic disagreement with the steam generation clearly observed in our experiment.

While there is no physical reason to expect that a macroscopic heat transfer model would be appropriate in realistic nonequilibrium nanoscale systems, it is interesting to speculate on why the conventional model fails. The most problematic assumption with this model is the neglect of the interfacial thermal resistance between the nanoparticle and the surrounding water. Interfaces present obstacles to heat flow, creating thermal barriers.

There are many possible mechanisms that could introduce thermal barriers, particularly at the nanoscale. One example is the Kapitza resistance for vibrational energy transfer,[300] which here can be induced through the surface potential induced shifts of the vibrational energies of water molecules adsorbed on the gold surface compared to water molecules in bulk. An energy mismatch of the vibrational modes of two nearby molecules prevents

energy transfer. In the present situation the mismatch of the vibrational energies of a layer of water molecules next to the nanoparticle and a layer further away would limit the energy transfer between these two layers and thus from the nanoparticle into the surrounding water. Another possible mechanism that could introduce a thermal barrier could be thermal desorption of adsorbed water molecules because of the nanoparticle heating. A spatial separation between the water molecules and the surface of the gold nanoparticle would result in an immediate loss of thermal contact, greatly reducing the heat transfer into the surrounding water.

It is interesting to note that the conventional model described above predicts a monotonically increasing temperature with decreasing thermal conductance, $k_0$. Thus for a sufficiently large thermal barrier, arbitrary large temperature increases would result even in the conventional model. Once a bubble has formed around the nanoparticle, the conventional model, which assumes direct contact between the nanoparticle and the surrounding liquid, clearly fails because the thermal conductance of water vapor is significantly smaller than that of water. If the dimension of the initially formed nanobubble is smaller than the mean free path of the water molecules, the thermal conductance will be even lower than what it would be for a macroscopic gas in equilibrium. While realistic modeling of heat transfer across the water layer is likely to be quite complex; beyond the naïve classical model and instead requiring a rigorous, atomistic molecular dynamics approach; this task lies beyond the scope of the present paper. Here we show that the observed bubble formation and steam generation do not violate energy conservation and can, just as observed, give rise to large water vapor bubbles.

The experiments show that bubble and steam generation occurs after nominally tabs =10 s of illumination. With the solar illumination intensity used in the experiment, a total energy of $Q_{abs}= t_{abs}$ x $P_{abs}$ = 1.7 x $10^{-7}$ J is absorbed by a single nanoparticle (Figure 7.6A).

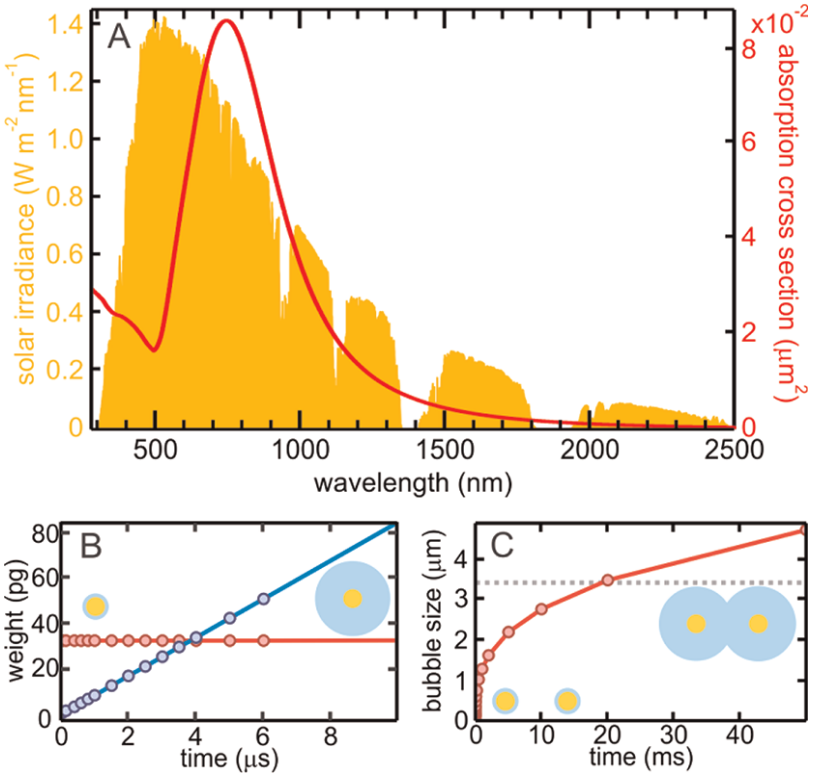


**Figure 7.6:** Steam bubble formation through solar absorption by gold nanoshells. (a) The absorption cross section of the gold nanoshells is tuned to overlap the solar spectral irradiance (AM 1.5 G). (b) Comparison of the combined weight of a gold nanoshell and its surrounding steam bubble (red curve) with the weight of the displaced water (blue curve) over time. After 4 μs, the density of the encapsulated nanoshell becomes less than that of the surrounding water, causing the nanoshell to rise to the surface, releasing the steam bubble. (c) Size of the steam bubble surrounding a nanoshell over time (red curve). After 20 ms of steam generation, the size of the bubbles becomes larger than half the

average distance between the nanoshells (horizontal gray line), allowing the bubbles to coalesce, thus further enhancing the steam generation process.

This is an enormous energy at the nanoscale. If none of this energy is dissipated into the surrounding water, the temperature of the nanoparticle would increase by 4.37 x 107 K. Since the experiment does not show any evidence of nanoparticle melting, it is clear that most of this energy is dissipated into the surrounding water. However, the experiment clearly reveals that this energy is not squandered by heating the liquid, but results instead in the generation of water vapor.

In the presence of a thermal barrier at the nanoparticle interface, the induced local temperature can be very large. We now make the simple assumption that the energy absorbed by the nanoparticle is partitioned between the metal and water vapor in a surrounding bubble, which for simplicity is assumed thermally isolated from the surrounding water. This assumption can be justified from the experimentally observed effect: bubbles and steam appear after just a few seconds, without appreciable bulk heating of the surrounding fluid.

The observed steam temperature is approximately 150°C. The internal pressure within the bubble is almost certainly larger than the ambient pressure of 1 atm due to surface tension, in particular for small bubbles. For simplicity, we assume an internal pressure of 2 atm. The creation of water vapor from liquid water at 25°C requires an energy of $q_{vapor}$=3.06x$10^{-21}$ J/nm3. The heating of the nanoparticle from 25 to 150°C costs an energy of $Q_{NP}$ = 7.30 x$10^{-13}$ J. In this model the radius R of the bubble can then be estimated from

$$\frac{4}{3}\pi(R_{bubble}^3 - R_{NP}^3)q_{vapor} + Q_{NP} = Q_{abs} \quad (7)$$

giving $R_{bubble}$ = 27.1 μm. This simple estimate is based on rudimentary approximations, but most importantly shows that macroscopic bubble formation around nanoparticles indeed is energetically possible. We note that the total mass of such a bubble including the nanoparticle is 9.54 x $10^{-11}$ g, which is smaller than the mass of the displaced water by 3 orders of magnitude. Such a bubble with its encapsulated nanoparticle is therefore expected to rise to the surface of the liquid, where the steam will be released, with the nanoparticle subsequently sinking back into the liquid. On the basis of this picture, we plot the increase in weight of the bubble-nanoparticle complex versus the weight of the displaced water, for the incident solar power in our experiment (Figure 7.6B). Here we see that after just 4 μs, the nanoparticle generated bubble is capable of buoyancy. Also, for the concentrations used in the experiment, the average nanoparticle separation in the liquid is 6 μm. With the present solar intensity, bubbles with their encapsulated nanoparticles are expected to be large enough to coalesce into neighboring nanoparticle-generated bubbles after just 20 ms (Figure 7.6C). For the case of two identical nanoparticle-bubble complexes, coalescence will double the volume of the vapor and double the heat absorption while only increasing the radius by a factor of $2^{1/3}$ and the surface area of the bubble by $4^{1/3}$. Since the heat transfer from the vapor into the surrounding liquid is proportional to the area of the vapor liquid interface, coalescence of bubbles reduces the heat transfer into the surrounding liquid.

While a more refined model is clearly needed, the observed effect introduces a multitude of legitimate questions and casts serious doubt on the appropriateness of the conventional macroscopic model as an apt description of nanoscale heat flow in this

context. This is a very important conclusion, because until now, the conventional macroscopic model has been the accepted canon by the vast majority of researchers in this field. As the bubble grows, energetic gas phase water molecules fueled by the hot nanoparticle surface will also sputter water molecules from the interior of the bubble-water interface, transferring some of their kinetic energy to the liquid. The kinetic distribution of water molecules inside the bubble is likely to be far from local thermal equilibrium. Optically induced electronic effects, such as intense local field enhancements or even optically excited electrons, may lead to the initial formation of a thin vapor around the nanoparticle. Once a thin bubble is formed, heat cannot transfer directly into the surrounding liquid, but instead must pass through the vapor layer with its much lower thermal conductivity. The coalescence of bubbles with their encapsulated nanoparticles may also play a crucial role in steam generation. Because the buoyancy of the encapsulated nanoparticles as calculated previously is large enough to bring the bubble complex to the surface of the liquid, the coalescence of bubbles is probably not essential for the release of the vapor shell. However, it may greatly reduce the heat loss of the nanoparticle-bubble complex into the liquid, thereby increasing the efficiency of solar steam generation.

**Distillation:** Nanoparticle-enabled vaporization can also be applied to the separation of liquids, for a solar-based distillation process with distillate fractions significantly richer in the more volatile component than the case of distillation using a conventional thermal heat source (Figure 7.7).

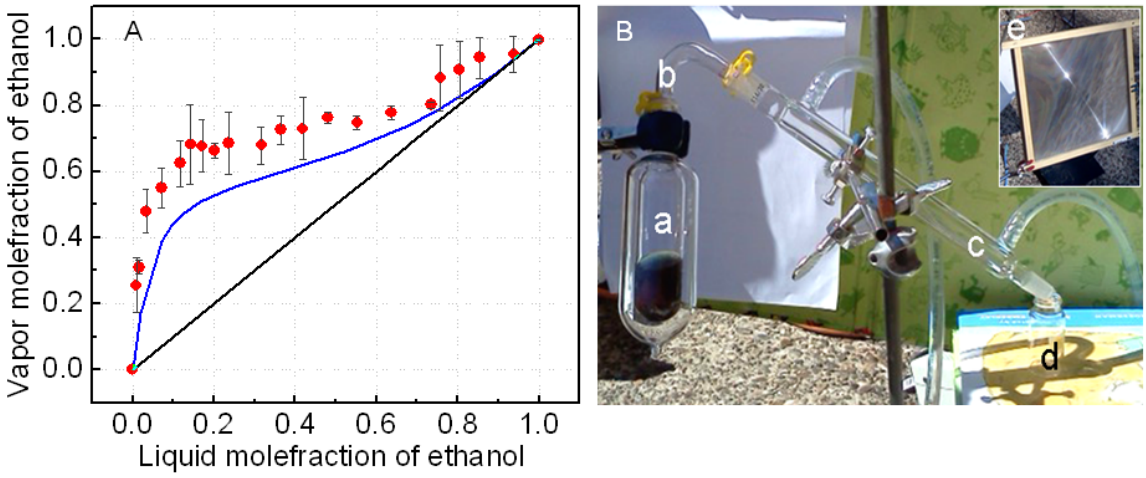


**Figure 7.7. Solar distillation of ethanol:** (A) Photo of the solar distillation apparatus including (a) vacuum-jacketed glass container, (b) connector tube, (c) water condenser, and (d) fraction collector vessel. The solution was irradiated by a (e) 26.67 x 26.67 cm Fresnel lens with a 44.5 cm focal length (inset). (B) Vapor-liquid diagram of ethanol-water fractions produced by solar distillation. Mole % of ethanol in vapor phase for Au nanoshell alcohol-water mixtures under solar exposure (red dots) and standard equilibrium distillation curve at 1 atm and 25°C (blue curve). The Au nanoshell concentration is 2.5 x $10^{10}$ particles/mL.

We distilled ethanol- water mixtures (20 mL) with Au nanoshell particle dispersants (2.5 x $10^{10}$ particles/mL) using focused sunlight (a 26 cm x 26 cm area Fresnel lens with a 44.5 cm focal length). The mixtures were initially contained in a 100 mL vessel with a vacuum jacket to prevent heat loss. Vapors generated by solar illumination were cooled by a simple water-cooled condenser (Figure 7.7A), and 10 drops of each distillate fraction were collected. The distillation samples were diluted (1/1000 in water) and analyzed by gas chromatography (GC) on a Hewlett-Packard 5890 GC equipped with a

glass column containing 80/120 Carbopack B-DA*/4% Carbowax 20 M (Supelco, Bellefonte, PA, USA) and a flame-ionization detector (Agilent Technologies). A 5 µL sample of the diluted distillate was injected into the GC unit, and the heating program was set to 250, 110, and 250°C for the injector, oven, and detector, respectively. Identification and quantification were performed using a calibration curve with ethanol standards prepared by diluting 200-proof ethanol with MQ water (Figure 7.8).

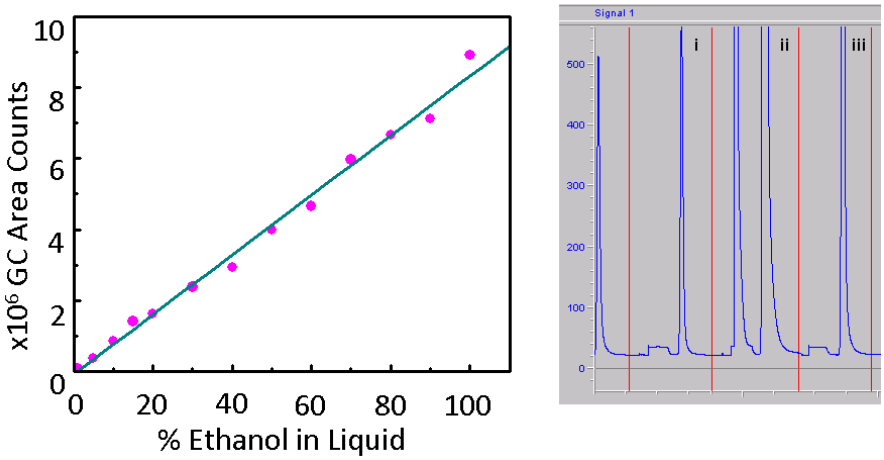


**Figure 7.8:** (A) The calibration curve used for determining the ethanol content in water-ethanol mixture after solar distillation process; (B) The GC signal of (i) ethanol reference, (ii) methanol-ethanol solution as reference, and (iii) ethanol from distillation process demonstrating that no degraded ethanol is detectable as a result of the solar distillation process.

The vapor-liquid phase diagram of ethanol and water produced by solar distillation, relative to a standard equilibrium distillation curve at 1 atm and 25°C, is shown in Figure 7.7B. The mole % ethanol obtained in the distillate is consistently higher than that obtained by conventional flash distillation, most likely because the hot surfaces of the illuminated nanoparticles induce preferential vaporization of the more volatile component

of the mixture. Analysis of the distillate showed no presence of particles in the distillate or any evidence of methanol, acetic acid, or other molecules that would result from chemical degradation of the ethanol. Regions of larger and smaller error bars reflect concentration ranges where qualitatively different behavior of the ethanol-water mixture was observed. For example, from 10% to 45% ethanol mole fraction, particlebased steam generation results in turbulent fluid behavior, while from 45% to 75% ethanol mole fraction, particle-based steam generation occurs with virtually no turbulence, under identical illumination conditions. The larger error bars in the regime of >75% ethanol mole fraction are due to the high levels of humidity in the air ambient. For this reason it is quite likely that the distillates are even higher in ethanol content than the measured averages plotted in the figure. The unusual behavior in these regimes and the effects of ambient humidity are being addressed in ongoing studies using conventional laser sources in nitrogen-purged environments.

The overall energy efficiency of the steam generation process in this unoptimized experimental geometry is 24%, which could be improved by minimizing losses, such as improving the collection optics by using reflectors. These results clearly indicate that solar steam generation is a process that has significant potential for use in a wide variety of energy- and sustainability-relevant applications. Solar driven, stand-alone waste processing or water purification systems could be developed based on this process. High-temperature (~115°C and above) steam produced directly using sunlight could also be used for compact sterilization or sanitation purposes, from the processing of medical waste to the cleaning of medical or dental equipment, minimizing the resource, time, and input chemical requirements demanded by current methods. With further development,

this approach may be adaptable to higher pressures and other working fluids to drive turbines in solar energy harvesting applications. This approach may also be modified to harvest radiant energy from sources other than the sun, for instance, for the capture of waste energy from geothermal, residential, or biological sources.

### 7.3 Conclusions

The results presented in chapter 7 clearly show that solar steam generation is a high-efficiency process that has broad potential for use in a wide variety of energy- and sustainability-relevant applications. Using absorptive nanoparticles dispersed in water, we demonstrate efficient direct steam generation using solar illumination. A thermodynamic analysis shows that 80% of the absorbed sunlight is converted into water vapor and only 20% of the absorbed light energy is converted into heating of the surrounding liquid. In an application to ethanol distillation, we show that the distillate contains a higher percentage of ethanol than what is predicted by the water-ethanol azeotrope. These findings cast doubts on the conventional macroscopic models for thermal transport between nanoparticles and their environment and suggest that significant thermal barriers may be present at the nanoparticle liquid-vapor bubble interfaces. Most importantly, our findings open up a wide range of novel compact solar energy applications such as distillation, desalination, and sterilization and sanitation applications in resource-poor locations.

# Chapter 8: A compact Solar Autoclave enabled by broadband light-harvesting nanoparticles

## 8.1 Introduction

According to the World Health Organization, health care-associated infections are the most prevalent adverse consequence of medical treatment worldwide.[301-303] Although this problem is disconcerting and costly in developed countries, its impact in developing regions is devastating.[304] More than one quarter of the human population worldwide lacks access to electricity, let alone the high power requirements necessary for modern sterilization systems. Because more than half of all people in developing regions lack access to all-weather roads, the channeling of a consistent supply of disposable sterilizing resources into these areas presents an even more ubiquitous challenge.[305] Consequently, addressing the problem of resource-constrained sterilization can be viewed as an effort to provide solutions to both power and supply chain constraints.

The fundamental cause of health care-associated (nosocomial) infections is prolonged or focused exposure to unsanitary conditions. Such conditions can be ameliorated through the use of sanitation and sterilization techniques. Sterilization involves the destruction of all microorganisms and their spores, while disinfection is a less robust process that involves the removal of microorganisms without complete sterilization.[306] One of the most effective approaches for sterilization of medical devices and materials is the use of an autoclave. The fundamental concept of an autoclave is to expose the media to be sterilized to saturated steam at an elevated temperature. Upon coming in contact with the medium to be sterilized, the saturated steam condenses from the gas phase to the liquid

phase, transferring its latent heat of vaporization to the material to be sterilized, and thus to any associated microbes on its surface. Such a rapid transfer of heat is extremely effective for denaturing proteins and may be used to destroy most known types of infectious agents, including bacteria, viruses or viral spores.

Steam-based autoclave systems neutralize potentially infectious microorganisms localized on solid surfaces or in liquid phase media by exposing them to high temperature pressurized steam. These devices are easy to operate, reliable, and are the most effective and efficient means of sterilization. Steam sterilization relies upon temperature and time of application to ensure irreversible destruction of all microorganisms, especially the endospores of bacteria which are considered especially thermally stable.

One promising technology that could address the lack of a reliable energy source in developing regions is solar power, which encompasses both photovoltaic and solar thermal energy generation. Solar thermal systems may achieve higher efficiencies in generating heat, but the large size of typical installations makes them economically unfeasible for small scale projects. In order to effectively apply solar power to an isolated sterilization system for a resource-constrained medical facility, the efficiency of these solar systems must be significantly improved.

In chapter 7 it has been demonstrated the use of broadband light-absorbing particles for solar steam generation.[307] A variety of nanoparticles such as metallic nanoshells, nanoshell aggregates, and carbon N115 nanoparticles, when immersed in aqueous solution and illuminated by sunlight, convert solar energy to steam with remarkably high efficiency. This results from the strong photothermal response of these types of nanoparticles, a characteristic that has previously been used to effectively ablate solid

tumors by irradiation with near-infrared laser light with tumor emission rates of nominally 100% [13,72,273,291,307-311] The nanoparticles create a large number of nucleation sites within the fluid volume, creating rapid and vigorous nonequilibrium boiling of the fluid prior to significant heating of the fluid volume, for low particle concentrations. For higher particle concentrations, both steam generation and fluid volume heating can occur: this results in rapid steam production occurring with higher steam temperatures than can be achieved using non-particle-based fluid heating (Fig. 8.1). Steam generation efficiency is nominally 80% for a variety of particles used.[307] In an aqueous solution, the nanoparticles are neither dispersed into the steam, nor degraded by the steam generation process, and therefore appear to be re-usable indefinitely. The only consumable is water, which needs not be sterile prior to use.

The temperature-time evolution of the nanoparticle-dispersed fluid and steam produced during solar irradiation is shown in Figure 8.1A, with and without the presence of nanoparticles. With nanoparticle dispersants, temperatures of both the liquid and the steam increase far more rapidly than that of pure water (Figure 8.1A(i,ii)), with the liquid reaching 100$^{o}$C three times faster with nanoparticle dispersants than the liquid without nanoparticles. The relative temperature evolution of the nanoparticle-dispersed and the control systems is also quite different: measurable steam production occurs already at a water temperature of ~70$^{o}$C, well below the steam production threshold of 90$^{o}$C for pure water. Perhaps most importantly, however, is the large difference in steady-state temperature achieved for the two systems: with the inclusion of nanoparticle dispersants, the temperature of both the water and the vapor increase well above the standard boiling point of water. In this case, an equilibrium temperature of 140$^{o}$C was easily achieved in

the nanoparticle-heated system. This temperature enables the use of solar steam for medical sterilization applications, as in a solar-driven autoclave.

The evolution of solar steam generation from Au nanoshells-water was quantified in an open loop system (Figure 8.1B) consisting of a 200 ml vessel isolated with a vacuum jacket to prevent heat loss, a pressure sensor, and two thermocouples to monitor both the liquid and the vapor temperature. The vessel was illuminated with solar radiation focused by a 0.69 $m^2$ Fresnel lens into the glass vessel containing 100mL of nanoparticle at a concentration of $10^{13}$ particles/$m^3$, or, alternatively, into water with no nanoparticles as a control. Upon solar illumination, the vapor was allowed to escape through a 0.4 mm diameter nozzle and the pressure and temperatures were recorded.

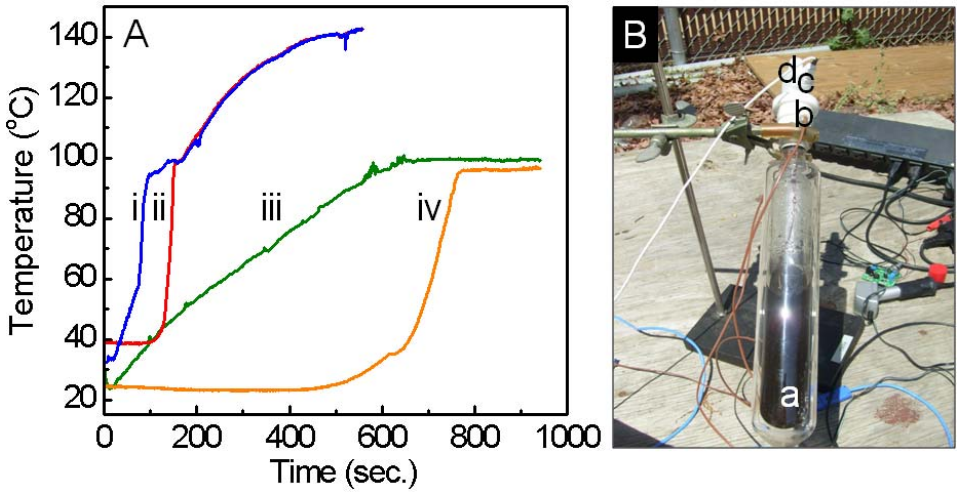


**Figure 8.1:** Temperature evolution of solar steam generation. (A) The temperature vs. time for Au nanoshell-dispersed water: (i - liquid, ii – vapor) and for water without nanoparticles (iii - liquid, iv – vapor) under solar exposure. (B) Photograph of system used in the temperature evolution of solar steam generation: (a) transparent vessel

isolated with a vacuum jacket to reduce thermal losses, (b) two thermocouples for sensing the solution and the steam temperature, (c) pressure sensor, and (d) 1/16 inch nozzle.

The ability of these types of particles to directly produce saturated steam under solar illumination naturally lends itself to the usage of these particles in a solar autoclave. Here we demonstrate a compact autoclave operating using only sunlight, where the steam for sterilization is produced by the absorption of sunlight by submicron particle absorbers. Using a simple Fresnel lens to deliver sunlight into the nanoparticle-dispersed aqueous working fluid, we deliver steam at a temperature of 115°C into a 14.2 liter volume for more than 30 minutes, sufficient for sterilization. Sterilization was verified using a standard Geobacillus stearothermophilus-based biological indicator.

### 8.2 Experimental

A closed-loop system, where steam is produced under solar illumination, transported into the sterilization volume, condensed and delivered back into the fluid vessel was designed (Figure 8.2). The design consists of three main subsystems: (I) the steam generation module, (II) the connection module, and (III) the sterilization module. More detailed schematics of the system are presented in the Appendix D (Figures D1, D2, and D3).

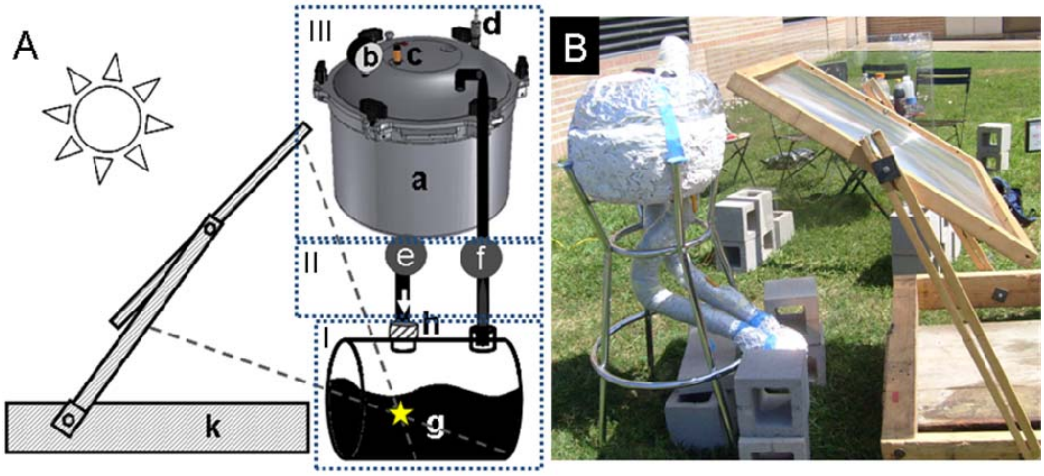


**Figure 8.2:** (A) Schematic of the compact solar autoclave showing: I: steam generation module, II: connection module, and III: sterilization module. The components of the system are: (a) sterilization vessel, (b) pressure sensor, (c) thermocouple sensor, (d) relief valve, (e-f) control valves, (g) solar collector containing the nanoparticle-based heater solution, (h) check valve, (k) solar concentrator (a plastic Fresnel lens of 0.67 $m^2$ surface area), and (B) a photograph of the solar closed loop system.

The particle solution is contained in an insulated glass module with two nozzles that lead to the connection module. The nanoparticles efficiently convert solar energy into heat, producing steam at their surfaces prior to a measurable temperature increase of the water. The solar steam generated within this module is channeled out one nozzle of the connection module into the sterilization module, where it condenses on the objects to be sterilized, returning as condensate to the steam generation module. A check valve at one port of the steam generation module ensures a unidirectional flow of steam throughout the entire system.

The sterilization module consists of an insulated pressure vessel (1915X Stovetop Autoclave: 14.2-liter capacity) that is large enough to sterilize full sets of medical or dental instruments needed for providing basic care. A condensate return hole (diameter of 0.86 cm) was milled on the bottom face of the 1915X Sterilizer, 10 cm away from the center. Similarly, a steam inlet hole (diameter of 0.86 cm) was milled on the lid of the sterilizing vessel; 10 cm away from the center. A finite element analysis (SolidWorks using the Tresca maximum) was performed to identify the mechanically weakest portions of the pressure vessel when placed under high stress conditions (Appendix D Figure D4). By varying the radial position of the hole in the base of the pressure vessel, a minimum factor of safety (vessel material strength/design load) under many different machining configurations was determined: a 0.86 hole 10 cm from the center of the pressure vessel was determined, with a minimum factor of safety of 3.35. In order to minimize heat losses from the steam generation module and the sterilization module, the system was insulated with a sealant (Great Stuff Fireblock Insulating Foam Sealant), applied to the surfaces of the vessels, and topped by a covering of aluminum foil.

The connection module consists of two parts: the steam connection, which allows steam to flow from the steam generation module to the sterilization module, and the condensate connection, which returns the condensate from the sterilization module (Figure D2 Appendix D). The steam connection consists of PTFE tubing insulated in fiberglass pipe wrap and a ball valve; the condensate connection consists of a ball valve, PTFE tubing insulated in fiberglass pipe wrap, a check valve, and a pressure release valve. Both units contain an adaptor to connect to the steam generation module.

The generated steam enters the sterilization module from the top of the vessel, forcing the unsterile air down and out of the vessel through the air exhaust tube, which is

connected to the control valve. Trapped unsterile air can have an insulating effect and prevent complete sterilization; therefore it is critical that all air be removed from the sterilization module. Once the unsterile air is purged from the system, the control valve is closed to allow pressure to build up in the vessel. The cycle is maintained at a minimum of 115 °C and 12 psig and a maximum of 140°C and 20 psig in all regions of the sterilization module throughout the duration of a sterilization cycle. The condensate is channeled back towards the steam generation module via a check valve when the hydrostatic pressure exceeds the maximum pressure of the valve (rated at 0.3 psi).

### 8.3 Results and Discussion

The steam temperature was monitored at both the steam connection and condensate connection directly adjacent to the sterilization module. These two locations are expected to have the highest and lowest steam temperatures, respectively, allowing us to measure the overall temperature gradient generated inside the sterilization module during the sterilization process. The steam temperature prior to and during a sterilization cycle is shown in Figure 8.3.

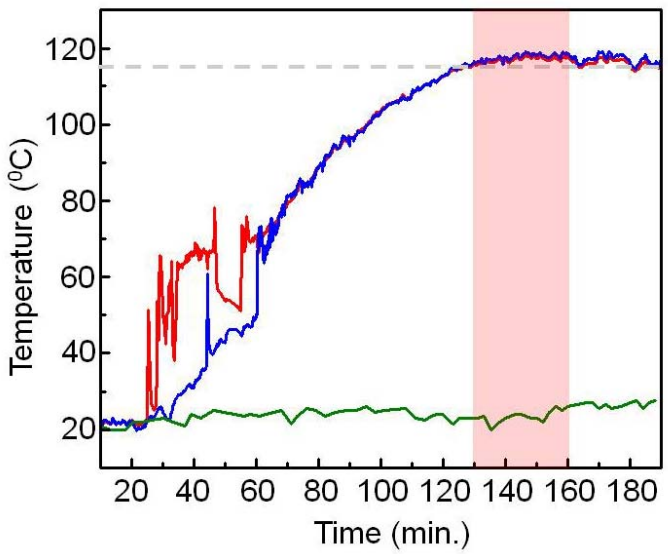


**Figure 8.3: The autoclave temperature evolution under solar illumination.** The steam temperature vs. time measured at the input and output of the sterilization module: input (top of vessel, red) and output (bottom of vessel, blue). The dashed line indicates the temperature required for sterilization and the red segment indicates the sterilization cycle (115°C for 30 minutes). The ambient temperature (green curve) was monitored as a reference.

The red curve in Figure 8.3 is the temperature of the steam at the inlet valve to the sterilization vessel, the blue curve is the temperature of the condensate at the sterilization vessel output, and the ambient temperature is the green curve. The dashed grey line in the figure represents the temperature required for sterilization (115°C). The irregular spikes in the temperature curves correspond to the time when steam begins to enter the vessel. The bottom thermocouple shows two major spikes during warm-up, which correspond to the release of unsterilized air from the sterilization module. The first spike induced turbulence in the system, resulting in exposure of the thermocouple briefly to hotter

steam. The second jump in the temperature data of the output thermocouple corresponds to the release of the remaining unsterilized air. Because air is an insulator, the temperature jumps up when it is released. To demonstrate the robustness and stability of this system, the data show that the autoclave is easily capable of maintaining a temperature over 115°C for twice the 30 minutes of sterilization time.

To test whether our system can achieve the Sterility Assurance Level defined by the Food and Drug Administration,[312] we operated the system through a cycle with the sterilization vessel containing commercial biological indicator strips for Geobacillus stearothermophilus, (EZTest Self-Contained Biological Indicator strips; SGM Biotech) a reference strain commonly used for sterilization testing. The test strips were secured in the sterilization module near the inlet stream and outlet stream taps. After completion of the cycle, the strips were incubated for 36 hours at 55-60°C. The results are shown in Figure 8.4.

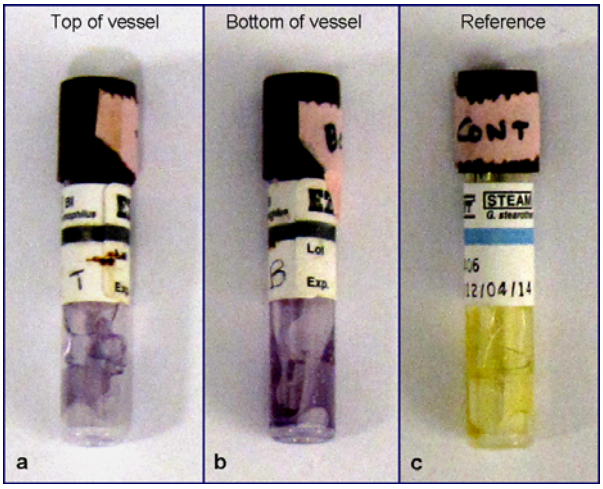


**Figure 8.4: Biological indicators used to test solar autoclave sterilization**. Test vials of Geobacillus stearothermophilus placed in various locations in the sterilization module:

(a) top of vessel, (b) bottom of vessel, (c) unprocessed control. Sterilization is confirmed by color change of vial.

The color change shown by the vials in Figure 8.3a and 8.3b relative to the control vial in Figure 8.3c indicates that sterilization is achieved by operating the solar autoclave through one 115$^{o}$C 30 minute cycle. If some spores survive a sterilization cycle, the biological indicator culture medium undergoes a color change from purple to yellow. The observed color change indicates that spore survival did not occur.

### 8.4 Conclusions

In conclusion, we have demonstrated a compact close-loop autoclave powered exclusively by sunlight and enabled by broadband, light-absorbing metallic nanoparticles. The system maintains temperatures higher then 115$^{o}$C and 12 psig pressure for a minimum of 30 minutes, in accordance with FDA sterilization requirements. Further refinements of this system would enable a faster heat-up time and higher operating temperatures which would shorten the sterilization cycle time significantly: 121$^{o}$C cycle time is 15 minutes; 134$^{o}$C cycle time is 3 minutes (with conventional energy sources this Autoclave operates on a 35 minute sterilization cycle). The system can easily be expanded to provide direct steam generation for applications such as large scale sterilization of human waste, electricity generation, or distillation.

# Chapter 9: A solar sterilizer for treatment of human waste

## 9.1 Introduction

The lack of readily available sterilization processes for human waste in the developing world is a major risk factor for the propagation of disease.[313-315] Around 2.6 billion people do not have access to modern sanitation and diarrheal diseases result in the deaths of 1.8 million people annually. Modern medical facilities in the developed world often use autoclave systems to sterilize waste products, as well as medical equipment that could contain harmful contagions.[316] The fundamental concept of an autoclave is to expose the unsterilized media to saturated steam, which transfers its latent heat of vaporization to any associated microbes on or in the media. Such a rapid transfer of heat is extremely effective in denaturing proteins and may be used to destroy most known types of infectious agents, including bacteria and viruses. Despite being a highly effective and well-established approach for waste remediation, steam-based sterilization is expensive in terms of both energy consumption and cost, limiting its larger-scale use in the developed world.

In chapter 8 it has been demonstrated a new way to dramatically enhance the efficiency of solar steam generation, achieved steam temperatures well above 100° C in compact geometries. The solar steam generation is completely solar powered which will vastly reduce the cost of steam-based sterilization.[307] The strong photothermal response of nanoparticles has been shown to effectively ablate solid tumors by irradiation with near-infrared laser light with tumor emission rates of nominally 100%, to induce dramatic localized heating and even to vaporize their host medium.[13,72,273-274,291,307,309-311,317] Our

method is based on metallic nanoparticles specifically designed to absorb light across the entire solar spectrum and produce steam with nominally 80% efficiency. The nanoparticles create a large number of nucleation sites within the fluid volume, creating rapid and vigorous non-equilibrium boiling of the fluid prior to significant heating of the fluid volume.[307] In an aqueous solution, the nanoparticles are neither dispersed into the steam, nor degraded by the steam generation process, and therefore appear to be re-usable indefinitely. The only consumable is water, which needs not be sterile prior to use.

### 9.2 Results and Discussion

The ability of the metalic nanoparticles to directly produce saturated steam under solar illumination naturally lends itself to the usage of these particles in larger applications such as the sterilization of human waste. We have built a power independent prototypical compact solar autoclave for human waste sterilization (Figure 9.1).

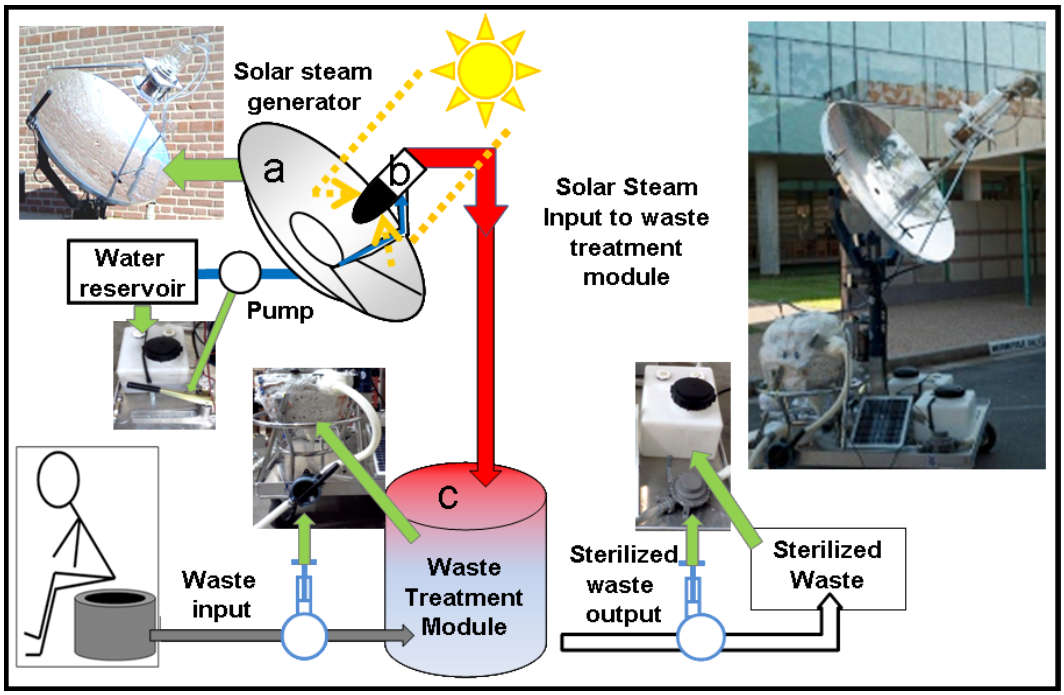

**Figure 9.1**: Schematic and photograph of the solar autoclave for human waste sterilization. The components of the system are: (a) solar concentrator (44-inch dish mirror) (b) heat collector containing metallic nanoparticles, (c) waste sterilization vessel that contains a pressure sensor, two thermocouple sensor, a steam relief valve, two hand pumps and valves that control the input and output of waste. The solar concentrator dish system has a dual tracking system powered by a small car battery recharged by a solar cell unit.

Using a 44 inch solar dish collector to focus sunlight into the nanoparticle-dispersed aqueous working fluid, we deliver steam into the sterilization volume (1915X Stovetop Autoclave: 14.2-liter capacity), a small "honey bucket" waste treatment volume suitable for sterilizing the weekly amount of solid and liquid waste produced by a household of 4 adults (35 liters). The reflective dish tracks the sun using an electronic system. The generated steam is transmitted to the autoclave via silicon tubing. The human waste is delivered to the autoclave by means of a mechanical pump, which can be easily operated by a single person. After the sterilization process, the sanitized waste is removed by gravity. Because of its modular design, the system can easily be expanded to provide direct steam generation for small- or large-scale applications involving sterilization or distillation.

The metallic nanoparticle solution is contained in a vacuum insulated glass system that efficiently converts solar energy into heat and produces steam at their surfaces prior to a measurable temperature increase of the water. The steam generated within this module is channeled out into the waste sterilization module, and maintained at 132°C for 5 minutes, the required duration time necessary for an ISO standard sterilization cycle. The steam temperature was monitored at both the steam connection and inside the waste solution of

the sterilization module. These two locations are expected to reach the sterilization temperature with slight thermal (gas and liquid phase) differences inside the sterilization module during the sterilization process. The steam temperature-time evolution of the nanoparticles-water solution produced during the sterilization cycle is shown in Figure 9.2A.

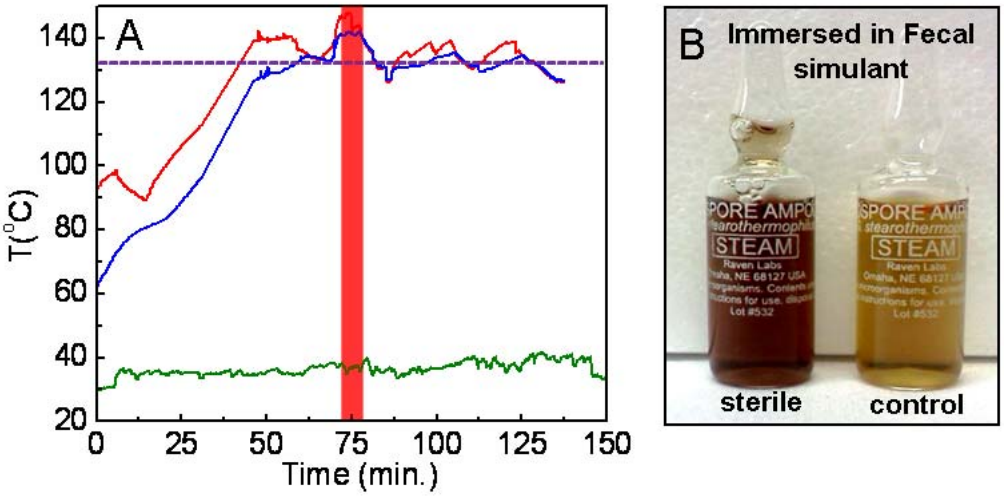


**Figure 9.2:** (A) The autoclave temperature evolution under solar illumination. The steam temperature vs. time measured at the input and output of the sterilization module: input (top of vessel, red) and output (bottom of vessel inside the fecal simulant, blue). The dashed line indicates the temperature required for sterilization and the red segment indicates the sterilization cycle (132°C for 5 minutes). The ambient temperature (green curve) was monitored as a reference. (B) Biological indicators of Geobacillus stearothermophilus placed in fecal stimulant and unprocessed control was used to test solar autoclave sterilization. The sterilization is confirmed by color change of vial.

The red curve in Figure 9.2A is the gas temperature of the steam measured at the vessel inlet valve, the blue curve is the temperature inside the artificial fecal material, and the ambient temperature is the green curve. The dashed grey line in the figure represents the desired temperature required for sterilization (132°C). The jump in the temperature data corresponds to the release of the steam due to the air release from all the system at the start-up producing an abrupt temperature increases. After an initial ramp up period of approximately 20 minutes the sterilization temperature is reached and the temperature-time curve continues to oscillate around this value due to the frequent release of steam from the sterilization vessel through the pressure safety valve. The solar thermal evolution data demonstrates that the autoclave is capable of maintaining a temperature around 132°C for more than 5 minutes.

To test whether the autoclave can achieve the sterility level, we operated the system through a cycle with the commercial biological indicator vials for Geobacillus stearothermophilus, (Mesa Labs, Inc.) immersed in a fecal simulator solution. After completion of the cycle, the vials were incubated for 36 hours at 55-60°C. The results are shown in Figure 9.2B. The color change shown by the autoclaved vials (left) relative to the control vial (right) indicates that sterilization is achieved. If some spores survive a sterilization cycle, the biological indicator culture medium undergoes a color change from purple to yellow.

### 9.3 Conclusions

In conclusion, we have built a power independent prototypical compact solar autoclave. Our method is based on metallic nanoparticles specifically designed to absorb light across

the entire solar spectrum and dramatically enhance the efficiency of solar steam generation. Our solar powered design will eliminate the usage costs compared to electrically power steam-based sterilization systems. Using a solar collector to focus sunlight into the nanoparticle-dispersed aqueous working fluid, we deliver steam at a temperature of 135°C into a 14.2 liter autoclave. Sterilization was verified using a standard Geobacillus stearothermophilus-based biological indicator. The nanoparticles are not consumed by the heating process and can be re-used indefinitely. The only consumable is water, which need not be sterile prior to use. The system can easily be expanded to provide direct steam generation for large scale human waste sterilization systems.

# Chapter 10: Solar Ethanol Distillation

## 10.1 Introduction

Energy use in chemical industries is dominated by the cost of separation, particularly distillation. The 40,000 U. S. commercial distillation columns in use consume 18% of all energy required by the manufacturing sector, estimated at a staggering 2.4 quadrillion Btu/yr. Despite this extraordinary energy cost, alternative separation methods are not competitive, in either volume produced or product purity. Distillation is the energy-consuming step in the processing of conventional and alternative transportation fuels, accounting for 70-85% of the energy costs in this critical sector of our economy.[318] Therefore, competitive costs for efficiently separating fluids are necessary.

In this chapter, we present a solar distillation system to distillate ethanol from an Au nanoshell ethanol-water mixture. Using the nanoparticle properties to evaporate liquids without heating the entire solution, the distillate is richer in alcohol and the azeotrope is overcome. The boiling/evaporation mechanism of Au-nanoshell water-ethanol mixtures is described as well. Finally, I extend this principle to other type of nanoparticles, for example, carbon nanoparticles.

Based on the solar vapor generation discussed in chapter 7 we demonstrate a new solar-based distillation method requiring no energy input by conventional sources, with the potential to replace, or significantly reduce, current energy-intensive distillation processing.[319] This method is based on the use of metallic light-harvesting nanoparticles that capture solar energy for direct liquid-vapor conversion, eliminating the energy-intensive requirement of heating the fluid volume. The nanoparticles are not transferred

into the vapor phase; they can be either dispersed throughout the fluid or bound to a transparent or porous support within the fluid volume. For a mixture of liquids differing in boiling points, the mole fraction of ethanol obtained in the distillate is higher than that obtained by thermal flash distillation which is due to the inherently non-equilibrium vaporization process. Here we further explore the solar distillation of the ethanol-water system. Ethanol is a biofuel energy substitute which has the potential of reducing the $CO_2$ emissions and oil dependence. [320]

Using a solar prototype distillation setup and ethanol as a proxy molecule, we investigate and demonstrate that the solar distillate fraction has a richer ethanol content compared with the conventional flash distillation, energy-intensive distillation method. The solar-illuminated particles achieve surface temperature well above the boiling points of the liquids in the Au nanoshell ethanol-water mixture. The resulting distillate is greatly enriched in the most volatile component of the mixture, accomplished in a solar-driven processing module.

## 10.2 Results and Discussions

**Distillation background:** Distillation is a physical process of separating two or more compounds with different boiling points. The boiling point of a mixture is a function of the vapor pressures of each component of a mixture. The vapor pressure is a result of molecule phase change from liquid to gas: $(\text{molecules})_{\text{liquid}} \Leftrightarrow (\text{molecules})_{\text{gas}}$. As the temperature increases, the kinetic energy of the molecules increases; as a result, the equilibrium shifts to the right increasing the vapor pressure. The boiling point of a liquid is defined as the temperature at which the vapor pressure is equal to the atmospheric

pressure. In the case of an ethanol-water mixture, a boiling mixture containing less than 95% of ethanol produces a vapor richer in alcohol than water (boiling temperatures: 78.4°C for ethanol and 100°C for water). However, at the 95% alcohol the vapor composition remains constant (i.e. the same alcohol composition in the vapor phase as in the boiling liquid at a given pressure and temperature). This point is known as azeotrope and the components cannot be further separated by simple distillation.

Azeotropes are mixtures with constant boiling temperature. There are two types of azeotropes: minimum-boiling azeotropes and maximum-boiling azeotropes. The ethanol-water azeotrope is an example of a minimum-boiling azeotrope. For example, the boiling point of ethanol-water azeotrope is 76.4°C, lower than its individual components. The presence of some specific groups (i.e. polar groups: O, N, Cl,) result in formation of azeotropes due to the strong molecular interaction (hydrogen bonding) as demonstrated in literature.[321-322] The deviation from the ideal case is determined by the balance between the mixture component internal forces. Therefore, separation of azeotropic mixtures has a great industrial interest.

**Solar Ethanol Distillation Setup**: To determine the ethanol % mole fraction we distilled ethanol-water mixtures (20 mL) with Au nanoshell particle dispersants (2.5 x $10^{10}$ particles/mL) using focused sunlight (a 26 cm x 26 cm area Fresnel lens with a 44.5 cm focal length, Green Power Science LLC). The mixtures were initially contained in a 50 mL vessel with a vacuum jacket to prevent heat loss. Vapors generated by solar illumination were condensed by a simple water-cooled condenser (Figure 10.1), and 10 drops of each distillate fraction were collected. The distillation samples were diluted (1/1000 in water) and analyzed by gas chromatography (GC) on a Hewlett-Packard 5890

GC equipped with a glass column containing 80/120 Carbopack B-DA*/4% Carbowax 20M (Supelco, Bellefonte, PA, USA) and a flame-ionization detector (Agilent Technologies). A 5 µL sample of the diluted distillate was injected into the GC unit, and the heating program was set to 250, 110, and 250°C for the injector, oven, and detector, respectively. Identification and quantification were performed using a calibration curve with ethanol standards prepared by diluting 200-proof ethanol from molecular biology (Sigma-Aldrich) with MQ water.

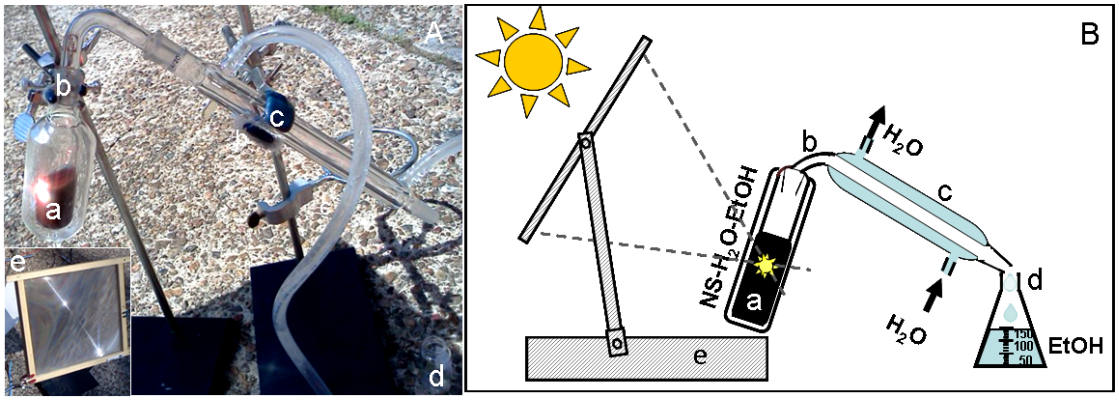


**Figure 10.1: Solar distillation of ethanol:** (A) Photo and (B) Schematics of the solar distillation setup including (a) vacuum-jacketed glass container, (b) connector tube, (c) water condenser, and (d) fraction collector vessel. The solution was irradiated by a (e) 26.67 x 26.67 cm Fresnel lens with a 44.5 cm focal length.

The vapor-liquid phase diagram of ethanol and water produced by solar distillation, relative to a standard equilibrium distillation curve at 1 atm and 25°C is shown in Figure 10.2A. The black line in the figure represents an equal concentration of alcohol in both the liquid and the vapor state.

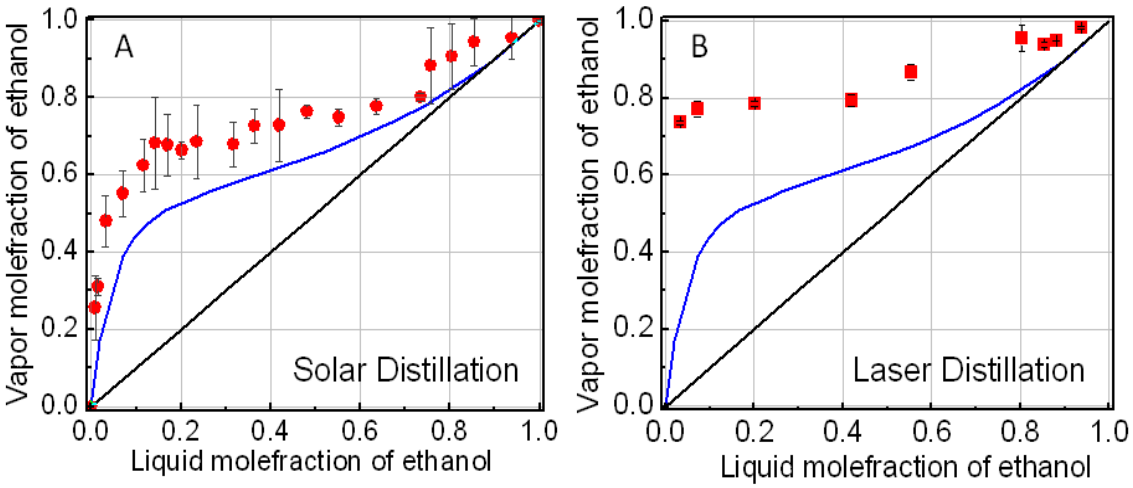


**Figure 10.2:** The vapor-liquid equilibrium diagram of alcohol-water fractions produced by distillation of Au nanoshell-alcohol-water mixtures. Mole % of ethanol in vapor phase for Au nanoshell alcohol-water mixtures under (A) solar, (B) laser exposure (red dots) and standard equilibrium distillation curve at 1 atm. and 25$^{o}$C (blue curve). The black line in the figures represents an equal concentration of alcohol in both the liquid and the vapor state. The initial Au-nanoshell concentration was 0.25x10$^{10}$particles/mL for all the measurements.

The mole fraction of ethanol obtained by solar irradiation in the distillate is higher than that obtained by conventional distillation because the hot surfaces of the illuminated nanoshells induce preferential vaporization for the more volatile component of the mixture. Regions of larger and smaller error bars reflect qualitatively different boiling behavior of the ethanol-water mixture. For example, from 0.1 to 0.45 ethanol mole fraction, particle-based steam generation results in turbulent fluid behavior, while from 0.45 to 0.75 ethanol mole fraction, particle-based steam generation occurs with virtually no turbulence, under identical illumination conditions. The larger error bars in the regime

of 0.75 to 1 ethanol mole fraction are due to the high levels of humidity in the air ambient. To understand the nanoshell based ethanol-water mixture evaporation behavior in these regimes and the effects of ambient humidity we perform the distillation experiments in nitrogen-purged environments using a laser source (illumination at 808 nm with continuous wave laser, 15W/cm$^2$) (see Figure 10.2B). The laser wavelength corresponds to the peak resonant wavelength of the nanoshells (Figure 1.3.2). Initially, the mixtures were contained in a 5mL vessel with a vacuum jacket to prevent heat loss. Vapors generated by laser exposure were condensed by a water-cooled condenser (Figure 10.1B), and 5 drops of each distillate fraction were collected. The distillation samples were diluted (1/1000 in water) and analyzed by HPLC system. The laser distillates ethanol mole fraction was even higher in ethanol content compared to the solar distillates ethanol mole fraction and this is because only 5 drops were collected (compared with 10 drops by solar) and also because the samples were analyzed by HPLC without delay therefore no water absorption occurred (Figure 10.2B).

An ethanol-water system will form an azeotrope due to the strong molecular interaction (hydrogen bonding) as demonstrated in literature.[321-322] The deviation from the ideal case is determined by the balance between water and ethanol internal forces. The vapor-liquid equilibrium diagram of alcohol-water fractions produced by distillation of Au nanoshell alcohol-water mixtures under solar/laser illumination shows no azeotrope. The difference in the vaporization temperature produces different compositions of the distilled fraction for each particular case.

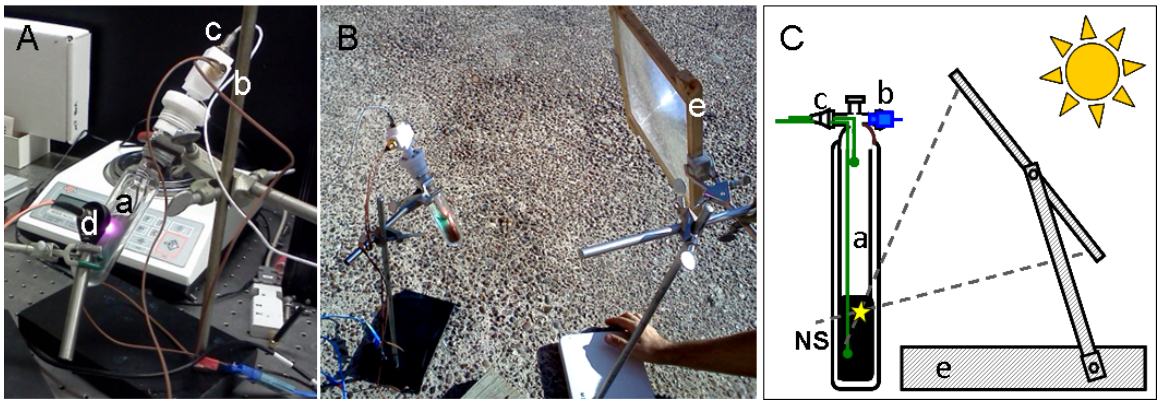


**Figure 10.3** Picture of the setup used to measure the heat of vaporization under (A) solar and (B) laser exposure and (C) Schematic of the setup: (a) vacuum jacketed glass container, (b) two thermocouples that measure the solution/steam temperature, and (c) a pressure sensor. The solution was irradiated by (d) 26cm x 26cm Fresnel lens with a 44 cm focal length, and a (e) 15 W power laser beam, 808nm.

To understand the nanoparticles effect on the vaporization process, the Au nanoshell ethanol-water mixtures were placed in a vessel with a vacuum jacket to prevent heat loss (Figure 10.3). A pressure sensor (PV350 pressure vacuum module adapter for a Fluke milivoltmeter, ECO-Tronic Pressure Transmitters) and two thermocouples (OMEGA Engineering, Inc.) were mounted to monitor both the liquid and the vapor temperature. A Fresnel lens was used to focus sunlight into the glass vessel containing 20mL of Au nanoshell ethanol-water mixtures at a concentration of $10^{10}$ particles/mL. Upon solar illumination, the vapor was allowed to escape through a 0.016 μm diameter nozzle and the pressure and temperatures were recorded. The temperature-pressure evolution of the nanoshell ethanol-water fluid and steam produced during solar irradiation for several ethanol mole fraction solutions is shown in Figure 10.4.

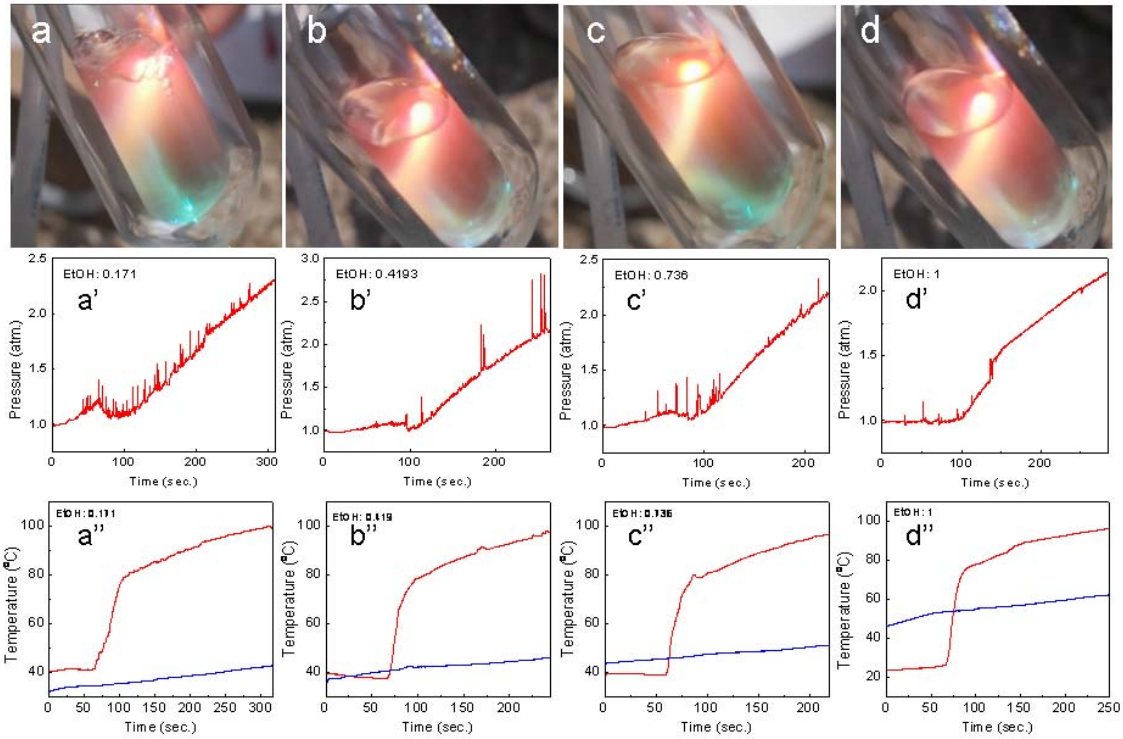


**Figure 10.4: Types of boiling during the distillation of Au nanoshell-ethanol-water mixtures:** The photographs show the boiling behaviour of the Au nanoshell-water mixture: (a) boiling, (b) few periodic explosions, (c) one initial explosion at the beginning of the heating where one bubble is generated and moves along the mixture surface with an oscillating motion, and (d) the evaporation without boiling. The time dependent (a'-d') pressure and (a''-d'') temperature (red-steam, blue-solution temperature) corresponds to each type of boiling.

Boiling, like evaporation, is the phase change of a liquid into gas state when its temperature reaches the boiling point (the pressure of liquid equal the atmospheric pressure). Boiling occurs at the solid-liquid interface when the liquid is in direct contact with a hot surface while evaporation occurs at the liquid-gas interface when the vapor

pressure is less than the saturation pressure of the liquid. The boiling process is characterized by the formation of bubbles at the hot solid-liquid interface. The bubbles grow in size and detached from the surfaces rising to the free surface of the liquid.

There are four types of phase boiling: pool boiling, nucleate boiling, transition boiling, and film evaporation.

Pool boiling is the phase where bubbles collapse in the liquid. As the temperature increases, the bubbles rise to the surface and enter the next phase; this process is called nucleate boiling. Transition boiling is the regime where high heat transfer can be achieved with relatively small increases in temperature. As the temperature increases, a large portion of the hot solid surfaces is covered by steam (insulator with low thermal conductivity) and the heat flow decreases. In this regime, both nucleate and film boiling partially occurs. The last stage is the film evaporation regime; the solid surface is completely covered by a continuous stable vapor film. The point where the heat flux is minimum is called Leidenfrost point (discovered in 1756 by J. C. Leidenfrost). The physical properties of hotter surface greatly affect the heat transfer. As the temperature increases even more, the heat flux starts to increases again as a result of heat transfer from the heated surface into the liquid through the vapor film through the radiation. The temperature at which the Leidenfros effect begins to occur is not easy to predict while depending on the fluid, the surface properties, impurities in the liquid.

Four types of boiling associated with the % mole fraction of ethanol-water mixtures have been identified: continuously explosive boiling (Figure 10.4a), infrequently explosive bubbles (Figure 10.4b), one time explosive boiling followed by the formation of a bubble that remains in motion on the surface of the mixture (Figure 10.4c), and

evaporation without bubbling (Figure 10.4d). Perhaps most importantly, however, is the pressure versus time data that gives information regarding the ethanol-water mixtures boiling behavior. The pressure versus time for all the significant boiling types associated with the ethanol mole fraction is presented in Figure 10.4a'-d'. Ethanol vapor generation from the nanoshell particle solution, containing 0.171 ethanol mole fraction, (Figure 10.4a') occurred in continuously micro-explosions which can be seen in the noisier pressure vs. time curve. The 0.42 ethanol mole fraction solution generates vapors on the nanoshell surfaces with bubble formation once in a while (Figure 10.4b'). The 0.73 ethanol mole fraction displays remarkable behavior since the bubble generated by explosion scatters across the liquid surface for an extended period of time. This response is referred to as the Leidenfrost effect which occurs when the vapors generated beneath the bubble forms an insulating layer at the mixture surface diminishing the energy transfer between the bubble and the solution.[323] Moreover, the Leidenfrost regime represents the transition regime between the explosive boiling and the film evaporation (Figure 10.4c'). For higher ethanol mole fraction, greater than 0.75, the solution evaporates without bubbling (Figure 10.4d'). Steam (red) temperature increases far more rapidly than the liquid (blue) temperature (blue) (Figure 10.4 a''-d''). The liquid temperature is approximately 40-50°C in the nanoparticle ethanol-water mixture. The system vaporization process is more efficient in this solar induced nonequilibrium system compared with the thermal heated system. Moreover, the Leidenfrost effect gives meaningful information regarding the temperature at nanoparticle surfaces far above the boiling point of liquid (the Leidenfrost point for water occurs at 210°C)[323].

Due to the four hydrogen-bonds of water, the ethanol molecules form a three-dimensional network of hydrogen-bonds. Theoretical and experimental studies show that ethanol water molecules do not mix randomly but, instead, form clusters due to the hydrogen bounding.[324-331] The cluster size depends on the ethanol water molecule ratio; for example, the ratio of ethanol:water at azeotrope is nine:one. Several structural models of pure water have been proposed for dimmers, bicycle-octamers, or icosahedral. The clusters formed are highly influenced by temperature and, as a result, interconvert between forms by bending hydrogen-bonds. In the ethanol-water systems the generated clusters weaken the hydrogen bonding network and consequently affect both mobility and viscosity of the solution. As a result, the entropy of the system increases compared with the pure components prior to mixing. N. Nishi, et all have shown that the cluster size variation for the solution with 40-80% ethanol concentrations is the same despite the variation in the ethanol content. In mixtures with rich water content, the water molecules form strong hydrogen-bonding shells around the ethyl group core and induce a large decrease in the enthalpy.[330,332] In ethanol content rich solutions, only one hydrogen is involved in network bonding; consequently, the solutions mainly contain linear chains or cyclic clusters.[331-332] The cluster structures affect the boiling behavior observed experimentally (as described) but also can be seen in the vaporization energy data (Figure 10.5).

The enthalpy (heat) of vaporization of the ethanol distillate mole fraction is calculated using Clausius-Clapeyron equation for the evaporation process:

$$\frac{d \ln p}{dT} = \frac{\Delta H_{vap}}{RT^2},$$

where p is the vapor pressure at the temperature T, $\Delta H_{vap}$ is the enthalpy of vaporization, R is the universal gas constant ($8.31 J \cdot K^{-1} \cdot mol^{-1}$), and T is the absolute temperature. The plot of the logarithm of ethanol-water mixture vapor pressure versus inverse thermodynamic vapor temperature is linear. From the slope of the line, vaporization enthalpy of the mixture was evaluated and the results are presented in Figure 10.5A. The line corresponds to the fitting curve with the equations (A) $y=42.32-23.26x+20.46x^2$ and (B) y=23.85e (-x/0.18199).

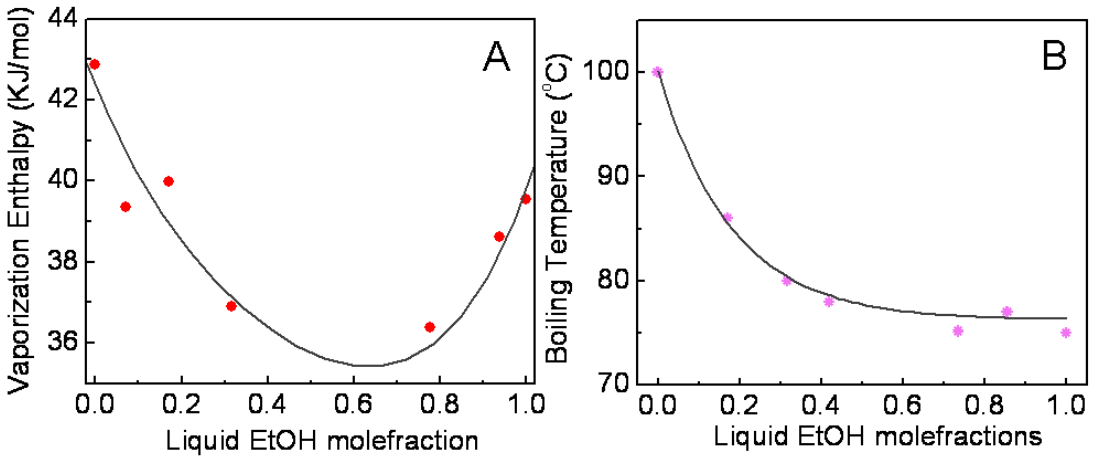


**Figure 10.5:** (A) Enthalpy (Heat) of vaporization and (B) Boiling temperature vs. mole fraction of the Au nanoshell-ethanol-water mixtures under solar illumination at atmospheric pressure.

For exothermic processes, the lower the content of ethanol and more hydrogen-bonding intermolecular interactions, the higher the enthalpy of vaporization. The steric effect of organic groups, conformation, and clusters size stability are also the determining factors for the enthalpy of vaporization. By adding water to the ethanol solution, the enthalpy decreases are also due to water attachment involving the breaking of ethanol-ethanol

bonds, which are very stable in the aqueous system. The vaporization enthalpy value obtained is similar to the literature suggesting the Au-nanoshell does not dramatically perturb the network or influence the cluster stability. Only the temperature gradient generated around nanoshell through illumination affects the hydrogen bond network. Consequently, higher alcohol content in the distillate is obtained when nanoparticles are involved. The cluster structure also affects the boiling temperatures, as observed in Figure 10.5B. A similar analysis for the Au nanoshell ethanol solution using solar/laser irradiation yielded comparable results (Figure 10.6).

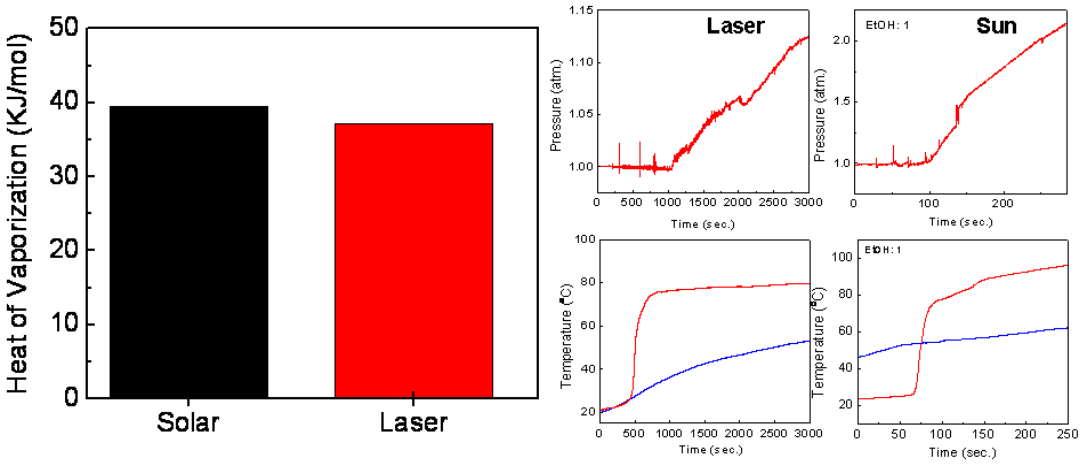


**Figure 10.6:** vaporization enthalpy of Au nanoshell suspend in proof ethanol under (black) solar and (red) NIR laser exposure and the Temperature/pressure vs. time curves used to calculate the vaporization enthalpy.

In chapter 7 it has been demonstrated that carbon nanoparticles can be used with the same heating efficiency when irradiated due to the very strong photothermal heating effects.[319] Using the same setup for ethanol distillation we distill ethanol-water mixture using carbon nanoparticles (purchased from Cabot, Inc. Billerica, MA, USA) with

equivalent optical densities as Au nanoshell. The condensed vapor was analyzed by GC and the results are presented in Figure 10.7.

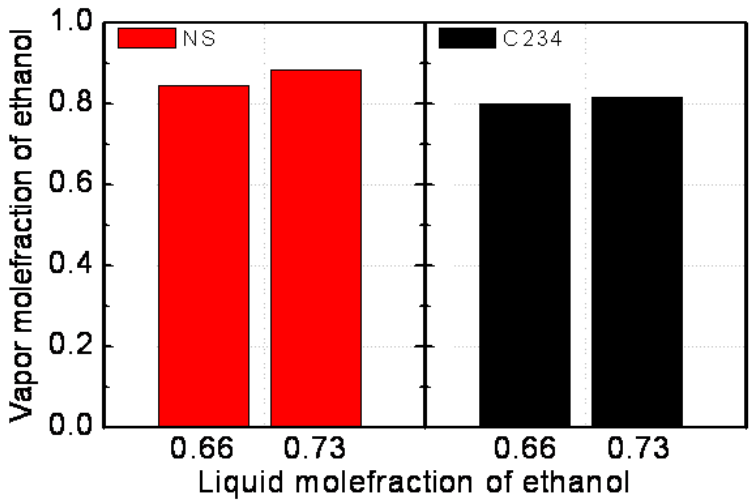


**Figure 10.7:** The vapor-liquid equilibrium diagram of alcohol-water fractions produced by distillation. Mole % of ethanol in distillate vapor phase: (red) Au nanoshell and (black) Carbon nanoparticles alcohol-water mixtures distillation under solar exposure.

The ethanol distillation mole fractions using carbon nanoparticles as a heating source was determined by GC using the ethanol calibration curve. The mole fractions have approximately the same value as the ethanol content obtained using Au-nanoshell as heating source. The metallic/carbon nanoparticle dispersants remain entirely in the vessel enabling the absence of particles in the distillate. This approach can be, in general, applied to separate liquids with different boiling points, accomplished in a simple and straightforward solar-driven processing module.

### 10.3 Conclusions

The results presented in chapter 10 clearly illustrate the % mole fraction of ethanol yielded with solar distillation is higher than thermal flash distillation due to an inherently non-equilibrium vaporization process induced only in the solar case. The presence of Au nanoshells in the ethanol-water mixtures creates four types of boiling-vaporization processes described in the pressure vs. time data. The vaporization enthalpy of ethanol-water mixture without Au nanoshell obtained by solar illumination is identical to the vaporization enthalpy obtained by thermal sources demonstrating the addition of Au nanoshells into ethanol-water solutions do not affected clusters structures. Only the temperature gradient generated by the nanostructures perturbs the local cluster structure; as a result, a high % mole fraction of ethanol was obtained by solar distillation. Metallic nanostructures provide an effective way to qualitatively separate and evaporate liquids at competitive costs by harvesting the solar energy. Accordingly, liquid generation using vapors without the heating of the entire mixture solution has promising potential for industrial purposes.

# Chapter 11: Gold self-similar metallic structures

## 11.1 Introduction

Over the past decade, the optical properties of metallic nanostructures have been extensively studied and manipulated through the development of new fabrication methods. Chemical synthesis offers large concentration samples ideal for ensemble measurements. By varying shape, size, and morphology, the functionality of nanoparticles is enhanced providing broad potential applications such as chemical sensors, electronic nanodevices, catalysis tools, biocompatibility devices, magnetic materials mechanisms, and carrier systems in photothermal cancer therapy.[333-340] The work presented in this chapter demonstrates the synthesis and plasmonic properties of Au self-similar structures. This system differs from those previously reported in the literature in that the black-colored Au self-similar structures has remarkable broad band optical properties due to the broad and efficient absorption spectrum of electromagnetic energy from a wide range of angles.

Metallic fractal structures with a high surface-to-volume ratio present extremely distinct interest in optoelectronics devices, surface-enhanced Raman spectroscopy, catalysis, or solar energy applications.[341-352] Moreover, the presence of sharp edges in three-dimensional nanostructures dramatically increases the plasmon electromagnetic field while amplifying the local molecular sensitivity detection. [353-356] By tailoring the surface plasmon energies of nanoparticles even more through structural control, we have created nanostructures with resonant properties spanning much of the solar spectrum. The cumulative structural variations of nanostructures including the multiple coral-like

branches of, random protrusions, surface porosity, and size variation lead to a broadening and red-shifting of their collective multi-modal plasmon peak to the mid-IR. Plasmonic Au self-similar structures serve as point-like black-body sites with an individual aqueous solution because of their remarkable broad-band optical properties. Their black color is due to the efficient broad spectrum absorption of the EM energy from a wide range of angles. The simple one step synthesis method of black-colored Au self-similar structures soluble in various solvents (i.e. water, methanol, ammonia, and ethylene glycol) represents a direct solar steam source.

### 11.2 Results and Discussions

Scanning electron microscope (SEM) measurements were performed to investigate the morphology and physical composition of the Au self-similar structures. SEM samples were prepared by evaporating a droplet of aqueous nanostructures solution onto a silicon waver substrate and measurements were performed using a FEI Quanta 400 field emission SEM at an acceleration voltage of 20kV scanning electron microscope. The SEM images clearly show the formation of Au self-similar structures that exhibit a very uniform size distribution of brunch's diameter, approximately 30 ± 5 nm (Figure 11.1). To understand the effect of PVP concentration on size and shape of Au self-similar structures formation, we performed a series of experiments with varying amounts of PVP (figure 11.1 i-iii). The SEM images illustrate a direct correlation between size and shape of nanostructures with respective PVP concentrations. At higher PVP concentrations, micron size Au self-similar structures are formed; while decreasing the PVP concentration, the flower contour detail prevails with a very uniform size distribution.

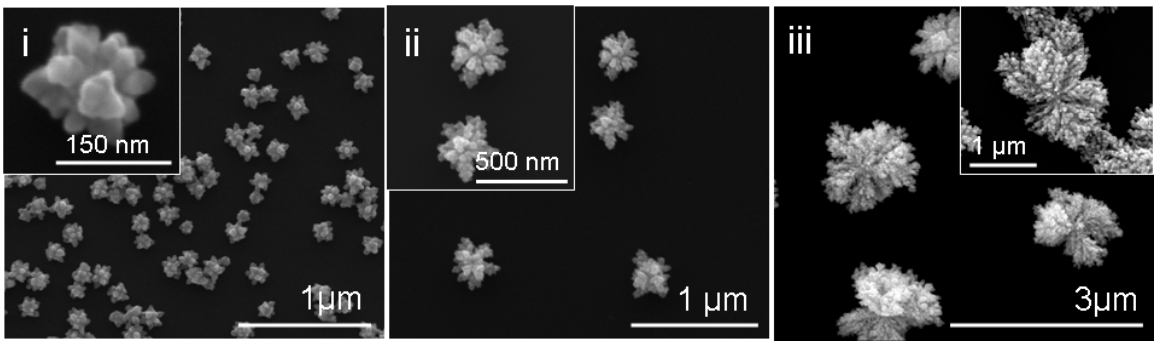


**Figure 11.1:** SEM images of Au self-similar nanostructures synthesized with different PVP concentration: (i) 6.25µM, (ii) 13.75µM and (iii) 25µM. The L-ascorbic acid concentration is constant 0.4M.

While the mixing order proves to be an influential part of particle synthesis, the L-ascorbic acid concentration is also significant (Figure 11.2). Several experiments were performed with increasing the concentration of amino-acid without PVP in solution. Well defined three-dimensional structures with inhomogeneities in growth of spike quantities (figure 11.2ii) are obtained. Nano-balls of different sizes were also obtained by increasing the concentration of L-ascorbic acid figure 11.2 i-iii. The PVP addition favored directional Au growth as well as prevention of nano-ball aggregation.

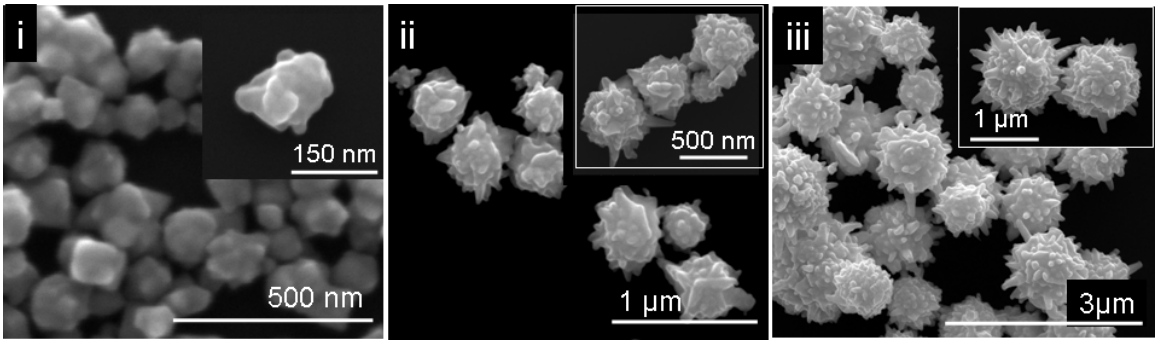


**Figure 11.2:** The SEM images of nanostructure synthesized with different L-ascorbic acid concentration (i) 0.02M, (ii) 0.2M and (iii) 0.4M.

Micro size Au self-similar structures present a significant interest as black-body aqueous micro-structures because of its remarkable broad band optical properties. The unique optical properties of the black-colored Au self-similar structures, as a function of size, are presented in Figure 11.3. The experimental UV-Vis-NIR extinction spectra of Au self-similar structures were recorded with a Varian Cary 5000 UV-Vis-NIR spectrophotometer. As we observe, the extinction spectra covers a wide spectral range, leading to considerably high photon absorption. Small size Au self-similar structures capture only a fraction of the visible region of the spectrum (Figure 11.3i), limiting their efficiency as solar absorbers. To better span the solar spectrum, larger size Au self-similar structures (approximately 500 nm) were synthesized (Figure 11.3ii). Increasing particle size broadens and shifts the plasmon-resonant absorption of the nanoparticle to near IR wavelengths region. Micro-size Au self-similar aggregate formation induces an additional long wavelength collective plasmon resonances[357] which extends the light-absorbing characteristics of the nanoparticles well into the infrared region of the spectrum (Fig. 11.3iii). The broad absorption span is mostly likely due to the structural diversity; the collective effects of surface protrusions of asperities contributes to significant broadening and red-shifting of the plasmon resonance.[345]

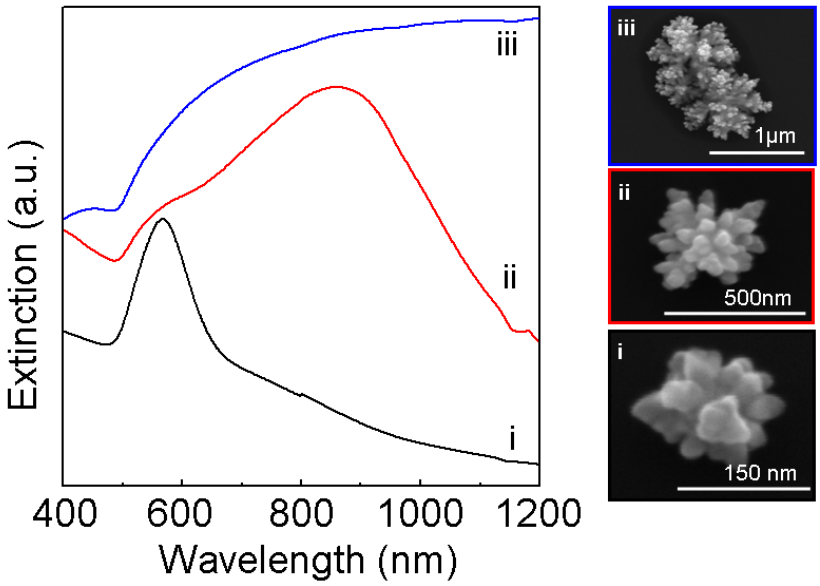


**Figure 11.3:** Extinction spectra of Au self-similar structures: (i) 150nm, (ii) 500nm, and (iii) 1µm diameters.

To comprehend the broadness of the local surface plasmon resonances, FTIR spectra of synthesized Au self-similar micro-structures were recorded with a Vertex 80v spectrophotometer (from Bruker Optics Inc) and with a Bruker Platinum (diamond single bounce) ATR. The instrument was equipment with a DTGS detector, a $CaF_2$ beam splitter, and a NIR source (tungsten lamp) for NIR spectra collection; a KBr beam splitter, a MIR source (globar), and a DTGS-FIR detector for MIR range; a DTGS-FIR detector, a Multilayer Mylar beam splitter, and a MIR source (globar) for FIR spectra collection. The scanning time was 5 minutes, the reflection data was converted to absorbance, and a baseline correction was performed. The FTIR spectrum presented in Figure 11.4 shows a large broad bandwidth absorbance with a maximum at 3µm followed by a broad tail into FIR.

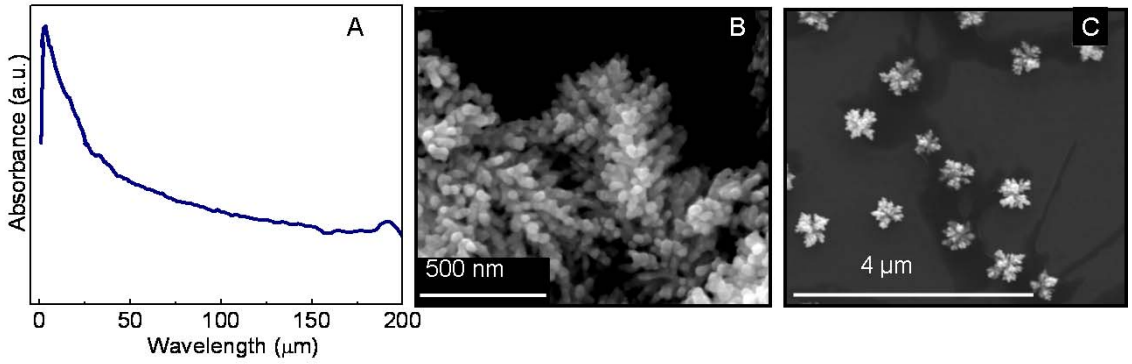


**Figure 11.4:** (A) FTIR spectra and (B,C) the corresponding SEM image of Au self-similar structures showing multiple gold branches of 25-30nm diameter and a very narrows size distribution.

The Brunauer-Emmett-Teller (BET) surface area and pore size distribution analysiswas performed to characterize the coral nanostructures. Figure 11.5A presents the nitrogen adsorption-desorption isotherms of the sample calcinated at 150°C for 8 hours. The isotherm exhibits a type IV isotherm (IUPAC, 1985) with a $N_2$ hysteresis loops in the desorption branch. As illustrated in the data, the isotherms are relatively flat which is nominally equivalent in the low-pressure region ($P/P_0 < 0.7$).In the high pressure region the isotherms form a loop due to the capillarity agglomeration phenomena indicative of a porous structure. Figure 11.5B confirms a bimodal pore size distribution, showing the first peak at the pore diameter of 2.9 nm and the second peak at 6.5 nm. The specific surface area of the Au self-similar structures is 10.84 $m^2/g$ which is calculated using the multipoint BET-equation (Figure 11.5C). The structural properties of Au self-similar structures are summarized in table 11.1. The porosity of the Au self-similar structures

amplifies the boiling nucleation and permits the water vapor to detach more quickly from the surface.

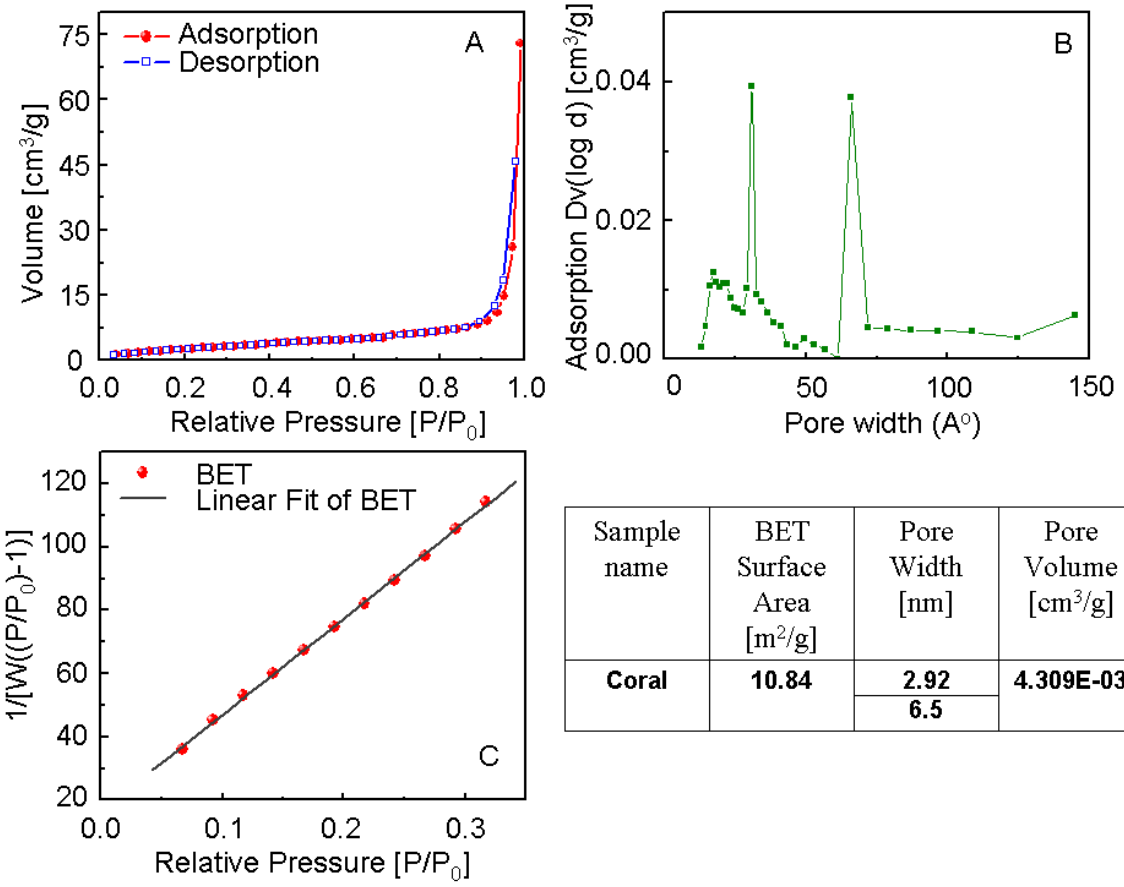


| Sample name | BET Surface Area [$m^2/g$] | Pore Width [nm] | Pore Volume [$cm^3/g$] |
|---|---|---|---|
| **Coral** | **10.84** | **2.92** | **4.309E-03** |
| | | **6.5** | |

**Figure 11.5:** (A) $N_2$ adsorption-desorption isotherms of gold corals using BET, (B) pore size distribution of the samples calcinated at 150ºC for 8 hours, (C) BET plots of Au self-similar structures. **Table 11.1:** Experimentally measured propertiesof Au self-similar structures using BET.

High-resolution X-ray photoelectron spectroscopy (XPS) measurements were performed to investigate the chemical composition and the purity of Au self-similar structures. XPS measurements were acquired with a PHI Quantera X-ray photoelectron spectrometer and the spectra (Figure 11.6A) display the binding energies for Au (4f 7/2)

at 83.6eV, Au (4f 5/2) at 87.3eV, Au ($4d^5$) at 345eV, Au ($3d^4$) at 355eV, and Au ($4p^3$) at 550eV of nanostructures. Thermal properties of Au self-similar structures were investigated by using a differential scanning calorimeter (DSC, TA Instruments, model STD Q600). A sample of approximately 29.512mg was placed inside a ceramic pan and placed in the DSC cell under nitrogen purge environment. Dynamic scans were performed on the samples at a heating rate of 5ºC/min, from room temperature to 975ºC. Thereafter, the sample was cooled to room temperature at a cooling rate of 15ºC/min then re-melted again until 1100ºC. Fig 11.6B displays the thermal profile of the Au self-similar structures. The melting point of the 1µm diameter Au self-similar structures is around 800ºC which was visibly verified via the colour change in the sample from black to yellow (Figure 11.6B insert). A new endothermic peak appears at 1065°C (red curve) as structures were allowed to continue heating which corresponds to the gold bulk melting temperature.

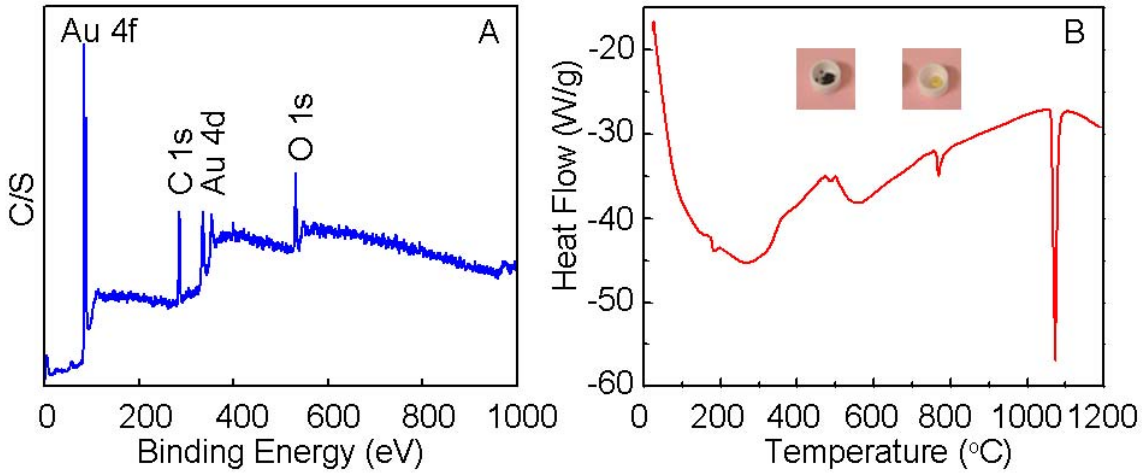


**Figure 11.6:** A heating scan at 15 deg $min^{-1}$ for (A) High-resolution XPS spectrum and (B) DSG spectrum of gold coral nanostructures. Insert are images of Au self-similar structures (black) powder in a ceramic pan illustrating the melted structure (yellow) at 800ºC.

## 11.3 Experimental

**Particle Fabrication:** The Au self-similar structures were synthesized according to a simple one-step method. [354,358-359] 50 mL aqueous solution of 1% $HAuCl_4$ (Sigma-Aldrich) aged for two-three weeks and 50 mL Polyvinyl pyridine (PVP, MW=160000g/mol) (Sigma-Aldrich) of 25μM were directly mixed with 50 mL aqueous solution of 0.4M L-ascorbic acid (reagent grade, fine crystal, Fisher Scientific) under stirring. The PVP solution was prepared by dissolving the calculated amount in approximately 20-30 mL ethanol solution and rescaled with MQ water until the final volume reached 50mL. The color of the solution changed from dark blue to black in a few minutes indicating the formation of Au self-similar structures (~1μm diameter). The Au self-similar structures were washed and resuspended in MQ water via centrifugation. The order of mixing solutions is important to note. If we first mix Au and L-ascorbic acid followed by the addition if PVP (noting the order change of PVP and L-ascorbic acid), the color of solution will become dark red-brown (200-500nm diameter), indicating the formation of Au self-similar nano-ball structures. The reaction can be described by eqn. (1):

$$2HAuCl_4 + 3C_6H_6O_4(OH)_2 = 2Au^0 + 3C_6H_6O_6 + 8HCl \quad (1)$$

The L-ascorbic acid reduces the aqueous chloroaurate ions at room temperature in the presence of PVP as the capping agent. Ethanol soluble PVP influences the crystallographic growth of gold leading to micro-aggregates of Au self-similar structures.

## 11.4 Conclusions

Black-colored Au self-similar structures with remarkable broad band optical properties were synthesized. The black color is due to the broad and efficient absorption spectrum of electromagnetic energy from a wide range of angles. A broad spectrum spanning into the FIR is ideal and defines Au self-similar structures as important candidates for numerous applications. In chapters 7, 8, 9, and 10, we have described the development of a highly efficient single step phase change process using broadband metallic nanostructures. However, due to the size of these particles that settle down over time due to gravity, a suspended structure embedded in a macromolecular network, mounted on fiberglass "scaffold" or any support that may easily float is crucial. Harvesting solar energy across a greater portion of the electromagnetic spectrum may be applied to many technologies that required localized heating and/or single step phase change.

# Chapter 12: Au nanorice assemble electrolytically into mesostars

## 12.1 Introduction

The assembly of materials and structures from constituent nanoparticles is currently an important topic of fundamental research, stimulated by the growth of numerous applications such as new optical devices,[360-361] chemical sensing,[362-363] composite materials,[364] catalysis,[365] and biomedicine.[366-367] In this chapter we report the formation of mesoscale star-shaped particles with a hierarchical substructure when aqueous suspensions of nanorice particles are introduced into an electrolytic cell. Reproduced with permission from R. Bardhan, O. Neumann, N. Mirin, H. Wang and N. J. Halas, *ACS Nano*, **2009,** 3, 266-272. Copyright 2009 American Chemical Society.

The design and synthesis of novel nanoparticles has been an important starting point, since nanoscale size, shape, and morphology determine the properties of larger materials assembled from nanoscale substituents. The hierarchical self-assembly of nanoscale building blocks can lead to the formation of complex supramolecular assemblies, frequently in striking similarity to structure formation in biological systems.

In this chapter we present a surprising observation of the formation of mesoscale star-shaped particles with a hierarchical substructure when an aqueous suspension of nanorice particles [368] is subjected to electrolysis. This unusual electrolytically assisted assembly is distinct from other electrochemically driven processes, such as the electrochemical synthesis of metal or metal oxide structures.[369-370] In this case, electrolysis transforms both the shape and composition of the nanorice particles. The nanorice particles consist of a prolate iron oxide (hematite, α-Fe2O3) core coated with a thin Au shell, where the

hyperbranched mesostars were composed of Au, iron oxide, and iron oxyhydroxide (goethite, α-FeOOH). To the best of our knowledge, the process of electrolyzing an aqueous suspension to transform nanoparticles into mesoscale structures has not been previously reported. This discovery may provide a new approach for the development of new structures and materials from nanoscale constituents.

## 12.2 Experimental

**A. Materials**: Ferric chloride ($FeCl_3.6H_2O$), (3-aminopropyl) triethoxysilane (APTES, 99%), tetrachloroauric acid ($HAuCl_4.3H_2O$), tetrakis hydroxymethyl phosphonium chloride (THPC), polyvinyl pyridine (PVP) were purchased from Sigma-Aldrich (St. Louis, MO). Formaldehyde (37%), sulfuric acid ($H_2SO_4$, 100%), hydrogen peroxide ($H_2O_2$, 30%), potassium dihydrogen phosphate ($KH_2PO_4$) and 200-proof ethanol were obtained from Fisher Scientific (Hampton, NH). All the chemicals were used as received without further purification. Platinum electrodes and platinum wire were purchased from Alfa Aesar. DC power supply was purchased from Hewlett-Packard. Quartz slides were purchasedfrom Technical Glass.

**B. Nanorice Fabrication**: Monodisperse spindle-shaped α-Fe2O3 nanoparticles and nanorice particles were fabricated as previously reported.[368,371] Briefly, α-Fe2O3 particles with an aspect ratio of 6.3 (340 nm ± 54 nm) were prepared by forced hydrolysis of ferric chloride solutions by reacting 100 mL of an aqueous mixture containing 2.0 x $10^{-2}$ M $FeCl_3$ and 4.0 x $10^{-4}$ M $KH_2PO_4$ at 100 °C for 72 h. The resulting precipitate was centrifuged and washed several times with water and ethanol and finally redispersed in 20 mL of ethanol. The surface of the α-Fe2O3 particles was functionalized with

organosilane molecules (APTES) to generate an amine-terminated surface. This was achieved by mixing 500 μL of APTES with 5 mL of ethanolic solution of hematite particles for 12 h under vigorous stirring. The resulting particles were centrifuged and redispersed in ethanol several times to remove excess APTES. These functionalized nanoparticles were decorated with small gold colloid (2-3 nm) prepared by the method reported by Duff et al.[372] Nanorice particles were fabricated via seed-mediated reduction of $AuCl_4^-$ ions onto the attached small colloid in the presence of formaldehyde.

**C. Nanoparticle Films for Optical Measurements:** Nanoparticle films were obtained by immobilizing them on PVP-functionalized quartz slides. Briefly, quartz slides were cleaned in piranha solution ($H_2SO_4$ (100%):$H_2O_2$ (30%) = 3:1) for 2 h, rinsed with $H_2O$ and 200 proof-ethanol and dried in a stream of $N_2$ gas. The slides were then immersed in a 1 wt % solution of PVP in ethanol for 24 h, followed by rinsing thoroughly in ethanol and drying with $N_2$ gas. The PVP-functionalized slides were immersed in aqueous solutions of nanorice, mesostars, hematite nanoparticles, and pyramidal mesostructures for 1 h. Upon removal from the individual solutions, the slides were rinsed with ethanol and dried with $N_2$ gas. This resulted in a monolayer of randomly oriented nanoparticles on the PVPfunctionalized slides.

**D. Characterization:** The nanoparticles were characterized by obtaining TEM images using a JEOL JEM-2010 TEM operated at 200 kV, SEM images using a FEI Quanta 400 field emission SEM at an acceleration voltage of 20 kV, XRD patterns by using a Rigaku Ultima II vertical-powder diffractometer (Cu Kα, λ=1.5418 Å), and absorption measurements using a Varian Cary 5000 UV-vis-NIR spectrophotometer.

### 11.3 Results and discussion

The electrolytic cell utilized to form the mesostars is shown in Figure 12.1. Platinum electrodes 0.020 mm wide were placed 0.014m apart in an aqueous suspension of nanorice particles ($10^9$particles/mL) and connected to a DC power supply. The nanorice particles utilized in these experiments consisted of prolate hematite cores with a longitudinal diameter of 340 ± 25 nm and a transverse diameter of 54 ± 6 nm, coated with a 22 ± 3 nm Au shell. At ambient temperature and pressure, a potential difference of 5 V was applied to the cell, and the particles self-assembled to form mesostars within 24 h. The mesostars were characterized using several analytical techniques to elucidate their formation mechanism, including electron microscopy, crystallography, and UV-vis spectroscopy.

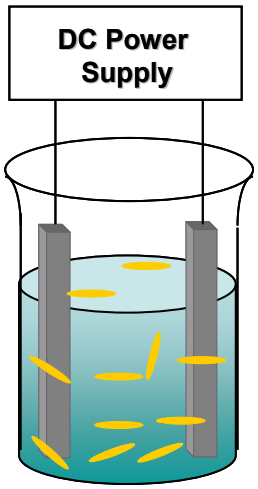


**Figure 12.1** Schematic representation of experimental set-up showing a DC power supply connected between two Pt electrodes (gray bars), separated by 0.014 m, immersed in aqueous gold nanorice solution.

The mesostars were typically 650 ± 80 nm in length and width and ~380 ± 30 nm in height, as shown in the scanning electron microscope (SEM) image in Figure 12.2A. All the mesostars observed in solution had similar shape and morphology but varied in size distribution. Powder X-ray diffraction (XRD) studies (Figure 12.2B) revealed a surprising transformation in the composition and crystal structure of the mesostars relative to the nanorice particles. XRD spectrum of α-Fe2O3 particles, which served as the core material of the nanorice is shown in Figure 12.2 B-i. These particles show a highly crystalline, hexagonal phase of α-Fe2O3 with cell parameters a =5.035 Å and c=13.747 Å and space group R3c (No. 167) (JCPDS card no. 98-000-0240). The XRD peak intensities correlate well with those from the powder diffraction intensity profile of α-Fe2O3. However, a preferential orientation of the α-Fe2O3 core particles is observed, a common feature among single crystalline nanoparticles. The XRD spectrum of nanorice (Figure 12.2B-ii) clearly demonstrates the presence of a crystalline Au shell covering the α-Fe2O3 cores. The crystal structure of the Au shell corresponds to the cubic phase of Au with cell parameters a = 4.078 Å and space group Fm3m (No. 225) (JCPDS card no. 98-000-0230). The Au shell on the α-Fe2O3 cores grows non-epitaxially as a polycrystal, which explains the absence of preferential orientation in the XRD spectrum of nanorice. The XRD spectrum of mesostars (Figure 12.2B-iii) reveals a mixture of peaks corresponding to α-FeOOH, α-Fe2O3, and Au. The α-FeOOH peaks suggest a partial transformation of α-Fe2O3 into α-FeOOH, which has an orthorhombic phase with lattice parameters a = 4.937 Å, b = 4.432 Å, and c = 2.994 Å, and space group P21nm (No. 31) (JCPDS card no. 00-026-0792). The strongest peak corresponding to the α-FeOOH (101) plane indicates that the mesostars are mostly composed of goethite, and also specifies a

preferential orientation of the goethite crystalline domains. Nanostars (B) XRD spectra of hematite cores (blue, showing α-$Fe_2O_3$ peaks) Au-nanorice (black, showing Au peaks), and Nanostars (red).

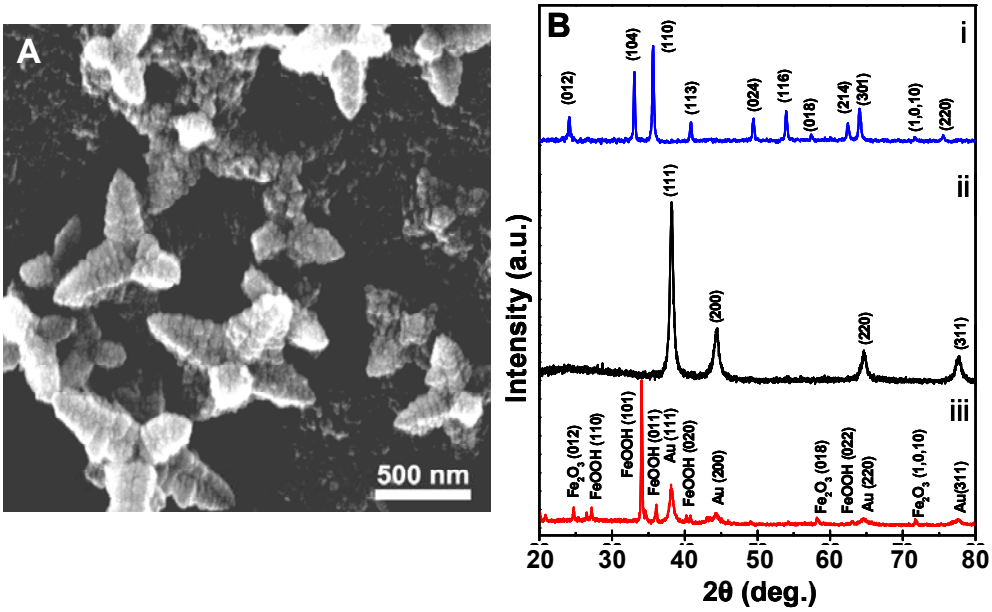


**Figure 12.2** Electron microscopy and crystallographic studies of mezostars prepared at 5V. (A) SEM image of Mezostars. (B) XRD spectra of (i) α-Fe2O3 cores, (ii) nanorice (showing gold peaks), and (iii) mezostars. The spectra are offset for clarity.

The observed alteration in structure and composition of nanorice particles to form mesostars was further studied using transmission electron microscopy (TEM) and electron diffraction (ED). TEM images with corresponding ED and selected area electron diffraction (SAED) patterns of mesostars are shown in Figure 12.3. A smaller star-shaped structure obtained within 6 h of electrolysis is shown in Figure 12.2A. The observed mesostar was polycrystalline as suggested by the ED ring pattern. The TEM micrograph

and corresponding SAED pattern of a mesostar formed after 24 h of electrolysis is shown in Figure 12.3B. The SAED pattern demonstrates an orthorhombic single crystalline area that is oriented toward the (200) plane and corresponds to α-FeOOH. In addition to the mesostars, α-FeOOH nanocrystals were observed in the solution mixture (Figure 12.3C). These nanocrystals demonstrated the orthorhombic phase of α-FeOOH that is preferentially oriented toward the [001] direction. The tips of the mesostars, shown in Figure 12.3D, also consisted of single crystalline domains of α-FeOOH oriented along the (200) plane. Dark-field TEM, an effective tool in observing lattice defects, grain boundaries, and ordered domain structures, was utilized to image the mesostar tip as shown in Figure 12.3E. The highly crystalline α-FeOOH domains are clearly demarcated by the lighter areas in Figure 12.3E. The darker central area indicates that this region is relatively dense and does not allow the electron beam to penetrate through. The TEM micrographs and SAED patterns in Figure 12.3A-E undoubtedly show that these mesostars have many crystalline domains of α-FeOOH, which explains the α-FeOOH peaks observed in the XRD spectrum of mesostars (Figure 12.2B-iii). The chemical composition of the observed mesostars was generally identical, composed mostly of α-FeOOH crystalline domains. However, the mesostars are also composed of Au as indicated by the XRD spectrum. A single mesostar is shown in Figure 12.3F. While its ED pattern (top inset) illustrates polycrystallinity, its SAED pattern (bottom inset) shows a face-centered cubic single crystalline domain of Au oriented along the (220) plane. Since these mesostructures were polycrystalline, individual crystallographic domains of Au, α-FeOOH, and α-Fe2O3 are difficult to determine for each particle; however, these representative TEM images confirm their composition.

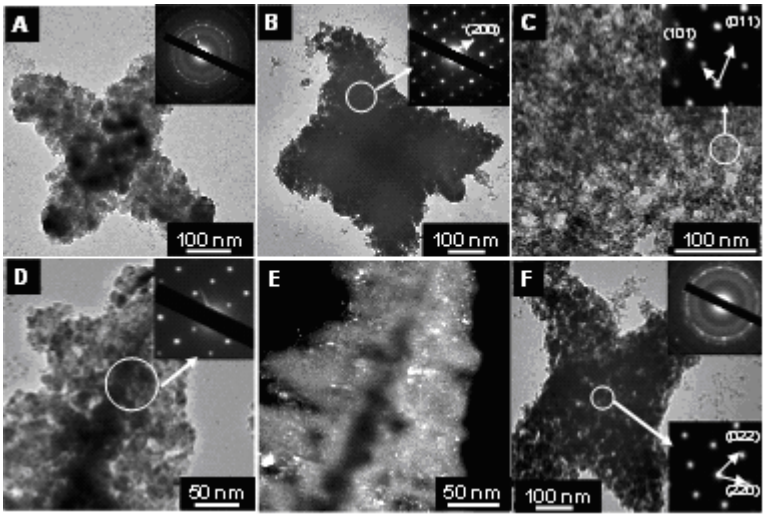


**Figure 12.3** TEM micrographs of (A) a star-shaped structure obtained after 6 h of electrolysis and ED pattern showing polycrystalline rings provided as inset, (B) a mesostar formed after 24 h of electrolysis and corresponding SAED pattern representing orthorhombic α-FeOOH single crystalline domain, (C) an α-FeOOH nanocrystals observed in solution and SAED pattern showing orthorhombic α-FeOOH single crystalline domain, (D) tip of a mesostar and corresponding SAED pattern representing orthorhombic α-FeOOH single crystalline area, (E) dark field image of mesostar tip corresponding to panel D, and (F) mesostar obtained after 24 h of electrolysis; ED pattern showing polycrystalline rings provided as top inset, and SAED pattern representing cubic Au single crystalline area provided as bottom inset. The selected area corresponding to the SAED patterns in panels B-D,F are shown in circle.

The phase transformation of α-FeOOH to α-$Fe_2O_3$ is known to occur via heat treatment by loss of $H_2O$ molecules[373] or by liquid phase transformation.[374] However, at present the reverse mechanism of α-$Fe_2O_3$ conversion to α-FeOOH is not well understood. The formation of α-FeOOH nanocrystals is strongly influenced by the presence of anions in

solution, the temperature of the reaction mixture, the pH, and the oxidizing agents.[375-376] The shape and size of α-FeOOH nanocrystals influence many of their physical properties, which consequently determine the morphological development of largerordered structures. The formation mechanism discussed below explains the morphological modification as well as the alteration in the composition of α-Fe2O3-Au nanorice particles to form mesostars composed of α-Fe2O3, Au, and α-FeOOH.

A systematic and controlled study of mesostar formation revealed electrolysis-induced complex assembly of nanorice particles to form these hierarchical structures. A schematic representation of the mesostar formation mechanism is shown in Figure 12.4A. Representative SEM images taken after 0, 2, 4, 6, 8, 10, 12, and 24 h of electrolysis are presented in Figure 12.4B in support of the proposed mesostar growth mechanism. The SEM image of nanorice particles is shown in Figure 12.4B-i. During electrolysis, the Au shell of nanorice particles is etched away, leaving residual Au islands and small Au colloid in the reaction mixture (Figure 12.4B-ii).

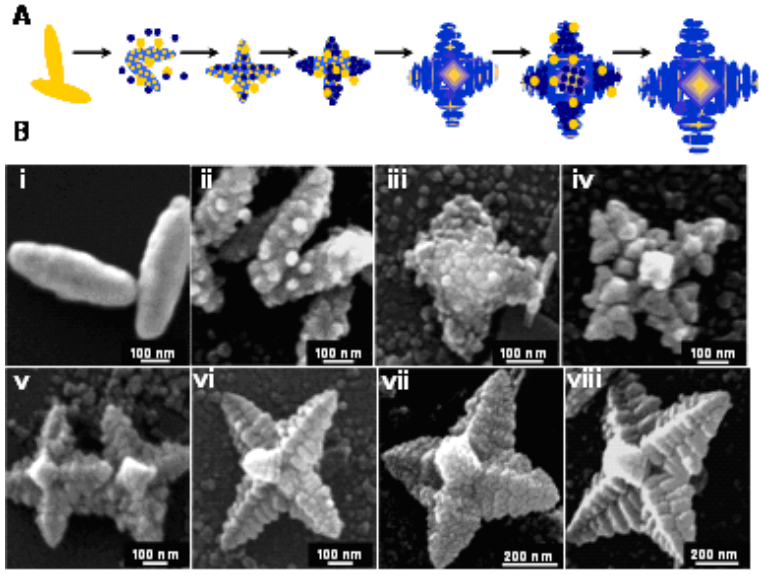

**Figure 12.4** (A) Schematic representation of mesostar formation mechanism. (B) SEM images supporting the mesostar formation mechanism starting with (i) nanorice, (ii) 2 h of electrolysis, (iii) 4, (iv) 6, (v) 8, (vi) 10, (vii) 12, and (viii) 24 h.

The etching process of the Au shell may result from two plausible mechanisms. First, active $O_2$ is produced during electrolysis (eq. 2) which has been shown to etch Au.[377] Second, active hydroxyl groups, which are also produced during electrolysis (eq 1), may react with the hematite core, altering its crystal structure. The subsequent recrystallization of the hematite core may then induce strain on the Au shell, causing it to partially etch.[378]

Cathode: $2H_2O_{(1)} + 2e^- \rightarrow H_{2\,(g)} + 2OH^-_{(aq)}$ $E_{red} = 0.00V$ (1)

Anode: $4OH^-_{(aq)} \rightarrow O_{2\,(g)} + 2H_2O_{(1)} + 4e^-$ $E_{ox} = -1.23V$ (2)

Active hydroxyl anions produced during electrolysis could also be incorporated into the hematite crystal lattice as hydroxyl defects, forming a metastable phase termed "hydrohematite" ($Fe_2O_3.H_2O$).[379-380] α-$Fe_2O_3$ possibly converts to α-FeOOH from the hydrohematite phase by replacement of oxygen atoms with hydroxyl ions:

$2Fe_2O_3 \cdot H_2O + 2OH^- + 2H^+ \rightarrow 4FeOOH + O_2 + 2H_2$ (3)

In addition to partial removal of the Au shell, the electrolysis process partially disintegrates the α-$Fe_2O_3$ particles, converting them into α-FeOOH nanocrystals (see Figure 12.3C). Subsequent to Au shell disintegration, the partially etched nanorice particles were completely coated with α-FeOOH nanocrystals and colloidal Au particles. These structures then preferentially aligned along their centers to form a cross-shaped structure (Figure 12.4B-iii). In some cases, end-to-end assembly occurred and formed long chains, but these were produced in relatively low yield (Figure 12.5).

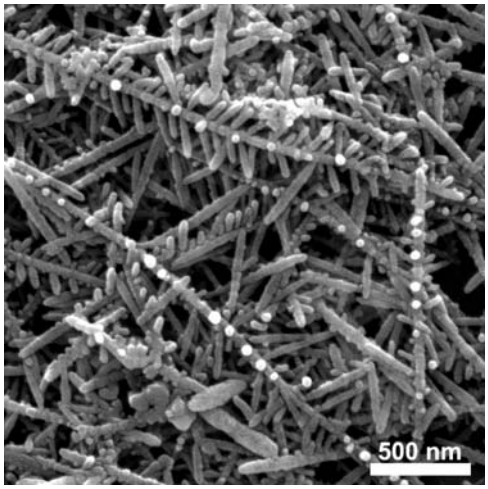


**Figure 12.5** SEM image of long chain branched structures obtained both at 5 V and 10 V in addition to the mesostars.

After 4 h of electrolysis, α-FeOOH nanocrystals assembled on the central axis of the cross structures, which was possibly the most convenient polarizable axis in the DC-field. This transformed the cross structures into star-shaped structures (Figure 12.4B iv,v). These star-shaped mesostructures continued to grow and after 24 h of electrolysis yielded hierarchical crystalline mesostars (Figure 12.4B vi_viii). The mesostars were formed in the bulk of solution and were not observed on the electrodes.

Colloidal Au particles that initially disintegrated from nanorice particles were also incorporated into these complex mesostructures. The conversion yield from nanorice particles to mesostars was ~50%. Since these mesostructures are larger in size than the nanorice, and the formation of mesostars is distinct from solution phase synthesis or seeded growth method, a lower conversion yield is expected.

These observations elucidate the α-Fe2O3 and Au peaks observed in the XRD spectra of mesostars (Figure 12.2B-iii) as well as the Au SAED pattern shown in Figure 12.3F.

The Au peaks in the XRD spectra could also be due to the residual colloidal Au particles in solution which disintegrated from the nanorice. These observations also explain the polycrystalline rings in the ED patterns (Figure 12.3A,F), which could be a consequence of self-assembly and oriented attachment of many α-FeOOH nanoparticles to form the mesostars.

The formation of the mesostars as a result of the specific oriented assembly of the α-FeOOH nanoparticles on the central axis of the cross structures could be due to defects in the α-FeOOH crystal structure and resulting magnetization in individual particles.[380-381] This magnetization results in weak interparticle magnetic interactions. Magnetism in α-FeOOH nanocrystals depends on several factors including the crystallinity of the particles, particle size, temperature, and surface defects. Bocquet et al.[375-376,382] proposed that as the size of α-FeOOH particles decreases, the number of crystal defects increases facilitating magnetic cluster ordering and reduced Neel temperature (TN). The TN of bulk α-FeOOH is ~398 K. The saturation magnetization values found in nanoscale materials are usually smaller than the corresponding bulk phases, provided that no change in ionic configurations occurs. Bocquet et al.[375] have reported a TN as low as ~261 K for α-FeOOH nanocrystals, which indicates they have a net magnetic moment at ambient temperature. Structural defects in α-FeOOH nanocrystals, such as iron and hydrogen vacancies, results in unpaired chains at the surface, which also contributes to a net increase in magnetization.[383-384] Thus, the formation of mesostars could have occurred because of the assembly of α-FeOOH nanocrystals along the most convenient polarizable axis in the DC-field as well as the weak interparticle magnetic interaction between the α-FeOOH nanocrystals.

A control experiment with the α-Fe2O3 cores without any Au shell was performed resulting in an alteration of the composition and morphology of the α-Fe2O3 nanoparticles (Figure 12.6). Very few pyramidal mesostructures (yield ~5%) were obtained, but mesostars were not observed.

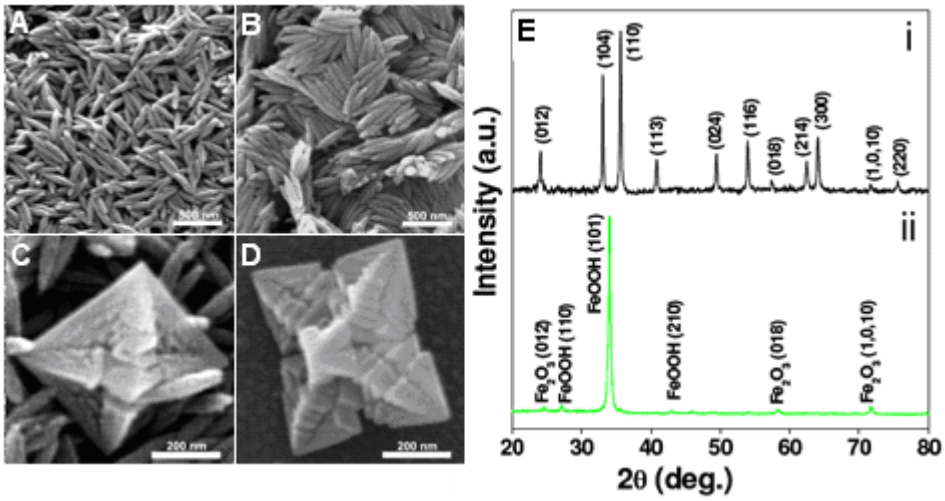


**Figure 12.6** SEM images of (A) α-$Fe_2O_3$ cores, (B) assembled α-$Fe_2O_3$ cores formed after 10 hrs of applying 5 V, (C) pyramidal mesostructures 500 ± 50 nm in length and width, and 350 ± 20 nm in height formed after 14 hrs, (D) larger pyramidal mesostructures 650 ± 100 nm in length and width, and 370 ± 50 nm in height formed after 24 hrs. (E) XRD spectra of (i) α-$Fe_2O_3$ cores, and (ii) pyramidal mesostructures.

Peaks corresponding to α-FeOOH were observed in the XRD spectrum of these pyramidal structures, which again indicate that α-Fe2O3 transforms into α-FeOOH via electrolysis in an aqueous media (Fig. 12.6E). The low yield of the pyramidal structures and absence of mesostars suggest that the Au shell may act as a direct agent in initiating nucleation sites for mesostar formation and facilitating shape evolution of these hierarchical mesostructures.

The formation mechanism of these hierarchical mesostructures was further established by studying the electrolysis-assisted assembly of nanorice particles as a function of voltage. The voltage between the electrodes was varied between 0.5 and 10 V, while the reaction time (24 h) and the distance between the electrodes (0.014 m) remained constant. At both 0.5 and 1 V, only aggregated nanorice particles were obtained, but mesostars were not observed (Figure 12.7A). This strongly indicates that below 1.23 V, the redox potential for $H_2O$ electrolysis, mesostar formation is not initiated. At 2 V, very few micrometer-sized star-shaped structures were observed, while most of the nanorice particles remained in solution (Figure 12.7B). These were large fractal structures, measuring ~4 ±0.2 μm in length and width, and 1.1 ± 0.2 μm in height. The small yield probably occurred because fewer nucleation sites for mesostar formation were initiated at lower voltage. This resulted in slower growth kinetics, which usually favors Ostwald ripening in order to minimize the overall surface free energy, resulting in the formation of larger but fewer stars. At 3 V, slightly smaller star-shaped structures with a length and width of 3.1 ± 0.7 μm and a height of 0.8 ± 0.3 μm were obtained. As the voltage was raised to 5 V, a higher yield of mesostars with a length and width of 650 ± 80 nm and a height of 380 ± 30 nm was observed. As the voltage was further increased to 10 V, a high yield of incomplete and deformed stars 450 ± 150 nm in length were obtained. These observations indicate that at higher voltage more nucleation sites are initiated leading to a higher rate of growth kinetics. This also results in the formation of distorted star-shaped morphologies with an overall decrease in size, and a larger size distribution.

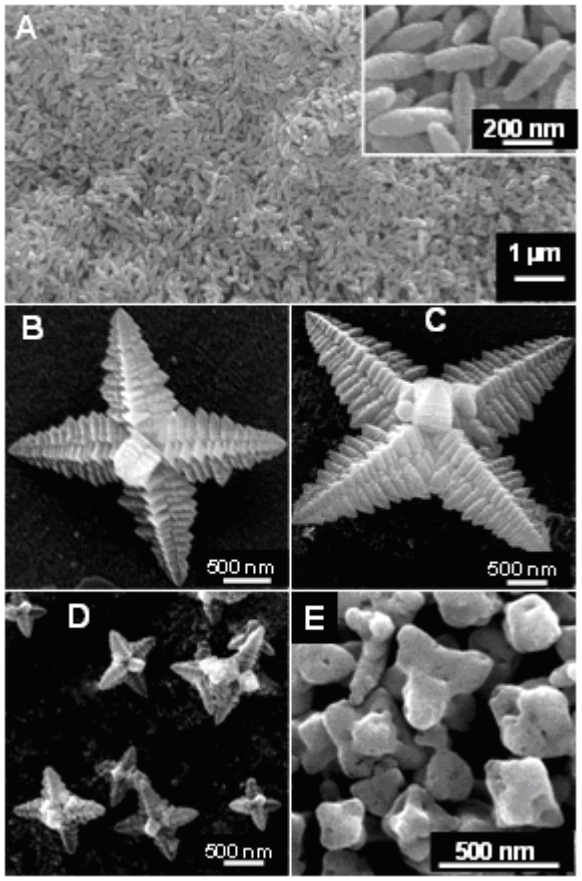


**Figure 12.7** SEM images of mesostructures obtained by varying the voltage while keeping electrolysis time constant at 24 h: (A) aggregated nanorice formed at 0.5 and 1 V and high resolution image provided as inset; (B) stars ~4 ± 0.2 μm in length and width, and 1.1 ± 0.2 μm in height formed at 2 V; (C) stars ~3.1 ± 0.7 μm in length and width, and 0.8 ± 0.3 μm in height obtained at 3 V; (D) mesostars 650 ± 80 nm in length and width, and 380 ± 30 nm in height observed at 5 V; and (E) distorted stars 450 ± 150 nm in length observed at 10 V.

In addition to electrolysis, the resulting crystal structure of these hierarchical self-assembled mesostructures can also be interpreted in the context of nucleation, oriented attachment, and Ostwald ripening. Nucleation in the reaction mixture results in small crystalline α-FeOOH primary particles which aggregate via oriented attachment to form

secondary particles. Oriented attachment involves self-organization of adjoining particles such that a regular crystallographic orientation is achieved followed by the joining of these particles at a planar interface. Oriented assembly usually results in single crystals, which could explain the single crystalline domains found in the mesostars (ED and SAED patterns shown in Figure 12.3). Several single crystalline domains then aggregate forming polycrystalline structures. The kinetics of crystal growth and coarsening strongly depend on various factors including the structure of the material, the surface chemistry of the particles resulting from the ions in the solution, and the interface between the crystals and surrounding solution.[385-387] With increasing time, Ostwald ripening controls the crystal growth by the diffusion of ions along the matrix-particle boundary resulting in larger particle sizes.[388-389] The observed morphology of the mesostars could be due to the simultaneous occurrence of adjacent particles in solution epitaxially assembling during the electrolysis process along the most convenient polarizable axis for DC-field as well as Ostwald ripening.

Since the optical properties of materials are governed by shape, size, and chemical composition, the extinction spectra of the α-Fe2O3 cores, Au-nanorice, and mesostars were compared using UV-vis spectroscopy (Figure 12.8). The extinction spectra were obtained by immobilizing the particles on quartz slides. The α-Fe2O3 cores showed an absorption maximum at ~390 nm, while nanorice demonstrated two separate peaks at 650 and 1100 nm. The strong plasmon resonance feature at 1100 nm was due to the longitudinal Plasmon mode of the nanorice while the weaker plasmon resonance at 650 nm was due to the transverse Plasmon mode of the nanorice particles.

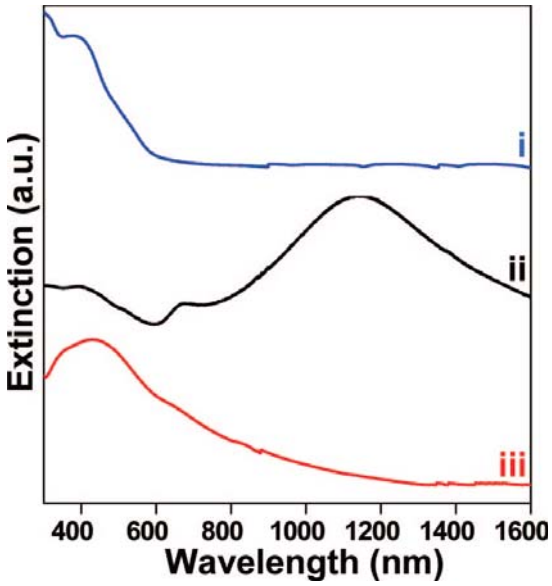


**Figure 12.8** Extinction spectra of (i) α-Fe2O3 cores with $\lambda_{max}$ ~ 390 nm, (ii) nanorice particles with longitudinal Plasmon $\lambda_{max}$ ~ 1100 nm and transverse plasmon $\lambda_{max}$ ~ 650 nm, and (iii) mesostars with $\lambda_{max}$ ~ 430 nm. The samples measured are monolayers of nanoparticles immobilized on PVPglass slides. The spectra are offset for clarity.

The optical spectrum of the mesostars is strikingly different from nanorice and revealed a broad peak with absorption maximum at 430 nm, which was attributable to the presence of α-Fe2O3, α-FeOOH, and Au. In the control experiment, the optical properties of the pyramidal mesostructures obtained with the hematite cores did not show any well-defined peak which additionally signifies the contribution of Au colloidal particles in the observed optical spectra of the mesostars.

### 12.4 Conclusions

In conclusion, we have observed the unusual formation of hierarchical mesostars via electrolysis of an aqueous suspension of nanorice particles. The Au-α- Fe2O3 nanorice

particles self-assembled into fractal mesostructures composed of α-Fe2O3, α-FeOOH, and Au. The remarkable differences in the geometry, composition, and properties between the nanorice particles and mesostars strongly indicate that electrolysis can significantly alter the morphology and constituent material of the nanostructures. A further examination of this striking assembly process could elucidate the unusual selfassembly processes observed in nature and biological systems. Further study of this system may be also promising in fundamental applications characteristic to hierarchical mesostructures.

## Chapter 13: Summary

The optical properties of metal nanoparticles may be used to manipulate light at the nanoscale since NS support surface plasmons, i.e. collective oscillations of the conduction electrons. These oscillations are resonant at frequencies that can be tailored by engineering the nanoparticle size, shape, or interparticle coupling with nanocluster ensembles. The strong field enhancement around metal nanoparticles enables conformation measurements of the analyte at metal surface and understanding of the interface processes. The SERS response of adenine, AMP, and poly-A at various pH was exploited to determine the adsorption and conformation of molecules on the Au nanoshells surface. The pH dependent SERS spectra were found to be reversible under experimental conditions. Spectral analysis indicates that the ring planes of both adenine and AMP are not lying flat but have upright orientation with a small angle from the surface normal. Those discoveries are critical for the future development and detection of DNA-protein/small molecule interaction.

Aptamers , rivals of antibodies both in therapeutic and diagnostic applications, consist of single stranded DNA or RNA that fold into well-defined three-dimensional conformations in the presence of specific molecular targets (proteins, peptides, vitamins and other organic or inorganic compounds). In addition, aptamers can undergo repeated cycles of denaturation-renaturation, freezing-thawing and long storage time without damaging their structure. Various detection methods have been reported for aptamer-protein/small molecules interaction such as: fluorescence, radio-labeling, electrochemical detection, electrophoretic mobility, piezoelectric, colorimetric, and molecular light

switching sensors have been reported. Most of these techniques suffer from complex label conjugation or sample preparation requirements. In this approach the secondary structure of aptamers was destroyed by thermal treatment, resulting in a linear conformation. As a result, a highly reproducible SERS spectrum was obtained. Platelet-Derived Growth Factor (PDGF) (a protein directly implicated in tumor progression) and three other small molecules including cocaine, procaine and benzocaine were used as a target molecule. Introduction of target molecules to thermally treated aptamers causes the aptamers to refold into their native hairpin states, which was monitored by quantifying the reproducibility of the SERS spectra observed from the aptamers. CD spectroscopy confirmed that the changes to the reproducibility of the SERS spectra were a result of conformational changes to the aptamer induced by thermal treatment and then target binding. The aptamer SERS system can be further developed to assess their binding specificity as well as the dynamics evolved in the adsorption/desorption process. This work represents the first label-free SERS study of conformational variation of aptamer induced by target binding.

In the examination of chiral molecules deposited on Au nanoparticles surface, the SEROA response was exploited to elucidate the stereochemistry of chiral molecules and the analyte's orientation on the metal surfaces. The two enantiomers used in this study are: (S)- and (R)-Tryptophan (Trp), and (SS)- and (RR)- Cysteine-Phenylalanine-Glycine-Glycine (Cys-Phe-Gly-Gly). Both play an important roll in analytical/biological detection of proteins and establish their folding and unfolding states. The reproducibility of SEROA spectrum gives information about the conformational binding. The lower SEROA reproducibility factor of Cys-Phe-Gly-Gly relative to Trp are attributed to the broader range of molecular surface conformations and convolutions of the Cys-Phe-Gly-

Gly backbone mode. The results suggest that both molecules are tilted to on the Au nanoparticle surfaces and the interaction between molecules with the metal surface did not introduce a new chiral center. We present for the first time an NIR-SEROA spectra of (S)-/(R)-Trp and (SS)-/(RR)- Cys-Phe-Gly-Gly molecules on a Au nanoparticle substrate. The chiral biomolecules are chemically identical but each with a different bioactivity is critical to distinguish them at low concentration in short time.

Molecule adsorption onto a solid surface can control a variety of interface processes. Here we study the effects of the adsorption onto gold nanoshells inhibiting oxidation of the infrared dye DNDTPC. The chemical and photo- stability of infrared dyes, strongly correlated with the dye structure, is asignificant prerequisite for many biological and industrial applications. The SERS spectra of un-oxidized DNDTPC on Au nanoshells are stable under oxidizing conditions, and are distinctly different from SERS spectra of oxidized DNDTPC. Density functional theory calculations indicate that the un-oxidized species is quite flat, but oxidation causes the $\pi$ conjugation of the molecule to break and the carbon backbone to rehybridize from $sp^2$ to $sp^3$. Moreover, the results suggest that geometric effects play a role in preventing the oxidation of DNDPTC that is adsorbed onto a nanoshell surface.

Plasmonic delivery vectors have been developed to deliver genetic materials, drugs, or organic molecules into the living cells. The local heating on the metal nanostructures surface was used to controllably release molecules. Due to their optical and thermal properties, nontoxicity, and highly controllable surface chemistry gold nanoshells have been used in this study. The nanoshells surfaces were functionalized with double stranded DNA (dsDNA) where one strand of DNA had a thiol group facilitating covalent

attachment to the gold surface. In addition, DAPI (4',6-diamidino-2-phe-nylindole) molecules, a stabile dye with negligible toxicity that binds preferentially to the minor grooves of the dsDNA, have been used as a delivery system to demonstrate and visualize the light-induced intracellular release. The NS-dsDNA-DAPI complex system was incubated with the H1299 cancer cells in serum containing cell culture medium. Upon NIR laser illumination the local heat generated by the nanoshells induced dehybridization of the dsDNA, releasing the DAPI molecules within living cells, where diffusion into the nucleus and binding to the genomic DNA of the cell occurs. The staining of the cell nucleus with the released DAPI was observed by fluorescence microscopy. Furthermore, the acytotoxicity assay demonstrated nanoshell uptake is nontoxic and the DAPI release process does not induce cell death.

In the second part of this thesis, a highly absorbing solar collector media has been developed with resonant properties that span much of the solar spectrum. Au nanoshells and Au self-similar particles with surprising broadband optical properties, large surface area, and high surface roughness were fabricated to function as black-body absorbers that serve as nucleation sites for heat transfer when dispersed in solution. Based on their ability to strongly absorb light at resonant wavelengths, the water-dispersed metallic particles produces vapor without the requirement of heating the fluid volume. Energy captured by light-harvesting nanoparticles is primarily directed to the vaporization of water into steam, eliminating the energy-intensive requirement of electrically heating the fluid volume. Additionally, by suspending the nanoparticles in water, the volumetric heat absorbers present several advantages compared to the surface heat absorbers: (i) a greater surface area (on which heat transfer occurs) capable of absorbing more photons in order

to convert light into both heat and energy, (ii) a decrease in the bubble lifetime due to high surface temperature, and (iii) an increase in interfacial turbulence by the water gradient temperature and the Brownian motion of the particles. These studies clearly show a liquid-vapor phase transition with greater efficiency approximately 80% in a thermodynamically open system, achieving steam temperatures well above 100$^{o}$C in a compact geometry.

To demonstrate the advantage of using water-dispersant nanoparticles, we design a solar distillation system, in which vapor is first generated in the vessel with the ability to escape through a nozzle and is secondly, cooled and collected in an ice bath using sunlight. In the case of particle-based solar distillation, we obtain a larger quantity and more efficient ethanol distillate compared with thermal flash distillation using solar-powered nanoparticle heating in an inherently non-equilibrium vaporization process.

Additionally, the vaporization process also leads to the production of saturated steam which is ideal for sterilizing medical tools or waste. The rapid transfer of heat from saturated steam is extremely effective in denaturing proteins and may be used to destroy most known types of infectious agents, (i.e. bacteria, viruses). A custom-built portable solar-autoclave system was build to demonstrate one of the most promising technologies that could address the lack of a reliable electric grid in developing regions. The system maintains temperatures higher then 115$^{o}$C for a minimum of 30 minutes, in accordance with FDA sterilization requirements. The steam generated in the autoclave successfully destroyed Geobacillus stearothermophilus bacteria. Most importantly, this approach can be applied to a wide range of solar energy applications such as desalination, sterilization, sanitation, or thermal energy.

Finally hierarchical self-assembly nanostructures with interesting optical properties are reported. Mesostars composed of Au, α-FeOOH, and α-$Fe_2O_3$ were formed by electrolytically induced assembly of an aqueous nanorice suspension. To the best of our knowledge, the process of electrolyzing an aqueous suspension to transform nanoparticles into mesoscale structures has not been previously reported. Further study of this system may be also promising in developing new hierarchical mesostructures for catalytically applications.

Plasmonic metal nanostructures form the basis for a number of applications ranging from medicine, drug delivery, catalysts in hydrogen storage systems, pesticides in agriculture, to solar energy. Plasmonic delivery vectors present a distinguishable interest due to their ability to deliver drugs, treat diseases, and visualize biological processes. Particularly, solar energy has triggered significant interest for its potential to provide power without relying on carbon-based fuels. With further development, the steam driven nano-heating system may be easily implemented to any solar systems with minimal adjustments.

## Reference:


(1) Mie, G. *Annalen Der Physik* **1908**, *25*, 377.

(2) Palpant, B.; Pre´vel, B.; Lerme´, J.; Cottancin, E.; Pellarin, M.; Treilleux, M.; Perez, A.; Vialle, J. L.; Broyer, M. *Phys. Rev. B* **1998**, *57*, 1963.

(3) Prodan, E.; Radloff, C.; Halas, N. J.; Nordlander, P. *Science* **2003**, *302*, 419.

(4) Hiep, H. M.; Endo, T.; Kerman, K.; Chikae, M.; Kim, D. K.; Yamamura, S.; Takamura, Y.; Tamiya, E. *Sci. Technol. Adv. Mater.* **2007**, *8*, 331.

(5) Hirsch, L. R.; Jackson, J. B.; Lee, A.; Halas, N. J.; West†, J. L. *Anal. Chem.* **2003**, *75*, 2377.

(6) Devi, G. R. *Cancer Gene Ther.* **2006**, *13*, 819.

(7) Fattal, E.; Bochota, A. *Advanced Drug Delivery Reviews* **2006**, *58*, 1203.

(8) Han, G.; Ghosh, P.; Rotello, V. M. *Nanomedicine* **2007**, *2*, 113.

(9) Huschka, R.; Neumann, O.; Barhoumi, A.; Halas, N. J. *Nano Lett.* **2010**, *10*, 4117.

(10) Hirsch, L. R.; Stafford, R. J.; Bankson, J. A.; Sershen, S. R.; Rivera, B.; Price, R. E.; Hazle, J. D.; Halas, N. J.; West, J. L. *Proc. Natl. Acad. Sci.* **2003**, *100*, 13549.

(11) O'Neal, D. P.; Hirsch, L. R.; Halas, N. J.; Payne, J. D.; West, J. L. *Cancer Lett.* **2004**, *209*, 171.

(12) Huang, X.; Jain, P. K.; El-Sayed, H. I.; El-Sayed, M. A. *Lasers Med. Sci.* **2008**, *23*, 217.

(13) Lal, S.; Clare, S. E.; Halas, N. J. *Acc. Chem. Res.* **2008**, *41*, 1842.

(14) Loo, C.; Lowery, A.; Halas, N. J.; West, J.; Drezek, R. *Nano Lett.* **2005**, *5*, 709.

(15) Park, K.; Lee, S.; Kang, E.; Kim, K.; Choi, K.; Kwon, I. C. *Adv. Funct. Mater.* **2009**, *19*, 1553.

(16) Liu, X.; Dai, Q.; Austin, L.; Coutts, J.; Knowles, G.; Zou, J.; Chen, H.; Huo, Q. *J. Am. Chem. Soc.* **2008**, *130*, 2780.

(17) Aaron, J.; Rosa, E. d. l.; Travis, K.; Harrison, N.; Burt, J.; Yacamán, M. J.; Sokolov, K. *Opt. Express* **2008**, *16*, 2153.

(18) Gobin, A. M.; Lee, M. H.; Halas, N. J.; James, W. D.; Drezek, R. A.; West, J. L. *NanoLett.* **2007**, *7*, 1929.

(19) Park, J.; Estrada, A.; Sharp, K.; Sang, K.; Schwartz, J. A.; Smith, D. K.; Coleman, C.; Payne, J. D.; Korgel, B. A.; Dunn, A. K.; Tunnell, J. W. *Opt. Express* **2008**, *16*, 1590.

(20) Adleman, J. R.; Boyd, D. A.; Goodwin, D. G.; Psaltis, D. *Nano Lett.* **2009**, *9*, 4417.

(21) Fang, N.; Liu, Z.; Yen, T. J.; Zhang, X. *Applied Physics a-Materials Science & Processing* **2005**, *80*, 1315.

(22) Linden, S.; Enkrich, C.; Dolling, G.; Klein, M. W.; Zhou, J.; Koschny, T.; Soukoulis, C. M.; Burger, S.; Schmidt, F.; Wegener, M. *Ieee Journal of Selected Topics in Quantum Electronics* **2006**, *12*, 1097.

(23) Dolling, G.; Wegener, M.; Soukoulis, C. M.; Linden, S. *Optics Lett.* **2007**, *32*, 53.

(24) Mohamed, M. B.; Ahmadi, T. S.; Link, S.; Braun, M.; El-Sayed, M. A. *Chem. Phys. Lett.* **2001**, *343*, 55.

(25) Richardson, H. H.; Hickman, Z. N.; Govorov, A. O.; Thomas, A. C.; Zhang, W.; Kordesch, M. E. *Nano Lett.* **2006**, *6*, 783.

(26) Zeng, N.; Murphy, A. B. *Nanotechnology* **2009**, *20*, 375702.

(27) Cole, J. R.; Mirin, N. A.; Knight, M. W.; Goodrich, G. P.; Halas, N. J. *J. Phys. Chem. C* **2009**, *113*, 12090.

(28) Oldenburg, S. J.; Averitt, R. D.; Westcott, S. L.; Halas, N. J. *Chem. Phys. Lett.* **1998**, *288*, 243.

(29) Averitt, R. D.; Sarkar, D.; Halas, N. J. *Phys. ReV. Lett.* **1997**, *78*, 4217.

(30) Tam, F.; Moran, C.; Halas, N. *J. Phys. Chem. B* **2004**, *108*, 17290.

(31) Oldenberg, S. J.; Averitt, R. D.; Westcott, S. L.; Halas, N. J. *Chem. Phys. Lett.* **1998**, *288*, 243.

(32) Bu¨ttner, M.; ger, H. K.; Gerhards, I.; Mathys, D.; Oelhafen, P. *Thin Solid Films* **2006**, *495*, 180.

(33) Wang, H.; Brandl, D. W.; Nordlander, P.; Halas, N. J. *Acc. Chem. Res.* **2007**, *40*, 53.

(34) Brandl, D. W.; N. A. Mirin; Nordlander, P. *J. Phys. Chem. B* **2006**, *110*, 12302.

(35) Tan, S. J.; Campolongo, M. J.; Luo, D.; Cheng, W. *Nat. Nanotechnology* **2011**, *6*, 268.

(36) Oldenburg, S. J.; Westcott, S. L.; Averitt, R. D.; Halas, N. J. *J. of Chem. Phys.* **1999**, *111*, 4729.

(37) Talley, C. E.; Huser, T.; Hollars, C. W.; Jusinski, L.; Laurence, T.; Lane, S. *Advances in Biophotonics B.C. Wolson et al. (Eds.) IOS Press* **2005**.

(38) Haynes, C. L.; McFarland, A. D.; Duyne, R. P. V. *Anal. Chem.* **2005**, *77*, 338A.

(39) Bosshard, C.; Spreiter, R.; Degiorgi, L.; Gu¨nter, P. *Phys. Rev. B* **2002**, *66*, 205107.

(40) Steinfeld, J. I.; Wormhoudt, J. *Annu. Rev. Phys. Chem.* **1998**, *49*, 203.

(41) Fleischmann, M.; Hendra, P. J.; McQuillan, A. J. *Chem. Phys. Lett.* **1974**, *26*, 163.

(42) Jeanmaire, D. L.; Duyne, R. P. V. *J. Electroanal. Chem.* **1977**, *84*, 1.

(43) Albrecht, M. G.; Creighton, J. A. *J. Am. Chem. Soc* **1977**, *99*, 5215.

(44) Banholzer, M. J.; Millstone, J. E.; Qin, L.; Mirkin, C. A. *Chem. Soc. Rev.* **2008**, *37*, 885.

(45) Nie, S. M.; Emery, S. R. *Science* **1997**, *275*, 1102.

(46) Kneipp, K.; Wang, Y.; Kneipp, H.; Perelman, L. T.; Itzkan, I.; Dasari, R.; Feld, M. S. *Phys. Rev. Lett.* **1997**, *78*, 1667.

(47) Xu, H. X.; Bjerneld, E. J.; Kall, M.; Borjesson, L. *Phys. Rev. Lett.* **1999**, *83*, 4357.

(48) Kneipp, K.; Wang, Y.; Kneipp, H.; Perelman, L. T.; Itzkan, I.; Dasari, R. R.; Feld, M. S. *Phys. Rev. Lett.* **1997**, *78*, 1667.

(49) Kambhampati, P.; Child, C. M.; Foster, M. C.; Campion, A. *J. Chem. Phys.* **1998**, *108*, 5013.

(50) Campion, A.; Kambhampati, P. *Chem. Soc. Rev.* **1998**, *27*, 241.

(51) Stiles, P. L.; Dieringer, J. A.; Shah, N. C.; Duyne, R. P. V. *Annu. Rev. Anal. Chem.* **2008**, *1*, 601.
(52) Barnes, W. L.; Dereux, A.; Ebbesen, T. W. *Nature* **2003**, *424*, 824.
(53) Wang, H.; Levin, C. S.; Halas, N. J. *J. Am. Chem. Soc* **2005**, *127*, 14992.
(54) Wang, H.; Halas, N. J. *Advanced Materials* **2008**, *20*, 820.
(55) Dick, L. A.; Haes, A. J.; Duyne, R. P. V. *J. Phys. Chem. B* **2000**, *104*, 11752.
(56) Lal, S.; Grady, N. K.; Goodrich, G. P.; Halas, N. J. *Nano Lett.* **2006**, *6*, 2338.
(57) Leffingwell, J. C. *Leffingwell Reports* **2003**, *3*, 1.
(58) Nafie, L. A. *Annu. Rev. Phys. Chem.* **1997**, *48*, 357.
(59) Blanch, E. W.; Hecht, L.; Barron, L. D. *Methods* **2003**, *29*, 196.
(60) Abdali, S. *J. Raman Spectrosc.* **2006**, *37*, 1341.
(61) Johannessen, C.; White, P. C.; Abdali, S. *J. Phys. Chem. A* **2007**, *111*, 7771.
(62) Abdali, S.; Blanch, E. W. *Chem. Soc. Rev.* **2008**, *37*, 980.
(63) Kneipp, H.; Kneipp, J.; Kneipp, K. *Anal. Chem.* **2006**, *78*, 1363.
(64) Osawa, M. *Bull Chem. Soc. Jpn.* **1997**, *70*, 2861.
(65) Kundu, J.; Le, F.; Nordlander, P.; Halas, N. J. *Chem. Phys. Lett.* **2008**, *452*, 115.
(66) Gray, S. K. *Plasmonics* **2007**, *2*, 143.
(67) Le, F.; Brandl, D. W.; Urzhumov, Y. A.; Wang, H.; Kundu, J.; Halas□, N. J.; Aizpurua, J.; Nordlander, P. *ACS Nano* **2008**, *2*, 707.
(68) Prodan, E.; Radloff, C.; Halas, N. J.; Nordlander, P. *Science* **2003**, *302*, 419.
(69) Yang, S.-C.; Kobori, H.; He, C. L.; Lin, M. H.; Chen, H. Y.; Li, C.; Kanehara, M.; Teranishi, T.; Gwo, S. *Nano. Lett.* **2010**, *10*, 632.
(70) Nordlander, P.; Oubre, C.; Prodan, E.; Li, K.; Stockman, M. I. *Nano. Lett.* **2004**, *4*, 899.
(71) Merabia, S.; Keblinski, P.; Joly, L.; Lewis, L. J.; Barrat, J. L. *Phys. Rev. E* **2009**, *79*, 1.
(72) Govorov, A. O.; Richardson, H. H. *Nano Today* **2007**, *2*, 30.
(73) Adleman, J. R.; Boyd, D. A.; Goodwin, D. G.; Psaltis, D. *Nano Lett.* **2009**, *9*, 4417.
(74) Langer, R. *Nature* **1998**, *392*, 5.
(75) Huschka, R.; Neumann, O.; Barhoumi, A.; Halas, N. J. *Nano Lett.* **2010**, *10*, 4117.
(76) Hirsch, L. R.; Stafford, R. J.; Bankson, J. A.; Sershen, S. R.; Rivera, B.; Price, R. E.; Hazle, J. D.; Halas, N. J.; West, J. L. *Proc. Natl. Acad. Sci.* **2003**, *100*, 13549.
(77) Lira-Cantu, M.; Sabio, A. M.; Brustenga, A.; Gomez-Romero, P. *Sol Energy Mater Sol Cells* **2005**, *87*, 685.
(78) Narimanov, N. E.; Kildishev, A. V. *Appl. Phys. Lett.* **2009**, *95*, 041106.
(79) Lehman, J.; Sanders, A.; Hanssen, L.; Wilthan, B.; Zeng, J.; Jensen, C. *Nano Lett.* **2010**, *10*, 3261.

(80) Lehman, J.; Theocharous, E.; Eppeldauer, G.; Pannell, C. *Meas Sci Tech* **2003**, *14*, 916.
(81) Granqvist, C. G. *Appl Opt* **1981**, *20*, 2606.
(82) Katz, E.; Willner, I. *Angew. Chem., Int. Ed.* **2004**, *43*, 6042
(83) Jain, P. K.; Huang, X. H.; El-Sayed, I. H.; El-Sayed, M. A. *Acc. Chem. Res.* **2008**, *41* 1578.
(84) Murphy, C. J.; Gole, A. M.; Stone, J. W.; Sisco, P. N.; Alkilany, A. M.; Goldsmith, E. C.; Baxter, S. C. *Acc. Chem. Res.* **2008**, *41*, 1721.
(85) Rosi, N. L.; Mirkin, C. A. *Chem. Rev.* **2005**, *105* 1547.
(86) Lu, Y.; Liu, J. *Acc. Chem. Res.* **2007**, *40*, 315.
(87) Dong, L. Q.; Zhou, J. Z.; Wu, L. L.; Dong, P.; Lin, Z. H. *Chem. Phys. Lett.* **2002**, *354*, 458.
(88) Braun, G.; Lee, S. J.; Dante, M.; Nguyen, T.-Q.; Moskovits, M.; Reich, N. *J. Am. Chem. Soc.* **2007**, *129*, 6378.
(89) Bell, S. E. J.; Sirimuthu, N. M. S. *J. Am. Chem. Soc.* **2006**, *128*, 15580.
(90) Green, M.; Liu, F.-M.; Cohen, L.; Ko¨llensperger, P.; Cass, T. *Faraday Discuss.* **2006**, *132*, 269.
(91) Barhoumi, A.; Zhang, D.; Tam, F.; Halas, N. J. *J. Am. Chem. Soc.* **2008**, *130*, 5523.
(92) Brown, K. A.; Park, S.; Hamad-Schifferli, K. *J. Phys. Chem. C* **2008**, *112*, 7517.
(93) Moskovits, M. *Rev. Mod. Phys.* **1985**, *57*, 783.
(94) Drachev, V. P.; Shalaev, V. M. *Top. Appl. Phys.* **2006**, *103*, 351.
(95) Osawa, M. *Top. Appl. Phys.* **2001**, *81*, 163−187.
(96) Ataka, K.; Heberle, J. *Anal. Bioanal. Chem.* **2007**, *388*, 47.
(97) Barlow, S. M.; Haq, S.; Raval, R. *Langmuir* **2001**, *17*, 3292
(98) Williams, J.; Haq, S.; Raval, R. *Surf. Sci.* **1996**, *368*, 303.
(99) McNutt, A.; Haq, S.; Raval, R. *Surf. Sci.* **2003**, *531*, 131.
(100) Kimura-Suda, H.; Petrovykh, D. Y.; Tarlov, M. J.; Whitman, L. J. *J. Am. Chem. Soc.* **2003**, *125*, 9014.
(101) Oldenburg, S. J.; Jackson, J. B.; Westcott, S. L.; Halas, N. J. *Appl. Phys. Lett.* **1999**, *75*, 2897−2899.
(102) Jackson, J. B.; Halas, N. J. *N. J. Proc. Natl. Acad. Sci. U.S.A.* **2004**, *101*, 17930.
(103) Kundu, J.; Le, F.; Nordlander, P.; Halas, N. J. *Chem. Phys. Lett.* **2008**, *452*, 115.
(104) Wang, H.; Kundu, J.; Halas, N. J. *Angew. Chem., Int. Ed.* **2007**, *46*, 9040.
(105) Lal, S.; Grady, N. K.; Kundu, J.; Levin, C. S.; Lassiter, J. B.; Halas, N. J. *Chem. Soc. Rev.* **2008**, *37*, 898.
(106) O¨stblom, M.; Liedberg, B.; Demers, L. M.; Mirkin, C. A. *J. Phys. Chem. B* **2005**, *109*, 15150.
(107) Yamada, T.; Shirasaka, K.; Takano, A.; Kawai, M. *Surf. Sci.* **2004**, *561*, 233.
(108) Chen, Q.; Frankel, D. J.; Richardson, N. V. *Langmuir* **2002**, *18*, 3219.
(109) Kim, S. K.; Joo, T. H.; Suh, S. W.; Kim, M. S. *J. Raman Spectrosc.* **1986**, *17*, 381.

(110) Koglin, E.; Sequaris, J. M.; Valenta, P. *J. Mol. Struct.* **1980**, *60*, 421.
(111) Suh, J. S.; Moskovits, M. *J. Am. Chem. Soc.* **1986**, *108*, 4711.
(112) Brabec, V.; Niki, K. *Collect. Czech. Chem. Commun.* **1986**, *51*, 167.
(113) Badr, Y.; Mahmoud, M. A. *Spectrochim. Acta., Part A* **2006**, *63*, 639.
(114) Giese, B.; McNaughton, D. *J. Phys. Chem. B* **2002**, *106*, 101.
(115) Demers, L. M.; O¨stblom, M.; Zhang, H.; Jang, N.-H.; Liedberg, B.; Mirkin, C. A. *J. Am. Chem. Soc.* **2002**, *124.*, 11248.
(116) Piana, S.; Bilic, A. *J. Phys. Chem. B* **2006**, *110*, 23467.
(117) Watanabe, T.; Kawanami, O.; Katoh, H.; Honda, K. *Surf. Sci.* **1985**, *158*, 341.
(118) Otto, C.; Tweel, T. J. J. V. d.; Mul, F. F. M. d.; Greve, J. J. *J. Raman Spectrosc.* **1986**, *17*, 289.
(119) Cardini, G.; Muniz-Miranda, M.; Pagliai, M.; Schettino, V. *Theor. Chem. Acc.* **2007**, *117*, 451.
(120) Muniz-Miranda, M.; Cardini, G.; Schettino, V. *Theor. Chem. Acc.* **2004**, *111*, 264.
(121) Mrozek, M. F.; Wasileski, S. A.; Weaver, M. J. *J. Am. Chem. Soc.* **2001**, *123*, 12817.
(122) Baia, M.; Baia, L.; Kiefer, W.; Popp, J. *J. Phys. Chem. B* **2004**, *108*, 17491.
(123) Frisch, M. J. e. a. *Gaussian Development Version, revision H.01, Gaussian, Inc.; Wallingford, CT* **2009**.
(124) Becke, A. D. *J. Chem. Phys.* **1993**, *98*, 5648.
(125) Lee, C.; Yang, W.; Parr, R. G. *Phys. Rebv. B* **1988**, *37*, 785.
(126) Vosko, S. H.; Wilk, L.; Nusair, M. *Can. J. Phys.* **1980**, *58*, 1200.
(127) Stephens, P. J.; Devlin, F. J.; Chabalowski, C. F.; Frisch, M. J. *J. Phys. Chem. A* **1994**, *98*, 11623.
(128) Sadlej, A. J. *Theor. Chim. Acta* **1992**, *81*, 339.
(129) Sadlej, A. J.; Urban, M. *J. Mol. Struct. (THEOCHEM)* **1991**, *80*, 147.
(130) Peterson, K. A.; Puzzarini, C. *Theor. Chem. Acc.* **2005**, *114*, 283−296.
(131) Miertus, S.; Scrocco, E.; Tomasi, J. *Chem. Phys.* **1981**, *55*, 117.
(132) Townsend, L. B. *Handbook of Biochemistry and Molecular Biology, Nucleic Acids, 3rd ed.; Fasman, D. G., Ed.; CRC Press: Cleveland, OH,* **1975**, *1*, 271.
(133) Kumler, W. D.; Eiler, J. J. *J. Am. Chem. Soc.* **1943**, *65*, 2355.
(134) Sa´nchez-Corte´s, S.; Garcı´a-Ramos, J. V. *J. Mol. Struct.* **1992**, *274*, 33.
(135) Bicknell-Broen, E.; Brown, K. G.; Person, W. B. *J. Raman Spectrosc.* **1981**, *11*, 356.
(136) Nowak, M. J.; Lapinski, L.; Kwiatowski, J. S.; Leszczyn˜ski, J. *J. Phys. Chem.*
**1996**, *100*, 3527−3534.
(137) Kyogoku, Y.; Lord, R. C.; Rich, A. *J. Am. Chem. Soc.* **1967**, *89*, 496.
(138) Angell, C. L. *J. Chem. Soc.* **1961**, 504.
(139) Khalil, F.; Brown, T. L. *J. Am. Chem. Soc.* **1964**, *86*, 5113.
(140) Itoh, K.; Minami, K.; Tsujino, T.; Kim, M. *J. Phys. Chem.* **1991**, *95*, 1339.
(141) Jensen, L. *J. Phys. Chem. A* **2009**, *113*, 4437
(142) Muniz-Miranda, M.; Sbrana, G. *J. Raman Spectrosc.* **1996**, *27*, 105.

(143) Muniz-Miranda, M. *J. Phys. Chem. A* **2000**, *104*, 7803.
(144) Guichelaar, M. A.; Reedijk, J. *J. R. Neth. Chem. Soc.* **1978**, *97*, 295.
(145) Ellington, A. D.; Szostak, J. W. *Nature* **1990**, *346*, 818.
(146) Robertson, D. L.; Joyce, G. F. *Nature* **1990**, *344*, 467.
(147) Tuerk, C.; Gold, L. *Science* **1990**, *249*, 505
(148) Bloomfield, V. A.; Crothers, D. M.; I. Tinoco, J. *Nucl. Acids Res., University Science Books, Sausalito, CA* **2000**.
(149) Zhang, Y.; Zhou, H.; Ou-Yang, Z.-C. *Biophys. J.* **2001**, *81*, 1133.
(150) Floege, J.; Ostendorf, T.; Janssen, U.; Burg, M.; Radeke, H. H.; Vargeese, C.; Gill, S. C.; Green, L. S.; Janjic´, N. *Am. J. Pathol.* **1999**, *154*, 169.
(151) Stojanovic, M. N.; Prada, P. d.; Landry, D. W. *J. Am. Chem. Soc.* **2001**, *123*, 4928.
(152) Lai, R. Y.; Plaxco, K. W.; Heeger, A. J. *Anal. Chem.* **2007**, *78*, 229.
(153) Huang, C. C.; Huang, Y. F.; Cao, Z.; Tan, W.; Chang, H. T. *Anal. Chem.* **2005**, *77*, 5735.
(154) Baker, B. R.; Lai, R. Y.; Wood, M. S.; Doctor, E. H.; Heeger, A. J.; Plaxco, K. W. *J. Am. Chem. Soc.* **2006**, *128*, 3138.
(155) Hermann, T.; Patel, D. J. *Science* **2000**, *287*, 820.
(156) Huang, C. C.; Chiu, S. H.; Huang, Y. F.; Chang, H. T. *Anal. Chem.* **2007**, *79*, 4798.
(157) Yang, C. J.; Jockusch, S.; Vicens, M.; Turro, N. J.; Tan, W. *PNAS* **2005,**, *102*, 17279.
(158) Hong, F.; Jung, M. C.; Meng, R.; Zhao, H.; Weber, S. G. *TrAC Trends in Analytical Chemistry* **2004**, *23*, xiii.
(159) Liu, J.; Lu, Y. *Angew. Chem Int. Ed* **2006**, *45*, 90.
(160) Stojanovic, M. N.; Landry, D. W. *J Am. Chem. Soc.* **2002**, *124*, 9678.
(161) Fredriksson, S.; Gullberg, M.; Jarvius, J.; Olsson, C.; Pietras, K.; Gústafsdóttir, S. M.; Östman, A.; Landegren, U. *Nat. Biotechnol.* **2002**, *20*, 473.
(162) Fang, X.; Sen, A.; Vicens, M.; Tan, W. *Chem. Bio. Chem.* **2003**, *4*, 829.
(163) Fang, X.; Cao, Z.; Beck, T.; Tan, W. *Anal. Chem.* **2001**, *73*, 5752.
(164) Zhao, J.; Zhang, X.; Yonzon, C.; Haes, A. J.; Duyne, R. P. V. *Nanomedicine* **2006**, *1*, 219.
(165) Braun, G.; Lee, S. J.; Dante, M.; Nguyen, T. Q.; Moskovits, M.; Reich, N. *J. Am. Chem. Soc.* **2007**, *129*, 6378.
(166) Shanmukh, S.; Jones, L.; Driskell, J.; Zhao, Y.; Dluhy, R.; Tripp, R. *Nano Lett.* **2006**, *6*, 2630.
(167) Camden, J. P.; Dieringer, J. A.; Zhao, J.; Van Duyne, R. P. *Acc. Chem. Res.* **2008**, *41*, 1653.
(168) Jackson, J. B.; Halas, N. J. *PNAS* **2004**, *101*, 17930.
(169) Michaels, A. M.; Jiang, J.; Brus, L. E. *J. Phys. Chem. B* **2000**, *104*, 11965.
(170) Ward, D. R.; Halas, N. J.; Ciszek, J. W.; Tour, J. M.; Wu, Y.; Nordlander, P.; Natelson, D. *Nano Lett.* **2008**, *8*, 919.
(171) Lal, S.; Grady, N. K.; Kundu, J.; Levin, C. S.; Halas, N. J. *Chem. Soc.Rev.* **2008**, *37*, 898.
(172) Barhoumi, A.; Zhang, D.; Tam, F.; Halas, N. J. *J. Am. Chem. Soc.* **2008**, *130*, 5523.

(173) Barhoumi, A.; Zhang, D.; Halas, N. J. *J. Am. Chem. Soc.* **2008**, *130*, 14040.
(174) Saenger, W.; Hunter, W. N.; Kennard, O. *Nature* **1986**, *324*, 385.
(175) Johnson, N. P.; Baase, W. A.; Hippel, P. H. *PNAS* **2004**, *101*, 3426.
(176) Mukerji, I.; Williams|, A. P. *Biochemistry* **2002**, *41*, 69.
(177) Malynych, S.; Luzinov, I.; Chumanov, G. *J. Phys. Chem. B* **2002**, *106*, 1280.
(178) Green, L. S.; Jellinek, D.; Jenison, R.; Östman, A.; Heldin, C.-H.; Janjic, N. *Biochemistry* **1996**, *35*, 14413.
(179) Balamurugan, S.; Obubuafo, A.; Soper, S. A.; McCarley, R. L.; Spivak, D. A. *Langmuir* **2006**, *22*, 6446.
(180) Gold, L.; Brody, E.; Heilig, J.; Singer, B. *Chem. Biol.* **2002**, *9*, 1259.
(181) Panyam, J.; Labhasetwar, V. *Adv. Drug Delivery Rev.* **2003**, *55*, 329.
(182) Niidome, T.; Huang, L. *Gene Ther.* **2002**, *9*, 1647.
(183) Shea, L. D.; Smiley, E.; Bonadio, J.; Mooney, D. J. *Nat. Biotechnol.* **1999**, *17*, 551.
(184) Richardson, T. P.; Peters, M. C.; Ennett, A. B.; Mooney, D. J. *Nat. Biotechnol.* **2001**, *19*, 1029.
(185) Kim, C. K.; Ghosh, P.; Pagliuca, C.; Zhu, Z. J.; Menichetti, S.; Rotello, V. M. *J. Am. Chem. Soc.* **2009**, *131*, 1360.
(186) LaVan, D. A.; McGuire, T.; Langer, R. *Nat. Biotechnol.* **2003**, *21*, 1184.
(187) Kim, S. Y.; Shin, I. L. G.; Lee, Y. M.; Cho, C. S.; Sung, Y. K. *J. Controlled Release* **1998**, *51*, 13.
(188) Chilkoti, A.; Dreher, M. R.; Meyer, D. E.; Raucher, D. *Adv. Drug Delivery Rev.* **2002**, *54*, 613.
(189) Boussif, O.; Lezoualch, F.; Zanta, M. A.; Mergny, M. D.; Scherman, D.; Demeneix, B.; Behr, J. P. *Proc. Natl. Acad. Sci. U.S.A.* **1995**, *92*, 7297.
(190) Shalek, A. K.; Robinson, J. T.; Karp, E. S.; Lee, J. S.; Ahn, D. R.; Yoon, M. H.; Sutton, A.; Jorgolli, M.; Gertner, R. S.; Gujral, T. S.; MacBeath, G.; Yang, E. G.; Park, H. *Proc. Natl. Acad. Sci. U.S.A.* **2010**, *107*, 1870.
(191) Chen, C. C.; Lin, Y. P.; Wang, C. W.; Tzeng, H. C.; Wu, C. H.; Chen, Y. C.; Chen, C. P.; Chen, L. C.; Wu, Y. C. *J. Am. Chem. Soc.* **2006**, *128*, 3709.
(192) Takahashi, H.; Niidome, Y.; Yamada, S. *Chem. Commun.* **2005** *17*, 2247.
(193) Wijaya, A.; Schaffer, S. B.; Pallares, I. G.; Hamad-Schifferli, K. *ACS Nano* **2009**, *3*, 80.
(194) Braun, G. B.; Pallaoro, A.; Wu, G. H.; Missirlis, D.; Zasadzinski, J. A.; Tirrell, M.; Reich, N. O. *ACS Nano* **2009**, *3*, 2007.
(195) Lee, S. E.; Liu, G. L.; Kim, F.; Lee, L. P. *Nano Lett.* **2009**, *9*, 562.
(196) Han, G.; You, C. C.; Kim, B. J.; Turingan, R. S.; Forbes, N. S.; Martin, C. T.; Rotello, V. M. *Angew. Chem., Int. Ed.* **2006**, *45*, 3165.
(197) Barhoumi, A.; Huschka, R.; Bardhan, R.; Knight, M. W.; Halas, N. J. *Chem. Phys. Lett.* **2009**, *482*, 171.
(198) Jones, M. R.; Millstone, J. E.; Giljohann, D. A.; Seferos, D. S.; Young, K. L.; Mirkin, C. A. *ChemPhysChem* **2009**, *10*, 1461.
(199) Prodan, E.; Nordlander, P.; Halas, N. J. *Nano Lett.* **2003**, *3*, 1411.

(200) Wang, H.; Brandl, D. W.; Nordlander, P.; Halas, N. J. *Acc. Chem. Res.* **2007**, *40*, 53.

(201) El-Sayed, I. H.; Huang, X.; El-Sayed, M. A. *Cancer Lett. (Amsterdam, Netherlands)* **2006**, *239*, 129.

(202) Hirsch, L. R.; Stafford, R. J.; Bankson, J. A.; Sershen, S. R.; Rivera, B.; Price, R. E.; Hazle, J. D.; Halas, N. J.; West, J. L. *Proc. Natl. Acad. Sci. U.S.A.* **2003**, *100*, 13549.

(203) Richardson, H. H.; Carlson, M. T.; Tandler, P. J.; Hernandez, P.; Govorov, A. O. *Nano Lett.* **2009**, *9*, 1139.

(204) Govorov, A. O.; Richardson, H. H. *Nano Today* **2007**, *2*, 30.

(205) Hirsch, L. R.; Jackson, J. B.; Lee, A.; Halas, N. J.; West, J. L. *Anal. Chem.* **2003**, *75*, 2377.

(206) Sershen, S. R.; Westcott, S. L.; Halas, N. J.; West, J. L. *J. Biomed. Mater. Res.* **2000**, *51*, 293.

(207) Hirsch, L. R.; Gobin, A. M.; Lowery, A. R.; Tam, F.; Drezek, R. A.; Halas, N. J.; West, J. L. *Ann. Biomed. Eng.* **2006**, *34*, 15.

(208) O'Neal, D. P.; Hirsch, L. R.; Halas, N. J.; Payne, J. D.; West, J. L. *Cancer Lett. (Amsterdam, Netherlands)* **2004**, *209*, 171.

(209) Choi, M. R.; Stanton-Maxey, K. J.; Stanley, J. K.; Levin, C. S.; Bardhan, R.; Akin, D.; Badve, S.; Sturgis, J.; Robinson, J. P.; Bashir, R.; Halas, N. J.; Clare, S. E. *Nano Lett.* **2007**, *7*, 3759.

(210) Weissleder, R. *Nat. Biotechnol.* **2001**, *19*, 316.

(211) Stephens, A. C.; Rivers, R. P. A. *Curr. Opin. Mol. Ther.* **2003**, *5*, 118.

(212) Neto, B. A. D.; Lapis, A. A. M. *Molecules* **2009**, *14*, 1725.

(213) Ihmels, H.; Otto, D. *Top. Curr. Chem.* **2005**, *258*, 161.

(214) Barcellona, M. L.; Gratton, E. *Eur. Biophys. J.* **1990**, *17*, 315.

(215) Manzini, G.; Xodo, L.; Barcellona, M. L.; Quadrifoglio, F. *J. Biosci.* **1985**, *8*, 699.

(216) Kapus´cins´ki, J.; Szer, W. *Nucleic Acids Res.* **1979**, *6*, 3519.

(217) Kubista, M.; Aakerman, B.; Norden, B. *Biochemistry* **1986**, *26*, 4545.

(218) Lin, M. S.; Comings, D. E.; Alfi, O. S. *Chromosoma* **1977**, *60*, 15.

(219) Jung, K. S.; Kim, M. S.; Lee, G. J.; Cho, T. S.; Kim, E. K.; Yi, S. Y. *Bull. Korean Chem. Soc.* **1997**, *18*, 510.

(220) Breusegem, S. Y.; Clegg, R. M.; Loontiens, F. G. *J. Mol. Biol.* **2002**, *315*, 1049.

(221) Ochsenkuhn, M. A.; Jess, P. R. T.; Stoquert, H.; Dholakia, K.; Campbell, C. J. *ACS Nano* **2009**, *3*, 3613.

(222) Chithrani, B. D.; Ghazani, A. A.; Chan, W. C. W. *Nano Lett.* **2006**, *6*, 662.

(223) Giljohann, D. A.; Seferos, D. S.; Patel, P. C.; Millstone, J. E.; Rosi, N. L.; Mirkin, C. A. *Nano Lett.* **2007**, *7*, 3818.

(224) Lydon, M. J.; Keeler, K. D.; Thomas, D. B. *J. Cell. Physiol.* **1980**, *102*, 175.

(225) Taylor, I. W. *J. Histochem. Cytochem.* **1980**, *28*, 1021.

(226) Dengler, W. A.; Schulte, J.; Berger, D. P.; Mertelsmann, R.; Fiebig, H. H. *Anti-Cancer Drugs* **1995**, *6*, 522.

(227) Hendry, L. B.; Mahesh, V. B.; Bransome, E. D.; Ewing, D. E. *Mutat. Res.* **2007**, *623*, 53.

(228) Wheate, N. J.; Brodie, C. R.; Collins, J. G.; Kemp, S.; Aldrich-Wright, J. R. *Mini-Rev. Med. Chem.* **2007**, *7*, 627.

(229) Dieguez, M.; Pamies, O.; Claver, C. *Chem. Rev.* **2004**, *104*, 3189

(230) Zhang, J.; Albelda, M. T.; Liu, Y.; Canary, J. W. *Chirality* **2005**, *17*, 404.

(231) Hicks, J. M. *American Chemical Society; ACS Symposium Series* **2002**.

(232) Hicks, J. M. *Am. Chem. Soc., Washington, DC* **2002**, *Chapter 1*, 2.

(233) Hug, W.; Hangartner, G. *J. Raman Spectrosc.* **1999**, *30*, 841.

(234) Abdali, S.; Blanch, E. W. *Chem. Soc. Rev.* **2008**, *37*, 980.

(235) Lassiter, J. B.; Aizpurua, J.; Hernandez, L. I.; Brandl, D. W.; Romero, I.; Lal, S.; Hafner, J. H.; Nordlander, P. e.; Halas., N. J. *Nano Lett.* **2008**, *8*, 1212.

(236) Janesko, B. G.; Scuseria, G. *J. Phys. Chem. C* **2009**, *113*, 9445.

(237) Jensen, L. *J. Phys. Chem A* **2009**, *113*, 4437.

(238) Nafie, L.

(239) Nafie, L. A.; Brinson, B. E.; Cao, X.; Rice, D.; Rahim, O.; Durkor, R. K.; Halas, N. *Appl. Spectrosc.* **2007**, *61*, 1103.

(240) Barron, L. D. *2nd Ed.; Cambridge University Press* **2004**.

(241) Acevedo, R.; Lombardini, R.; Halas, N. J.; Johnson, B. R. *J. Phys. Chem. A* **2009**, *113*, 13173.

(242) Blanch, E. W.; Bell, A. F.; Hecht, L.; Day, L. A.; Barron, L. D. *J. Mol. Bio.* **1999**, *290*, 1.

(243) Blanch, E. W.; Hecht, L.; Day, L. A.; Pederson, D. M.; Barron, L. D. *J. Am. Chem. Soc.* **2001**, *123*, 4863.

(244) Jacob, C. R.; Luber, S.; Reiher, M. *Chem. Phys. Chem.* **2008**, *9*, 2177.

(245) Delgado, J. M.; Orts, J. M.; Pe´rez, J. M.; Ro, A. *J. Electroanalytical Chem.* **2008**, 130.

(246) Zhang, D.; Ben-Amotz, D. *Appl. Spectrosc.* **2000**, *54*, 1379.

(247) Podstawka, E.; Kudelski, A.; Proniewicz, L. M. *Surface Sci.* **2007**, *601*, 4971.

(248) Lin-Vien, D.; Colthup, N. B.; Fateley, W. G.; Grasselli, J. G. *The Handbook of Infrared and Raman Charactoristic Frequencies of Organic Molecules*; Academic Press. Inc.: San Diego, CA, 1991.

(249) Behar-Levy, H.; Neumann, O.; Naaman, R.; Avnir, D. *Adv. Mater.* **2007**, *19*, 1207.

(250) Yannopapas, V. *Optics Lett.* **2009**, *34*, 632.

(251) Nishida, N.; Yao, H.; Kimura, K. *Langmuir* **2008**, *24*, 2759.

(252) Trusova, V. M.; Gorbenko, G. P.; Deligeorgiev, T.; Gadjev, N.; Vasilev, A. *J Fluoresc* **2009**.

(253) Shapiro, B. I. *Russian Chemical Reviews* **1997**, *66*, 255.

(254) Spitler, M.; Parkinson, B. A. *Langmuir* **1986**, *2*, 549.

(255) Chen, P.; Li, J.; Qian, Z.; Zheng, D.; Okasaki, T.; Hayami, M. *Dyes and Pigments* **1998**, *37*, 213.

(256) White, G.; Pruett, J. G. *Optics Letters* **1981**, *6*, 473.

(257) Elsaesser, T.; Kaiser, W. *Topics in Applied Physics, Dye Lasers: 25 Years Ed.: Dr. Michael Stuke, Springer Berlin / Heidelberg* **1992**, *70*.

(258) Tong, L. K. J.; Glesmann, M. C. *J. Am. Chem. Soc.* **1956**, *78*, 5827.
(259) Aitken, C. E.; Marshall, R. A.; Puglisiz, J. D. *Biophysical Journal* **2008**, *94*, 1826.
(260) Arunkumar, E.; Forbes, C. C.; Smith, B. D. *Eur. J. Org. Chem.* **2005**, 4051.
(261) Wanga, L.; Penga, X.; Songa, F.; Lua, E.; Cuia, J.; Gaoa, X.; Lua, R. *Dyes and Pigments* **2004**, *61*, 103.
(262) Liao, W.-Y.; Li, M. C.; Hu, A. T.; Lee, S. *Jpn. J. Appl. Phys.* **2003**, *42*, 3447.
(263) Amiot, C. L.; Xu, S.; Liang, S.; Pan, L.; Zhao, J. X. *Sensors* **2008**, *8*, 3082.
(264) Abdullah, F. H.; Rauf, M. A.; S.Ashraf, S. *Dyes and Pigments* **2007**, *72*, 349.
(265) Hirsch, L. R.; Jackson, J. B.; Lee, A.; Halas, N. J.; West, J. L. *Anal. Chem.* **2003**, *75*, 2377.
(266) Hirsch, L. R.; Stafford, R. J.; Bankson, J. A.; Sershen, S. R.; Rivera, B.; Price, R. E.; Hazle, J. D.; Halas, N. J.; West, J. L. *PNAS* **2003**, *11*, 13549.
(267) Fofang, N. T.; Park, T. H.; Neumann, O.; Mirin, N. A.; Nordlander, P.; Halas, N. J. *Nano. Lett.* **2008**, *8*, 3481.
(268) Bishnoi, S. W.; Rozell, C. J.; Levin, C. S.; Gheith, M. K.; Johnson, B. R.; Johnson, D. H.; Halas, N. J. *Nano. Lett.* **2006**, *6*, 1687.
(269) Oldenburg, S. J.; Averitt, R. D.; Westcott, S. L.; Halas, N. J. *Chem. Phys. Lett.* **1998**, *288*, 243.
(270) Oldenburg, S. J.; Jackson, J. B.; Westcott, S. L.; .Halas, N. J. *Applied Physics Letters* **1999**, *75*, 2897.
(271) Luzzi, A.; Lovegrove, K. *Encyclopedia of Energy, Elsevier Inc.* **2004**, *5*, 669
(272) Meier, A.; Gremaud, N.; Steinfeld, A. *Energy Convers. Manage.* **2005**, *46*, 905.
(273) Hirsch, L. R.; Stafford, R. J.; Bankson, J. A.; Sershen, S. R.; Rivera, B.; Price, R. E.; Hazle, J. D.; Halas, N. J.; West, J. L. *Proc Natl Acad Sci U S A.* **2003**, *11*, 13549.
(274) Lukianova-Hleb, E. Y.; Lapotko, D. O. *Nano Lett.* **2009**.
(275) Chen, X.; Chen, Y. T.; Yan, M.; Qiu, M. *ACS Nano* **2012**, *6*, 2550.
(276) Carlson, M. T.; Green, A. J.; Richardson, H. H. *Nano Lett.* **2012**, *12*, 1534.
(277) Baffou, G.; Bon, P.; Savatier, J.; Polleux, J.; Zhu, M.; Merlin, M.; Rigneault, H.; Monneret, S. *ACS Nano* **2012**, *6*, 2452.
(278) Donner, J. S.; Baffou, G.; McCloskey, D.; Quidant, R. *ACS Nano* **2012**, *5*, 5457.
(279) Ye, E. Y.; Win, K. T.; Tan, H. R.; Lin, M.; Teng, C. P.; Mlayah, A.; Han, M. Y. *J. Am. Chem. Soc* **2011**, *133*, 8506.
(280) Liu, Z. W.; Hung, W. H.; Aykol, M.; Valley, D.; Cronin, S. B. *Nanotechnology* **2010**, *21*.
(281) Ma, H. Y.; Bendix, P. M.; Oddershede, L. B. *Nano Lett.* **2012**, *12*, 3954.
(282) Baffou, G.; Quidant, R.; Abajo, F. J. G. d. *ACS Nano* **2010**, *4*, 709.
(283) Sanchot, A.; Baffou, G.; Marty, R.; Arbouet, A.; Quidant, R.; Girard, C.; Dujardin, E. *ACS Nano* **2012**, *6*, 3434.

(284) Zhu, M.; Baffou, G.; Meyerbroker, N.; Polleux, J. *ACS Nano* **2012**, *6*, 7227.
(285) Gao, Y.; Yuan, Z.; Gao, S. W. *J. Chem. Phys.* **2011**, *134*.
(286) Skirtach, A. G.; Dejugnat, C.; Braun, D.; Susha, A. S.; Rogach, A. L.; Parak, W. J.; Mohwald, H.; Sukhorukov, G. B. *Nano Lett.* **2005**, *5*, 1371.
(287) Boyer, D.; Tamarat, P.; Maali, A.; Lounis, B.; Orrit, M. *Science* **2002**, *297*, 1160.
(288) Moon, H. K.; Lee, S. H.; Choi, H. C. *ACS Nano* **2009**, *3*, 3707.
(289) Han, D. X.; Meng, Z. G.; Wu, D. X.; Zhang, C. Y.; Zhu, H. T. *Nanoscale Res. Lett.* **2011**, *6*.
(290) Otanicar, T. P.; Phelan, P. E.; Golden, J. S. *Solar Energy* **2009**, *83*, 969.
(291) Otanicar, T. P.; Phelan, P. E.; Prasher, R. S.; Rosengarten, G.; Taylor, R. A. *J. Renewable Sustainable Energy* **2010**, *2*, 033102.
(292) Roper, D. K.; Ahn, W.; Hoepfner, M. *J. Phys. Chem. C* **2007**, *111*, 3636.
(293) Huttmann, G.; Birngruber, R. *IEEE Journal of Selected Topics in Quantum Electronics* **1999**, *5*, 954.
(294) Lapotko, D. *Optics Express* **2009**, *17*, 2538.
(295) Oldenburg, S. J.; Averitt, R. D.; Westcott, S. L.; Halas, N. J. *J. Chem. Phys. Lett.* **1998**, *288*, 243.
(296) Oldenburg, S. J.; Jackson, J. B.; Westcott, S. L.; Halas, N. J. *Appl. Phys. Lett.* **1999**, *75*, 2897.
(297) Amini, A.; Owen, I. *Flow Meas. Instrum.* **1995**, *6*, 41.
(298) Low, D. A. *Ed. Longmans, Green and Co. 39 Paternoster Row, London* **1920**.
(299) Ramires, M. L. V.; Decastro, C. A. N.; Nagasaka, Y.; Nagashima, A.; Assael, M. J.; Wakeham, W. A. *J. Phys. Chem. Ref. Data* **1995**, *24*, 1377.
(300) Eastman, J. A.; Phillpot, S. R.; Choi, S. U. S.; Keblinski, P. *Annu. Rev. Mater. Res* **2004**, *34*, 219.
(301) Organization, W. H. *http://www.who.int/gpsc/country_work/burden_hcai/en/index.html* **2010**.
(302) Organization, W. H. *http://apps.who.int/medicinedocs/documents/s16355e/s16355e.pdf.* **2002**.
(303) Organization, W. H. *www.who.int/entity/medical_devices/poster_a18.pdf* **2010**.
(304) Orrett, F. A.; Brooks, P. J.; Richardson, E. G. *Infection Control and Hospital Epidemiology* **1998**, *19*, 136.
(305) Pacific, U. N. E. a. S. C. f. A. a. t. *http://www.unescap.org/pdd/publications/ themestudy2006/9_ch3.pdf.* **2006**.
(306) Rutala, W. A.; Weber, D. J. *MMWR Morb Mortal Wkly Rep, in press*.
(307) Neumann, O.; Urban, A. S.; Day, J.; Lal, S.; Nordlander, P.; Halas, N. J. *ACS Nano* **2012**, *(Accepted, 10.1021/nn304948h).*
(308) Richardson, H. H.; Carlson, M. T.; Tandler, P. J.; Hernandez, P.; Govorov, A. O. *Nano Lett.* **2009**, *9*, 1139.
(309) O'Neal, P. D.; Hirsch, L. R.; Halas, N. J.; Payne, J. D.; West, J. L. *Cancer Lett.* **2004**, *209*, 171.

(310) Huang, X.; Jain, P. K.; HI, H. I. E.-S.; El-Sayed, M. A. *Lasers Med. Sci.* **2008**, *23*, 217.
(311) Lee, J. Y.; P, P. P. *Optics Express* **2010**, *18*, 10078.
(312) Branch, I. C. D. *http://www.fda.gov/downloads/MedicalDevices/DeviceRegulationandGuidance/GuidanceDocuments/UCM081341.pdf.* **1993**.
(313) Organization, W. H. *http://www.who.int/gpsc/country_work/burden_hcai/en/index.html.* **2010**.
(314) Organization, W. H. *http://apps.who.int/medicinedocs/documents/s16355e/s16355e.pdf* **2002**.
(315) Organization, W. H. *www.who.int/entity/medical_devices/poster_a18.pdf* **2010**.
(316) Rutala, W. A.; Weber, D. J. *MMWR Morb Mortal Wkly Rep in press.*
(317) Taylor, R. A.; Phelan, P. E.; Otanicar, T.; Adrian, R. J.; Prasher, R. S. *App. Phys. Letter* **2009**, *95*, 1619071.
(318) Jorapur, R. M.; Rajvanshi, A. K. *ISES Solar World Congress Proceedings* **1991**, *I*, 772.
(319) Neumann, O.; Urban, A. S.; Day, J.; Lal, S.; Nordlander, P.; Halas, N. J. *ACS Nano* **2012**, *(Accepted, 10.1021/nn304948h).*
(320) Martinez-Frias, J.; Aceves, S. M.; Flowers, D. L. *J. Energy Res. Tech. ASME* **2007**, *129*, 332.
(321) Madson, P. W. *KATZEN International, Inc., Cincinnati, Ohio, USA.*
(322) Murti, P. S.; Winkle, M. v. *Ind. Eng. Chem.* **1957**, *3*, 72.
(323) Walker, J. *http://www.wiley.com/college/phy/halliday320005/pdf/leidenfrost_essay.pdf*.
(324) Mejı´a, S. M.; Mills, M. J. L.; Shaik, M. S.; Mondragona, F.; Popelier, P. L. A. *Phys. Chem. Chem. Phys.* **2011**, *13*, 7821.
(325) Soper, A. K.; Dougan, L.; Crain, J.; Finney, J. L. *J. Phys. Chem. B* **2006**, *110*, 3472.
(326) Nedic´, M.; Wassermann, T. N.; Xue, Z.; Zielke, P.; Suhm, M. A. *Phys. Chem. Chem. Phys.* **2008**, *10*, 5953.
(327) Wensink, E. J. W.; Hoffmann, A. C.; Maaren, P. J. v.; Spoela, D. v. d. *J. Chem. Phys.* **2003**, *119*, 7308.
(328) Scatena, L. F.; Brown, M. G.; Richmond, G. L. *Science* **2001**, *292*, 908.
(329) Coussan, S.; Roubin, P.; Perchard, J. P. *J. Phys. Chem. A* **2004**, *108*, 7331.
(330) Nishi, N.; Koga, K.; Ohshima, C.; Yamamoto, K.; Nagashima, U.; Nagami, K. *J. Am. Chem. Soc.* **1988**, *110*, 5246.
(331) Wakisaka, A.; Abdoul-Carime, H.; Yamamotob, Y.; Kiyozumi, Y. *J. Chem. Soc., Faraday T rans.* **1998**, *94*, 369.
(332) Nishi, N.; Takahashi, S.; Matsumoto, M.; Tanaka, A.; Muraya, K.; Takamuku, T.; Yamaguchi, T. *J. Phys. Chem. A* **1995**, *99*, 462.
(333) Daniel, M. C.; Astruc, D. *Chem. Rev.* **2004**, *104*, 293.
(334) Burda, C.; Chen, X.; Narayanan, R.; El-Sayed, M. A. *Chem. Rev.* **2005**, *105*, 1025.
(335) Elghanian, R.; Storhoff, J. J.; Mucic, R. C.; Letsinger, R. L.; Mirkin, C. A. *Science* **1997**, *227*, 1078.

(336) Haes, J. A.; Hall, P. W.; Chang, L.; Klein, W. L.; Duyne, R. P. V. *Nano Lett.* **2004**, *4*, 1029.

(337) Liao, H. G.; Jiang, Y. X.; Zhou, Z. Y.; Chen, S. P.; Sun, S. G. *Angew. Chem.* **2008**, *47*, 9100.

(338) O'Neal, D. P.; Hirsch, L. R.; Halas, N. J.; Payne, D. J.; West, L. J. *Canc. Lett.* **2004**, *209*, 171.

(339) Sau, T. K.; Rogach, A. L.; Ja¨ckel, F.; Klar, T. A.; Feldmann, J. *Adv. Mater.* **2009**, *21*, 1.

(340) Eustis, S.; El-Sayed, M. A. *Chem. Soc. Rev.* **2006**, *35*, 209.

(341) Zhao, L.; Ji, X.; Sun, X.; Li, J.; Yang, W.; Peng, X. *J. Phys. Chem. C* **2009**, *113*, 16645.

(342) Jena, B. K.; Raj, C. R. *Langmuir* **2007**, *23*, 4064.

(343) Wang, W.; Cui, H. *J. Phys. Chem. C* **2008**, *112*, 10759.

(344) Sajanlal, P. R.; Pradeep, T. *Nano Res* **2009**, *2*, 306.

(345) Nehl, C. L.; Liao, H.; Hafner, J. H. *Nano Lett.* **2006**, *6*, 683.

(346) Esenturk, E. N.; Walker, A. R. H. *J. Raman Spectrosc.* **2008**, *40*, 86.

(347) Winkler, K.; Kaminska, A.; Wojciechowski, T.; Holyst, R.; Fialkowski, M. *Plasmonics* **2011**, *6*, 697.

(348) Guo, S.; Wang, E. *J. Coll. Interf. Sci.* **2007**, *315*, 795.

(349) Neumann, O.; Urban, A. S.; Day, J.; Lal, S.; Nordlander, P.; Halas, N. J. *ACS Nano* **2013**, *7*, 42.

(350) Liu, Z.; Hou, W.; Pavaskar, P.; Aykol, M.; Cronin, S. B. *Nano Lett.* **2011**, *11*, 1111.

(351) Linic, S.; Christopher, P.; Ingram, D. B. *Nature Materials* **2011**, *10*, 911.

(352) Anker, J. N.; Hall, W. P.; O.Lyandres; Shah, N. C.; Zhao, J.; Duyne, R. P. V. *Nature Materials* **2008**, *7*, 442

(353) Hao, F.; Nehl, C. L.; Hafner, J. H.; Nordlander, P. *Nano Lett.* **2007**, *7*, 729.

(354) Kumar, P. S.; Pastoriza-Santos, I.; Rodr´ıguez-Gonz´alez, B.; Abajo, F. J. G. d.; Liz-Marz´an, L. M. *Nanotechnology* **2008**, *19*, 015606 (6pp).

(355) Aydin, K.; Ferry, V. E.; Briggs, R. M.; Atwater, H. A. *Nature Communication* **2011**, *DOI: 10.1038/ncomms1528*.

(356) Day, J. K.; Neumann, O.; Grady, N. K.; Halas, N. J. *ACS Nano* **2010**, *4*, 7566.

(357) Fan, J. A.; Wu, C. H.; Bao, K.; Bao, J. M.; Bardhan, R.; Halas, N. J.; Manoharan, V. N.; Nordlander, P.; Shvets, G.; Capasso, F. *Science* **2010**, *328*, 1135.

(358) Wu, C.; Mosher, B. P.; Zeng, T. *Mater. Res. Soc. Symp. Proc.* **2005**, *879E*, Z6.3.1.

(359) Li, C.; Cai, W.; Cao, B.; Sun, F.; Li, Y.; Kan, C.; Zhang, L. *Adv. Funct. Mater.* **2006**, *16*, 83.

(360) Huang, M. C. Y.; Zhou, Y.; Chang-Hasnain, C. J. *Nat. Photonics* **2008**, *2*, 180.

(361) Caruge, J. M.; Halpert, J. E.; Wood, V.; Bulovic´, V.; Bawendi, M. G. *Nat. Photonics* **2008**, *2*, 247.

(362) Mack, N. H.; Wackerly, J. W.; Malyarchuk, V.; Rogers, J. A.; Moore, J. S.; Nuzzo, R. G. *Nano Lett.* **2007**, *7*, 733.

(363) Lal, S.; Link, S.; Halas, N. J. *Nat. Photonics* **2007**, *1*, 641.

(364) Parker, A. R.; Townley, H. E. *Nat. Nanotechnol* **2007**, *2*, 347.
(365) Tang, L.; Shi, L.; Bonneau, C.; Sun, J.; Yue, H.; Ojuva, A.; B. L. Lee; Kritikos, M.; Bell, R. G.; Bacsik, Z.; Mink, J.; Zou, X. *Nat. Mater* **2008**, *7*, 381.
(366) Gao, L.; Zhuang, J.; Nie, L.; Zhang, J.; Zhang, Y.; Gu, N.; Wang, T.; Feng, J.; Yang, D.; Perrett, S.; Yan, X. *Nat. Nanotechnol.* **2007**, *2*, 577.
(367) Ladet, S.; David, L.; Domard, A. *Nature* **2008**, *452*, 76.
(368) Wang, H.; Brandl, D. W.; Le, F.; Nordlander, P.; Halas, N. J. *Nano Lett.* **2006**, *6*, 827.
(369) Thorp, J. C.; Sieradzki, K.; Tang, L.; Crozier, P. A.; Misra, A.; Nastasi, M.; Mitlin, D.; Picraux, S. T. *Appl. Phys. Lett.* **2006**, *88*, 033110.
(370) Yang, D.; Meng, G.; Zhang, S.; Hao, Y.; An, X.; Wei, Q.; Yeab, M.; Zhang, L. *Chem. Commun.* **2007**, *17*, 1733.
(371) Ozaki, M.; Kratohvil, S.; Matijevic, E. *J. Colloid lnterface Sci.* **1984**, *102*, 146.
(372) Duff, D. G.; Baiker, A.; Edwards, P. P. *Langmuir* **1993**, *9*, 2301.
(373) Li, S.; Zhang, H.; Wu, J.; Ma, X.; Yang, D. *Cryst. Growth Des.* **2006**, *6*, 351.
(374) Chen, R.; Chen, H.; Wei, Y.; Hou, D. *J. Phys. Chem. C* **2007**, *111*, 16453.
(375) Bocquet, S.; Pollard, R. J.; Cashion, J. D. *Phys. Rev. B* **1992**, *46*, 11657.
(376) Bocquet, S.; Hill, A. J. *Phys. Chem. Miner.* **1995**, *22*, 524.
(377) Wang, H.; Goodrich, G. P.; Tam, F.; Oubre, C.; Nordlander, P.; Halas, N. J. *J. Phys. Chem. B* **2005**, *109*, 11083.
(378) Bae, D. H.; Lee, M. H.; Kim, K. T.; Kim, W. T.; Kim, D. H. *J. Alloys Compd.* **2002**, *342*, 445.
(379) Chernyshova, I. V.; Hochella, M. F. J.; Madden, A. S. *Phys. Chem. Chem. Phys.* **2007**, *9*, 1736.
(380) Pomie`s, M. P.; Morin, G.; Vignaud, C. *Eur. J. Solid State Inorg. Chem.* **1998**, *35*, 9.
(381) Morup, S.; Madsen, M. B.; Franck, J.; Villadsen, J.; Koch, C. J. W. *J. Magn. Magn. Mater* **1983**, *40*, 163.
(382) Bocquet, S.; Kennedy, S. J. *J. Magn. Magn. Mater.* **1992**, *109*, 260.
(383) Guyodo, Y.; Mostrom, A.; Penn, R. L.; Banerjee, S. K. *Geophys. Res. Lett.* **2003**, *30*, 19.
(384) Barrero, C. A.; Betancur, J. D.; Greneche, J. M.; Goya, G. F.; Berquo, T. S. *Geophys. J. Int.* **2006**, *164*, 331.
(385) Ahniyaz, A.; Sakamoto, Y.; Bergstrom, L. *Proc. Nat. Acad. Sci. U.S.A.* **2007**, *104*, 17570.
(386) Penn, R. L.; Stone, A. T.; Veblen, D. R. *J. Phys. Chem. B* **2001**, *105*, 4690.
(387) Li, W.-J.; Shi, E.-W.; Zhong, W.-Z.; Yin, Z.-W. *J. Cryst. Growth* **1999**, *203*, 186.
(388) Banfield, J. F.; Welch, S. A.; Zhang, H.; Ebert, T. T.; Penn, R. L. *Science* **2000**, *289*, 751.
(389) Penn, R. L.; Banfield, J. F. *Science* **1998**, *281*, 969.
(390) Kubista, M.; Akerman, B.; Nordén, B. *Biochemistry* **1986**, *26*, 4545.

(391) Manzini, G.; Barcellona, M. L.; Avitabile, M.; Quadrifoglio, F. *Nucl. Acids Res.* **1983**, *11*, 8861.

# APENDIX A

## Calculated and experimental frequencies of adenine

| Mode | Freq ($cm^{-1}$) | Plane | Assignment |
|---|---|---|---|
| 1' | 3692 | in | str $NH_2$ (antisymmetric) |
| 2' | 3603 | in | str N9-H |
| 3' | 3570 | in | str NH2(symmetric), N1-H |
| 4' | 3564 | in | str NH2(symmetric), N1-H |
| 5' | 3238 | in | str C8-H |
| 6' | 3198 | in | str C2-H |
| 1 | 1722 | in | sciss $NH_2$, str C6-N10, C5-C6, bend N1-H |
| 2 | 1652 | in | str C6-N1, C2-N3, bend N1-H, C2-H, sciss $NH_2$ |
| 3 | 1628 | in | sciss $NH_2$, bend N1-H |
| 4 | 1607 | in | str C2-N3, N3-C4, bend N1-H, C2-H, N9-H |
| 5 | 1520 | in | str C4-C5, N7-C8, N3-C4, bend C8-H, sciss $NH_2$ |
| 6 | 1480 | in | str C6-N1, C5-N7, C5-C6, C2-N3, C4-N9, bend N10-H |
| 7 | 1452 | in | str C4-N9, N7-C8, C6-N10, bend N1-H, C2-H, |
| 8 | 1428 | in | bend N1-H, C2-H, N9-H, str N1-C2 |
| 9 | 1407 | in | bend N9-H, str C8-N9, bend N1-H, C2-H |
| 10 | 1371 | in | bend C2-H, C8-H, str C5-N7 |
| 11 | 1337 | in | bend C2-H, N9-H, C8-H, str C5-N7, C6-N1 |
| 12 | 1261 | in | bend C8-H, N9-H, rock $NH_2$ |
| 13 | 1174 | in | rock $NH_2$, bend N1-H, C2-H, C8-H, str N1-C2 |
| 14 | 1132 | in | str N1-C2, bend N1-H, C8-H |
| 15 | 1076 | in | str C8-N9, bend N9-H, C8-H |
| 16 | 1000 | in | rock $NH_2$ |
| 17 | 969 | out | wag C2-H |
| 18 | 943 | in | def R5 (sqz group N7-C8-N9) |
| 19 | 926 | out | wag C8-H |
| 20 | 902 | in | def R6 (sqz N1-C2-N3) |
| 21 | 820 | out | def R6 (wag C4-C5-C6), wag C8-H |
| 22 | 721 | in | Ring breath whole molecule |
| 23 | 705 | out | wag N1-H, def R5, R6 (wag C4-C5-C6, wag N3-C4-N9) |
| 24 | 679 | out | wag N1-H, def R5 (wag C5-N7-C8, C8-N9-C4) |
| 25 | 657 | out | wag N9-H, N1-H, def R5 (wag C5-N7-C8) |
| 26 | 633 | out | wag N9-H, def R5, R6 (wag N7-C8-N9, C6-N1-C2) |
| 27 | 617 | in | def R5, R6 (sqz group C4-C5-C6, N1-C6-N10, C5-N7-C8) |
| 28 | 567 | out | wag N1-C2-N3, wag C4-N9-C8 |
| 29 | 534 | out | tors $NH_2$, wag N1-H |
| 30 | 528 | in | def R6 (sqz group N1-C6-C5, N10-C6-C5 |
| 31 | 513 | in | def R6 (sqz group C2-N3-C4, N1-C6-C5 |
| 32 | 363 | out | wag N10-H |
| 33 | 291 | out | def R6 (wag N1-C2-N3-C4) |
| 34 | 276 | in | bend C6-$NH_2$ |
| 35 | 219 | out | Butterfly |
| 36 | 174 | out | tors molecule, wag C6-$NH_2$ |

**Table A1.** Calculated gas-phase B3LYP/Sadlej and experimental frequencies of adenine

[a]As in Ref. 7, primes are modes not tabulated in Ref. 34
[b]Experimental values from Ref. 34
[c] B3LYP/6-311++G(d,p) values from Ref. 34
[d]Bend, bending; breath, breathing; def, deformation; rock, rocking; sciss, scissoring; str, stretching; wag, wagging; R5, five membered ring; R6, six membered ring.

**Table A2.** Calculated gas-phase B3LYP/Sadlej vibrational frequencies of adenine-H+, protonation at nitrogen N1

| Mode | Freq ($cm^{-1}$) | Plane | Assignment |
|---|---|---|---|
| 1' | 3692 | in | str $NH_2$ (antisymmetric) |
| 2' | 3603 | in | str N9-H |
| 3' | 3570 | in | str NH2(symmetric), N1-H |
| 4' | 3564 | in | str NH2(symmetric), N1-H |
| 5' | 3238 | in | str C8-H |
| 6' | 3198 | in | str C2-H |
| 1 | 1722 | in | sciss $NH_2$, str C6-N10, C5-C6, bend N1-H |
| 2 | 1652 | in | str C6-N1, C2-N3, bend N1-H, C2-H, sciss $NH_2$ |
| 3 | 1628 | in | sciss $NH_2$, bend N1-H |
| 4 | 1607 | in | str C2-N3, N3-C4, bend N1-H, C2-H, N9-H |
| 5 | 1520 | in | str C4-C5, N7-C8, N3-C4, bend C8-H, sciss $NH_2$ |
| 6 | 1480 | in | str C6-N1, C5-N7, C5-C6, C2-N3, C4-N9, bend N10-H |
| 7 | 1452 | in | str C4-N9, N7-C8, C6-N10, bend N1-H, C2-H, |
| 8 | 1428 | in | bend N1-H, C2-H, N9-H, str N1-C2 |
| 9 | 1407 | in | bend N9-H, str C8-N9, bend N1-H, C2-H |
| 10 | 1371 | in | bend C2-H, C8-H, str C5-N7 |
| 11 | 1337 | in | bend C2-H, N9-H, C8-H, str C5-N7, C6-N1 |
| 12 | 1261 | in | bend C8-H, N9-H, rock $NH_2$ |
| 13 | 1174 | in | rock $NH_2$, bend N1-H, C2-H, C8-H, str N1-C2 |
| 14 | 1132 | in | str N1-C2, bend N1-H, C8-H |
| 15 | 1076 | in | str C8-N9, bend N9-H, C8-H |
| 16 | 1000 | in | rock $NH_2$ |
| 17 | 969 | out | wag C2-H |
| 18 | 943 | in | def R5 (sqz group N7-C8-N9) |
| 19 | 926 | out | wag C8-H |
| 20 | 902 | in | def R6 (sqz N1-C2-N3) |
| 21 | 820 | out | def R6 (wag C4-C5-C6), wag C8-H |
| 22 | 721 | in | Ring breath whole molecule |
| 23 | 705 | out | wag N1-H, def R5, R6 (wag C4-C5-C6, wag N3-C4-N9) |
| 24 | 679 | out | wag N1-H, def R5 (wag C5-N7-C8, C8-N9-C4) |
| 25 | 657 | out | wag N9-H, N1-H, def R5 (wag C5-N7-C8) |
| 26 | 633 | out | wag N9-H, def R5, R6 (wag N7-C8-N9, C6-N1-C2) |
| 27 | 617 | in | def R5, R6 (sqz group C4-C5-C6, N1-C6-N10, C5-N7-C8) |
| 28 | 567 | out | wag N1-C2-N3, wag C4-N9-C8 |
| 29 | 534 | out | tors $NH_2$, wag N1-H |
| 30 | 528 | in | def R6 (sqz group N1-C6-C5, N10-C6-C5 |
| 31 | 513 | in | def R6 (sqz group C2-N3-C4, N1-C6-C5 |
| 32 | 363 | out | wag N10-H |
| 33 | 291 | out | def R6 (wag N1-C2-N3-C4) |
| 34 | 276 | in | bend C6-$NH_2$ |
| 35 | 219 | out | Butterfly |
| 36 | 174 | out | tors molecule, wag C6-$NH_2$ |

**Table A3.** Calculated gas-phase B3LYP/Sadlej/aug-cc-pVTZ-PP vibrational frequencies of adenine-Au+, with Au bound at nitrogen N3

| Mode | Freq ($cm^{-1}$) | Plane | Assignment |
|---|---|---|---|
| 1' | 3704 | in | str $NH_2$ (antisymmetric) |
| 2' | 3619 | in | str N9-H |
| 3' | 3571 | in | str $NH_2$ (symmetric) |
| 4' | 3239 | in | str C8-H |
| 5' | 3192 | in | str C2-H |
| 1 | 1686 | in | sciss $NH_2$, str C6-N10, C5-C6 |
| 2 | 1628 | in | str N3-C4, N1-C2, N7-C8, bend N9-H |
| 3 | 1618 | in | sciss $NH_2$ |
| 4 | 1529 | in | str N7-C8, bend C8-H, C2-H, sciss $NH_2$ |
| 5 | 1506 | in | str N1-C2, N1-C6, N7-C8, bend C2-H, sciss $NH_2$ |
| 6 | 1497 | in | str N1-C6, N1-C2, bend N9-H |
| 7 | 1459 | in | str C4-C5, C4-N7, N1-C2, bend C2-H |
| 8 | 1402 | in | bend C2-H, N9-H |
| 9 | 1373 | in | bend C8-H, N9-H, C2-H, str C8-N9 |
| 10 | 1331 | in | str C5-N7, N1-C2, C2-N3, bend C8-H, N9-H |
| 11 | 1258 | in | bend C8-H, N9-H, C2-H, rock $NH_2$ |
| 12 | 1228 | in | rock $NH_2$, str C2-N3 |
| 13 | 1160 | in | bend C8-H, N10-H, str N3-Au, C4-N9, N3-C4, C6-N10 |
| 14 | 1069 | in | str C8-N9, bend N9-H, C8-H |
| 15 | 1012 | in | rock $NH_2$, str C6-N1 |
| 16 | 990 | out | wag C2-H |
| 17 | 942 | in | def R5 (sqz group N7-C8-N9) |
| 18 | 933 | in | def R6 (sqz group N1-C2-N3), R5 (str C5-N7) |
| 19 | 899 | out | wag C8-H |
| 20 | 808 | out | def R6 (wag C4-C5-C6), wag C8-H |
| 21 | 743 | in | Ring breathing |
| 22 | 692 | out | def R5, R6 (tors C4-C5-C6, wag N3-C4-N9) |
| 23 | 661 | out | def R5 (wag C5-N7-C8, C8-N9-C4), wag C8-H, N9-H, tors $NH_2$ |
| 24 | 612 | in | def R6 (sqz group C4-C5-C6, N1-C6-N10, R5 (sqz group C5-N7-C8) |
| 25 | 611 | out | tors $NH_2$ |
| 26 | 554 | in | def R6 (sqz group N1-C6-C5, C2-N3-C4) , str N3-Au |
| 27 | 549 | out | wag N9-H, N1-C2-N3 |
| 28 | 536 | in | def R5, R6 (sqz group N3-C4-N9, N10-C6-C5 |
| 29 | 532 | out | wag N1-C2-N3, wag C4-N9-C8 |
| 30 | 449 | out | wag $NH_2$ |
| 31 | 323 | out | wag N3-Au, tors N1-C2-N3-C4 |
| 32 | 284 | in | bend C6-$NH_2$ |
| 33 | 218 | out | butterfly |
| 34 | 196 | in | str N3-Au |
| 35 | 170 | out | R5, R6 torsion |
| 36 | 115 | in | N3-Au rock |
| 37 | 64 | out | N3-Au wag |

**TABLE A4.** Calculated gas-phase B3LYP/Sadlej/aug-cc-pVTZ-PP vibrational frequencies of adenine-Au+, with Au bound at nitrogen N7

| Mode | Freq ($cm^{-1}$) | Plane | Assignment |
|---|---|---|---|
| 1' | 3714 | in | str $NH_2$ (antisymmetric) |
| 2' | 3597 | in | str N9-H |
| 3' | 3578 | in | str $NH_2$ (symmetric) |
| 4' | 3262 | in | str C8-H |
| 5' | 3181 | in | str C2-H |
| 1 | 1671 | in | sciss $NH_2$, str C6-N10, N1-C2, C5-C6, C5-C4 |
| 2 | 1643 | in | sciss $NH_2$, str C5-C6, N3-C4, rock N9-H |
| 3 | 1607 | in | sciss $NH_2$, str C5-C6 |
| 4 | 1539 | in | str N7-C8, C8-N9, bend C8-H, C2-H, sciss $NH_2$ |
| 5 | 1506 | in | bend C2-H, C8-H, N9-H, str N1-C6, str C2-N3, sciss $NH_2$ |
| 6 | 1457 | in | bend C2-H, N9-H, str C8-N9 |
| 7 | 1419 | in | str C4-C5, C4-N7, C6-N10, bend N9-H, C2-H |
| 8 | 1371 | in | str N1-C2, N3-C4, C4-C5, C6-N1, bend C2-H |
| 9 | 1361 | in | bend C2-H, N10-H |
| 10 | 1324 | in | str C5-N7, C2-N3, C5-C6, wag C8-H, rock $NH_2$ |
| 11 | 1267 | in | bend C8-H, N9-H, str C2-N3, C5-N7 |
| 12 | 1234 | in | rock $NH_2$, str C5-N7, C6-N1, bend N9-H, C8-H |
| 13 | 1160 | in | bend N9-H, str C4-N9 |
| 14 | 1123 | in | bend N9-H, C8-H |
| 15 | 1039 | out | wag C2-H |
| 16 | 1016 | in | rock $NH_2$, str C6-N1 |
| 17 | 994 | in | def R5 (sqz group N7-C8-N9), rock $NH_2$, str N7-Au |
| 18 | 889 | in | def R6 (sqz group N1-C2-N3), str C5-N7, C4-N9 |
| 19 | 882 | out | wag C8-H |
| 20 | 816 | out | def R6 (wag C4-C5-C6), wag C8-H |
| 21 | 727 | in | Ring breathing |
| 22 | 688 | out | def R5, R6 (tors C4-C5-C6, wag N3-C4-N9) |
| 23 | 659 | out | wag N9-H |
| 24 | 621 | in | def R6 (sqz group C4-C5-C6, N1-C6-N10, R5 (sqz group C5-N7-C8) |
| 25 | 612 | out | wag N7-C8-N9, wag N1-C2-N3 |
| 26 | 556 | out | wag N1-C2-N3, wag C8, N9 |
| 27 | 535 | in/out | tors $NH_2$, def R6 (sqz group N1-C6-C5, C2-N3-C4 ) |
| 28 | 527 | in/out | tors $NH_2$, def R6 (sqz group C2-N3-C4, C2-N1-C6 ) |
| 29 | 515 | in/out | tors $NH_2$ |
| 30 | 322 | in | bend C6-$NH_2$ |
| 31 | 308 | out | wag N1-C2-N3-C4 |
| 32 | 235 | in/out | str N7-Au, wag $NH_2$ |
| 33 | 219 | in/out | butterfly, str N7-Au |
| 34 | 186 | out | wag N10-H, wag N7-Au |
| 35 | 177 | out | wag N10-H, wag N7-Au |
| 36 | 96 | in | N7-Au rock |
| 37 | 34 | out | N7-Au wag |

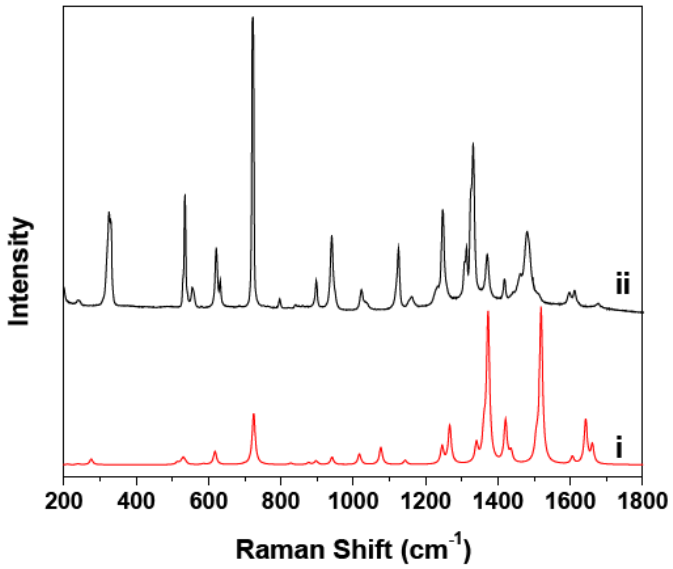


**Figure A1** (i) Calculated B3LYP/Sadlej vibrational Raman spectrum of adenine, and (ii) experimental powder Raman spectrum of adenine. Calculated Raman activities are broadened by Lorentzians of width 10 $cm^{-1}$, intensities are in arbitrary units.

# APENDIX B

## Nanoshell-dsDNA-DAPI complex characterization

**Fluorescence spectroscopy**: The fluorescence measurements in solution were completed on a spectrometer [Cary Eclipse (Varian) multi-cell Peltier] system.

**Circular Dichroism (CD):** The CD measurements were performed using a JASCO J-810 spectropolarimeter equipped with a Peltier-type temperature control system for wavelengths ranging from 180 to 800 nm.

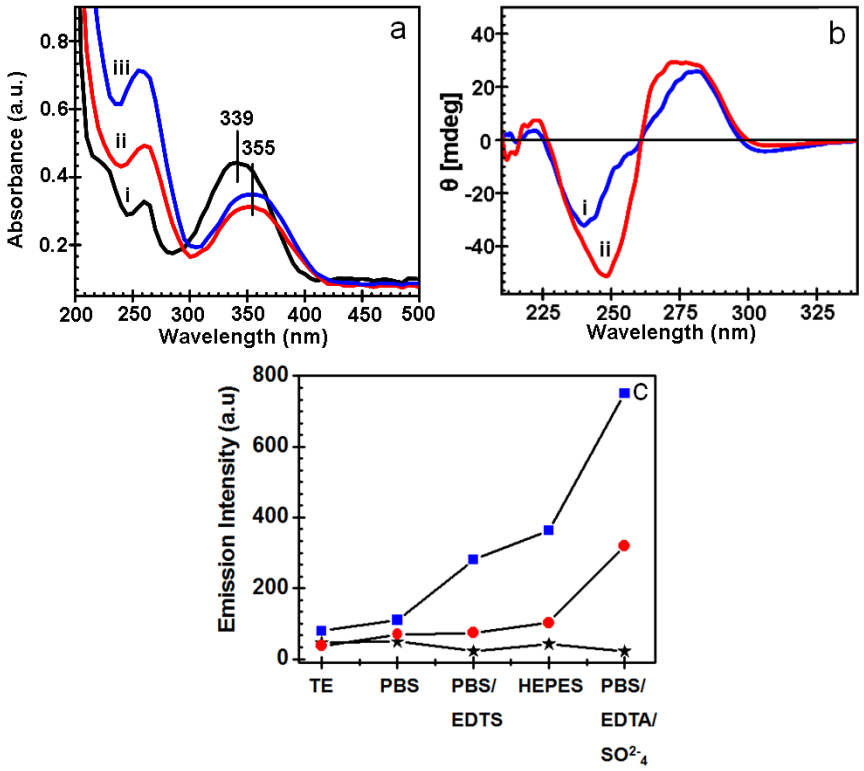


Figure B1: (a) Absorption spectra of (i) DAPI alone, (ii) DAPI with ssDNA, and (iii) DAPI with dsDNA solutions (b) CD spectra of (i) dsDNA, (ii) dsDNA with DAPI. (c) Effect of the different buffers at the same pH=7.5 on the fluorescent emission spectra of DAPI associated with dsDNA at 458nm.

UV-Vis absorption and Circular Dichroism (CD) were used to characterize the binding of DAPI to *ds*DNA and is presented in Figure B1. Intercalation of DAPI into *ds*DNA was confirmed by the red shift in the absorption spectra (Figure B1a). CD measurements were performed to investigate the *ds*DNA and DAPI intercalation (Figure B1b). The dsDNA CD spectrum is characterized by two positive peaks at 278 nm, 221 nm and a negative one at 240 nm; introducing the DAPI molecules to the *ds*DNA solution causes a blue shift of the CD packs at 275 nm and 247 nm respectively. Figure S1c shows the effect of the different buffers at the same pH=7.5 on the fluorescent emission spectra of DAPI associated with *ds*DNA at 458nm. The significant increase in the fluorescence quantum yield revealed by the emission spectra in figure B1c has been achieved by adding sodium sulfate.

Previous studies have shown that the fluorescence of DAPI is enhanced by A-T base-pairs.[214,216,218-219,390-391] Our studies correlate well to these previous findings that DAPI affinity increases with the number of minor grooves of A/T-rich binding sites, Figure B2. The enhancement of fluorescence intensity is significantly bigger for 26 bp DNA oligo compared with the 50bp DNA oligo. Even though the 50 bp DNA oligo has a higher percentage of A-T base pairs, the 26 bp DNA oligo has higher fluorescence intensity. This is because the 26 bp oligo was designed with multiple A-T rich regions. Previous reports find that the strength of the DAPI binding to DNA is dependent upon the sequence of the A-T rich regions in the following order: ATT > TAAT ≈ATAT > TATA ≈TTAA (shown in a decreasing order).[220]

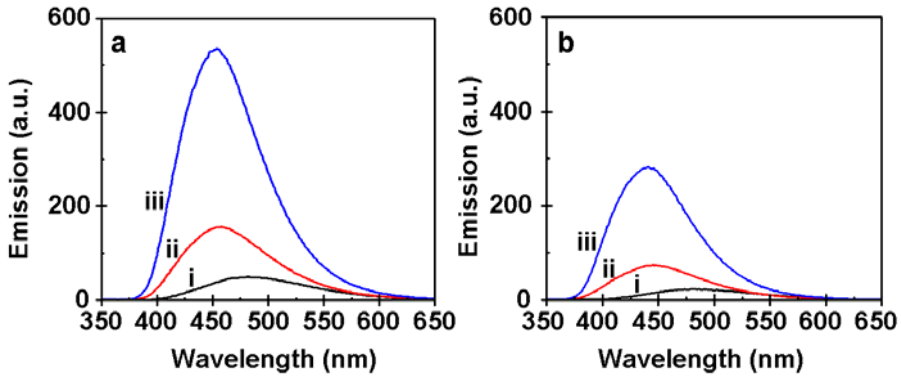


**Figure B2:** Fluorescence spectra of (i) DAPI alone, (ii) DAPI with ssDNA, and (iii) DAPI with dsDNA solutions; (A) 26 bp DNA and (B) 50 bp DNA oligonucleotide, demonstrating the affinity for AT-rich binding sites. The DNA oligonucleotides used in this study are: 26-bp DNA oligo: 5'-GAT ATC CTA TAC GGA ATT CGA ATT CG-3' and 50bp DNA oligo: 5'-GAC TGC GAC CAA CCT AGC CTG CTA TGA TGT ACG GTC AAC CTG ATT GCC GC-3'

To quantify the increase in DAPI fluorescence observed after laser treatment, the average area of the DAPI fluorescence per cell was determined before and after laser treatment (Figure S5c). Alexa Fluor 488 WGA (wheat germ agglutinin) was used to outline the cell membrane and to mark the area of each cell, and then the DAPI fluorescence intensity within this area was quantified. If the DAPI fluorescence intensity of a pixel was statistically greater than the background fluorescence, it was counted. The average percentage a real increase of DAPI fluorescence per cell was then calculated by dividing the number of fluorescent pixels in each cell image by the total number of pixels corresponding to the area of the cell. The standard deviation was found by analyzing eight epifluorescence images. This observed increase in DAPI fluorescence after laser

treatment (10%) demonstrates that the NS-*ds*DNA complex effectively released its guest molecules from the *ds*DNA host carriers inside the cells.

The relatively low average increase in DAPI fluorescence per cell can be explained by several factors. The cell-to-cell variation of DAPI fluorescence is relatively large. The epifluorescence images (Figure B3a-b) reveal that some cells show a dramatic increase in DAPI fluorescence per cell, while others show virtually no increase. This cell-to-cell variation likely reflects both NS-*ds*DNA-DAPI uptake efficiency and efficiency of light-induced DAPI release. One possible way to decrease the variation in NS-*ds*DNA-DAPI particle uptake would be to increase the number of NS-*ds*DNA-DAPI particles by attaching a targeting moiety on the NS surface such as cholesterol or antibodies.

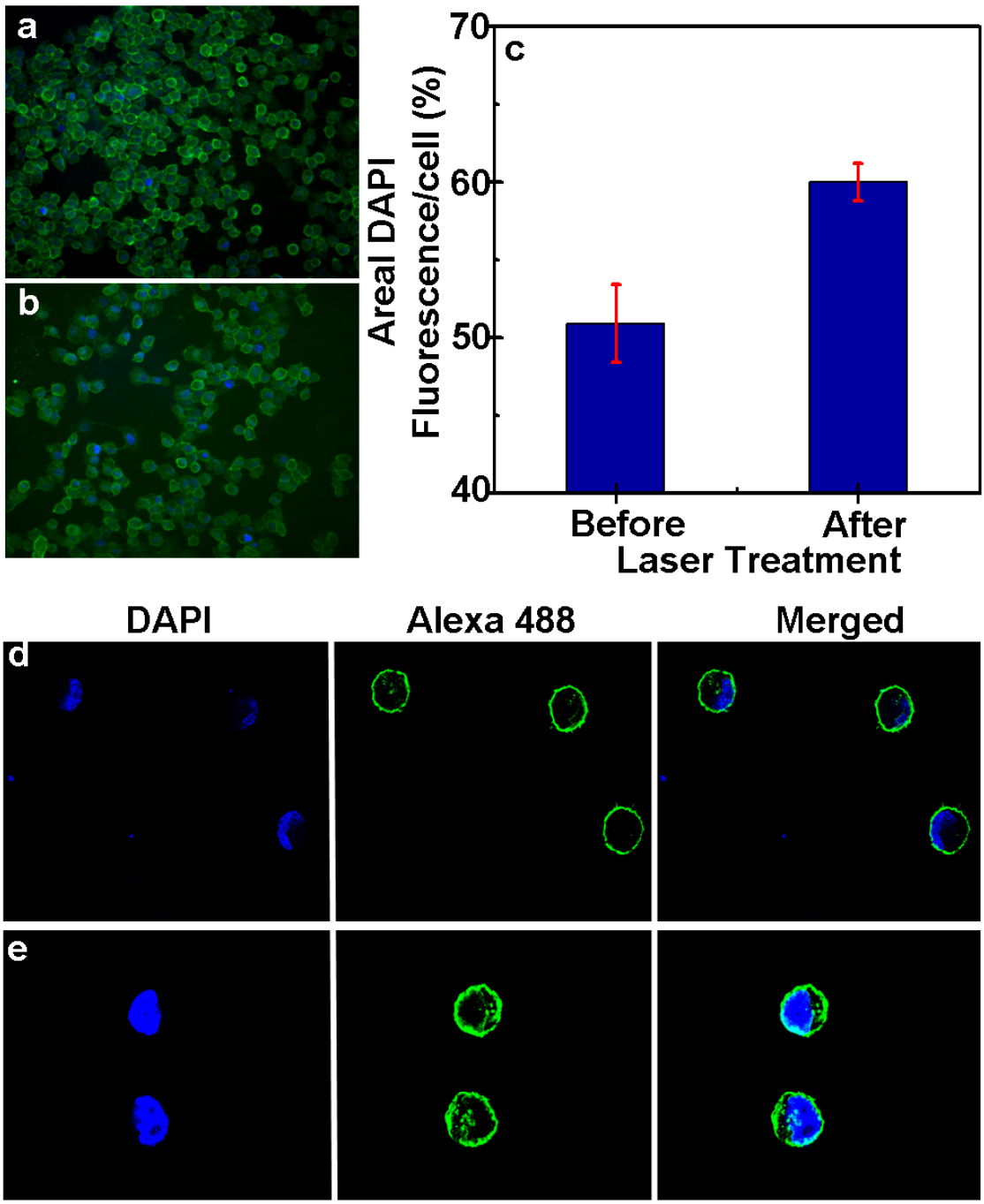


Figure B3. Light-induced DAPI release and nucleus staining. (a-b) Epifluorescence images of H1299 cells incubated with NS-*ds*DNA-DAPI before (a) and after (b) laser treatment. (c) Quantitative analysis of the average area of DAPI fluorescence per cell

obtained from eight epifluorescence images. (d, e) Confocal images of H1299 cells incubated with NS-*ds*DNA-DAPI before (d) and after (e) laser treatment.

These targeting molecules would then preferentially bind to receptors on the cell membrane surface that would facilitate internalization of the NS-dsDNA-DAPI into the cell increasing the cell uptake and reducing the variation from cell to cell. Variation in release efficiencies would also contribute to variation in the increase of areal DAPI fluorescence per cell. Previous work demonstrates that light-induced dsDNA dehybridization from nanoshells results in ~50% dehybridization on average.[197]

Some nanoshells within cells may release more DAPI then others depending on their accessibility to illumination, again resulting in variation of a real DAPI fluorescence per cell. To examine the light-induced release process with higher resolution, higher magnification confocal images of individual H1299 cells with a significant increase in DAPI fluorescence were obtained (Figure B3d-e). These confocal images of cells incubated with NS-dsDNA-DAPI complexes before (Figure B3d) and after (Figure B3e) laser treatment show a significant increase in a real DAPI fluorescence.

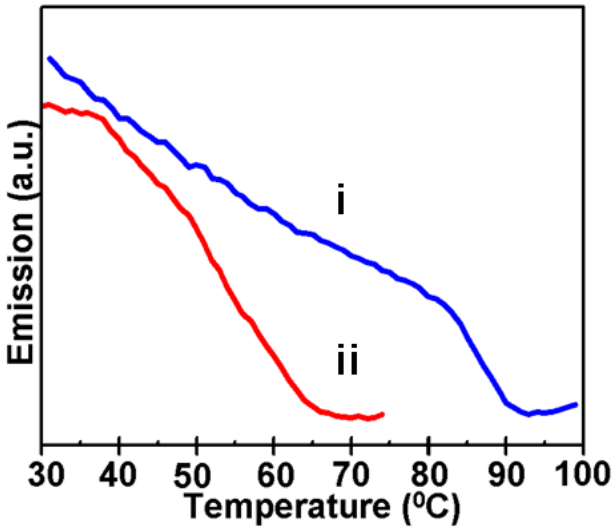


Figure B4. Fluorescence emission of DAPI as a function of temperature (heat rate is of 1°C/min) showing reversible binding of DAPI (i) from *ds*DNA in solution and (ii) from NS-*ds*DNA-DAPI complexes. As the DAPI is released, the fluorescence emission intensity decreases.

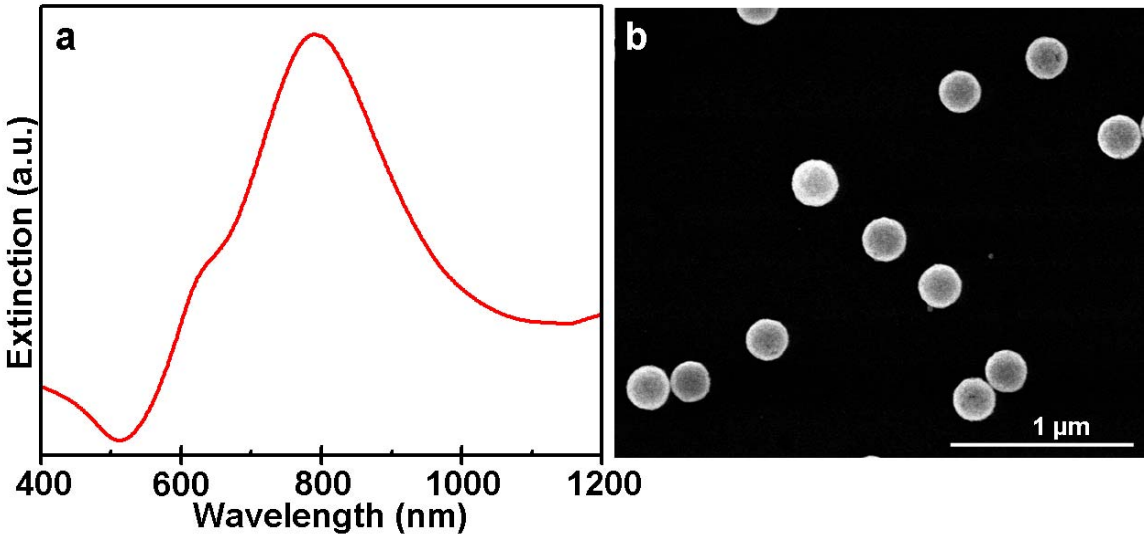


Figure B5. (a) Extinction spectra of $[r_1, r_2]$ = [63, 78] nm NSs in water. (b) SEM image of NSs on silicon substrate.

# APENDIX C

## Inhibition of DNDTPC-P dye oxidation through adsorption on nanoshells surface

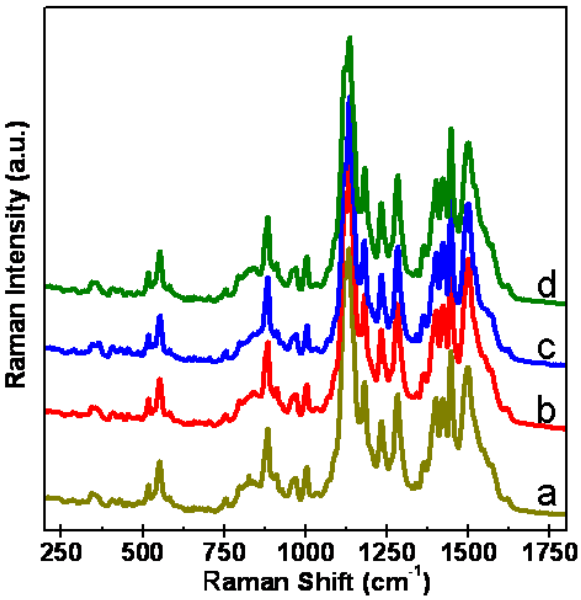


**Figure C1** SERS spectra of DNDTPC-P dye in fresh state attached to nanoshell surface taken after (a) 5 min., (b) 10 min., (c) 20 min, and (d) 60 min. Spectra reproducibility prove that DNDTPC-P dye is chemically stable once is attached to NS

| Frequencies ($cm^{-1}$) | Assignment |
|---|---|
| 1677 | Naphthyl C=C stretch |
| 1645 | Linker C=C stretch |
| 1625 | Linker C=C stretch |
| 1616 | Linker and naphthyl C=C stretch |
| 1584 | C2=C3, C4=C5 stretch |
| 1566 | Naphthyl C-H bend |
| 1557 | Linker C= Cstretch, C-H bend |
| 1540 | N-CH3 C-H bend |
| 1509 | Coupled C-H bends across pi system |
| 1497 | CH2 bends |
| 1493 | CH2 bends |
| 1483 | Coupled C-H bends across pi system |
| 1449 | CH2 rocks, C2-H bend |
| 1422 | C6-H, C8-H bend |
| 1417 | C2-H, C4-H bend |
| 1384 | CH2 wags |
| 1351 | CH2 wags |
| 1304 | CH2 torsions |
| 1275 | C2-H, C4-H bend |
| 1252 | CH2 C-H bend, C6-H bend |
| 1228 | CH2 C-H bend, C4-H, C6-H bend |
| 1196 | Naphthyl C-H bend |
| 1181 | CH2 C-H rock |
| 1176 | N-CH3 torsion |
| 1171 | Naphthyl C-H bend |

| | |
|---|---|
| 1153 | N-CH3 C-H bend |
| 1084 | N-CH3 stretch, N-CH3 C-H bend bend |
| 1006 | Naphthyl ring deformation |
| 989 | CH2 C-C stretch |
| 952 | CH2 C-C stretch |
| 944 | CH2 C-C stretch |
| 930 | Bridge C-H wag |
| 929 | Bridge C-H wag |
| 927 | Napthyl ring deformation |
| 905 | CH2 C-H2 rock |
| 819 | C1-H wag |
| 769 | CH2 C-H2 rock |
| 695 | Naphthyl ring deformation |
| 687 | Naphthyl ring deformation |
| 672 | Naphthyl ring deformation |
| 586 | C4-H , C6-H wag |
| 553 | Naphthyl ring deformation |
| 520 | Napthyl out-of-plane C-H wag |

**Table C1.** Calculated assignments of the Raman-active vibrational modes of DNDTPC ("ip" represents in-plane and "def" stands for deformation).

# APENDIX D

## A Compact Solar Autoclave enabled by broadband light-harvesting nanoparticles:

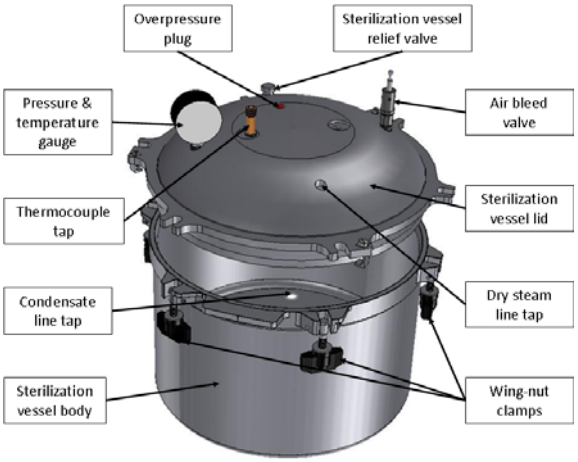


**Figure D1** The autoclave unit

The sterilization vessel is a lightly modified stovetop autoclave. It is composed of a body, in which the majority of the vessels volume is held, and the lid, which is threaded onto the body using a set of wing-nuts. Steam is channeled through a specially machined port in the top of the lid, and condensate is returned through the bottom of the vessel.

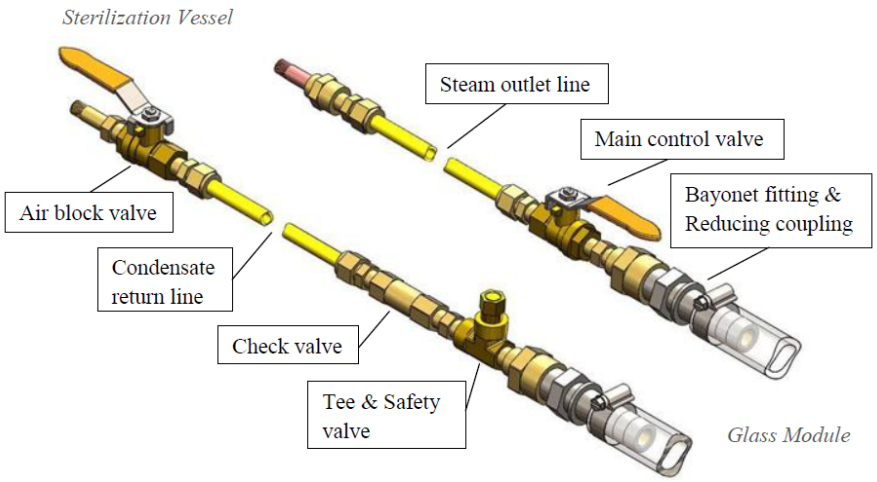


**Figure D2** The physical layout of the primary components that make up the connection system for the autoclave.

The connection system is composed of the steam line leading from the glass module to the sterilization vessel, the condensate line leading from the bottom of the sterilization vessel to the glass sterilization vessel.

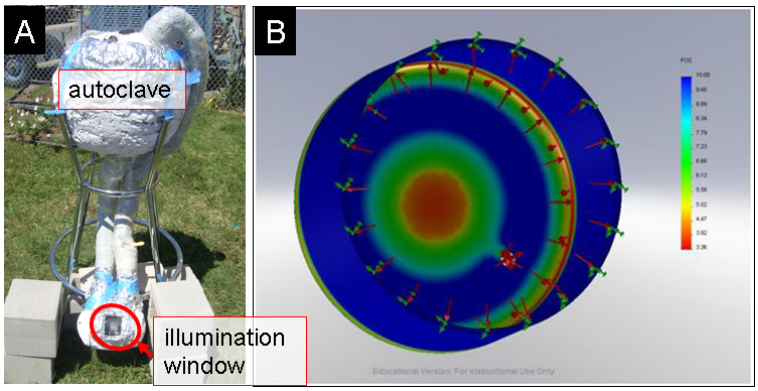


**Figure D3** (A) The photograph of the solar close-loop system and (B) the results from one of the Finite Element Analyses that were run to determine the best location for the steam condensate tap in the sterilization vessel.